

NASA/TM-2002-

James L. Mueller¹ and Giulietta S. Fargion²
Editors

¹ *CHORS, San Diego State University, San Diego, California*

² *Science Applications International Corporation, Beltsville, Maryland*

Ocean Optics Protocols For Satellite Ocean Color Sensor Validation, Revision 3, Part I

J. L. Mueller, C. Pietras, S. B. Hooker, D. K. Clark, A. Morel, R. Frouin, B.G. Mitchell, R. R. Bidigare, C. Trees, J. Werdell, G. S. Fargion, R. Arnone, R. W. Austin, S. Bailey, W. Broenkow, S. W. Brown, K. Carder, C. Davis, J. Dore, M. Feinholz, S. Flora, Z.P. Lee, B. Holben, B. C. Johnson, M. Kahru, D. M. Karl, Y. S Kim, K. D. Knobelspiesse, C. R. McClain, S. McLean, M. Miller, C. D. Mobley, J. Porter, R.G. Steward, M. Stramska, L. Van Heukelem, K. Voss, J. Wieland, M. A. Yarbrough and M. Yuen.

National Aeronautical and
Space administration

Goddard Space Flight Space Center
Greenbelt, Maryland 20771

February 2002

NASA/TM-2002-

James L. Mueller¹ and Giulietta S. Fargion²
Editors

¹ *CHORS, San Diego State University, San Diego, California*

² *Science Applications International Corporation, Beltsville, Maryland*

Ocean Optics Protocols For Satellite Ocean Color Sensor Validation, Revision 3, Part I

J. L. Mueller, C. Trees and R. W. Austin
*CHORS, San Diego, State University, San
Diego, California*

C. Pietras and G. S. Fargion
*Science Applications International
Corporation, Maryland*

S. Hooker, B. Holben and C. R. McClain
*NASA, Goddard Space Flight Center,
Greenbelt, Maryland*

D. K. Clark and M. Yuen
*NOAA National Environmental Satellite Data
Information Service, Suitland, Maryland*

A. Morel
*Laboratoire d'Océanographie, Université
Pierre et Marie Curie, France*

R. Frouin, B. Greg Mitchell, M. Kahru,
J. Wieland and M. Stramska

*Scripps Institution of Oceanography,
University of California, California*

R. R. Bidigare, D. M. Karl and J. Dore
*Department of Oceanography, University of
Hawaii, Hawaii*

P. J. Werdell and K. D. Knobelspiesse
Science Systems & Applications Inc., Maryland

R. Arnone
*Naval Research Laboratory, Stennis Space
Center, Mississippi*

S. Bailey
Futuretech Corporation, Greenbelt, Maryland

W. Broenkow, M. Feinholz, S. Flora and
M. A. Yarbrough,
Moss Landing Marine Laboratory, California
K. Carder, Z.P. Lee and R.G. Steward
University of South Florida, Florida
C. Davis

Naval Research Laboratory, Washington DC
B. C. Johnson and S. W. Brown
*National Institute of Standards and
Technology, Maryland*

Y. S. Kim
Data Systems Technologies, Inc., Maryland
S. McLean

Satlantic Inc., Halifax, Nova Scotia, Canada
M. Miller

*Department of Applied Science, Brookhaven
National Laboratory, New York*

C. D. Mobley
Sequoia Scientific Inc., Redmond, Washington
J. Porter

*School of Ocean & Earth Science and
Technology, University of Hawaii, Hawaii*

L. Van Heukelem
*University of Maryland Center for
Environmental Science, Maryland*

K. Voss
*Physics Department, University of Miami,
Florida*

National Aeronautical and
Space administration

Goddard Space Flight Space Center
Greenbelt, Maryland 20771

February 2002

Preface

This document stipulates protocols for measuring bio-optical and radiometric data for the Sensor Intercomparison and Merger for Biological and Interdisciplinary Oceanic Studies (SIMBIOS) Project activities and algorithm development. This document supersedes the earlier version (Fargion and Mueller 2000) and is organized into four parts:

- *Introductory Background:* The initial part covers perspectives on ocean color research and validation (Chapter 1), fundamental definitions, terminology, relationships and conventions used throughout the protocol document (Chapter 2), and requirements for specific *in situ* observations (Chapter 3).
- *Instrument Characteristics:* This group of chapters begins with a review of instrument performance characteristics required for *in situ* observations to support validation (Chapter 4), and the subsequent chapters cover detailed instrument specifications and underlying rationale (Chapter 5) and protocols for instrument calibration and characterization standards and methods (Chapters 6 through 8).
- *Field Measurements and Data Analysis:* The methods used in the field to make the *in situ* measurements needed for ocean color validation, together with methods of analyzing the data, are briefly, but comprehensively, reviewed in Chapter 9. The remaining chapters of this part provide detailed measurement and data analysis protocols for in-water radiometric profiles (Chapter 10), the Marine Optical Buoy (MOBY) radiometric observatory for vicarious calibration of satellite ocean color sensors (Chapter 11), above water measurements of remote sensing reflectance (Chapter 12), determinations of exact normalized water-leaving radiance (Chapter 13), atmospheric radiometric measurements to determine aerosol optical thickness and sky radiance distributions (Chapter 14), determination of absorption spectra from water samples (Chapter 15), and determination of phytoplankton pigment concentrations using HPLC (Chapter 16) and fluorometric (Chapter 17) methods.
- *Data Reporting and Archival:* Chapter 18 describes the methods and procedures for data archival, data synthesis and merging, and quality control applicable to the SeaWiFS Bio-optical Archive and Storage System (SeaBASS), which is maintained to support ocean color validation for the SeaWiFS, SIMBIOS and other cooperating satellite sensor projects. Current SeaBASS file content and formatting requirements are given in Appendix B.

What is new in Revision 3 to the ocean optics protocol document, as compared to Revision 2 (Fargion and Mueller 2000). The most obvious changes are the insertion of 3 new chapters into the document, and the renumbering of the other chapters to accommodate them. The new chapters are:

1. Chapter 2, *Fundamental Definitions, Relationships and Conventions*, introduces the radiometric quantities, inherent optical properties, fundamental concepts and terminology underlying the *in situ* measurement and analysis protocols discussed throughout the document. The chapter also discusses the scales adopted in these protocols for such quantities as extraterrestrial solar irradiance, and the absorption and scattering coefficients of pure water.
2. Chapter 11, *MOBY, A Radiometric Buoy for Performance Monitoring and Vicarious Calibration of Satellite Ocean Color Sensors: Measurement and Data Analysis Protocols*, documents the specific measurement and data analysis protocols used in the operation of this critical radiometric observatory. The MOBY normalized water-leaving radiance time series has provided the principal, common basis for vicarious calibration of every satellite ocean color sensor in operation since 1996.
3. Chapter 13, *Normalized Water-Leaving Radiance and Remote Sensing Reflectance: Bidirectional Reflectance and Other Factors*, develops the physical basis underlying the bidirectional aspects of the ocean's reflectance, and presents methods for removing this effect to determine *exact normalized water-leaving radiance*, the only form of water-leaving radiance suitable for comparisons between determinations based on satellite and *in situ* measurements.

Aside from renumbering, several of the chapters carried over from Revision 2 have been revisited and significantly revised, while others have been modified only slightly. The two chapters providing overviews of Instrument Characteristics (Chapter 4) and Field Measurements and Data Analysis (Chapter 9) have been revised to reflect the changed content of those two major parts of the document. Chapter 15, covering

protocols for laboratory spectrophotometric determinations of absorption by particles and dissolved materials in seawater samples, has been significantly revised to condense the workshop results reported in the Revision 2 version into more focused descriptions of measurement and analysis protocols; the more detailed workshop results and background in the original version of this chapter (as cited in the present version) comprise the single case where material presented in Revision 2 is not completely superceded by the present document. Protocols for HPLC measurements of concentrations of phytoplankton pigments (Chapter 16) and fluorometric measurements of chlorophyll a concentration (Chapter 17) have been significantly updated and revised. Protocols for characterization of radiometers (Chapter 6) and for calibration of, and measurements using, sun photometers and sky radiance instruments (Chapters 7 and 14) have been updated significantly, but modestly, and modifications to the remaining chapters are all relatively minor.

Although the present document represents another significant, incremental improvement in the ocean optics protocols, there are several protocols that have either been overtaken by recent technological progress, or have been otherwise identified as inadequate. Some of the deficiencies and corrective steps that will be taken in Revision 4, scheduled for completion in 2002, include:

- The present state of the art in instruments and methods for determining *inherent optical properties* (IOP) is described only via abstract-level summaries in Chapters 4 and 9. A new chapter will provide more complete and up-to-date IOP related protocols.
- Another new chapter will address methods for *radiometric and bio-optical measurements from moored and drifting buoys*. These methods have much in common with, but also differ in many important respects from, those implemented for the highly specialized MOBY vicarious calibration observatory (Chapter 11).
- *Radiometric measurements from aircraft* are discussed at several points in the present protocols, but detailed methods are nowhere discussed. A third new chapter will be included in Revision 4 to rectify this omission.
- Recent advances, at the National Institute of Standards and Technology (NIST), in radiometric standards, methods of calibration, and stray light characterization have outdated much of the material in the current protocols for characterization of radiometers (Chapter 6). Key improvements relate to the *NIST 2000 detector based scale of spectral irradiance*, and the *NIST Spectral Irradiance and Radiance responsivity Calibrations with Uniform Sources (SIRCUS)* facility. An important goal for Revision 4 is to update the characterization protocols of Chapter 6 to reflect these state-of-the-art methods.

This technical report is not meant as a substitute for scientific literature. Instead, it will provide a ready and responsive vehicle for the multitude of technical reports issued by an operational Project. The contributions are published as submitted, after only minor editing to correct obvious grammatical or clerical errors.

Table of Contents and Author List

CHAPTER 1.....	1
<i>OCEAN COLOR RADIOMETRY AND BIO-OPTICS</i>	
<i>James L. Mueller, Roswell W. Austin, Giulietta S. Fargion and Charles R. McClain</i>	
CHAPTER 2.....	10
<i>FUNDAMENTAL DEFINITIONS, RELATIONSHIPS AND CONVENTIONS</i>	
<i>James L. Mueller and Andre Morel</i>	
CHAPTER 3.....	29
<i>DATA REQUIREMENTS FOR OCEAN COLOR ALGORITHMS AND VALIDATION</i>	
<i>James L. Mueller, Giulietta S. Fargion and Charles R. McClain</i>	
CHAPTER 4.....	39
<i>INSTRUMENT SPECIFICATIONS, CHARACTERIZATION AND CALIBRATION OVERVIEW</i>	
<i>James L. Mueller</i>	
CHAPTER 5.....	48
<i>INSTRUMENT PERFORMANCE SPECIFICATIONS</i>	
<i>James L. Mueller and Roswell Austin</i>	
CHAPTER 6.....	60
<i>CHARACTERIZATION OF OCEANOGRAPHIC AND ATMOSPHERIC RADIOMETERS</i>	
<i>James L. Mueller and Roswell Austin</i>	
CHAPTER 7.....	76
<i>CALIBRATION OF SUN PHOTOMETERS AND SKY RADIANCE SENSORS</i>	
<i>Christophe Pietras, Mark Miller, Kirk D. Knobelspiesse, Robert Frouin, Brent Holben and Ken Voss</i>	
CHAPTER 8.....	91
<i>STABILITY MONITORING OF FIELD RADIOMETERS USING PORTABLE SOURCES</i>	
<i>Stanford B. Hooker</i>	
CHAPTER 9.....	100
<i>OVERVIEW OF MEASUREMENT AND DATA ANALYSIS PROTOCOLS</i>	
<i>James L. Mueller</i>	
CHAPTER 10.....	123
<i>IN-WATER RADIOMETRIC PROFILE MEASUREMENTS AND DATA ANALYSIS PROTOCOLS.</i>	
<i>James L. Mueller</i>	

Chapter 1

Ocean Color Radiometry and Bio-Optics

James L. Mueller¹, Roswell W. Austin¹, Giulietta S. Fargion² and Charles R. McClain³

¹*Center for Hydro-Optics and Remote Sensing, San Diego State University, California*

²*Science Applications International Corporation, Beltsville, Maryland*

³*NASA, Goddard Space Flight Center, Greenbelt, Maryland*

1.1 INTRODUCTION

During the period from *circa* 1985 to 1991, the National Aeronautics and Space Administration (NASA) charged a series of successive science working groups with the task of recommending guidelines, goals and mission design criteria for future satellite ocean color remote sensors. The deliberations of these working groups were based on the ocean color science community's experiences with the Nimbus-7 Coastal Zone Color Scanner (CZCS). On the one hand, the highly successful CZCS mission firmly established ocean color remote sensing as a powerful tool for monitoring and studying the bio-optical properties of the global ocean. On the other hand, the radiometric responsivities of the CZCS channels declined progressively with time throughout its 8-year operating life, which just as firmly established the need to independently verify a satellite sensor's performance using *in situ* measurements of the ocean and atmosphere. From those two general perspectives, the principal recommendations of these NASA Ocean Color Science Working Groups (collectively) included:

1. **Baseline satellite ocean color products** should include
 - a. Normalized water-leaving radiances $L_{\text{WN}}(\lambda)$ (Gordon and Clark, 1981),
 - b. Aerosol radiances $L_a(\lambda)$,
 - c. Chlorophyll *a* concentration Chl [mg m^{-3}],
 - d. The diffuse attenuation coefficient $K(490)$ at a wavelength of 490 nm, and
 - e. Calibrated radiances $L_t(\lambda)$ observed at the satellite.
2. **Principal goals for product uncertainties** should be
 - a. Less than **5 % uncertainty** in $L_{\text{WN}}(\lambda)$ and
 - b. Less than **35 % uncertainty** in Chl .
3. An **ongoing satellite ocean color sensor system validation program** is necessary, using *in situ* measurements of ocean radiometric and bio-optical properties, and of atmospheric optical properties, to verify system performance - including algorithms - immediately after launch and throughout a satellite ocean color sensor's operating lifetime.

These and other recommendations of the earlier working groups were endorsed by the Sea-viewing Wide Field-of-view Sensor (SeaWiFS) Science Team and accepted by NASA. Of particular significance in the present context, the SeaWiFS Project Office moved immediately to implement a SeaWiFS Validation Plan designed to assure a best effort to achieve the above product uncertainty goals (McClain *et al.* 1992). A critical aspect of the validation plan was that *in situ* radiometric, optical and bio-optical measurements of uniformly high quality and accuracy be obtained for verifying SeaWiFS system performance and product uncertainties. Therefore, in 1991 the SeaWiFS Project Office sponsored a workshop to recommend appropriate measurements, instrument specifications, and protocols specifying methods of calibration, field measurements, and data analysis necessary to support SeaWiFS validation, leading to the first publication

of *Ocean Optics Protocols for SeaWiFS Validation* (Mueller and Austin 1992). Continued discourse within the ocean color research community led to Revisions 1 (Mueller and Austin 1995) and 2 (Fargion and Mueller 2000) of these protocols.

The Ocean Optics Protocols for Satellite Ocean Color Sensor Validation (Revision 3.0) are intended to provide standards, which if followed carefully and documented appropriately, will assure that any particular set of optical measurements will be acceptable for ocean color sensor validation and algorithm development. These protocols are guidelines and may be somewhat conservative. In the case of ship shadow avoidance, for example, there are some circumstances in which acceptable radiometric profiles may be acquired considerably closer to a ship than is specified here (Section 10.2). When the protocols are not followed in such cases, however, it is incumbent upon the investigator to explicitly demonstrate that the actual error levels are within tolerance. Close adherence to these protocols is the most straightforward way for an investigator to establish a measurement that is uncontaminated by artifacts, such as ship shadow, and is accurate enough to meet the requirements of satellite ocean color product validation.

Finally, having a standard set of measurement protocols is indispensable in developing consistency across the variety of international satellite ocean color missions either recently launched or scheduled for launch in the next few years. While each mission has its own validation effort, the mission validation teams should not need to define separate validation measurement requirements. In the U.S., for instance, ocean color validation support is derived from four separate funding programs, i.e., the SeaWiFS Project, Moderate Resolution Imaging Spectroradiometer (MODIS) validation program, the Earth Observing System (EOS) calibration and validation program, and the Sensor Intercomparison for Marine Biology and Interdisciplinary Oceanic Studies (SIMBIOS) Project (McClain and Fargion, 1999a, 1999b). Continued development and refinement of these protocols help ensure coordination, collaboration, and communication between those involved.

1.2 OBJECTIVES

Immediate concerns focused the early versions of the Ocean Optics Protocols (Mueller and Austin 1992, 1995) on specific preparations for the SeaWiFS mission. In the interim, not only SeaWiFS, but the Japanese Ocean Color Temperature Sensor (OCTS), the Polarization Detection Environmental Radiometer (POLDER), and the MODIS global coverage ocean color systems have been successfully launched and brought into operation, and the near-term launch of several other such systems is anticipated (Appendix A). The SIMBIOS Program goal is to assist the international ocean color community in developing a multi-year time-series of calibrated radiances that transcends the spatial and temporal boundaries of individual missions (Barnes *et al.* 2001). Specific objectives are to: (1) quantify the relative accuracies of the products from each mission, (2) work with each project to improve the level of confidence and compatibility among the products, and (3) develop methodologies for generating merged level-3 products. SIMBIOS has identified the primary instruments to be used for developing global data sets. These instruments are SeaWiFS, OCTS, POLDER [Advanced Earth Observing Satellite (ADEOS)-I and II], MODIS (Terra and Aqua), Multi-angle Imaging SpectroRadiometer (MISR), Medium Resolution Imaging Spectrometer (MERIS), and Global Line Imager (GLI). The products from other missions [e.g., Ocean Color Imager (OCI), Ocean Scanning Multispectral Imager (OSMI), and Modular Optoelectronic Scanner (MOS)] will be tracked and evaluated, but are not considered as key data sources for a combined global data set.

The scope of the protocols was, therefore, broadened to support development of bio-optical databases that meet the expanded requirements of the SIMBIOS goals and objectives (Fargion and Mueller 2000). The key objective addressed by the original working group was to recommend protocols and standards for supporting *in situ* optical measurements. The original objectives remain valid today, albeit with broader requirements for detailed measurements and sensor characteristics (e.g. wavelength characteristics). The generalized protocol objectives address the following subject areas:

1. The required and useful optical parameters to be used for validation of satellite ocean color sensor normalized water-leaving radiances and atmospheric correction algorithms, and for monitoring each satellite sensor's calibration and stability, will be defined.

2. The instrumentation requirements, and standards for measuring the parameters in item 1, including definitions of measured quantities, wavelengths, field-of-view (FOV) and band specifications, sensitivity, uncertainty and stability, will be delineated.
3. The optical instrument characterization, intercalibration standards, and related protocols will be defined. This objective includes the following subjects:
 - a) laboratory calibration and characterization measurements, uncertainties, and procedures to be applied to instruments used in satellite ocean color sensor validation and algorithm development activities;
 - b) pre- and post-deployment measurements and procedures to be followed with moored instrumentation; and
 - c) methods for instrument calibration and characterization, and the requirements for record keeping and traceability, including intercalibrations of radiometric and optical standards between participating laboratories.
4. The at-sea optical sampling strategy and protocols will be standardized. This objective includes such considerations as:
 - a) the rationale and justifications for moored, underway, drifting, shipboard, and airborne measurements;
 - b) ship shadow avoidance, depth resolution in optical profiles, and total sampling depths; and
 - c) time of day, sky conditions, season, and geographic considerations.
5. The analysis approaches to be used shall be refined. This objective includes recommended procedures and methodologies for generating derived variables from *in situ* observations, for example normalized water-leaving radiance $L_{\text{WN}}(\lambda)$ (Gordon and Clark 1981) and exact normalized water-leaving radiance $L_{\text{WN}}^{\text{ex}}(\lambda)$ (Morel and Gentili 1996; Chapter 13) from $L_u(z, \lambda)$, and $K_d(z, \lambda)$ from $E_d(z, \lambda)$.
6. Protocols for ancillary measurements, data archiving, database population, and access to data will be standardized.
7. The required atmospheric measurements will be defined, and the degree to which standard methodologies are available will be evaluated.

Specific methods for development and validation of bio-optical algorithms for ocean color sensors are only briefly examined in this report. Nonetheless, the scope of the optics protocols includes data requirements and sampling strategies for bio-optical and radiometric measurements supporting these activities. This topic includes the following subjects:

1. Discrete chlorophyll *a* and pigment concentrations will be measured using for high performance liquid chromatography (HPLC) pigment sampling and analysis, protocols and standards for which closely follow those adopted by the Joint Global Ocean Flux Study (JGOFS) (UNESCO 1994).
2. An assessment will be made of the roles of underway, moored, and discrete fluorescence measurements, how such measurements are calibrated, and their usefulness for satellite data product validation. Protocols are included for fluorometric measurement of chlorophyll *a* concentration, again closely following the counterpart JGOFS protocols (UNESCO 1994).
3. The need for biogeochemical measurements of colored dissolved organic material (CDOM), coccoliths, suspended sediment, detritus, etc., will be examined on the basis of baseline product requirements. Protocols are included here for *in situ* and laboratory measurements of spectral absorption by CDOM, and by suspended particles. The other aspects of this topic are addressed in more general terms.

1.3 SENSOR CALIBRATION

The individual satellite sensor project offices, as well as the SIMBIOS Project, must make every effort to track the sensor's performance throughout the duration of the mission. Since SeaWiFS, for example, is designed for a five-year mission, it was certain from the outset that the sensor calibration at each wavelength would change in some unpredictable manner as a function of time. Experience with the CZCS showed it is very difficult to determine a sensor's calibration once it has been launched (Viollier 1982, Gordon *et al.* 1983, Hovis *et al.* 1985, Mueller 1985, Gordon 1987, and Evans and Gordon 1994). Similar problems have been encountered with other earth observing systems, such as the National Oceanic and Atmospheric Administration (NOAA) Advanced Very High Resolution Radiometer (AVHRR) (Brown and Evans 1985 and Weinreb *et al.* 1990). Because of the large atmospheric contribution to the total observed radiances (Gordon 1981) and the great sensitivity of the bio-optical algorithms to the estimated water-leaving radiances (Clark 1981), small errors in the calibration can induce sizable errors in derived geophysical products, rendering them useless for many applications.

By processing large quantities of so-called “clear-water” imagery, *i.e.* in water with pigment concentrations less than 0.25 mg m^{-3} (Gordon and Clark 1981), Evans and Gordon (1994) were able to develop a vicarious calibration that was used in the global processing of the entire CZCS data set (Esaias *et al.* 1986, Feldman *et al.* 1989 and McClain *et al.* 1993). The approach, however, required assumptions that may limit the scientific utility of ocean color imagery. Specifically, the normalized clear water-leaving radiances, $L_{WN}(443)$, $L_{WN}(520)$, and $L_{WN}(550)$, were assumed to be 1.40, 0.48, and 0.30 $\text{mW cm}^2\mu\text{m}^{-1}\text{sr}^{-1}$, respectively. The Angstrom exponents were assumed to be zero, and certain geographical regions, such as the Sargasso Sea, were assumed to be clear-water sites at all times. Under these assumptions, the clear-water L_{WN} values were used to calculate calibration adjustment coefficients to bring CZCS derived L_{WN} values into agreement for these regions. The vicarious calibration of the 443 nm band is tenuous, because of the great variability in $L_{WN}(443)$ even in clear water. Additionally, certain command and engineering data from the NIMBUS-7 platform were not archived, so that a detailed analysis of possible effects related to the spacecraft environment and the effects of spacecraft operation on the calibration could not be performed.

Unlike CZCS, SeaWiFS and other modern ocean color sensors routinely produce geophysical fields in a near-real time, operational mode for distribution to the science community. This aspect, as well as merger of multi-satellite data sets spanning many years, necessitates constant evaluation of system performance and derived products for all of the sensors. Therefore, a consistent multifaceted approach to address problems of sensitivity degradation and sensor characterization is required on a continuing basis. The goal is to ensure that satellite derived water-leaving radiances are accurately known and meet the specifications of the individual missions and SIMBIOS.

As implemented by the SeaWiFS Project Office, for example, the validation program includes both onboard and vicarious calibration approaches (McClain *et al.* 1998, 2000a, 2000b; Barnes *et al.* 1999a, 2000a, 2000b, 2000c). SeaWiFS has a solar measuring diffuser plate to reference the response to the sun and is also capable of periodically imaging the moon by maneuvering the spacecraft (Barnes *et al.* 1999b). MODIS and some other ocean color sensors have similar capabilities. The vicarious calibration program incorporates measurements of water-leaving radiances, and other related quantities, from ships, drifting buoys, and fixed moorings, to develop time series and geographically diverse samples of oceanic and atmospheric data. Each approach has advantages and disadvantages, but when combined, they should provide a complementary and comprehensive data set that will be sufficient to monitor short-term changes and long-term trends in the sensor's performance.

Presently, the SIMBIOS Project uses a combination of satellite and *in situ* observations from geographically diverse vicarious calibration test sites as a means of comparing ocean color satellite instruments. Using this vicarious calibration approach, results retrieved from different sensors can be meaningfully compared and possibly merged (Barnes *et al.* 2001). More importantly, one can use the same procedure, with *in situ* ocean and atmospheric optical property measurements, to recalibrate satellite sensors (Fargion *et al.*, 1999, 2000; Fargion and McClain 2000).

The SIMBIOS calibration strategy is to focus on regions and circumstances where the optical properties of the marine atmosphere and ocean are well understood and homogeneous, *i.e.* where the errors

in the atmospheric correction and the *in situ* optical measurements are expected to be minimal. The Marine Optical Buoy (MOBY), near the island of Lanai, Hawaii, provides the principal instrumented test site for vicarious calibration measurements (Clark *et al.* 1997; see also Chapter 11). The MOBY project officially supports the validation of ocean color data that is collected by SeaWiFS and MODIS. In addition, MOBY has been successfully used for OCTS and POLDER and indirectly for MOS (Wang and Franz, 1999) vicarious calibrations.

1.4 BIO-OPTICAL ALGORITHMS

The SeaWiFS Project Office, and each of the counterpart ocean color sensor projects, is responsible for producing a standard set of derived products. The oceanic products include chlorophyll concentration, $K_d(490)$, and $L_{WN}(\lambda, \theta, \phi)$ at 5 wavelengths (see Chapter 13 regarding the significance of the angular dependency).

The basic quantities to be computed from the sensor radiances are the water-leaving radiances, from which all other derived products except the aerosol products are computed. Every effort must be made to ensure these radiances meet the goal of no more than 5 % uncertainty in case-1 waters. This requires the atmospheric correction algorithms to be considerably more sophisticated than were the original CZCS algorithms.

The baseline bio-optical products must meet the SeaWiFS, MODIS, other sensors, and SIMBIOS Project accuracy requirements over a variety of water masses. The CZCS algorithms were based on a data set consisting of fewer than 50 data points (only 14 observations were available for the band-2-to-band-3 ratio algorithm) and performed poorly in regions of high concentrations of phytoplankton pigments, suspended sediment, or CDOM, and in coccolithophorid blooms (Groom and Holligan 1987). Accurate estimates of the baseline products are essential if SeaWiFS is to be useful in programs such as the Joint Global Ocean Flux Study (JGOFS) [National Academy of Science (NAS) 1984], carbon cycle research, and climate change research.

SeaWiFS, and the other modern ocean color sensors, have the capability, due to improvements in the signal-to-noise ratio (SNR), digitization, dynamic range, and wavelength selection, to increase the accuracy of these products and to flag areas where anomalies or low confidence conditions exist. Clearly, a much larger database is needed for developing and validating a broader variety of bio-optical algorithms, some of which will be region specific. The radiometric, optical, and chemical field observations used in deriving bio-optical algorithms and for vicarious calibration of the sensor must, therefore, conform to stringent, uniform requirements with respect to instrument calibration and characterization, and methods of observation.

The SeaWiFS and SIMBIOS Projects jointly manage a program to compare the various atmospheric correction and bio-optical algorithms proposed by the science community (Wang and Bailey 2000, McClain *et al.* 2000a, 2000b; O'Reilly *et al.* 2000). The purpose of this program is to independently evaluate suggested improvements, or additions, to the SeaWiFS and merged products. This component of the calibration and algorithm development program runs in parallel with, but off-line from, operational processing and provides an essential mechanism for incorporating data and analyses from the community at large (Barnes *et al.* 2001).

1.5 VICARIOUS CALIBRATION

For ocean observations, it is easy to show (Gordon 1987 and Gordon 1988) that satellite sensor calibration requirements based on the quality of the existing CZCS pigment algorithms exceed currently available capabilities. Furthermore, the sensor calibration is unlikely to remain unchanged through launch and five years of operation in orbit. The only foreseeable way of approaching the ocean calibration needs is through vicarious calibration, *i.e.*, fine tuning the calibration in orbit.

Gordon (1987) described the detailed method used to achieve vicarious calibration for the CZCS. First, the calibration was initialized after launch by forcing agreement between the sensor-determined radiance and the expected radiance based on radiometric measurements made at the surface under clear

atmospheric conditions. Next, since the CZCS responsivity was observed to be time dependent, the algorithms were applied to other scenes characterized by bio-optical surface measurements and more typical atmospheres, and the calibration was adjusted until the measured water-leaving radiances were reproduced. Finally, the surface measurements of pigments were combined with satellite pigment estimates for a wide variety of atmospheric conditions, and the radiance calibration was fine tuned until the best agreement was obtained between the retrieved and true pigments.

The CZCS vicarious calibration was not radiometric. It was a calibration of the entire system - sensor plus algorithms. To predict the radiance measured at the satellite, L_t , the water-leaving radiance, aerosol optical thickness, and aerosol phase function are all required. Also needed are ancillary data, including the surface pressure, wind speed, and ozone optical thickness. For vicarious calibration and validation, these data are obtained by measuring the upwelling radiance distribution just beneath the surface, along with the aerosol optical thickness and the sky radiance, at the time of the satellite overpass. The sky radiance is used to deduce the required information about the aerosol phase function (Voss and Zibordi 1989). The data set is finally used to deduce L_t , at the top of the atmosphere, coincident with a SeaWiFS overpass from which the calibration is initialized (Clark *et al.* 1997).

The present approach used by the SIMBIOS and SeaWiFS Projects is to develop a Level-1b to Level-2 software package (MSI12) which is capable of processing data from multiple ocean color sensors using the standard SeaWiFS atmospheric correction algorithms of Gordon and Wang (1994a, 1994b). The integration of a new sensor into MSI12 involves the development of a set of input functions and derivation of bandpass specific quantities such as Rayleigh scattering tables and Rayleigh-aerosol transmittance tables. Once the processing capability has been established, the vicarious calibration can be tuned using “match-up data” from the MOBY site, and/or cross calibration with another sensor. For example, Wang and Franz (1999) used SeaWiFS normalized remote sensing reflectances and aerosol models to successfully re-calibrate the MOS spectral channels.

Using this approach, the SIMBIOS Project can provide a completely independent assessment of instrument calibration and sensor-to-sensor relative calibration. The Project also provides insight to the sensor teams on how differences in calibration techniques and atmospheric correction algorithms propagate through the processing to produce differences in retrieved optical properties of the water. It must be stressed that this exercise is absolutely essential for calibrating the ocean color systems, *i.e.* sensors plus algorithms, and that it cannot be implemented without a high quality surface data set obtained simultaneously with the satellite imagery.

1.6 AEROSOL OPTICAL THICKNESS VALIDATION

Aerosol optical thickness products determined from the satellite ocean color data itself are critical factors in the uncertainty budgets of atmospheric correction algorithms (Gordon and Wang 1994a) and results of vicarious calibrations (Clark *et al.* 1997; Gordon 1981, 1987, 1988). The SIMBIOS Project is validating the SeaWiFS aerosol optical products by comparing them to *in situ* measurements (Wang *et al.*, 2000). A second, related objective of these comparisons is to determine the validity of the aerosol models currently used by SeaWiFS for atmospheric correction.

The principal source of *in situ* aerosol observations is the Aerosol Robotic Network (AERONET). AERONET is a network of ground-based automated sun photometers owned by national agencies and universities (Holben *et al.* 1998). AERONET data provides globally distributed, near-real time observations of aerosol spectral optical depths, aerosol size distributions, and precipitable water. Because the majority of the AERONET stations are at continental locations, SIMBIOS augmented the network with 12 additional island and coastal sites, including Lanai and Oahu Hawaii, Ascension Island, Bahrain, Tahiti, Wallops Island, South Korea, Turkey, Argentina, Azores and Perth. The SIMBIOS Project also has shipboard and hand-held sun photometers (MicroTops, PREDE, and SIMBAD) and an aerosol-profiling LIDAR system. These instruments are calibrated in collaboration with the AERONET Program at NASA Goddard Space Flight Center (GSFC) and loaned to investigators staging SIMBIOS sponsored research expeditions.

1.7 COMMUNITY PARTICIPATION

The SeaWiFS and SIMBIOS Project Offices rely on the oceanographic community to perform field research for atmospheric and bio-optical algorithm development, and for all of the *in situ* data collection for vicarious sensor calibration. The SIMBIOS Project sponsors a subset of these observations, but many projects sponsored by the NASA Research and Application Program, other government agencies and the international ocean color research community all make major contributions to the global multi-year effort.

The SIMBIOS Project has undertaken the challenge of coordinating the *in situ* observations contributed by these various programs, linking it to ocean color imagery from the international ensemble of satellite sensors, and making the overall data sets available to the ocean color research community (McClain and Fargion 1999a, 1999b). A workable strategy to meet those challenges first requires a clear definition of the observations, uncertainties, and data collection protocols associated with each type of activity. The purpose of this document is to clarify these requirements.

1.8 PROTOCOL DOCUMENT ORGANIZATION

The chapters of this document are organized into 4 parts:

1. The first 3 chapters are introductory in nature. Chapter 1 introduces perspectives on ocean color research and validation, Chapter 2 provides fundamental definitions and conventions used throughout the document, and Chapter 3 defines requirements for *in situ* observations.
2. Chapters 4 through 8 address the characteristics and performance specifications of the instruments used for *in situ* observation, and provide protocols for their calibration and characterization. Chapter 4 provides an overview of instrument specifications and characterization, together with brief protocol descriptions for instrument types that are not covered by a separate chapter.
3. Chapters 9 through 17 provide detailed protocols describing methods for making each type of field measurement and associated data analysis. Chapter 9 provides an overview of measurement and data analysis topics, together with protocols for measurements that are not covered by a separate chapter.
4. Finally, Chapter 18 addresses the methods and procedures for data archival and quality control procedures.

REFERENCES

- Barnes, R. A., R. E. Eplee, F. S. Patt, and C. R. McClain 1999a: Changes in the radiometric sensitivity of SeaWiFS determined from lunar and solar-based Measurements. *Applied Optics*, **38**, 4649-4669.
- Barnes, R.A., R.E. Eplee, Jr., S.F. Biggar, K.J. Thome, E.F. Zalewski, P.N. Slater, and A.W. Holmes 1999b: The SeaWiFS Solar Radiation-Based Calibration and the Transfer-to-Orbit Experiment. *NASA Tech. Memo. 1999--206892, Vol. 5*, S.B. Hooker and E.R. Firestone, Eds., NASA Goddard Space Flight Center, 28 pp.
- Barnes, R.A., R.E. Eplee, Jr., W.D. Robinson, G.M. Schmidt, F.S. Patt, S.W. Bailey, M. Wang and C.R. McClain, 2000a: The calibration of SeaWiFS, *Proc. 2000 Conf on Characterization and Radiometric Calibration for Remote Sensing*, Logan, Utah, Sept. 19-21, 2000.
- Barnes, R.A., R.E. Eplee, Jr., W.D. Robinson, G.M. Schmidt, F.S. Patt, S.W. Bailey, M. Wang and C.R. McClain, 2000b: The calibration of SeaWiFS on-orbit. In: *Earth Observing Systems V*. (W.L. Barnes, Ed.), *Proc. SPIE Vol. 4135*: 281-293.
- Barnes, R.A., R.E. Eplee, Jr., S.F. Biggar, K.J. Thome, E.F. Zalewski, P.N. Slater and A.W. Holmes, 2000c. SeaWiFS transfer-to-orbit experiment, *Appl. Opt.*, **39**: 5620-5631.
- Barnes, R.A., D.K. Clark, W.E. Esaias, G.S. Fargion, G. C. Feldman and C.R. McClain, 2001. Development of a consistent multi-sensor global ocean color time series. *Proc. International Workshop on Geo-Spatial Knowledge Processing for Natural Resource Management*, 28-29 June

- 2001, (A. Belward, E. Biinaghi, P.A. Brivio, G.A. Lanzaroni and G. Tosti, Eds.), Univ. of Insubria, Varese, Italy, pp 13-28.
- Brown, O. B., and R. H. Evans 1985: Calibration of Advanced Very High Resolution Radiometer infrared observations. *J. Geophys. Res.*, **90**, 11,667-11,677.
- Clark, D. K., 1981: Phytoplankton pigment algorithms for the Nimbus-7 CZCS. *Oceanography from Space*, J.F.R. Gower Ed., Plenum Press, 227-238.
- Clark, D.K., H.R. Gordon, K.J. Voss, Y. Ge, W. Broenkow, and C.C. Trees, 1997: Validation of atmospheric correction over oceans. *J. Geophys. Res.*, **102**, 17,209-17,217.
- Esaías, W., G. Feldman, C.R. McClain, and J. Elrod, 1986: Satellite observations of oceanic primary productivity. *EOS, Trans. AGU*, **67**, 835--837.
- Evans, R.H., and H.R. Gordon, 1994: Coastal zone color scanner system calibration: A retrospective examination. *J. Geophys. Res.*, **99**, 7,293--7,307.
- Fargion G.S., C.R. McClain, H. Fukushima, J.M. Nicolas and R.A. Barnes, 1999: Ocean color instrument intercomparisons and cross-calibrations by the SIMBIOS Project. *SPIE Vol.* **3870**, 397-403.
- Fargion, G.S. and C.R. McClain, 2000: Three years of ocean color instrument intercomparisons and cross-calibrations by the SIMBIOS Project (1997-2000), In: *Remote Sensing of the Ocean and Sea Ice 2000* (C.R. Bostater, Jr. and R. Santoleri, Eds.), Proc. SPIE Vol. **4172**: pp44-55.
- Fargion, G., C.R. McClain and R.A. Barnes, 2000: Ocean color instrument intercomparisons and cross-calibration by the SIMBIOS Project (1999-2000). In: *Earth Observing Systems V* (W.L. Barnes, Ed.), Proc. SPIE Vol. **4135**: 411-420.
- Fargion, G.S. and J.L. Mueller, 2000: *Ocean Optics Protocols for Satellite Ocean Color Sensor Validation, Revision 2*, NASA TM 2001-209955, NASA Goddard Space Flight Center, Greenbelt, Maryland, 184 pp.
- Feldman, G., N. Kuring, C. Ng, W. Esaías, C. McClain, J. Elrod, N. Maynard, D. Endres, R. Evans, J. Brown, S. Walsh, M. Carle, and G. Podesta, 1989: Ocean Color: Availability of the global data set. *EOS, Trans. AGU*, **70**, 634.
- Groom, S.B., and P.M. Holligan, 1987: Remote sensing of coccolithophorid blooms. *Adv. Space Res.*, **7**, 73--78.
- Gordon, H.R. and D.K. Clark, 1981: Clear water radiance for atmospheric correction of coastal zone color scanner imagery. *Appl. Opt.*, **20**, 4,175-4,180.
- Gordon, H.R., 1981: Reduction of error introduced in the processing of coastal zone color scanner-type imagery resulting from sensor calibration and solar irradiance uncertainty. *Appl. Opt.*, **20**, 207--210.
- Gordon H.R., J.W. Brown, O.B. Brown, R.H. Evans, and D.K. Clark 1983: Nimbus-7 CZCS: Reduction of its radiometric sensitivity with time. *Appl. Opt.*, **24**, 3,929-3,931.
- Gordon H.R., 1987: Calibration requirements and methodology for remote sensors viewing the ocean in the visible. *Remote Sens. Environ.*, **22**, 103-126
- Gordon H.R., 1988: Ocean color remote sensing systems: radiometric requirements. *Recent Advances in Sensors, Radiometry, and Data Processing for Remote Sensing*, P.N. Slater, Ed. SPIE, **924**, 151-157.
- Gordon, H.R. and M. Wang, 1994a: Retrieval of water-leaving radiance and aerosol optical thickness over the oceans with SeaWiFS: A preliminary algorithm, *Appl. Opt.*, **33**, 443-452.
- Gordon, H.R. and M. Wang, 1994b: Influence of oceanic whitecaps on atmospheric correction of ocean color sensors, *Appl. Opt.*, **33**, 7,754-7,763.
- Holben, B.N., T.F. Eck, I. Slutsker, D. Tanre, J.P. Buis, A. Setzer, E. Vermote, J.A. Reagan, Y.J. Kaufman, T. Nakajima, F. Leaven, I. Jankowiak, and A. Smirnov, 1998: AERONET – a federated instrument network and data archive for aerosol characterization. *Remote Sens. Environ.*, **66**, 1-16.

- Hovis W.A., J.S. Knoll, and G.R. Smith, 1985: Aircraft measurements for calibration of a orbiting spacecraft sensor. *Appl. Opt.*, **24**, 407-410.
- McClain, C.R., W.E. Esaias, W. Barnes, B. Guenther, D. Endres, S. Hooker, G. Mitchell and R. Barnes, 1992: Calibration and Validation Plan for SeaWiFS. *NASA Tech. Memo. 104566, Vol. 3*, S.B. Hooker and E.R. Firestone, Eds., NASA Goddard Space Flight Center, Greenbelt, Maryland, 41pp.
- McClain, C.R., G. Feldman and W.E. Esaias, 1993: Biological Oceanic Productivity, in *Atlas of Satellite Observations Related to Global Change*, R.Gurney, J.L.Foster (Eds.), Cambridge Press, NY, 251-263, 470 pp.
- McClain, C.R., M. Cleave, G. Feldman, W. Gregg and S.B. Hooker, 1998: Science quality SeaWiFS Data for global biosphere research. *Sea Technology*, **39**, 10-16.
- McClain, C.R. and G.S. Fargion, 1999a: SIMBIOS Project 1998 Annual Report, *NASA Tech. Memo. 1999-208645*, NASA Goddard Space Flight Center, Greenbelt, Maryland, 105 pp.
- McClain, C.R. and G.S. Fargion, 1999b: SIMBIOS Project 1999 Annual Report, *NASA Tech. Memo. 1999-209486*, NASA Goddard Space Flight Center, Greenbelt, Maryland, 128 pp.
- McClain C.R., E. Ainsworth, R. Barnes, R. Epley et al. , 2000, 2000a: SeaWiFS Postlaunch Calibration and Validation Part 1, *NASA TM 2000-206892, Vol. 9*, *NASA Tech. Memo. 104566*, S.B. Hooker and E.R. Firestone, Eds., NASA Goddard Space flight center, Greenbelt, Maryland (in press).
- McClain C.R., R. A. Barnes, R. E. Eplee, Jr., B. A. Franz, et al., 2000b: SeaWiFS Postlaunch Calibration and Validation Part 2, *NASA TM 2000-206892, Vol. 10*, *NASA Tech. Memo. 104566*, S.B. Hooker and E.R. Firestone, Eds., NASA Goddard Space flight center, Greenbelt, Maryland (in press).
- Morel and Gentili, 1996: Diffuse reflectance of oceanic waters. III. Implication of bidirectionality for the remote sensing problem, *Appl. Opt.*, **35**, 4,850-4,862.
- Mueller, J.L. 1985: Nimbus-7 CZCS: electronic overshoot due to cloud reflectance. *Appl. Opt.*, **27**, 438-440.
- Mueller, J.L. and R.W. Austin, 1992: Ocean Optics Protocols for SeaWiFS Validation. *NASA Tech. Memo. 104566, Vol. 5*, S.B. Hooker and E.R. Firestone, Eds., NASA Goddard Space flight center, Greenbelt, Maryland, 45 pp.
- Mueller, J.L. and R.W. Austin, 1995: Ocean Optics Protocols for SeaWiFS Validation, Revision 1. *NASA Tech. Memo. 104566, Vol. 25*, S.B. Hooker and E.R. Firestone, Eds., NASA Goddard Space flight center, Greenbelt, Maryland, 66 pp.
- O'Reilly J. E., S. Maritorena, D. Siegel et al., 2000 SeaWiFS Postlaunch Calibration and Validation Part 3, *NASA TM 2000-206892, Vol. 11*, *NASA Tech. Memo. 104566*, S.B. Hooker and E.R. Firestone, Eds., NASA Goddard Space flight center, Greenbelt, Maryland (in press).
- UNESCO, 1994: Protocols for the Joint Global Ocean Flux Study (JGOFS) Core Measurements, *Manual and Guides* 29, 170pp.
- Viollier, M., 1982: Radiance calibration of the Coastal Zone Color Scanner: a proposed adjustment. *Appl. Opt.*, **21**, 1,142--1,145.
- Voss, K. J. and G. Zibordi, 1989: Radiometric and geometric calibration of a spectral electro-optic "fisheye" camera radiance distribution system. *J. Atmos. Ocean. Tech.*, **6**, 652-662.
- Wang, M. and B.A. Franz, 1999: Comparing the ocean color measurements between MOS and SeaWiFS. *IEEE Trans. Geosci. Remote Sens.*, in press.
- Wang, M., S. Bailey, C. Pietras and C. R. McClain, 2000: Correction of Sun Glint Contamination on the SeaWiFS Aerosol Optical Thickness Retrievals, in McClain et al., SeaWiFS Postlaunch Calibration and Validation Analyses, Part 1, *NASA TM 2000-206892, Vol. 9*, in press.
- Weinreb, M.P., G. Hamilton, S. Brown, and R.J. Koczor, 1990: Nonlinear corrections in calibration of Advanced Very High Resolution Radiometer infrared channels. *J. Geophys. Res.*, **95**, 7,381--7,388.

Chapter 2

Fundamental Definitions, Relationships and Conventions

James L. Mueller¹ and Andre Morel²

¹*Center for Hydro-Optics and Remote Sensing, San Diego State University, California*

²*Laboratoire d’Oceanographie, Universite Pierre et Marie Curie, France*

2.1 INTRODUCTION

The fundamental radiometric and optical quantities, physical relationships, terminology, and conventions underlying ocean color science are drawn from an extensive and growing literature. The present *Ocean Optics Protocols for Satellite Ocean Color Sensor Validation* document and its predecessors (Fargion and Mueller 2000; Mueller and Austin 1992, 1995) are attempts to distill a uniform set of concepts, methods and conventions applied to *in situ* measurements, data analyses and interpretations appropriate for validating the operational performance and derived products associated with satellite ocean color sensors. Basic ocean optical and radiative transfer concepts, definitions and terminology used throughout the protocols are adapted from, *e.g.*, Preisendorfer (1960, 1976), Jerlov (1976), Morel and Smith (1982), more recent literature cited extensively in the individual chapters, and workshop discussions associated with the successive revisions of the document. Comprehensive treatments of radiative transfer concepts and methods relevant to ocean color are provided by, *e.g.*, Mobley (1994) and Preisendorfer (1976). Choices of particular published scales for, *e.g.*, mean extraterrestrial solar spectral irradiance and the spectral absorption and scattering spectra of pure water, originate with usage in the Nimbus-7 Coast Zone Color Scanner and SeaWiFS programs, recent literature, and working group discussions specifically related to the protocols; these scale conventions are expected to continue to evolve (*e.g.* Section 2.8 below).

The purpose of the present chapter is a first attempt to present a succinct summary of the key definitions, relationships, conventions and terminology currently adopted for use throughout the protocol document. In the previous revisions (Mueller and Fargion 2001; Mueller and Austin 1992, 1995), uniform usage in these areas was maintained by carefully editing each new, or significantly revised, chapter. As the scope and breadth of chapter authorship has expanded, authors new to the protocols have introduced variant terminology and conventions that pose an increasingly burdensome editorial task. It is hoped that by collecting the most common aspects of this topic in one place as a source guide for authors and co-authors of protocol chapters, a more uniform usage and terminology may result. As with all chapters of the protocols, it is fully expected that, in the future, this first attempt will be significantly revised and improved through constructive criticism and suggestions from the ocean color research community at large. In particular, the present chapter does not yet address important fundamental quantities, concepts and relationships of atmospheric optics, as they relate to ocean color science. This omission results purely from a lack of adequate time, within the schedule for publication of the protocol document (Revision 3), to write this important topic and it will be added in the next revision.

2.2 GEOMETRY

Remote Sensing Coordinate System

Figure 2.1 illustrates an arbitrary Cartesian coordinate system, with a source illuminating the origin from direction $\hat{\mathbf{S}}$, a unit-length vector oriented at (zenith, azimuth) angles (θ_0, ϕ_0) , and a detector viewing the origin from direction $\hat{\mathbf{D}}$ oriented at (θ, ϕ) . The orthonormal basis vectors $(\hat{\mathbf{x}}, \hat{\mathbf{y}}, \hat{\mathbf{z}})$, defined in matrix notation as

$$\hat{\mathbf{x}} = \begin{bmatrix} 1 \\ 0 \\ 0 \end{bmatrix}, \hat{\mathbf{y}} = \begin{bmatrix} 0 \\ 1 \\ 0 \end{bmatrix} \text{ and } \hat{\mathbf{z}} = \begin{bmatrix} 0 \\ 0 \\ 1 \end{bmatrix}, \quad (2.1)$$

define the coordinate system illustrated in Figure 2.1. The Cartesian representation of the unit-length vector pointing toward the detector is

$$\hat{\mathbf{D}} = \begin{bmatrix} \sin \theta \cos \phi \\ \sin \theta \sin \phi \\ \cos \theta \end{bmatrix}, \quad (2.2)$$

and the source direction vector coordinates are

$$\hat{\mathbf{S}} = \begin{bmatrix} \sin \theta_o \cos \phi_o \\ \sin \theta_o \sin \phi_o \\ \cos \theta_o \end{bmatrix}. \quad (2.3)$$

Photon flux from the source is transmitted through the origin in direction

$$\hat{\mathbf{T}} = -\hat{\mathbf{S}} = \begin{bmatrix} -\sin \theta_o \cos \phi_o \\ -\sin \theta_o \sin \phi_o \\ -\cos \theta_o \end{bmatrix}. \quad (2.4)$$

The scattering angle Ψ , through which photons are redirected from direction $\hat{\mathbf{T}}$ into direction $\hat{\mathbf{D}}$, in the view of the detector, is determined as $\cos \Psi = \hat{\mathbf{T}} \cdot \hat{\mathbf{D}}$, which from (2.2) and (2.4) expands in this coordinate frame as

$$\cos \Psi = -\cos \theta \cos \theta_o - \sin \theta \sin \theta_o (\cos \phi \cos \phi_o + \sin \phi \sin \phi_o).$$

Invoking the identity $\cos(\phi - \phi_o) = \cos \phi \cos \phi_o + \sin \phi \sin \phi_o$, the scattering angle in the remote sensing coordinate system may be expressed

$$\cos \Psi = -\cos \theta \cos \theta_o - \sin \theta \sin \theta_o \cos(\phi - \phi_o). \quad (2.5)$$

The complete derivation of (2.5), although straightforward, is given here because the sign of the second term has been incorrectly reversed in some literature sources (*e.g.* Gordon *et al.* 1983 and Liou 1980).

In the context of ocean color remote sensing, the $\hat{\mathbf{x}}\hat{\mathbf{y}}$ -plane would be parallel to, and $\hat{\mathbf{z}}$ the unit normal to, the sea surface, the source would be the sun, and the detector a satellite ocean color sensor. A common convention appearing throughout this protocol document (*e.g.* see Chapters 12 and 13) is to rotate the local coordinates so that the x -axis is aligned with the solar azimuth and $\phi_o \equiv 0$.

Instrument Coordinate System

When working with instruments designed to measure transmission of light along a path, or light scattered at a particular angle from that path, it is more convenient to rotate the coordinate system as illustrated in Figure 2.2. The collimated source is placed at $-\hat{\mathbf{z}}$ and “Detector 1” at $\hat{\mathbf{z}}$ to measure transmission of flux transmitted along that axis over the distance between source and sensor. “Detector 2” views the beam at the origin and zenith angle θ , and the associated scattering angle in this coordinate frame is simply $\Psi = \theta$. In ocean optics, it may ordinarily be assumed that scattering is azimuthally isotropic in the coordinate reference of Fig. 2, so that one need not consider ϕ dependence of scattering.

Scattering Angle Invariance

It is important to keep in mind that the relationship of the scattering angle Ψ to the angular orientation of the scattered (viewing) path relative to the transmission path is identical in Figures 2.1 and 2.2. Determining Ψ is simpler and more intuitive in the representation of Figure 2.2, when the origin and orientation of the transmission path are held fixed, and only the direction from which the origin is viewed

varies. For a satellite remotely sensed ocean color image, on the other hand, both the source (transmission) and sensor (viewing) directions change continuously from pixel to pixel, and it is more convenient to place the origin at each pixel (Figure 2.1) and determine Ψ using (2.5).

Plane and Solid Angles

In plane geometry, quantities are represented in 2-dimensional Cartesian (x, y) , or polar (r, θ) , coordinates. The natural measure of angular distance in plane coordinates is the **radian**, defined as the angle subtending an arc of unit length on the perimeter of the *unit circle* (i.e. a circle of radius $r=1$). There are 2π radians in a full circle. The units of an angle are, by convention, taken implicitly to be radians (without units notation), unless they are explicitly specified to be in degrees. These simple definitions and concepts are widely understood and used by the public at large.

Radiometry and optics intrinsically involve vector quantities that must be represented in 3-dimensional (x, y, z) , or (r, θ, ϕ) , coordinates (Figure 2.1). It is also necessary to associate 3-dimensional **solid angles** with many radiometric and optical quantities. Following the definition of the 2-dimensional radian, the natural measure of solid angles in 3-dimensions is the **steradian** (denoted **sr**), defined as the solid angle subtending a unit area on the surface of the *unit sphere* (again $r=1$). The geometry relating surface area on the unit sphere to angles θ and ϕ is illustrated in Figure 2.3. The differential area on the surface of a sphere of radius r is determined as $da = r^2 \sin \theta d\theta d\phi$, and on the unit sphere $da = \sin \theta d\theta d\phi$ (Figure 2.3). By definition, a given solid angle Ω corresponding to angular intervals $\Delta\theta$ and $\Delta\phi$ is determined as

$$\Omega = \int_{\Delta\phi} \int_{\Delta\theta} \sin \theta d\theta d\phi, \text{ sr}, \quad (2.6)$$

from which we define the differential solid angle as

$$d\omega \equiv \sin \theta d\theta d\phi, \text{ sr}. \quad (2.7)$$

2.3 IRRADIANCE AND RADIANCE

Taking radiant flux F to be the flow of radiant energy, e.g. in μW , through a point on a plane surface, **irradiance** is defined as $E \equiv \frac{dF}{da}$, $\mu\text{W cm}^{-2}$, the radiant flux per unit area through that point from all directions in the hemisphere above the surface. The direction associated with E is the normal to the surface. **Radiance** at a point on a surface is the radiant flux per unit solid angle from direction (θ, ϕ) , per unit area, $da \cos \theta$, normal to the direction of flow, and is defined as $L(\theta, \phi) \equiv \frac{d^2 F}{d\omega da \cos \theta} = \frac{dE}{\cos \theta d\omega}$, $\mu\text{W cm}^{-2} \text{sr}^{-1}$. Combining these definitions and (2.7) we have the relationship between irradiance and radiance incident on a plane as

$$E = \int_0^{2\pi} \int_0^{\frac{\pi}{2}} L(\theta, \phi) \cos \theta \sin \theta d\theta d\phi, \mu\text{W cm}^{-2}. \quad (2.8)$$

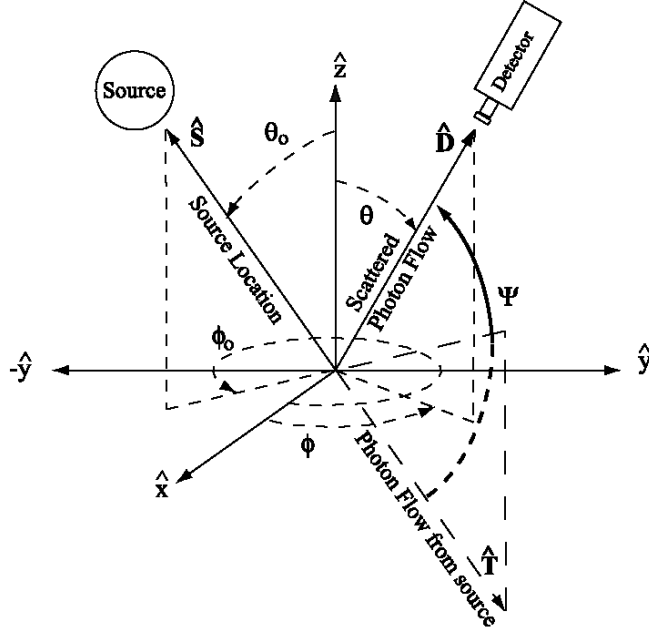


Figure 2.1: The directions of source \hat{S} and detector \hat{D} direction vectors relative to the origin of the coordinate frame adopted throughout the ocean optics protocols. The zenith and azimuth angles (θ_o, ϕ_o) are reserved for source directions, and the notation (θ, ϕ) applies to the direction of the detector location, or any other general direction, depending on the context. The unit-length vector $\hat{T} = -\hat{S}$ defines the direction of radiant flux from the source transmitted through the origin, and Ψ is the angle through which radiant flux is scattered from the transmitted beam \hat{T} into the view of the detector in direction \hat{D} .

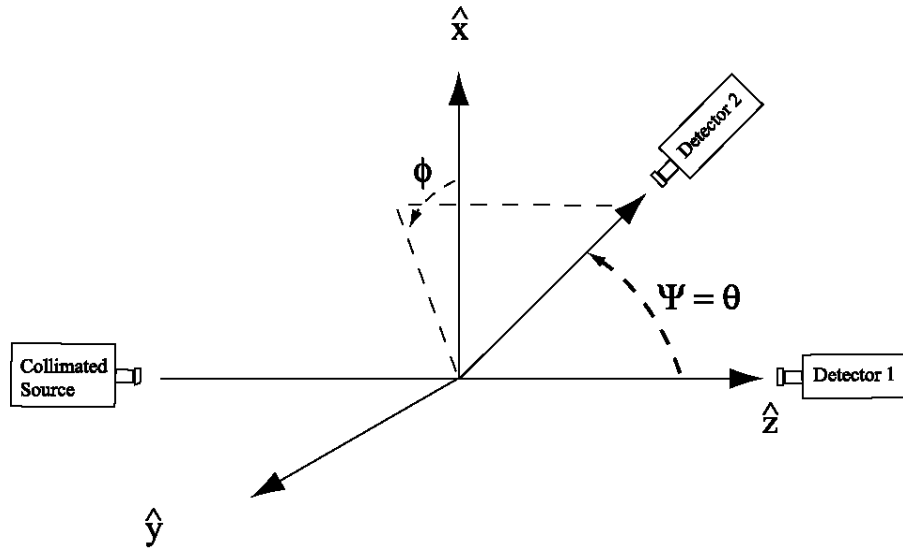


Figure 2.2: A local coordinate frame rotated to align the source and detector-1 locations along the z -axis. Detector-2, located in direction (θ, ϕ) , views the origin to measure radiant flux scattered from the transmitted beam through angle Ψ . This local coordinate system is usually adopted for beam transmissometers and instruments designed to measure the volume scattering function (VSF) $\beta(\lambda, \Psi)$, because the scattering angle Ψ is more easily visualized and computed in this framework than in the representation of Figure 2.1. For a beam transmissometer, the path length is simply the distance between the source and detector-1 along the z -axis. For a VSF meter, the working volume is defined by the intersection of the field of view of detector-1 with the beam geometry of the source.

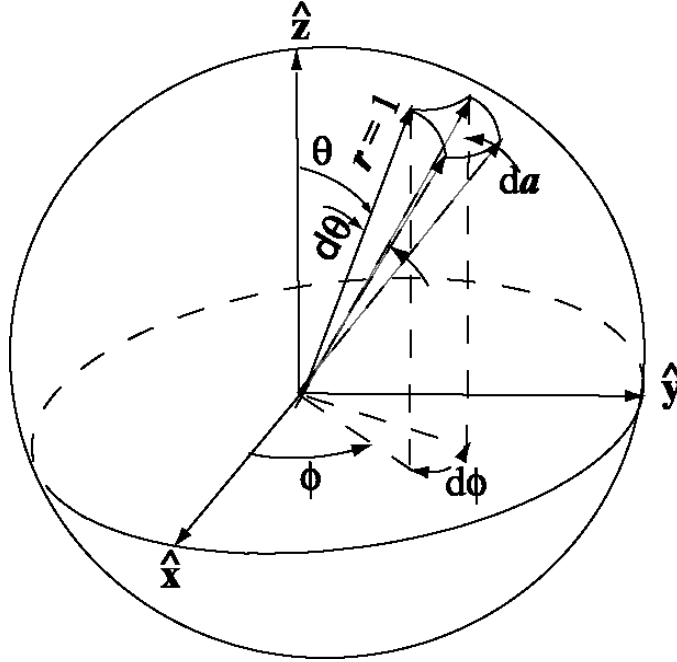


Figure 2.3: Illustration representing the relationship between differential angles $d\theta$ and $d\phi$ and the area da subtended on a sphere of unit radius. From the above, it is easily seen that $da = \sin\theta d\theta d\phi$.

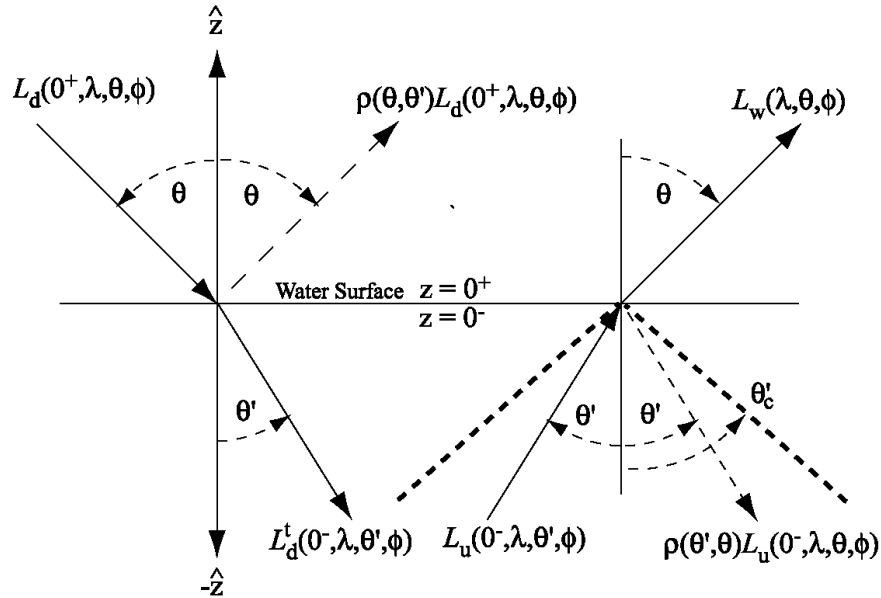


Figure 2.4: Reflection and refraction angles - in the plane of the paper - at the air-sea interface. Solid arrows represent radiant flux directions incident on and transmitted through the interface. Dashed arrows represent radiant flux reflected from the interface. The bold dashed lines represent the boundaries, in water, of the cone defined by the critical angle $\theta_c \approx 48^\circ$, beyond which radiant flux is totally reflected downward into the medium. The left-hand diagram represents the case for radiant flux incident from above ($z=0^+$) on, and reflected from, the surface at zenith angle θ , and transmitted through the interface at the refracted nadir angle θ' below the surface. The right-hand diagram represents the case for radiant flux incident from below ($z=0^-$) on, and reflected from, the surface at nadir angle θ' , and transmitted through the interface at zenith angle θ in air. The symbols θ for zenith angles in air, and θ' for nadir angles in water, are adopted and reserved for this purpose throughout the ocean optics protocol document.

Irradiance and *radiance*, unless qualified as **spectral** quantities, include the flux of photons at all wavelengths.

Spectral irradiance is defined as $E(\lambda) \equiv \frac{dF}{d\lambda}$, $\mu\text{W cm}^{-2}\text{nm}^{-1}$, and **spectral radiance** as $L(\lambda, \theta, \phi) \equiv \frac{dL(\theta, \phi)}{d\lambda}$, $\mu\text{W cm}^{-2}\text{nm}^{-1}\text{sr}^{-1}$, so from (2.8) we have for **downward spectral irradiance** incident on a plane surface from above

$$E_d(\lambda) = \int_0^{2\pi} \int_0^{\frac{\pi}{2}} L(\lambda, \theta, \phi) \cos \theta \sin \theta d\theta d\phi, \mu\text{W cm}^{-2}\text{nm}^{-1}, \quad (2.9)$$

and for **upward spectral irradiance** incident on the xy-plane from below (Figure 2.1)

$$E_u(\lambda) = - \int_0^{2\pi} \int_{\frac{\pi}{2}}^{\pi} L(\lambda, \theta, \phi) \cos \theta \sin \theta d\theta d\phi, \mu\text{W cm}^{-2}\text{nm}^{-1}. \quad (2.10)$$

Vector spectral irradiance, the net vertical radiant flux per unit area through a point from above and below the xy-plane¹, is by definition

$$\vec{E}(\lambda) = \int_0^{2\pi} \int_0^{\frac{\pi}{2}} L(\lambda, \theta, \phi) \cos \theta \sin \theta d\theta d\phi, \mu\text{W cm}^{-2}\text{nm}^{-1}, \quad (2.11)$$

or by inspection of (2.9) and (2.10), it is apparent that

$$\vec{E}(\lambda) = E_d(\lambda) - E_u(\lambda), \mu\text{W cm}^{-2}\text{nm}^{-1}. \quad (2.12)$$

Spectral scalar irradiance is the total flux of photons at wavelength λ per unit area (normal to the flux direction) from all directions through a point in space, or

$$\overset{\circ}{E}(\lambda) = \int_0^{2\pi} \int_0^{\pi} L(\lambda, \theta, \phi) \sin \theta d\theta d\phi, \mu\text{W cm}^{-2}\text{nm}^{-1}. \quad (2.13)$$

If an opaque surface of infinite extent is present at the xy-plane, as might be emulated with an instrument having a small spherical diffuser atop an opaque circular plate blocking flux from the lower hemisphere, the total flux through a point is the **downward spectral scalar irradiance**

$$\overset{\circ}{E}_d(\lambda) = \int_0^{2\pi} \int_0^{\frac{\pi}{2}} L(\lambda, \theta, \phi) \sin \theta d\theta d\phi, \mu\text{W cm}^{-2}\text{nm}^{-1}, \quad (2.14)$$

and conversely for the underside of the xy-plane the **upward spectral scalar irradiance** is

$$\overset{\circ}{E}_u(\lambda) = \int_0^{2\pi} \int_{\frac{\pi}{2}}^{\pi} L(\lambda, \theta, \phi) \sin \theta d\theta d\phi, \mu\text{W cm}^{-2}\text{nm}^{-1}, \quad (2.15)$$

and in this case $\overset{\circ}{E}(\lambda) = \overset{\circ}{E}_d(\lambda) + \overset{\circ}{E}_u(\lambda)$.

The symbol $\bar{F}_o(\lambda)$ is traditionally used in atmospheric optics to describe the **solar spectral irradiance above the earth's atmosphere** on a plane normal to the direction of the sun, and when the earth is at its mean distance from the sun. The symbol $\bar{F}_o(\lambda)$ is kept in these protocols, for consistency with the literature providing scales of its values (Section 2.8 below), even though it represents irradiance and should otherwise be denoted using the symbol E.

¹ This is actually only the vertical component of vector spectral irradiance (Preisendorfer 1964, 1976; Mobley 1994), but the distinction is commonly omitted in the ocean optics literature.

2.4 INHERENT OPTICAL PROPERTIES OF SEAWATER

The *inherent optical properties (IOP)* of a medium, a term originating with Preisendorfer (1960), are quantities characterizing how a light field propagating through a given point in the medium is modified by the physical processes of absorption and scattering. The IOP are material properties of the medium, and they are independent of the geometric properties of the vector light field.

In contrast to the IOP, measurements of spectral irradiance and radiance propagating through a medium are dependent on the geometric distribution of the light field, as well as on the IOP of the medium. Under varying illumination conditions, such as variations in solar azimuth and zenith angle, these *apparent optical properties (AOP)* will vary also. The AOP are measurements of the vector light field in the sea, as determined by the surface illumination boundary conditions (the part of the downward radiance field at depth $z = 0$ that is transmitted through the surface from above) and the IOP. The bidirectional character of the ocean's remote sensing reflectance, which results from interaction of surface boundary conditions and the IOP, is examined in detail in Chapter 13.

Coefficients of Absorption, Scattering and Beam Attenuation

Consider a narrow collimated beam, of cross-sectional area Δa , of monochromatic spectral energy flux $F_i(\lambda)$, $\mu\text{W nm}^{-1}$, incident normal to the xy -plane at the origin of Figure 2.2. As the flux is transmitted over a distance Δz along the z -axis², a fraction $A(\lambda) = \frac{F_A(\lambda)}{F_i(\lambda)}$ will interact with and be absorbed by water molecules, or particles, another fraction $B(\lambda) = \frac{F_B(\lambda)}{F_i(\lambda)}$ will be scattered out of the beam into other directions, and the remaining fraction $T(\lambda) = \frac{F_T(\lambda)}{F_i(\lambda)}$ will be transmitted through the volume $\Delta a \Delta z \text{ cm}^2\text{m}$.

The dimensionless fractions $A(\lambda)$, $B(\lambda)$, and $T(\lambda)$ are, respectively, the spectral absorptance, spectral scatterance, and spectral transmittance of the medium (*e.g.*, Mobley 1994). If there are no other sources in the medium, $A(\lambda) + B(\lambda) + T(\lambda) = 1$, and in the limits $\Delta a \rightarrow 0$ and $\Delta z \rightarrow 0$, we may write

$$\lim_{\Delta a \rightarrow 0} \lim_{\Delta z \rightarrow 0} \left\{ \frac{F_T(\lambda) - F_i(\lambda)}{\Delta a \Delta z} = - \frac{A(\lambda) + B(\lambda)}{\Delta z} \frac{F_i(\lambda)}{\Delta a} \right\}, \mu\text{W cm}^{-2}\text{nm}^{-1}\text{m}^{-1}. \quad (2.16)$$

Since by definition $E(\lambda) = \frac{F(\lambda)}{\Delta a}$, (2.16) may be written in differential form in terms of incident spectral irradiance as

$$\frac{dE_i(\lambda)}{dz} = -[a(\lambda) + b(\lambda)]E_i(\lambda) = -c(\lambda)E_i(\lambda), \mu\text{W cm}^{-2}\text{nm}^{-1}\text{m}^{-1}, \quad (2.17)$$

where $a(\lambda)$ is the *spectral volume absorption coefficient* $a(\lambda) = \lim_{\Delta z \rightarrow 0} \frac{A(\lambda)}{\Delta z}$, m^{-1} , $b(\lambda)$ is the *spectral volume scattering coefficient* $b(\lambda) = \lim_{\Delta z \rightarrow 0} \frac{B(\lambda)}{\Delta z}$, m^{-1} , and $c(\lambda)$ is the *spectral volume beam attenuation coefficient*,

$$c(\lambda) = a(\lambda) + b(\lambda), \text{ m}^{-1}. \quad (2.18)$$

² In the present context, the variable z in Fig. 2.2 does not correspond to depth in the water column, as it does elsewhere throughout this document. In Fig. 2.2 and the introduction of IOP, the z -axis defines only the direction of the optical path of radiant flux transmitted from the collimated source to “detector 1”, and the angular orientation of the coordinate frame in the medium is arbitrary and irrelevant.

The Volume Scattering Function

The directional scatterance $B(\lambda, \Psi, \phi) \equiv \frac{F_s(\lambda, \Psi, \phi)}{F_i(\lambda)}$ is the fraction of incident radiant flux scattered from the volume $\Delta a \Delta z$ into a solid angle increment $\Delta \Omega$ centered in direction (Ψ, ϕ) . Recall that $\Psi = \theta$ in the coordinate frame of Figure 2.2. In ocean optics, it is usually assumed that scattering of unpolarized light is azimuthally symmetric about the beam, and therefore, it is independent of ϕ in the coordinate frame of Figure 2.2. Following the derivation described by Mobley (1994), the **spectral volume scattering function (VSF)** may be defined as

$$\beta(\lambda, \Psi) = \lim_{\Delta \Omega \rightarrow 0} \lim_{\Delta z \rightarrow 0} \left\{ \frac{F_s(\lambda, \Psi, \phi)}{F_i(\lambda) \Delta \Omega \Delta z} \right\}, \text{ sr}^{-1} \text{ m}^{-1}. \quad (2.19)$$

The spectral radiant intensity $I_s(\lambda, \Psi, \phi)$ scattered from a point into direction (Ψ, ϕ) - as might be calculated for scattering by spherical particles using Mie theory, for example - is $I_s(\lambda, \Psi, \phi) = \lim_{\Delta \Omega \rightarrow 0} \frac{F_s(\lambda, \Psi, \phi)}{\Delta \Omega}$, $\mu\text{W nm}^{-1} \text{ sr}^{-1}$. With appropriate substitutions, therefore, the definition of the VSF (2.19) may be rewritten as (Mobley 1994)

$$\beta(\lambda, \Psi) = \lim_{\Delta a \rightarrow 0} \lim_{\Delta z \rightarrow 0} \left\{ \frac{I_s(\lambda, \Psi, \phi)}{E_i(\lambda) \Delta a \Delta z} \right\}, \text{ sr}^{-1} \text{ m}^{-1}. \quad (2.20)$$

The volume scattering coefficient is related to the VSF as

$$b(\lambda) = 2\pi \int_0^\pi \beta(\lambda, \Psi) \sin \Psi d\Psi, \text{ m}^{-1}. \quad (2.21)$$

The non-dimensional **volume scattering phase function**, characterizing the shape of the VSF, is defined as

$$\tilde{\beta}(\lambda, \Psi) \equiv \frac{\beta(\lambda, \Psi)}{b(\lambda)}. \quad (2.22)$$

The volume scattering phase function gives the probability that, if a photon is scattered at all it will be redirected through angle Ψ , while the volume scattering coefficient characterizes the strength of the scattering process per unit pathlength.

The Backscattering Coefficient

The fraction per unit pathlength of the incident radiant flux scattered in the backward direction, *i.e.* $\Psi > \frac{\pi}{2}$, is the **volume backscattering coefficient**

$$b_b(\lambda) = 2\pi \int_{\frac{\pi}{2}}^\pi \beta(\lambda, \Psi) \sin \Psi d\Psi, \text{ m}^{-1}. \quad (2.23)$$

The normalized backscattering coefficient, giving the probability that a scattered photon will be scattered through an angle $\Psi > \frac{\pi}{2}$, is defined as

$$\tilde{b}_b(\lambda) \equiv \frac{b_b(\lambda)}{b(\lambda)}, \quad (2.24)$$

or by combining (2.22) and (2.23)

$$\tilde{b}_b(\lambda) = 2\pi \int_{\frac{\pi}{2}}^\pi \tilde{\beta}(\lambda, \Psi) \sin \Psi d\Psi, \text{ m}^{-1}. \quad (2.25)$$

The Single Scattering Albedo

The single scattering albedo

$$\varpi(\lambda) \equiv \frac{b(\lambda)}{a(\lambda) + b(\lambda)}, \quad (2.26)$$

alternatively denoted as ϖ_o , parameterizes the relative contribution of scattering to total attenuation of light in the medium and is also called the *probability of photon survival*, for a photon that interacts with the medium.

Fluorescence and Raman Scattering

The IOP of seawater discussed above deal only with absorption and elastic scattering by molecules and particles. The radiant field in water also includes *inelastic scattering* contributions due to radiant energy absorbed by the medium at one wavelength, and emitted at a longer wavelength. The coefficients characterizing these internal sources of radiant energy are also IOP of the medium. Fluorescence emission by chlorophyll *a*, other phytoplankton pigments, and dissolved organic molecular compounds is one important inelastic scattering process in seawater (Chapter 13). Raman scattering by water molecules is the other important inelastic scattering process in the sea (Section 10.4 and Chapter 13).

Additive Property of Inherent Optical Properties

The IOP of natural seawater are a combination of IOP of pure water (molecular scattering and absorption), materials dissolved in seawater (also molecular scattering and absorption), and suspended particles (particle scattering and absorption). Therefore, each individual IOP may be expanded as the sum of contributions by each of these material components.

For absorption,

$$a(\lambda) = a_w(\lambda) + a_p(\lambda) + a_g(\lambda), \text{ m}^{-1}, \quad (2.27)$$

where a_w , a_p and a_g are the absorption coefficients of pure water, particles and dissolved organic materials, respectively.

It is usually assumed that molecular scattering by dissolved organic materials is indistinguishable from molecular scattering by water, so that the VSF expands as

$$\beta(\lambda) = \beta_w(\lambda) + \beta_p(\lambda), \text{ m}^{-1}, \quad (2.28)$$

where β_w and β_p are respectively the VSFs of water and particles. Given the expansion of the absorption coefficient and VSF, it is straightforward to determine the expansions of all other IOP by combining (2.27) and (2.28) with equations (2.18) through (2.26).

It is possible to further partition absorption and scattering coefficients to account for mixtures of different types of particles, or dissolved materials (see, *e.g.*, Chapter 15).

Inherent Optical Properties of Pure Water

For purposes of these protocols, the coefficients for molecular absorption by pure water $a_w(\lambda) \text{ m}^{-1}$, are adopted from Sogandares and Fry (1997) for wavelengths between 340 nm and 380 nm, Pope and Fry (1997) for wavelengths between 380 nm and 700 nm, and Smith and Baker (1981) for wavelengths between 700 nm and 800 nm.

The volume scattering coefficients of pure water, $b_w(\lambda) \text{ m}^{-1}$, are given by Morel (1974). The molecular (Rayleigh) scattering phase function is

$$\tilde{\beta}_w(\Psi) = \frac{3(1 + \cos^2 \Psi)}{16\pi}, \quad (2.29)$$

or more generally

$$\tilde{\beta}_w(\Psi) = \frac{3(1+\delta)\left(1 + \frac{1-\delta}{1+\delta}\cos^2\Psi\right)}{8\pi(2+\delta)}, \quad (2.30)$$

where δ is the depolarization ratio, which has an average value $\bar{\delta} \approx 0.09$ (Morel 1974).

IOP and Radiant Field Relationships Distributed in a Medium

The foregoing IOP definitions and relationships, presented above via equations (2.16) through (2.26), are expressed in a local coordinate system (Figure 2.2) that provides a convenient framework for describing measurement concepts. To apply the IOP and these relationships to vector radiant fields in the atmosphere ocean system, it is necessary to take account of variations with location of the IOP and vector radiant fields throughout the medium. The local “instrument coordinates” of Figure 2.2 are not useful in this context, and it is more appropriate to express the IOP and radiant field relationships in the coordinate frame of Figure 2.1, where the xy-plane is parallel to the air-sea interface and the z-axis is fixed as the local vertical. In this more general framework, an optical transmission path vector (r, θ, ϕ) is not restricted to $(r, 0, 0)$, as in Figure 2.2 and the above IOP definitions, so that the incremental pathlength Δz appearing in (2.16) through (2.20) becomes $\Delta r \equiv \frac{\Delta z}{\cos\theta}$, where θ is the zenith angle in the direction of photon flow³. As discussed in

Section 2.2, the scattering angle $\Psi \neq \theta$ in the more general coordinate frame of Figure 2.1, but must be determined using (2.5). Moreover, azimuthally symmetric scattering about a transmission beam, while still assumed, is no longer synonymous with ϕ - independence of scattering.

Unless stated otherwise, it is assumed throughout the protocols that horizontal variations in IOP are negligible compared to vertical variations, so that the spatial distributions of the primary IOP are expressed as $a(z, \lambda)$, $b(z, \lambda)$, $c(z, \lambda)$, and $\beta(z, \lambda, \Psi)$. This so-called “plane-parallel assumption” does not suggest that IOP do not vary with geographic position, but simply that horizontal variations are weak enough to be neglected in radiative transfer calculations related to the ocean color problem. It is recognized that this assumption may break down in Case-2 water masses, and other special circumstances, where 3-dimensional radiative transfer processes must be taken into account.

The incident spectral radiance distribution at the origin associated with a perfectly collimated source incident on the plane normal to $\hat{\mathbf{S}} = (r=1, \theta_o, \phi_o)$ (Figure 2.1) is related to the incident spectral irradiance

$$E_i(\lambda, \theta_o, \phi_o) = \int_0^{2\pi} \int_0^\pi L_i(\lambda, \theta, \phi) \cos(\theta - \theta_o) \delta(\theta - \theta_o) \delta(\phi - \phi_o) \sin\theta d\theta d\phi, \text{ where the Dirac delta function } \delta(\theta - \theta_o) \text{ is}$$

$$\delta(\theta - \theta_o) \equiv \begin{cases} 1, & \theta = \theta_o, \\ 0, & \text{otherwise,} \end{cases}$$

and similarly for $\delta(\phi - \phi_o)$, so that within the constraints of this construct

$$E_i(\lambda, \theta_o, \phi_o) = \lim_{\Delta\Omega \rightarrow 0} L_i(\lambda, \theta_o, \phi_o) \Delta\Omega. \text{ Scattered radiance } L_s(\lambda, \theta, \phi) = \lim_{\Delta a \rightarrow 0} \frac{I_s(\lambda, \theta, \phi)}{\Delta a}, \text{ } \mu\text{W cm}^{-2} \text{ nm}^{-1} \text{ sr}^{-1},$$

i.e. radiance is radiant intensity per unit area (Mobley 1994). Using these relationships in differential form, and taking account of the depth dependence of IOP and coordinate transformations, equation (2.17) may be rewritten as

³ Note that for the source direction and transmission vector conventions of Figure 2.2, $\theta = \pi - \theta_o$, and $\cos\theta = -\cos\theta_o$.

$$\begin{aligned} \frac{dE_i(z, \lambda, \theta_o, \phi_o)}{dz} \cos(\pi - \theta_o) &= -[a(z, \lambda) + b(z, \lambda)] E_i(z, \lambda, \theta_o, \phi_o) \\ &= -c(z, \lambda) E_i(z, \lambda, \theta_o, \phi_o), \mu\text{W cm}^{-2} \text{nm}^{-1} \text{m}^{-1}, \end{aligned} \quad (2.31)$$

and equation (2.20) as

$$\frac{d^2 L_s(z, \lambda, \theta, \phi)}{dz d\omega} \cos \theta = \beta(z, \lambda, \Psi) L_i(z, \lambda, \theta_o, \phi_o),$$

or for more general radiance distributions, the scattered radiance per unit pathlength is expressed as

$$\frac{dL_s(z, \lambda, \theta, \phi)}{dz} \cos \theta = \int_0^{2\pi} \int_0^\pi \beta(z, \lambda, \Psi) L_i(z, \lambda, \theta_o, \phi_o) \sin \theta_o d\theta_o d\phi_o, \mu\text{W cm}^{-2} \text{nm}^{-1} \text{sr}^{-1} \text{m}^{-1}. \quad (2.32)$$

2.5 REFLECTION AND REFRACTION AT THE SEA SURFACE

The geometric aspects of reflection from, and refracted transmission through, the air-sea interface are illustrated in Figure 2.4. The water surface is located at depth $z = 0$, and the upper side of the interface is denoted $z = 0^+$, while the underside of the interface at the same depth is denoted $z = 0^-$. Ray paths indicating radiance incident on, or transmitted through, the interface are illustrated as solid arrows. Ray paths indicating radiance reflected from the interface are shown as dashed arrows.

The Refractive Index of a Medium

The complex refractive index of a medium is denoted $m(\lambda) = n(\lambda) + in'(\lambda)$. The real part of the refractive index, $n(\lambda)$, is the ratio of the speed of light in one medium relative to that in another. The imaginary part, $n'(\lambda)$, is directly related to the volume absorption coefficient $a(\lambda)$ of the medium. The complex refractive index is another IOP of seawater. The imaginary part of the refractive index is not utilized in the present version of the protocols, and further use of the term “*refractive index*” is taken to mean the real part $n(\lambda)$.

The refractive index of air is approximately independent of wavelength with value $n \approx 1$. The refractive index of water relative to air is approximately $n_w(\lambda) \cong 1.34$. Its wavelength dependence, while weak throughout the visible spectrum, may be computed for fresh water from the empirical relationship (Austin and Halikas 1976) as

$$n_w(\lambda) = 1.325147 + \frac{6.6096}{\lambda - 137.1924}. \quad (2.33)$$

Austin and Halikas (1976) also tabulated variations in $n_w(\lambda)$ for seawater as a function of temperature and salinity; these variations are also weak, for visible wavelengths, and may be neglected for most applications discussed in these protocols.

Snell's Law of Refraction at a Plane Interface Between Two Media

Because the speed of light in seawater is approximately $\frac{3}{4}$ of that in air, radiance incident on the sea surface at angle θ is refracted to an angle θ' that is closer to the vertical (left-hand diagram in Figure 2.4). The reverse process takes place when upward radiance incident from below is transmitted across the interface into air (right-hand diagram of Figure 2.4). The angles θ and θ' are related by Snell's Law of Refraction

$$n = \frac{\sin \theta}{\sin \theta'}. \quad (2.34)$$

Downward radiance from solid angle Ω sr in air that is transmitted through the interface, converges into a smaller solid angle Ω' sr in water. The reverse process, solid angle divergence, occurs when radiance is transmitted upward from water to air. By combining (2.6) with (2.34), it may be shown that the solid angles are related as $\Omega = n_w^2 \Omega'$, where we neglect the weak wavelength dependence for wavelengths of interest in these protocols. There are two important consequences of the refractive radiance convergence/divergence relationship. The first is that downward radiance incident on the sea surface from the entire upper hemisphere converges in water into the cone defined by the critical angle $\theta'_c \cong 48.3^\circ$, for $n_w \cong 1.34$, and conversely light transmitted upward as water-leaving radiance originates entirely within the critical angle cone. The second important consequence is that upward radiance incident on the sea surface from below at angles $\theta' > \theta'_c$ is totally reflected internally and contributes strongly to the downward radiance field at $z = 0^-$. The occurrence of total internal reflectance of upward radiance beyond the critical angle explains why although approximately 97% of downward irradiance is transmitted through the interface into water, only about 52% of upward irradiance is transmitted through the interface into the air (see also Chapter 13).

Reflection at the Sea Surface

Reflectance from a plane surface is determined by the Fresnel Reflectance function,

$$\rho_F(\theta, \theta') = \frac{1}{2} \left[\frac{\sin^2(\theta - \theta')}{\sin^2(\theta + \theta')} + \frac{\tan^2(\theta - \theta')}{\tan^2(\theta + \theta')} \right], \quad (2.35)$$

where the first and second terms in vertical brackets are the reflectances for light components polarized, respectively, perpendicular and parallel to the plane of incidence. The plane of incidence as illustrated in Figure 2.1, for example, is the plane defined by the z -axis and the solar vector $\hat{\mathbf{S}}$. As above, the angles θ and θ' are the incidence angles in air and water, as related by (2.34), and the angle of reflection is equal to the angle of incidence, either above, or below the surface (Figure 2.4). An important property of (2.35) is that $\rho_F(\theta', \theta) = \rho_F(\theta, \theta')$, *i.e.* the reflectance for light incident from below at angle θ' and refracted on transmission to angle θ in air, is the same as reflectance for light incident from above at angle θ and refracted to angle θ' in water. When $\theta = \theta' = 0$, *i.e.* for normal incidence,

$$\rho_F(0, 0) = \left[\frac{n-1}{n+1} \right]^2, \quad (2.36)$$

and for an air-water interface $\rho_F(0, 0) \cong 0.02$.

Were the sea surface a flat plane, its reflectance $\rho(\theta', \theta; W) = \rho(\theta, \theta'; W)$ would be simply the Fresnel reflectance as given in (2.35). However, wave roughness elements are always present on the sea surface, and its slope spectrum is related to wind speed W by the empirical relationship of Cox and Munk (1954). Even when $W = 0$, variation of surface tension induced by the passage of swell generates capillary waves to create a surface slope spectrum of small, but significant, amplitude. The Fresnel reflectance does hold locally for each tilted wave facet, so the reflectance of the sea surface $\rho(\theta, \theta'; W)$ may be modeled by combining the Cox-Munk (1954) equations for the slope spectrum with (2.35) (Austin 1974; Morel and Gentili 1996; Mobley, 1999). The determination and applications of $\rho(\theta, \theta'; W)$ are discussed at more length in Chapters 12 and 13, and in references cited in those chapters.

Radiance Transmittance Through the Sea Surface

With reference to Figure 2.4, the downward transmittance of radiance through the interface is given by

$$L_d^t(0^-, \lambda, \theta', \phi) = L_d(0^+, \lambda, \theta, \phi) n^2 [1 - \rho(\theta, \theta'; W)], \quad (2.37)$$

and upward transmittance by

$$L_w(\lambda, \theta, \phi) = L_u(0^-, \lambda, \theta', \phi) \frac{[1 - \rho(\theta', \theta; W)]}{n^2}, \quad (2.38)$$

where $L_w(\lambda, \theta, \phi)$ is **water-leaving radiance**, which is defined only at $z = 0^+$ and the explicit depth notation is omitted.

2.6 THE RADIATIVE TRANSFER EQUATION

The propagation of radiance through the sea, assuming that IOP are horizontally homogeneous, is governed by the radiative transfer equation (RTE)

$$\begin{aligned} \frac{dL(z, \lambda, \theta', \phi)}{dz} \cos \theta' = & -c(z, \lambda) L(z, \lambda, \theta', \phi) + \int_0^{2\pi} \int_0^\pi \beta(z, \lambda, \Psi) L(z, \lambda, \theta'_o, \phi_o) \sin \theta'_o d\theta'_o d\phi_o + \\ & L_r(z, \lambda) + L_f(z, \lambda), \mu\text{W cm}^{-2}\text{nm}^{-1}\text{sr}^{-1}\text{m}^{-1}, \end{aligned} \quad (2.39)$$

where z is depth in m, $L_r(z, \lambda)$ and $L_f(z, \lambda)$ are, respectively, inelastic scattering radiance emissions (assumed to be isotropic) due to Raman scattering by water and fluorescence by particles and dissolved matter (see also Chapters 10 and 13), and the other variables are previously defined. Angular relationships in (2.39) are as in Figure 2.1 and the scattering angle Ψ is related to angles (θ', ϕ) and (θ'_o, ϕ_o) by equation (2.5). The first term on the right-hand-side of (2.39) accounts for attenuation of radiance transmitted over path $\frac{dz}{\cos \theta'}$, and the second term represents the increase in radiance over that path due to photons scattered into direction (θ', ϕ) from all other (source) angles (θ'_o, ϕ_o) (Fig. 2.1). The combined radiance increase contributed by the three elastic and inelastic scattering source terms is called **path radiance**, following Preisendorfer (1964).

The RTE, equation (2.39), is given here as a compact way to describe the basic relationship between the IOP and vector radiant fields in water. The reader interested in methods of solving the RTE for a given vertical distribution of IOP and surface boundary conditions, $L_d^i(0^-, \lambda, \theta', \phi)$ and $\rho(\theta, \theta'; W)$, is referred to, *e.g.*, Mobley (1994) and references cited there. Solutions to the RTE figure prominently in the determination of exact normalized water-leaving radiance, as described in Chapter 13.

The Beer-Lambert-Bouguer Law

In the absence of other sources, a collimated beam of radiance $L(\lambda, \theta, \phi)$ transmitted through seawater at a depth z m is attenuated along path $|\Delta r(\theta', \phi)| = \left| \frac{\Delta z}{\cos \theta'} \right|$ as

$$\frac{dL(z, \lambda, \theta', \phi)}{dz} \cos \theta' = -c(z, \lambda) L(z, \lambda, \theta', \phi), \mu\text{W cm}^{-2}\text{nm}^{-1}\text{m}^{-1}, \quad (2.40)$$

under the same assumptions leading to (2.39). The solution to (2.40) for transmission of radiance over a path of length Δr is

$$L(z + \Delta z, \lambda, \theta', \phi) = L(z, \lambda, \theta', \phi) e^{-\frac{1}{\cos \theta'} \int_{\Delta z}^0 c(z, \lambda) dz}, \mu\text{W cm}^{-2}\text{nm}^{-1}. \quad (2.41)$$

Equation (2.41) is called the Beer-Lambert-Bouguer Law, and represents only the attenuation term in the RTE, (2.39).

The Beer-Lambert-Bouguer Law in the form of (2.41) is applicable only in a purely absorbing medium, or in a situation where a single source produces a narrow collimated beam that is transmitted to a detector over a distance short enough that multiple scattering path radiance is negligible (*e.g.* the source to

detector-1 path of Figure 2.2). The latter case is the basis for determining $c(\lambda)$ using a beam transmissometer (Sections 4.6 and 9.4).

2.7 RADIOMETRIC QUANTITIES IN OCEAN COLOR REMOTE SENSING

Radiance Fields at the Sea Surface in Water and Air

The boundary conditions for the radiative transfer formulation of the ocean color remote sensing problem are the downward radiance field $L_d^-(0^-, \lambda, \theta', \phi)$ and the wind-speed dependent reflectance $\rho(\theta, \theta'; W)$. Equation (2.37) relates these boundary conditions to the incident downward radiance field $L_d(0^+, \lambda, \theta, \phi)$ above the surface.

The downward radiance field $L_d^-(0^-, \lambda, \theta', \phi)$ is transmitted into the medium, where it is absorbed and redistributed by scattering, as in (2.39), to produce the radiance fields $L_d(z, \lambda, \theta', \phi)$ and $L_u(z, \lambda, \theta', \phi)$. As illustrated in Figure 2.4, part of the upwelling radiance field $L_u(0^-, \lambda, \theta', \phi)$ is reflected downward at the interface (all of it for $\theta' > \theta_c^-$), so that the total downward radiance field at $z = 0^-$ is

$$L_d^-(0^-, \lambda, \theta', \phi) = L_d(0^-, \lambda, \theta', \phi) + \rho(\theta', \theta; W) L_u(0^-, \lambda, \theta', \phi). \quad (2.42)$$

The upwelling radiance field in air at $z = 0^+$ is water leaving radiance, as given by (2.38), combined with the radiance field reflected upward at the surface, i.e.

$$L_u(0^+, \lambda, \theta, \phi) = L_w(\lambda, \theta, \phi) + \rho(\theta, \theta'; W) L_d(0^+, \lambda, \theta, \phi). \quad (2.43)$$

Irradiance at the Sea Surface in Water and Air

The downward and upward irradiance in water and air at the interface are determined by integrating the vector radiance fields, using the general relationships (2.9) and (2.10) above, to determine **downward spectral irradiance** above the interface

$$E_d(0^+, \lambda) \equiv \int_0^{2\pi} \int_0^{\frac{\pi}{2}} L_d(0^+, \lambda, \theta, \phi) \cos \theta \sin \theta d\theta d\phi, \quad (2.44)$$

which is often denoted $E_s(\lambda) \equiv E_d(0^+, \lambda)$ throughout the protocol chapters, **downwelled spectral irradiance** just beneath the interface

$$E_d(0^-, \lambda) \equiv \int_0^{2\pi} \int_0^{\frac{\pi}{2}} L_d(0^-, \lambda, \theta', \phi) \cos \theta' \sin \theta' d\theta' d\phi, \quad (2.45)$$

upwelled spectral irradiance just beneath the interface

$$E_u(0^-, \lambda) \equiv \int_0^{2\pi} \int_0^{\frac{\pi}{2}} L_u(0^-, \lambda, \theta', \phi) \cos \theta' \sin \theta' d\theta' d\phi, \text{ and} \quad (2.46)$$

and **upwelled spectral irradiance** just above the interface

$$E_u(0^+, \lambda) \equiv \int_0^{2\pi} \int_0^{\frac{\pi}{2}} L_u(0^+, \lambda, \theta, \phi) \cos \theta \sin \theta d\theta d\phi, \mu\text{W cm}^{-2}\text{nm}^{-1}. \quad (2.47)$$

It should be noted that because of the contributions of reflected radiance away from each side of the interface, as expressed in (2.42) and (2.43), one couldn't determine, *e.g.*, $E_d(0^-, \lambda)$ by simply transmitting $E_d(0^+, \lambda)$ downward across the interface.

Vertical Profiles of Irradiance and Radiance in Natural Waters

Given solutions to the RTE (2.39) for particular surface boundary conditions and IOP profiles within the water column, it is straightforward to substitute the depth variable z to extend equations (2.45) and (2.46) to define the profiles of downwelling and upwelling spectral irradiance $E_d(z, \lambda)$ and $E_u(z, \lambda)$, respectively. However, radiance distribution profiles $L_d(z, \lambda, \theta', \phi)$ and $L_u(z, \lambda, \theta', \phi)$ are not ordinarily measured as functions of depth, and so it is assumed that diffuse attenuation of $E_d(z, \lambda)$ and $E_u(z, \lambda)$ follows the form of the Beer-Lambert-Bouguer Law as

$$E_d(z, \lambda) = E_d(0^-, \lambda) e^{-\int_0^z K_d(z, \lambda) dz}, \quad (2.48)$$

and

$$E_u(z, \lambda) = E_u(0^-, \lambda) e^{-\int_0^z K_u(z, \lambda) dz}, \quad (2.49)$$

where $K_d(z, \lambda)$ and $K_u(z, \lambda)$ are the respective **diffuse attenuation coefficients** for downwelled and upwelled spectral irradiance. Methods for determining $K_d(z, \lambda)$ and $K_u(z, \lambda)$ from measured profiles of $E_d(z, \lambda)$ and $E_u(z, \lambda)$ are described in Chapter 10.

It is also common to measure vertical profiles of nadir-viewing upwelled radiance $L_u(z, \lambda) \equiv L_u(z, \lambda, 0, 0)$. It is assumed that the vertical attenuation of upwelled radiance also follows the form of the Beer-Lambert-Bouguer Law as

$$L_u(z, \lambda) = L_u(0^-, \lambda) e^{-\int_0^z K_L(z, \lambda) dz}, \quad (2.50)$$

where $K_L(z, \lambda)$ is the diffuse attenuation coefficient for $L_u(z, \lambda)$. Methods for determining $K_L(z, \lambda)$ from measured profiles of $L_u(z, \lambda)$, and for determining $L_u(0^-, \lambda)$ by using (2.48) to extrapolate the measured $L_u(z, \lambda)$ profile to the surface, are given in Chapter 10.

Reflectance of Irradiance and Radiance in Natural Waters

Irradiance reflectance is defined as

$$R(z, \lambda) \equiv \frac{E_u(z, \lambda)}{E_d(z, \lambda)}. \quad (2.51)$$

Following Austin (1974) and Morel and Gentili (1996) the upwelled irradiance and radiance fields at $z = 0^-$ are related as

$$Q(0^-, \lambda, \theta', \phi) \equiv \frac{E_u(0^-, \lambda)}{L_u(0^-, \lambda, \theta', \phi)}, \text{ sr}, \quad (2.52)$$

so that radiance reflectance may be determined in turn as

$$L_u(0^-, \lambda, \theta', \phi) = \frac{E_d(0^-, \lambda) R(0^-, \lambda)}{Q(0^-, \lambda, \theta', \phi)}. \quad (2.53)$$

Given $L_u(0^-, \lambda, \theta', \phi)$, water-leaving radiance $L_w(\lambda, \theta, \phi)$ may be determined from (2.38).

All of the quantities in (2.53), and therefore also $L_w(\lambda, \theta, \phi)$, are AOP that are dependent on the surface boundary conditions and IOP of the water body. It is clear, therefore, that the remote sensing reflectance

$$R_{RS}(\lambda, \theta, \phi) = \frac{L_w(\lambda, \theta, \phi)}{E_d(0^+, \lambda)} \quad (2.54)$$

is also an AOP, and has a bidirectional nature that is dependent (in a first approximation) on solar zenith angle θ_o . In early attempts to account for this bidirectionality, Gordon and Clark (1981) assumed the factor Q to be a constant, following Austin (1974), and defined normalized water-leaving radiance $L_{WN}(\lambda)$ as that radiance which would be observed if the sun were at zenith and at mean earth-sun distance and there were no atmosphere, i.e.

$$L_{WN}(\lambda) = L_w(\lambda, \theta, \phi) \frac{\bar{F}_o(\lambda)}{E_d(0^+, \lambda)}, \quad (2.55)$$

where $\bar{F}_o(\lambda)$ is the extraterrestrial solar flux at mean earth-sun distance (Neckel and Labs 1984). Morel and Gentili (1991, 1993, 1996) demonstrated conclusively, however, that Q is not constant and that $L_{WN}(\lambda)$ remains an AOP with dependence on IOP, solar zenith angle, and surface roughness conditions. They further showed that by properly relating $Q(0^-, \lambda, \theta', \phi)$ and $R(0^-, \lambda)$ to IOP and θ_o , and relating $E_d(0^-, \lambda)$ to $E_d(0^+, \lambda)$ for a given θ_o and $\rho(\theta', \theta; W)$, it is possible to transform $L_{WN}(\lambda)$ into an exact normalized water-leaving radiance $L_{WN}^{ex}(\lambda)$ that has been properly adjusted to remove bidirectional reflectance effects. The reader is referred to Chapter 13 for a detailed discussion relating reflectance to IOP and θ_o , and describing the physical processes and approximations that relate water-leaving radiance to exact normalized water-leaving radiance. This is a critical topic and protocol chapter, because $L_{WN}^{ex}(\lambda)$ is the only valid form of water-leaving radiance by which measurements from satellite ocean color sensors and *in situ* radiometers may be compared.

2.8 EXTRATERRESTRIAL SOLAR FLUX SPECTRUM

SeaWiFS, MODIS and CZCS algorithms, are all predicated on using a single determination of the spectrum of extraterrestrial solar irradiance for the average distance between the earth and sun, $\bar{F}_o(\lambda)$. Within the SeaWiFS and MODIS ocean color remote sensing and ocean optics communities, for instance, the presently accepted extraterrestrial solar flux spectrum is that of Neckel and Labs (1984). There is less unanimity in the atmospheric community, and in some segments of the international remote sensing community, in the choice of a “standard” solar spectrum (*e.g.*, MERIS).

It is important that a single, common standard solar flux spectrum be used in every aspect of research and validation in ocean color remote sensing. The extraterrestrial solar flux enters into normalization of water leaving radiance, calibration and interpretation of atmospheric radiation measurements, and

atmospheric correction algorithms for all satellite ocean color radiometers. For example, if normalized water leaving radiance were computed from *in situ* measurements using a “better” estimate of the solar flux, in lieu of Neckel and Labs (1984), a comparison with a satellite determination of normalized water-leaving radiance would be biased by the difference between the two solar spectra. There is some evidence (Biggar 1998; Schmid *et al.* 1998) that the recent measurements of Thuillier *et al.* (1998a, 1998b) are more consistent with NIST traceable lamp-based irradiance and radiance sources. On the basis of such findings, it seems clear that NASA and the international ocean color community should reconsider the choice of a standard for extraterrestrial solar flux. Assuming that a change would improve the uncertainty budget of, *e.g.* atmospheric correction validations, the expected benefits are obvious. On the other hand, adopting a different solar spectrum would require significant changes in the software used for operational processing and validation analyses within SeaWiFS, MODIS and other ocean color satellite project offices. Any such transition must be planned and implemented comprehensively in a forum that embraces the entire international community.

The choice of any of the published $\bar{F}_o(\lambda)$ scales cited above will have no discernable effect on the internal uncertainty budget of the vicarious calibration for any individual satellite ocean color sensor (M. Wang, Pers. Comm.). Exact normalized water leaving radiances $L_{\text{WN}}^{\text{ex}}(\lambda)$ determined from a satellite sensor depend only on atmospheric transmittance, solar zenith angle and earth sun distance, as $\bar{F}_o(\lambda)$ cancels in the determination of $L_{\text{WN}}(\lambda)$ [equation (13.18)]. Therefore, $L_{\text{WN}}^{\text{ex}}(\lambda)$ determinations are directly comparable between two sensors without consideration of the choices of $\bar{F}_o(\lambda)$ scales. The consequences of arbitrary $\bar{F}_o(\lambda)$ scale selections between sensors are:

1. The ratios of sensor-specific $\bar{F}_o(\lambda)$ scales values must be used to directly compare aperture radiances measured above the atmosphere $[L_{\text{TOA}}(\lambda)]$ by two sensors using different $\bar{F}_o(\lambda)$ scales for vicarious calibration;
2. When measured surface irradiance at sea level is used to determine $L_{\text{WN}}(\lambda) = L_{\text{w}}(\lambda, \theta, \phi) \frac{\bar{F}_o(\lambda)}{E_s(\lambda)}$ [equation (13.8)] from *in situ* field radiometric data, $L_{\text{WN}}(\lambda)$ and $L_{\text{WN}}^{\text{ex}}(\lambda)$ must be computed using the particular $\bar{F}_o(\lambda)$ scale of each sensor to which that data is to be compared. On the other hand, if the same method used to determine $L_{\text{WN}}(\lambda)$ for a satellite sensor is used with *in situ* data [equation (13.18)], *e.g.* as with the MOBY $L_{\text{WN}}(\lambda)$ time-series (Chapter 11), differences in $\bar{F}_o(\lambda)$ scales need not be considered. The uncertainty budget of the second (13.18) approach is dominated by uncertainties in the modeled atmospheric transmittance, and neglect of cloud effects in the model. Atmospheric transmittance and cloud effects are included implicitly in measured, actual $E_s(\lambda)$, and the uncertainty budget of the first (13.8) approach combines the uncertainties of $E_s(\lambda)$ measurements and the selected $\bar{F}_o(\lambda)$ scale. Present knowledge of the relative uncertainties of $L_{\text{WN}}^{\text{ex}}(\lambda)$ determined using these two approaches is insufficient to justify a clear-cut choice of a preferred method.

The three alternatives are:

1. Ignore the matter, leave the choice of $\bar{F}_o(\lambda)$ scale to each ocean color sensor team, and do not use measured surface irradiances to determine $L_{\text{WN}}^{\text{ex}}(\lambda)$ from *in situ* measurements used for validation or vicarious calibration;

2. Publish the particular $\bar{F}_o(\lambda)$ adopted by each satellite ocean color sensor project, thus allowing the use of measured $E_s(\lambda)$ in the determination of $L_{WN}^{ex}(\lambda)$ from *in situ* field data; or
3. Adopt a common international standard scale of $\bar{F}_o(\lambda)$ for use by the entire international ocean color community with all satellite ocean color sensors and associated *in situ* validation data.

Option 1 is the obviously simplest to implement, and it is not mutually exclusive with Option 2. Neither is Option 2 difficult to implement, since it requires only that each satellite ocean color sensor project publish the $\bar{F}_o(\lambda)$ scale that it uses. Option 3 would be more transparent to the user, in that one need not pay attention to which $\bar{F}_o(\lambda)$ scale to use with a particular satellite sensor for any purpose, but it may be more costly and difficult to implement. An informal working group is currently considering these issues and options under the auspices of the International Ocean Color Coordinating Group (IOCCG).

Pending future recommendations by the IOCCG, the present Ocean Optics Protocols assume that any analysis, or application, involving extraterrestrial solar irradiance $\bar{F}_o(\lambda)$ uses the scale of Neckel and Labs (1984).

REFERENCES

- Austin, R.W., 1974: The remote sensing of spectral radiance from below the ocean surface. In: *Optical Aspects of Oceanography*, N.G. Jerlov and E.S. Nielson, Eds., pp 317-344.
- Austin, R.W. and G. Halikas, 1976: The index of refraction of seawater. *SIO Ref. 76-1*, Vis. Lab., Scripps Inst. of Oceanography, La Jolla, California, 64pp.
- Biggar, S.F. 1998: Calibration of a visible and near-infrared portable transfer radiometer. *Metrologia*, **35**: 701-706.
- Cox, C. and W. Munk, 1954. Measurement of the roughness of the sea surface from photographs of the sun's glitter. *J. of the Opt Soc. of Am.* **44**(11). 838-850.
- Fargion, G.S. and J.L. Mueller, 2000: *Ocean Optics Protocols for Satellite Ocean Color Sensor Validation, Revision 2*, NASA TM 2001-209955, NASA Goddard Space Flight Center, Greenbelt, Maryland, 184
- Gordon, H.R., D.K. Clark, J.W. Brown, O.B. Brown, R.H. Evans, and W.W. Broenkow, 1983. Phytoplankton pigment concentrations in the middle Atlantic bight: comparison of ship determinations and CZCS estimates. *Appl. Opt.* **22**(1): 20-36.
- Jerlov, N.G., 1976: *Marine Optics*, Elsevier, New York, 231pp.
- Liou, K-N, 1980: *An Introduction to Atmospheric Radiation*, Academic Press, New York, 392pp.
- Mobley, C.D., 1994: *Light and Water; Radiative Transfer in Natural Waters*. Academic Press, San Diego, California. 592pp.
- Mobley, C.D., 1999: Estimation of the remote-sensing reflectance from above-surface measurements. *Appl. Opt.* **38**: 7442-7455.
- Morel, A., 1974: Optical properties of pure water and pure sea water. In: *Optical Aspects of Oceanography*, N.G. Jerlov and E.S. Nielson, Eds., pp1-23.
- Morel, A., and B. Gentili, 1991: Diffuse reflectance of oceanic waters. I. Its dependence on sun angle as influenced by the molecular scattering contribution. *Appl. Opt.*, **30**, 4,427-4,438.
- Morel, A., and B. Gentili, 1993: Diffuse reflectance of oceanic waters. II. Bidirectional aspects. *Appl. Opt.* **32**: 6,864-6,879.

- Morel, A., and B. Gentili, 1996: Diffuse reflectance of oceanic waters. III. Implication of bidirectionality for the remote-sensing problem. *Appl. Opt.* **35**: 4850-4862.
- Morel, A. and R.C. Smith, 1982. Terminology and Units in Optical oceanography. *Marine Geodesy*, **5**(4). 335-350.
- Mueller, J.L. and R.W. Austin, 1992: Ocean Optics Protocols for SeaWiFS Validation. *NASA Tech. Memo. 104566, Vol. 5*, S.B. Hooker and E.R. Firestone, Eds., NASA Goddard Space flight center, Greenbelt, Maryland, 45 pp.
- Mueller, J.L. and R.W. Austin, 1995: Ocean Optics Protocols for SeaWiFS Validation, Revision 1. *NASA Tech. Memo. 104566, Vol. 25*, S.B. Hooker and E.R. Firestone, Eds., NASA Goddard Space flight center, Greenbelt, Maryland, 66 pp.
- Neckel, H., and D. Labs, 1984: The solar radiation between 3,300 and 12,500 AA. *Solar Phys.*, **90**: 205--258.
- Preisendorfer, R.W. 1960: *Recommendation on the standardization of concepts, terminology and notation of hydrologic optics*. Scripps Inst. Of Oceanogr., SIO Report, 96pp.
- Preisendorfer, R.W. 1964: A model for radiant distribution in natural hydrosols. In: *Physical Aspects of Light in the Sea*, J.C. Tyler [Ed.]. Univ. Hawaii Press, Honolulu, Hawaii, pp. 51-60.
- Preisendorfer, R.W., 1976: Hydrologic Optics, in 6 volumes: Vol. 1: Introduction, 218pp (NTIS PB-259 793/8ST); Vol. 2: Foundations, 400 pp (NTIS PB-259 794/6ST); Vol. 3: Solutions, 246 pp (NTIS PB-259 795/3ST); Vol. 4: Imbeddings, 207 pp (NTIS PB-259 796/1ST); Vol. 5: Properties, 296 pp (NTIS PB-259 797/9ST); Vol. 6: Surfaces, 390 pp (NTIS PB-268 704/4ST), Pacific Mar. Environ. Lab/NOAA Seattle, WA. (Available from Natl. Tech. Inform. Serv., Springfield, VA 22161, using the above NTIS numbers.)
- Schmid, B., P.R. Spyak, S.F. Biggar, C. Wehrli, J. Seider, T. Ingold, C. Matzler and N. Kampfer. 1998: Evaluation of the applicability of solar and lamp radiometric calibrations of a precision Sun photometer operating between 300 and 1025 nm. *Appl. Opt.* **37**: 3923-3941.
- Thuillier, G., M. Herse, P.S. Simon, D. Labs, H. Mandel, D. Gillotay and T. Foujols. 1998a: The visible solar spectral irradiance from 350 to 850 nm as measured by the SOLSPEC spectrometer during the Atlas I mission. *Solar Phys.* **177**: 41-61.
- Thuillier, G., M Herse, P.C. Simon, D. Labs, H. Mandel and D. Gillotay, 1998b: Observation of the solar spectral irradiance from 200 nm to 870 nm during the ATLAS 1 and ATLAS 2 missions by the SOLSPEC spectrometer. *Metrologia*, **35**: 689-695.

Chapter 3

Data Requirements for Ocean Color Algorithms and Validation

James L. Mueller¹, Giulietta S. Fargion² and Charles R. McClain³

¹*Center for Hydro-Optics and Remote Sensing, San Diego State University, California*

²*Science Applications International Corporation, Beltsville, Maryland*

³*NASA, Goddard Space Flight Center, Greenbelt, Maryland*

3.1 INTRODUCTION

The principal *in situ* variables to be measured, or derived from measurements, for satellite ocean color sensor validation, and algorithm development and validation, are listed in Table 3.1. The variables are grouped, in Table 3.1, into four related groups: Radiometric Quantities (both oceanic and atmospheric), Inherent Optical Properties (IOP) of sea water, Biogeochemical and Bio-Optical Properties of sea water, and Ancillary Data and Metadata required to support the use, analysis, interpretation, and quality assessment of the other data. Those *in situ* variables that are measured are classified into three categories of descending priority.

The first category of measurements, flagged “Required” in Table 3.1, is the minimum subset required for validating a satellite sensor’s radiometric performance, exact normalized water-leaving radiances (Chapter 13), and fundamental derived products, including chlorophyll *a* concentration, aerosol optical thickness, and *K*(490), and for associated algorithm development and validation.

The second category, flagged “Highly Desired” in Table 3.1, are measurements that supplement the minimum subset and are needed for investigations focused on atmospheric correction algorithms and aerosols, relationships between IOP and remote sensing reflectance, and/or Case 3 algorithms.

The third category, flagged “Specialized Measurement” in Table 3.1, are measurements which either address aspects of ocean bio-optics that are secondary to satellite remote sensing, or require highly specialized equipment that is not readily available to the community at large.

A fourth category, flagged as “Derived”, comprises key quantities that are either calculated from the *in situ* measurements, or are derived from models. The above set of variables is also listed in Table 3.2, to identify the satellite ocean color sensor application for which each measurement is needed. Table 3.2 also provides an index of the protocol chapters addressing each *in situ* measurement.

3.2 RADIOMETRIC QUANTITIES

Surface incident spectral irradiance in air, $E_s(\lambda) \equiv E_d(0^+, \lambda)$, downwelled spectral irradiance, $E_d(z, \lambda)$, and upwelled spectral radiance, $L_u(z, \lambda)$, are the fundamental measurable quantities needed to derive normalized water-leaving radiances (or equivalently remote sensing reflectance) in most circumstances. Other radiometric properties listed in Table 3.1, including sky radiance and normal solar irradiance, are also important *in situ* measurements in the SIMBIOS ocean color validation program. Also listed are critical radiometric quantities that are calculated, or derived, from *in situ* measurements. In some cases, listed radiometric quantities may be derived, wholly or in part, from other non-radiometric measurements listed in the table. For example, remote sensing reflectance may either be calculated directly as the ratio of water-leaving radiance $L_w(\lambda)$ to incident irradiance, $L_w(\lambda):E_s(\lambda)$, or it may be modeled as a function of the IOP ratio of the backscattering to absorption coefficients, $b_b(\lambda):a(\lambda)$, and the Bidirectional Reflectance Distribution Function (BRDF) (Chapter 13).

Downwelled spectral irradiance, $E_d(z, \lambda)$, is required to compute the diffuse attenuation coefficient, $K_d(z, \lambda)$, which in turn, is needed for diffuse attenuation coefficient algorithm development (Austin and Petzold 1981; Mueller and Trees 1997; Mueller 2000), and for optically weighting the pigment concentrations to be estimated from remotely sensed ocean color (Gordon and Clark 1980). As with $L_u(0^-, \lambda)$, $E_d(z, \lambda)$, must be determined by extrapolation from a profile of $E_d(z, \lambda)$, over the upper few diffuse attenuation lengths and reconciled with the direct surface measurement above the water of $E_s(\lambda)$ plus downward reflection of $E_u(0^-, \lambda)$.

Upwelled spectral radiance, $L_u(0^-, \lambda)$ is the in-water variable which, when propagated upward through the sea surface, leads to the measured value of $L_w(\lambda)$. $L_w(\lambda)$ is, in turn, adjusted using $E_s(\lambda)$ to derive the normalized water-leaving radiance, $L_{wn}(\lambda)$, for a no-atmosphere, zenith sun at the mean earth-sun distance. Unfortunately, it is not practical to measure $L_u(0^-, \lambda)$ precisely at an infinitesimal depth below the surface. Therefore, the profile of $L_u(z, \lambda)$, must be measured over the upper few optical depths with sufficient accuracy to determine $K_L(z, \lambda)$ for $L_u(z, \lambda)$, and to propagate $L_u(z, \lambda)$ to the surface. At near-infrared (NIR) wavelengths, the first optical attenuation length is confined to the upper few tens of centimeters. Determination of $L_u(0^-, \lambda)$, in this situation is more challenging and will require special instruments and experiment designs to accommodate the effects of instrument self-shading, wave focusing, small-scale variability, possible fluorescence, Raman scattering, and extremely small working volumes. Similar complications arise at all wavelengths in case 2 waters. For algorithm development and validation in these difficult cases, measurements of inherent optical properties (IOP), including coefficients of absorption $a(z, \lambda)$, beam attenuation $c(z, \lambda)$ and backscattering $b_b(z, \lambda)$, and spectral fluorescence, may be usefully combined with $E_d(z, \lambda)$, and $L_u(z, \lambda)$ measured with specially designed radiometers, and $L_{sfc}(\lambda, \theta, \phi, \theta_o, \phi_o)$ and $L_{sky}(\lambda, \theta, \phi, \theta_o, \phi_o)$ measured above-water.

Upwelled spectral irradiance, $E_u(z, \lambda)$, is a useful measurement, in addition to $E_d(z, \lambda)$ and $L_u(z, \lambda)$, because there exist both empirical and theoretical relationships between IOP, phytoplankton pigments, SPM, and irradiance reflectance. $L_u(0^-, \lambda)$ and $E_u(0^-, \lambda)$ are related by the factor $Q_n(\lambda)$, which has been shown to vary with solar zenith angle (Chapter 13; Morel and Gentili 1993, 1996; Morel, Voss and Gentili 1995). Combined measurements of $L_u(0^-, \lambda)$ and $E_u(0^-, \lambda)$ will be extremely useful in determining $Q_n(\lambda)$, which will in turn, allow traceability of the measurements by the SIMBIOS ensemble of satellite ocean color sensors to previously derived irradiance reflectance relationships and algorithms.

Radiance distribution measurements $L_u(z, \lambda, \theta', \phi')$ just beneath the sea surface will be required for quantifying the angular distribution of water-leaving radiance at stations used for system calibration initialization and long-term system characterization. These measurements will also necessary to determine the BRDF of the water and verify the models used to normalize water-leaving radiance for variations in viewing and solar zenith angles (Chapter 13 and references cited therein).

Water Surface Radiance (in air), $L_{sfc}(\lambda, \theta, \phi, \theta_o, \phi_o)$, measured from the deck of a ship (or a low-flying aircraft) is a potentially useful substitute for $L_w(\lambda)$ determined from in-water $L_u(0^-, \lambda)$. The measured surface radiance is the sum of water-leaving radiance and sky radiance reflected from the wave-roughened sea surface. The principal, and significant, source of uncertainty in this approach is associated with removal of reflected sky radiance from the total signal (Chapter 12).

Surface incident spectral irradiance, $E_s(\lambda)$, is usually measured on a ship well above the water. In some previous versions of these protocols (Mueller and Austin 1992, 1995), it was suggested that $E_s(\lambda)$ might alternatively be determined from measurements of $E_d(0^-, \lambda)$ made some distance from the ship using a radiometer floated just beneath the surface. The community has gained experience with this approach and found that wave-induced fluctuations in near-surface irradiance produce an uncertainty in $E_d(0^-, \lambda)$ approaching 10 % in even ideal cases (Siegel *et al.* 1995). $E_s(\lambda)$ varies due to fluctuations in cloud cover and aerosols, and with time of day, *i.e.*, solar zenith angle. Profiles of $E_d(z, \lambda)$, and $L_u(z, \lambda)$, must be normalized to account for these sources of variability during a cast.

Normal Solar Irradiance spectra $E_N(\lambda, \theta_o, \phi_o)$ should be measured using a sun photometer to determine atmospheric transmittance and aerosol optical depths at each station. These data are particularly needed to verify the atmospheric corrections in direct match-up comparisons between satellite ocean color sensor $L_{WN}^{ex}(\lambda)$ estimates and those determined from in-water measurements of $L_u(z, \lambda)$.

Sky radiance, $L_{sky}(\lambda, \theta, \phi, \theta_o, \phi_o)$, is required to enable estimation of the aerosol phase function through inversion of the radiative transfer equation. It is also useful for estimating the mean cosine of the transmitted light field in the water. The sky radiance should be measured directly; for the latter application, however, it need only be estimated by occulting the sun's image on a deck cell measuring the incident spectral radiance from the sun and sky. The mean cosine at the surface can be used with profile measurements of $E_d(z, \lambda)$, $E_u(z, \lambda)$, and $c(\lambda)$ to estimate $b_b(\lambda)$ (Gordon 1991). An ability to exploit this and similar relationships will greatly enhance both development and verification of bio-optical algorithms, especially in case 2 waters. The spectral sky radiance distribution over zenith and azimuth angles is required to determine the aerosol scattering phase functions at radiometric comparison stations during system initialization cruises. It is also measured routinely at a network of fixed island and coastal sites distributed around the world. Finally, $L_{sky}(\lambda, \theta, \phi, \theta_o, \phi_o)$ is measured and multiplied by the reflectance of the sea surface to derive $L_w(\lambda, \theta, \phi)$ from $L_{sfc}(\lambda, \theta, \phi, \theta_o, \phi_o)$ measurements.

Diffuse Sky Irradiance, $E_{sky}(\lambda)$, may be measured using a fast-rotating, shipboard version of a Shadowband Radiometer, or by manually obscuring the direct solar irradiance, $E_{sun}(\lambda)$, component of $E_s(\lambda)$. This measurement is extremely useful for determining the ratio $E_{sun}(\lambda):E_{sky}(\lambda)$, which is a critical factor in self-shading corrections to $L_u(z, \lambda)$ and $E_u(z, \lambda)$ measurements (Gordon and Ding 1992).

3.3 INHERENT OPTICAL PROPERTIES

Inherent Optical Properties (IOP) must be measured for development and validation of the ocean color semi-analytic case 2 chlorophyll *a* algorithm. This algorithm is based on an explicit theoretical function of the ratio of backscattering to absorption, $b_b(\lambda):a(\lambda)$. This ratio is also an important factor in the BRDF models underlying the exact normalization of water-leaving radiance for solar and viewing azimuth and zenith angles (Chapter 13). Due to recent advances in instrumentation, it is now practical to routinely measure *in situ* profiles of *absorption* $a(z, \lambda)$, *beam attenuation* $c(z, \lambda)$ and *backscattering* $b_b(z, \lambda)$ coefficients. The scattering coefficient may therefore also be obtained as $b(z, \lambda) = c(z, \lambda) - a(z, \lambda)$. The IOP also provide critical factors in the Gordon and Ding (1992) model used to correct upwelled radiance and irradiance measurements for instrument self shading. Future algorithm development and validation experiments involving these algorithms must, therefore, include absorption, beam attenuation, and backscattering measurements. It is anticipated that new instruments, now under development and testing, will allow *in situ* measurements of the volume scattering function $\beta(z, \lambda, \Psi)$ (Chapter 2). Measurements

of $\beta(z, \lambda, \Psi)$ will be very useful in advancing remote sensing reflectance models and algorithms involving the BRDF (Chapter 13).

The *particle absorption coefficient*, $a_p(z, \lambda)$, which is comprised of absorption by living, dead, and inorganic particles, is a useful variable for modeling the portion of solar energy that is absorbed by phytoplankton and bacteria. A laboratory spectrophotometer may be used to measure $a_p(z, \lambda)$ of particles filtered from seawater samples collected at depth z , or it may be computed as the difference between *in situ* measurements with a pair of filtered (CDOM absorption) and unfiltered (total absorption) instruments.

The *colored dissolved material (CDOM) absorption coefficient*, $a_g(z, \lambda)$, is an important contributor to total absorption in many coastal waters. Because CDOM, variously referred to as *gelbstoffe*, *gilvin*, or *yellow-matter*, absorbs very strongly in the blue, its undetected presence can create large regional uncertainties in chlorophyll *a* retrievals from ocean color image data. The CDOM absorption coefficient $a_g(z, \lambda)$ may either be measured *in situ* by installing a 0.2 μm filter in the water intake port of an absorption and beam attenuation meter, or in the laboratory using a spectrophotometer to measure absorption by filtered seawater, typically over a 10 cm path.

The *non-pigmented particle absorption coefficient*, $a_d(z, \lambda)$, accounting for absorption of light by detritus (or tripton), represents a major loss of light which would otherwise be available to the phytoplankton component of the marine hydrosol. In many cases, absorption by detritus is a significant term in the marine radiative transfer processes, and its determination is useful for phytoplankton production models and for modeling the light field. The spectral absorption coefficient $a_d(z, \lambda)$ using the $a_p(z, \lambda)$ filters, after they are washed with hot methanol to remove phytoplankton pigments (Chapter 15).

3.4 BIOGEOCHEMICAL AND BIO-OPTICAL QUANTITIES

Phytoplankton pigment composition will be determined using the HPLC method to develop and validate ocean color pigment algorithms, and to assess the effects of accessory pigment concentrations on water-leaving spectral radiances (Chapter 16). These data may also be used to calibrate continuous profiles of *in situ* fluorescence. *Chlorophyll a and pheopigment concentrations* will also be determined using the *fluorometric method* (Chapter 17). The HPLC chlorophyll *a* concentrations are more accurate than fluorometric concentrations, which are often biased systematically throughout a particular geographic region and time of year. On the other hand, fluorometric measurements of chlorophyll *a* concentration are both far easier and less expensive to perform, allowing a far greater number of pigment validation samples to be acquired on a given cruise than if HPLC sampling were used alone. If a well-distributed subset of pigment filter samples from each validation cruise are reserved for HPLC measurements, it is possible and operationally effective to derive regional and temporal corrections to scale fluorometric and HPLC chlorophyll *a* concentrations into close agreement.

Phycobilipigments, present in cyanobacteria and cryptophytes, are treated separately from the HPLC fat-soluble pigments. Phycoerythrin and phycocyanin are the two major groups of phycobilipigments found in the marine environment. The concentration of these water-soluble pigments is important due to the contribution of solar stimulated phycoerythrin fluorescence to the underwater light field, and also to characterize the phytoplankton population. At times, species that contain phycobilipigment can account for a large fraction of the primary productivity (especially in oligotrophic waters) and have been difficult to quantify due to their small size. Although neither SeaWiFS nor MODIS contains bands at the absorption or fluorescence peaks of phycobilipigments, future satellite ocean color sensors, including GLI and MERIS will have appropriate bands. The present protocols do not specify methods for measuring phycobilipigments, but qualitative concentrations may be obtained today using a fluorometric approach, and a new capillary electrophoresis method is currently under development (C. Kinkade, personal comm.). A new chapter giving protocols for measuring this important group of phytoplankton pigments may emerge in the near future.

Coccolith concentration, which is the number density of small plates (coccoliths) composed of calcium carbonate (CaCO_3), is very important to light scattering. Coccoliths are produced in copious amounts by

marine phytoplankton called coccolithophorids. Scattering of light by coccoliths is highly apparent in visible wavelength satellite imagery, because they perturb the usual relationships between water-leaving radiances and pigment concentration, and therefore, adversely impact atmospheric corrections (Balch *et al.* 1991, Voss *et al.* 1998). Additionally, coccolith formation, sinking, and dissolution are significant factors in the ocean carbon flux budget. It is, therefore, necessary to measure coccolith concentration, both as number density and CaCO_3 concentration, to aid in 1) the correction of chlorophyll *a* concentration algorithms, 2) coccolith algorithm development, and 3) atmospheric correction development and validation. This present version (3.0) of the ocean optics protocols does not cover methods for measuring coccolith concentration. Such protocols may be included in a future revision.

Total Suspended Matter (SPM) measurements are required to assess the effect of suspended sediment on the derived products. SPM is of primary importance in coastal waters, where simple radiance ratio algorithms for SPM have uncertainties equivalent to, or greater than, those for estimating chlorophyll-like pigment concentration. Organic suspended matter and inorganic suspended matter concentrations are fractions of SPM; this partitioning of SPM is particularly useful in process studies.

Continuous profile measurements of *in situ* chlorophyll *a* fluorescence intensity are exceptionally useful as guidance in analyzing profiles of $E_d(z, \lambda)$, $L_u(z, \lambda)$, and $E_u(z, \lambda)$ to derive profiles of $K_d(z, \lambda)$, $K_L(z, \lambda)$, and $K_u(z, \lambda)$, respectively. Moreover if these profiles are viewed in real time, they are also useful guides for taking water samples at depths that allow the vertical structure of pigment concentration profiles to be accurately resolved in the top optical depth and to determine subsurface maxima in chlorophyll concentration. Finally, the continuous *in situ* chlorophyll *a* fluorescence profile may be used to interpolate HPLC, or extracted fluorescence, measurements of chlorophyll *a* concentrations from water samples at discrete depths. It is desirable to make these measurements simultaneously with IOP profiles, and also those of irradiance and radiance if it can be done in a way to avoid self-shading of the radiometers.

3.5 ANCILLARY DATA AND METADATA

The geographic location and time at which *in situ* validation data are acquired are essential information that must be included in every data submission under the SIMBIOS program. The obvious metadata items in this context are *latitude, longitude, date and time (UTC)*. Expressing date and time in UTC is also essential, even though it may be helpful to also list local date and time with a validation station's metadata. Too often, field investigators neglect to identify (or possibly even keep track of) the time zone used by a data-logging computer to enter time into data records.

Sea state, expressed as significant wave height in m, must be reported with *in situ* validation measurements. *Whitecap conditions*, expressed as the estimated fractional area covered, are also useful and highly desired. Digital photographs documenting surface wave and whitecap conditions during radiometric measurements are also helpful. This information is essential for identifying measurements made under questionable environmental conditions.

Wind speed and direction are required to generate, through models, estimates of the surface wave slope distribution, which will be used to calculate reflected skylight and sun glint in radiative transfer models (Cox and Munk 1954). Wind speed is an essential parameter for computing exact normalized water-leaving radiance from measured water leaving radiance emerging from the ocean at zenith angles greater than 25° (Chapter 13). Surface wave models driven by wind velocity may also be used to provide quantitative estimates of surface wave induced radiometric fluctuations. Qualitatively, wind velocity, and photographs or videotape recordings of sea state, will be useful for assessing station data quality.

Surface barometric pressure measurements are required to validate both atmospheric correction algorithms and the surface pressures derived from operational weather analyses for use in processing satellite ocean color data

Cloud cover (expressed as fractional coverage in octals, or percent) is essential metadata used for assessing data quality and screening questionable cases from algorithm development and validation analyses. A description of sky conditions near the sun and satellite zenith and azimuth angles, including

whether the sun is obscured during observations, is also important information. Cloud type information is also useful, as are photographs of sky conditions.

Secchi depth measurements are required for real-time assessment of water transparency during a station and as a quality check during analysis of radiometric profiles.

Water depth, z in m, is important information for screening data from shallow water cases where bottom reflections may be present in water-leaving radiance measurements.

Hydrographic data, *water temperature* (T), and *salinity* (S), derived from *conductivity, temperature, and depth* (CTD) profiles, are useful for characterizing the physical water mass regime in which an optical profile is measured. A T - S characterization is especially important near ocean fronts and eddies where interleaving water masses of very different biogeochemical composition, and therefore fundamentally different bio-optical properties, can produce complex spatial and temporal patterns of near-surface optical properties. In these circumstances, T - S profiles can provide an indication of whether a station location is suitable for reliable remote sensing validation and algorithm development comparisons. The $T(z)$ and $S(z)$ measurements are also needed for corrections to pure water absorption in processing IOP measurements.

3.6 PROCESS MODEL RELATED DATA

Other types of *in situ* measurements are also important in the context of ocean color validation, because they are needed either to support, or validate, process models that are derived with the aid of ocean color image data. Primary productivity models are, perhaps, the foremost example of these secondary products of satellite ocean color measurements. The *in situ* measurements needed to support such models, and other scientific investigations and applications that may exploit ocean color data products, are undeniably important and closely related to the quantities listed in Table 3.1. These measurements are not, however, essential to algorithm development and validation of products derived from the ocean color data directly. In the future, the scope of the ocean optics protocols may be expanded to embrace methods for measuring and/or analyzing some of these variables, but at present they are not included. Some of the more important measurements of this class are briefly described in this section, but none of them are discussed in detail.

Aerosol concentration samples using high volume techniques will be useful, in conjunction with aerosol optical depth spectra determined from sun photometer measurements, for chemical, size, and absorption characterization of aerosols, especially in studies of the effects of Saharan and Asian dust clouds on atmospheric corrections.

Particulates, both Particulate Organic Carbon (POC) and Particulate Organic Nitrogen (PON), are required for process studies to help characterize the adaptive state of phytoplankton and to inventory critical biogeochemical elements.

Dissolved Organic Carbon (DOC) has been shown to be a major pool of carbon in the oceans. Quantification of the transformations of this pool is crucial to understanding the marine carbon cycle. The Colored Dissolved Organic Material (CDOM) fraction of the DOC is highly absorbent in the blue range, thus decreasing blue water-leaving radiances, and it must be taken into consideration for pigment concentration algorithms. DOC measurements are needed to develop robust relationships between CDOM and DOC, which are needed to evaluate the usefulness of ocean color observations for estimating DOC concentrations.

CDOM concentrations are required to assess the effect of *Gelbstoff* on blue water-leaving radiances and chlorophyll concentration. This is of primary importance in case 2 waters, but is also relevant to phytoplankton degradation products in case 1 waters.

Humic and fulvic acids comprise the bulk of CDOM and have different specific spectral absorption coefficients. Their concentrations are useful for determining the correction used for phytoplankton pigment concentration algorithms in case 2 waters and for estimating CDOM from ocean color observations.

Particle size spectra are very useful for in-water radiative transfer calculations, particularly if measurements include particles smaller than 1 μm .

Particle fluorescence, measured using laser sources in single-cell flow systems, may be used to calculate particle scattering-to-fluorescence ratios for evaluating the population structure of the plankton (both phyto- and zooplankton).

Phytoplankton species counts are important because species-to-species variability in optical and physiological properties represents a major source of variability in bio-optical algorithms and primary productivity models. This has been recognized, but it is generally ignored in remote sensing algorithms due to the tedious nature of species enumeration, the small sizes of many species, and the large number of species involved. This information, however, at various levels of rigor, is useful in evaluating the population and pigment composition. This is especially important for some groups, such as coccolithophorids.

Primary productivity, using the radioactive isotope ^{14}C estimation method, is not strictly required for validation of water-leaving radiances or system initialization. It is a MODIS product and will be a SeaWiFS product in the future. It will, moreover, be extremely useful for process study applications of ocean color data if these measurements are made at the same time that the water column optical properties are determined. These data will aid in the development of models of primary production using satellite ocean color observations, a goal which is central to all global ocean color mission. Of special importance are determinations of key photo-physiological parameters derived from production measurements as functions of irradiance. If ^{14}C productivity measurements are made, they should conform to the *JGOFS Core Measurements Protocols* (UNESCO 1994).

REFERENCES

- Austin, R.W., and T.J. Petzold, 1981: The determination of diffuse attenuation coefficient of sea water using the Coastal Zone Color Scanner. *Oceanography from Space*, J.F.R. Gower, Ed., Plenum Press, 239-256.
- Balch, W.M., P.M. Holligan, S.G. Ackleson, and K.J. Voss, 1991: Biological and optical properties of mesoscale coccolithophore blooms in the Gulf of Maine. *Limnol. Oceanogr.*, **36**, 629-643.
- Cox, C., and W. Munk, 1954: Measurements of the roughness of the sea surface from photographs of the sun's glitter. *J. Opt. Soc. Am.*, **44**, 838-850.
- Gordon, H.R., 1991: Absorption and scattering estimates from irradiance measurements: Monte Carlo simulations. *Limnol. Oceanogr.*, **36**: 769-777.
- Gordon, H.R., and D.K. Clark, 1980: Remote sensing optical properties of a stratified ocean: an improved interpretation. *Appl. Optics*, **19**: 3,428--3,430.
- Gordon, H.R., and K. Dign, 1992: Self shading of in-water optical instruments. *Limnol. Oceanogr.*, **37**, 491-500.
- Morel, A., and B. Gentili, 1993: Diffuse reflectance of oceanic waters. II. Bidirectional aspects. *Appl. Opt.*, **32**: 6,864--6,879.
- Morel, A., and B. Gentili, 1996: Diffuse reflectance of oceanic waters. III. Implication of bidirectionality for the remote-sensing problem. *Appl. Optics*, **35**: 4850-4862.
- Morel, A., K.J. Voss, and B. Gentili, 1995: Bidirectional reflectance of oceanic waters: a comparison of modeled and measured upward radiance fields. *J. Geophys. Res.* **100**: 13,143-13,151.
- Mueller, J.L., and R.W. Austin, 1992: Ocean Optics Protocols for SeaWiFS Validation. *NASA Tech. Memo. 104566, Vol. 5*, S.B. Hooker and E.R. Firestone, Eds., NASA Goddard Space Flight Center, Greenbelt, Maryland, 43 pp.
- Mueller, J.L., and R.W. Austin, 1995: Ocean Optics Protocols for SeaWiFS Validation, Revision 1. *NASA Tech. Memo. 104566, Vol. 25*, S.B. Hooker, E.R. Firestone and J.G. Acker, Eds., NASA Goddard Space Flight Center, Greenbelt, Maryland, 67 pp.
- Mueller, J.L. and C.C. Trees, 1997: Revised SeaWiFS prelaunch algorithm for the diffuse attenuations coefficient K(490). In: Yeh, et al. Case Studies for SeaWiFS Calibration and Validation, Part 4. *NASA*

Tech. Memo. 104566, Vol. 41, S.B. Hooker, E.R. Firestone and J.G. Acker, Eds., NASA Goddard Space Flight Center, Greenbelt, Maryland, 18-21.

UNESCO, 1994: Protocols for the Joint Global Ocean Flux Study (JGOFS) Core Measurements. *JGOFS Manuals and Guides*, 29, Scientific Committee on Oceanic Research, 40 p.

Siegel, D.A., M.C. O'Brien, J.C. Sorensen, D.A. Konnoff, E.A. Brody, J.L. Mueller, C.O. Davis, W.J. Rhea, and S.B. Hooker, 1995. Results of the SeaWiFS Data Analysis Round-Robin, July 1994 (DARR-94). *NASA Tech. Memo. 104566, Vol. 26*, S.B. Hooker and E.R. Firestone, Eds., NASA Goddard Space Flight Center, Greenbelt, MD. 58pp.

Voss, K.J., W.M. Balch and K.A. Kilpatrick, 1998: Scattering and attenuation properties of *Emiliania huxleyi* cells and their detached coccoliths, *Limnol. Oceanogr.*, **43**(5): 870-876.

Table 3.1: Principal *in situ* observations for satellite ocean color system validation, and algorithm development and validation. The right-hand column identifies and classifies measurements as: (a) required for minimal validation match-ups; (b) highly desired and important for general algorithm development and validation; (c) specialized measurements of important, but restricted, applicability to algorithm development and validation (for the present); and (d) calculated or derived quantities.

	Required	Highly Desired	Specialized Measurement	Derived
<i>Radiometric Quantities</i>				
Downwelled Irradiance $E_d(z, \lambda)$	✓			
Upwelled Radiance $L_u(z, \lambda) = L(z, \lambda, 0, 0)$	✓			
Upwelled Irradiance $E_u(z, \lambda)$			✓	
Radiance Distribution in water $L(z, \lambda, \theta', \phi')$			✓	
Water Surface Radiance in air $L_{sfc}(\lambda, \theta, \phi)$		✓		
Incident Irradiance in air $E_s(\lambda) = E_d(0^+, \lambda)$	✓			
Normal Solar Irradiance $E_N(\lambda, \theta_o, \phi_o)$	✓			
Sky Radiance $L_{sky}(\lambda, \theta, \phi)$		✓		
Diffuse Sky Irradiance $E_{sky}(\lambda)$		✓		
Direct Sun Irradiance $E_{sun}(\lambda) = E_s(\lambda) - E_{sky}(\lambda)$				✓
Water-Leaving Radiance $L_w(\lambda, \theta, \phi, \theta_o, \phi_o)$				✓
Remote Sensing Reflectance $R_{RS}(\lambda, \theta, \phi, \theta_o, \phi_o)$				✓
Attenuation Coefficient $K(z, \lambda)$ for $E_d(z, \lambda)$ and $L_u(z, \lambda)$				✓
Ocean Bidirectional Reflectance Distribution Function BRDF				✓
Aerosol Optical Depth $\tau_a(\lambda)$	✓			
Aerosol Phase Function $P_a(\lambda, \Psi)$				✓
Absorbing Aerosol Height Profiles (LIDAR Profilometer)			✓	
<i>Inherent Optical Properties</i>				
Beam Attenuation Coefficient $c(z, \lambda)$		✓		
Absorption Coefficient $a(z, \lambda)$		✓		
Backscattering Coefficient $b_b(z, \lambda)$		✓		
Scattering Coefficient $b(z, \lambda) = c(z, \lambda) - a(z, \lambda)$				✓
Volume Scattering Function $\beta(z, \lambda, \Psi)$			✓	
Particle Absorption Coefficient $a_p(z, \lambda)$		✓		✓
Dissolved Material (CDOM) Absorption Coefficient $a_g(z, \lambda)$		✓		
Non-Pigmented Particle Absorption Coefficient $a_d(z, \lambda)$		✓		
Phytoplankton Absorption Coefficient $a_{\phi}(z, \lambda)$		✓		
<i>Biogeochemical and Bio-Optical Quantities</i>				
Phytoplankton Pigment Composition (HPLC method)	✓			
Chlorophyll <i>a</i> and Phaeopigments Conc. (Fluorometric method)	✓			
Phycobiliprotein Concentrations			✓	
Coccolith Concentrations			✓	
Total Suspended Particulate Material (SPM)			✓	
Fluorescence Intensity, <i>in situ</i> profile $F(z)$		✓		
Ancillary Data and Metadata				
Latitude and Longitude	✓			
Date and Time (UTC)	✓			
Wave Height	✓			
Whitecap Conditions (fractional amount of surface)		✓		
Wind Speed, <i>W</i> , and Direction	✓			
Surface Barometric Pressure	✓			
Cloud Cover (amount, and sun obscuration information)	✓			
Cloud Type		✓		
Secchi Depth	✓			
Water Depth	✓			
Conductivity and Temperature over Depth (CTD) $T(z)$, $S(z)$		✓		

Table 3.2: Principal *in situ* observations for satellite ocean color system validation, and algorithm development and validation. The right-hand column identifies the protocol chapters and suggested applications. The application keys are: System Validation (1); Radiometric System Performance Validation and Vicarious Calibration (2); Atmospheric Correction Validation (3); Atmospheric Product Validation (4); Bio-Optical Product Validation (5); Algorithm Development and Validation (6); Atmospheric Property and Correction Algorithms (7); Bio-Optical Algorithms (8); IOP Algorithms and Semi-Analytic IOP-Based Algorithms (9); Normalized $L_{WN}(\lambda)$ and $R_{RS}(\lambda)$ Algorithms (10); Metadata (all applications) (11) ; Quality Control (12); and All Above Applications (13).

	Protocol Chapters	Applications Keys
<i>Radiometric Quantities</i>		
Downwelled Irradiance $E_d(z, \lambda)$	10	1,5,6,8-10
Upwelled Radiance $L_u(z, \lambda) = L(z, \lambda, 0, 0)$	10-12	1-3,5,6,8-10
Upwelled Irradiance $E_u(z, \lambda)$	10	6,9,10
Radiance Distribution in water $L(z, \lambda, \theta, \phi)$	TBD	1,2,6,9,10
Water Surface Radiance in air $L_{sf}(\lambda, \theta, \phi)$	12	1-3,5,6,8-10
Incident Irradiance in air $E_s(\lambda) = E_d(0^+, \lambda)$	7, 10-14	1,6,8,9,10,13
Normal Solar Irradiance $E_N(\lambda, \theta_o, \phi_o)$	7, 14	1-4,6,7,10,12
Sky Radiance $L_{sky}(\lambda, \theta, \phi)$	12, 11, 14	1-4,6,7,10
Diffuse Sky Irradiance $E_{sky}(\lambda)$	7, 14	1,6,13
Direct Sun Irradiance $E_{sun}(\lambda) = E_s(\lambda) - E_{sky}(\lambda)$	7, 14	1,6,13
Water-Leaving Radiance $L_w(\lambda, \theta, \phi, \theta_o, \phi_o)$	10-13	1,6,13
Remote Sensing Reflectance $R_{RS}(\lambda, \theta, \phi, \theta_o, \phi_o)$	10-13	1,6,13
Attenuation Coefficient $K(z, \lambda)$ for $E_d(z, \lambda)$ and $L_u(z, \lambda)$	10	1,5,6,8,9
Ocean Bidirectional Reflectance Distribution Function BRDF	TBD	1,6,13
Aerosol Optical Depth $\tau_a(\lambda)$	14	1-3,4,6,7
Aerosol Phase Function $P_a(\lambda, \Psi)$	14	1-3,4,6,7
Absorbing Aerosol Height Profiles (LIDAR Profilometer)	TBD	1-3,6,7
<i>Inherent Optical Properties</i>		
Beam Attenuation Coefficient $c(z, \lambda)$	TBD	1,5,6,8-10
Absorption Coefficient $a(z, \lambda)$	TBD	1,5,6,8-10
Backscattering Coefficient $b_b(z, \lambda)$	TBD	1,5,6,8-10
Scattering Coefficient $b(z, \lambda) = c(z, \lambda) - a(z, \lambda)$	TBD	1,5,6,8-10
Volume Scattering Function $\beta(z, \lambda, \Psi)$	TBD	1,5,6,8-10
Particle Absorption Coefficient $a_p(z, \lambda)$	15	1,5,6,8,9
Dissolved Material (CDOM) Absorption Coefficient $a_g(z, \lambda)$	15	1,5,6,8,9
Non-Pigmented Particle Absorption Coefficient $a_d(z, \lambda)$	15	1,5,6,8,9
Phytoplankton Absorption Coefficient $a_{\phi}(z, \lambda)$	15	1,5,6,8,9
<i>Biogeochemical and Bio-Optical Quantities</i>		
Phytoplankton Pigment Composition (HPLC method)	16	1,5,6,8,9
Chlorophyll a and Phaeopigments Conc. (Fluorometric method)	17	1,5,6,8
Phycobiliprotein Concentrations	TBD	6,8
Coccolith Concentrations	TBD	1,5,6,8,9,12
Total Suspended Particulate Material (SPM)	9	5,6,8,12
Fluorescence Intensity, <i>in situ</i> profile $F(z)$	17	12
<i>Ancillary Data and Metadata</i>		
Latitude and Longitude	9	11
Date and Time (UTC)	9	11
Wave Height	9	12
Whitecap Conditions (fractional amount of surface)	9	12
Wind Speed and Direction	9	1-3,6,10,12
Surface Barometric Pressure	9	1,2,5
Cloud Cover (amount, and sun obscuration information)	9	6,10,12
Cloud Type	9	12
Secchi Depth	9	12
Water Depth	9	12
Conductivity and Temperature over Depth (CTD) $T(z)$, $S(z)$	9	9,10,12

Chapter 4

Instrument Specifications, Characterization and Calibration Overview

James L. Mueller

Center for Hydro-Optics and Remote Sensing, San Diego State University, California

4.1 INTRODUCTION

A central focus of the SIMBIOS program, and of independent validation activities in the SeaWiFS and other ocean color sensor projects, is the estimation of uncertainties in satellite determinations of normalized water-leaving radiance (or equivalently, normalized remote-sensing reflectance), atmospheric correction and bio-optical algorithms, and derived products. In most cases, statistical comparisons with *in situ* measurements – or quantities derived from *in situ* measurements – play a central role in estimating the uncertainties in the satellite ocean color measurements, algorithms and derived products. The uncertainty budgets of *in situ* measurements used for comparisons are obvious critical factors in such validation analyses, as also are details and uncertainties of critical design and performance characteristics of the instruments with which they are measured.

This and the next several chapters specify appropriate instrument characteristics and describe accepted laboratory procedures for characterizing instruments to determine and verify their compliance with those specifications. Detailed characterization and calibration protocols for radiometers and sun photometers are provided in Chapters 5, 6 and 7. The status of each of these chapters, and topic areas in each where future advances and/or changes may be appropriate, are discussed briefly in sections 4.2 through 4.5. A shortcoming of the present protocols is that a similarly in-depth treatment is not provided for characterization and calibration of instruments used to measure inherent optical properties (IOP). The current state of the art regarding IOP instrument calibration is briefly abstracted below in Section 4.6. This document does not provide detailed methods for calibrating meteorological sensors, CTD instruments, pressure transducers, and other ancillary sensors. Sections 4.7 through 4.9 emphasize the importance of using properly calibrated sensors to make these important supporting measurements, but a well-established infrastructure for these calibration services exists within the general oceanographic and atmospheric communities.

4.2 INSTRUMENT PERFORMANCE SPECIFICATIONS

Chapter 5 provides detailed specifications for performance-related characteristics of radiometers, and other types of instruments, that measure *in situ* variables used to validate satellite ocean color sensors, algorithms and derived products. The specifications in this revision (3.0) to the protocols are unchanged from those in Revision 2 (Fargion and Mueller 2000).

Time constraints and conflicting schedule demands of key individuals precluded adequate community-wide review, debate and refinement of specifications in a few areas where instrument development has progressed significantly. Topic areas that should be reviewed thoroughly in preparation of this chapter for Revision 3 of the Ocean Optics Protocols (2001) include specifications of performance-related characteristics of:

1. hyperspectral radiance and irradiance spectrometers (but see Chapter 11), especially those based on miniature fiber-optic monochromators; and
2. instruments used to measure IOP (absorption, beam attenuation and backscattering) *in situ*.

4.3 CHARACTERIZATION OF OCEANOGRAPHIC AND ATMOSPHERIC RADIOMETERS

The procedures given here in Chapter 6 are essentially those from Mueller and Austin (1995). Changes and additions primarily reflect results and lessons learned from the SeaWiFS Intercomparison Round-Robin Experiment (SIRREX) series (e.g. Mueller *et al.* 1996; Johnson *et al.* 1996) and deal primarily with methods for transferring the NIST scale of spectral irradiance from an FEL lamp source to the responsivity scales of oceanographic and atmospheric radiometers. The SIMBIOS and SeaWiFS Project Offices are continuing the SIRREX, now SIMBIOS Radiometric Intercalibration (SIMRIC), series to assure maintenance of consistent radiometric calibration uncertainties throughout the community (Riley and Bailey 1998; G. Meister, personal comm.) and for better determination of, *e.g.*, quantitative uncertainties associated with radiance calibrations using Spectralon plaques (S. Hooker, pers. comm.).

The Chapter 6 protocols recommend experimental determination of immersion factors for every individual underwater irradiance collector. In Mueller and Austin (1995), it was suggested that immersion factors determined for a prototype irradiance collector could be used for other radiance collectors of the same size, design and material specifications. The results of Mueller (1995) demonstrated that individual deviations between collectors of the same design, size and materials may be as large as 8 %, with a 3 % Root-Mean-Square (RMS) uncertainty for the group of such instruments tested. Using replicated tests and variations in setup configuration for each instrument tested, the experimental uncertainty associated with the immersion factor characterization procedure was shown to be less than 1 % (Mueller 1995). Topic areas in Chapter 6 that should be reviewed and considered for possible inclusion in Revision 4 (2002) include:

1. Methods for applying to ocean radiometers (K. Carder and R. Steward, pers. comm.) the sun-based methods used in the atmospheric radiation community for calibrating sun photometers (Chapter 7 of these protocols; Schmid *et al.* 1998) and other radiometers (Biggar 1998). In this regard, the question of continuing to use the Neckel and Labs (1984) $\bar{F}_o(\lambda)$ spectrum, or an alternative such as that of Thuillier *et al.* (1998), will become critically important (see the discussion in Chapter 2).
2. Uncertainty budgets associated with the use of Spectralon reflectance plaques for calibrating radiance sensors continue to be inadequately understood, a difficulty noted during the last SIMRIC exercise (G. Meister, personal comm.).
3. Improved methods for characterizing stray-light, spectral calibration, and slit responses in monochromator based hyperspectral spectrometers, which are increasingly being adopted and used within the ocean color research community. The innovative recent application, by NIST, of integrating-sphere sources illuminated by tunable LASERs to this problem represents a major advance (Chapters 6 and 11).

4.4 CALIBRATION OF SUN PHOTOMETERS AND SKY RADIANCE SENSORS

Chapter 7 is not significantly changed from Revision 2 (Mueller and Fargion 2000), where it appeared for the first time as Chapter 6. The calibration and characterization of sun photometers and sky radiance sensors was covered very briefly in Mueller and Austin (1995), and no detailed method descriptions were provided. These Chapter 7 protocols are based on the methods developed within the atmospheric radiation community, and by the AERONET Project at GSFC and its collaborating institutions around the world. Protocols for calibrating Shadowband Radiometers are also new to the Ocean Optics Protocols. There is some overlap between Chapters 5 and 6, but the redundancies are not a serious drawback.

4.5 STABILITY MONITORING OF FIELD RADIOMETERS USING PORTABLE SOURCES

Mueller and Austin (1995) recommended the development and use of portable standards to verify the stability of radiometers during deployment on research cruises, or other field deployments, of several

weeks duration. These general recommendations were based on limited experience with prototype analog sources developed by Austin and his colleagues in the 1980's at the Scripps Visibility Laboratory. Since 1995, joint research by investigators at NIST and GSFC developed a much-improved prototype of a portable source, the SeaWiFS Quality Monitor (SQM), suitable for shipboard use (Johnson *et al.* 1998) and demonstrated its ability to verify stability of radiometers with an uncertainty < 1 % (Hooker and Aiken 1998). Subsequently, less expensive versions of the SQM have been developed and become commercially available. Chapter 8 (formerly Chapter 7 in Fargion and Mueller 2000) provides a review of this development, detailed protocols for using SQM devices in the field, and uncertainty budgets.

4.6 CALIBRATION OF INHERENT OPTICAL PROPERTY SENSORS

Many significant improvements have been made, over the last five years, in the development and understanding of instruments used to measure inherent optical properties (IOP). Today, *in situ* profile determinations of the coefficients of absorption $a(z, \lambda)$, beam attenuation $c(z, \lambda)$ and backscattering $b_b(z, \lambda)$ – all in m^{-1} – are almost routinely made and reported by many investigators in the ocean optics and ocean color remote sensing communities. However, key members of the IOP community continue an active debate on the relative merits of alternative design characteristics of, and methods for calibrating and using, these first and second-generation instruments. In the case of some instruments and measurements, *e.g.* the AC9 absorption and beam attenuation meters (see below), a *de facto* consensus is emerging on methods and uncertainty budgets. In these cases, it remains only to draft protocols and pass it through a critical review by the community; a focused workshop is often the surest way to do this quickly. In other cases, technical questions and valid criticisms remain to be answered before protocols can be distilled from various proposed methods; additional research to sort out uncertainties is clearly needed here.

The present version of the Ocean Optics Protocols does not provide complete protocols, or even provisional protocols, for either *in situ* measurements of IOP, or calibration of IOP instruments. It is planned to remedy that omission in a future revision of this document by including new chapters on *in situ* measurements of absorption, beam attenuation and backscattering. For the present, however, the closest thing to protocols are the methods and calibrations specified by instrument manufacturers, a few published journal articles, and informal instructions and reference materials provided via the world-wide web by a few recognized experts in various aspects of IOP measurements.

Pure Water Absorption and Scattering Coefficients

The recommended values for the volume absorption coefficients of pure water, $a_w(\lambda) \text{ m}^{-1}$, are those of Sogandares and Fry (1997) for wavelengths between 340 nm and 380 nm, Pope and Fry (1997) for wavelengths between 380 nm and 700 nm, and Smith and Baker (1981) for wavelengths between 700 nm and 800 nm. The recommended values for the volume scattering coefficients of pure water, $b_w(\lambda) \text{ m}^{-1}$, are those of Morel (1974).

Single-Wavelength Transmissometers

Relatively simple single-wavelength (usually near 660 nm) transmissometers have been in widespread use for two decades. Although the beam attenuation coefficients $c(z, 660)$ obtained with these devices are no longer state of the art measurements, the profiles of this variable are strongly correlated with concentrations of suspended particles. Protocols for using these instruments are unchanged from those in Mueller and Austin (1995).

The manufacturer first calibrates a transmissometer of this type by measuring its response in pure water. He also measures the open and blocked (dark) sensor responses in air and records these as *factory air calibration* coefficients. The user must perform air calibrations in the field. When transmissometer profiles are analysed (Chapter 9), the field and factory air calibrations are used to compensate for drift in the instrument's sensitivity over time.

The windows on the beam transmissometer must be cleaned with lens cleaner or a mild detergent solution and a soft cloth or tissue, rinsed with distilled water, then rinsed with isopropyl alcohol and wiped

dry. An approximate *air calibration* reading should be made before every cast to verify that the windows are clean. A transmissometer *dark voltage* should also be measured at this time. These *on-deck air calibrations* are not, however, very reliable measures of temporal drift or degradation in the instrument's source or detector. In the humid, or even wet, environment on the deck of a ship, the windows are often quickly obscured by condensation, and the glass also tends to absorb enough water to affect transmission slightly (Zaneveld pers. comm.). A very careful air calibration should be performed before and after each cruise under dry laboratory conditions. During an extended cruise, it is also recommended to remove the instrument to a dry location in a shipboard laboratory, and after allowing several hours for the windows to dehydrate, a careful air calibration should be performed. Only the laboratory air calibrations should be used in the final processing of beam transmissometer data.

Both the laboratory condition air calibration and dark voltages, and the factory calibration voltages, assume the data acquisition system measures instrument response as true volts. It is imperative, therefore, to calibrate the end-to-end analog-to-digital (A/D) data acquisition system and characterize its response \tilde{V} to known input voltages \hat{V} . Corrections in the form of a linear function

$$\hat{V} = g(T)\tilde{V} + f(T), \quad (4.1)$$

where T is temperature, must usually be applied to external voltage inputs recorded with the A/D circuits of CTDs or profiling radiometer systems. The range dependent A/D bias coefficients should be determined at approximately 5°C intervals, over the range from 0°C to 25°C , to characterize the temperature sensitivity of the data acquisition system.

Absorption and Beam Attenuation Meters

The discussion in this section pertains only to instruments and calibration for *in situ* measurements of absorption. Protocols for laboratory spectrophotometric measurements of absorption by particles filtered from water samples, and by colored dissolved organic material (CDOM) in filtrate, are contained in Chapter 15 of this document.

It is increasingly common for ocean color investigators to measure the coefficients of absorption $a(\lambda)$ and beam attenuation $c(\lambda)$ using dual path transmissometers. In the beam attenuation path, a detector measures the light transmitted over the open path from a collimated source; both absorbed and scattered photons are attenuated. In the absorption part of the instrument, a beam of light passes through the center of a tube having a reflective wall that redirects most scattered photons into the forward direction toward a large detector which fills the exit cross section; only those photons that are either absorbed, or scattered in the backward direction, are attenuated. Because the backscattering by marine particles is a small fraction of their total scattering, it is possible to model this contribution and subtract it to obtain $a(\lambda)$ within a reasonable uncertainty. These devices may also be used to measure absorption by CDOM if a $0.4\ \mu\text{m}$ filter is inserted in the instrument's intake port. Since the beam attenuation coefficient is the sum of absorption and scattering, *i.e.*

$$c(\lambda) = a(\lambda) + b(\lambda), \text{ m}^{-1}, \quad (4.2)$$

it is also possible to determine the total scattering coefficient $b(\lambda)$ as the difference between the measured values of $c(\lambda)$ and $a(\lambda)$.

Perhaps the best known example of this class of instruments is the AC9, which uses interference filters to measure $a(\lambda)$ and $c(\lambda)$ at 9 wavelengths. The AC9 is manufactured by WetLABS of Philomath, OR. Alternative instrument designs are also commercially available, e.g. from HOBILABS of Moss Landing, CA and other manufacturers. These protocols make no recommendations regarding specific manufacturers or instruments, and examples of specific instruments are included here only for purposes of illustrating general characteristics and procedures.

The instrument manufacturer performs two *factory calibration* procedures to first determine the instrument's temperature dependence, and second to record its response when optically clean water is being measured. To obtain good data, it is absolutely essential to repeat this second calibration measurement frequently (typically once per day) in the field. Protocols for carrying out calibrations are provided by each instrument's manufacturer. Additional protocols for calibrating the AC9, expanding on methods described

in Twardowski *et al.* (1999), and other IOP instruments have been developed by the Optical Oceanography Group at Oregon State University and may be accessed via <http://photon.oce.orst.edu/> (S. Pegau, Pers. Comm). Perhaps the most challenging aspects of these protocols deal with methods for using reverse-osmosis filtration systems to obtain optically pure water in the field, and with procedures to verify the optical purity of the water.

Backscattering Meters

There is little historic data on the variation of the shape of the volume scattering function (VSF), $\beta(\Psi, \lambda)$, in the backward direction. Petzold (1972) described the scattering function for selected natural waters measured with the General Angle Scattering Meter (GASM). This reference is the one most widely used to describe shapes of $\beta(\Psi, \lambda)$. Balch *et al.* (1994) have published new *in situ* measurements, again using GASM, describing the shape of $\beta(\theta, \lambda)$ for marine hydrosols. Recently, measurements of the VSF using new instrument designs have begun to appear. For example, Mobley *et al.* (2001) demonstrate the sensitivity of remote sensing reflectance to correctness of the backscattering fraction of the VSF as measured using the new meters.

The GASM, built *circa* 1970 at the Scripps Institution of Oceanography's Visibility Laboratory (Petzold 1972), consists of a lamp focused into a cylindrical beam, and a narrow field of view detector mounted to swing in an arc to view the beam at many off-axis scattering angles between approximately 10° and 170° . At each incremental angle, the instrument pauses and light scattered from the source beam into the detector's field of view is measured. The phase functions at different wavelengths are determined by changing interference filters. The next generation of instruments were designed to measure $\beta(\Psi, \lambda)$ at a single wavelength (typically 532 nm) and a single angle, e.g. 150° (Maffione *et al.* 1991) or 170° (Smart 1992). The first commercial versions of these so-called *backscattering meters*, the HydroScat series of instruments manufactured by HOBILABS Inc. (www.hobilabs.com), measure scattering at a centroid angle of 140° at several fixed wavelengths (Maffione and Dana 1997). A more recent entry into this market is the ECO-VSF series of scattering meters manufactured by WETLABS (www.wetlabs.com), which are designed to measure scattering at a single wavelength (450, 530 or 650 nm) but at three scattering centroid angles 100° , 120° and 150° .

Any sensor designed to measure $\beta(\Psi, \lambda)$, at any nominal scattering angle Ψ , actually measures a weighted integral of radiance scattered from a working volume defined by the intersection of the illumination source beam and angular field of view of the detector system. The source illumination is attenuated by the factor $e^{-r(\Psi)c(\lambda)}$ over the slightly varying pathlength $r(\Psi)$ from source to detector through each infinitesimal element of the finite working volume. If both source illumination and detector angular response functions are azimuthally symmetric about their nominal axes, and the working volume is very small, the integral may be expressed in the relatively simple conceptual form

$$\bar{\beta}(\bar{\lambda}, \bar{\Psi}; c) = 2\pi \int_{\Delta\lambda} \int_0^\pi \beta(\lambda, \Psi) W(\lambda, \Psi; c) \sin \Psi d\Psi d\lambda, \text{ m}^{-1} \text{sr}^{-1}, \quad (4.3)$$

where the weighting function $W(\lambda, \Psi; c)$ accounts for the angular Ψ and wavelength λ dependencies of illumination and detector response functions, and attenuation over a variable pathlength, in each each infinitesimal subelement of the working volume. The parameters $\bar{\Psi}$ and $\bar{\lambda}$ are respectively the centroid scattering angle and wavelength of the weighted integral. The functional form and detailed parametric dependencies of the weighting function are greatly abstracted in (4.3), which is presented here only as a conceptual framework for the discussion. The weighting function can be measured by moving a Spectralon reflective target through the working volume (Maffione and Dana 1997), a procedure that also serves to calibrate the device. Alternatively, if the spectral and geometric distribution functions of the source illumination and detector response are well characterized, the weighting function can be calculated from first principles (Zaneveld and Twardowski, Pers. Comm), albeit based on a geometrically more complicated form of the integral equation abstracted here as (4.3). Given the weighting function, the scattering sensor may be calibrated by measuring its response to scattering by polystyrene spheres, the scattering functions of which may be accurately determined using Mie scattering computations (Zaneveld and Twardowski, Pers. Comm).

The scattering parameter of principal interest in the context of the Ocean Optics Protocols for Satellite Ocean Color Sensor Validation is the backscattering coefficient

$$b_b(\lambda) = 2\pi \int_{\frac{\pi}{2}}^{\pi} \beta(\lambda, \Psi) \sin \Psi d\Psi, \quad (4.4)$$

assuming azimuthal symmetry. Clearly none of the sensors described above measure $b_b(\lambda)$. To estimate the backscattering from measured $\bar{\beta}(\bar{\lambda}, \bar{\Psi}; c)$ at a single angle, one invokes the mean value theorem to observe that there must be at least one angle Ψ^* for which (4.4) reduces to

$$b_b(\lambda) = 2\pi\beta(\lambda, \Psi^*) \int_{\frac{\pi}{2}}^{\pi} \sin \Psi d\Psi = 2\pi\beta(\lambda, \Psi^*). \quad (4.5)$$

Clearly, Ψ^* will vary between volume scattering functions of differing shape in the backward direction, and measured values $\bar{\beta}(\bar{\lambda}, \bar{\Psi}; c) \neq \beta(\lambda, \Psi^*)$ even if $\bar{\Psi} = \Psi^*$ and $\bar{\lambda} = \lambda$. Oishi (1990) carried out a series of Mie scattering calculations for polydispersions of spheres, assuming a variety of different size distributions similar to those observed for marine hydrosols. He then assumed there would be some constant θ^* at which backscattering coefficients calculated with (4.5) would be linearly related to exact values of $b_b(\lambda)$ with a reasonable level of RMS uncertainty. He therefore revised (4.5) to the form

$$\hat{b}_b(\lambda) = 2\pi\chi\beta(\lambda, \Psi^*) \quad (4.6)$$

and found the minimum RMS deviations at $\Psi^* = 120^\circ$ with $\chi = 1.14$, but the smallest maximum prediction error occurred at $\Psi^* = 140^\circ$ with $\chi = 1.08$. Maffione and Dana (1997) independently repeated an analysis similar to Oishi's (1990) and found that, for $\Psi^* = 140^\circ$ with $\chi = 1.08$, the uncertainty in backscattering coefficients estimated with (4.6) is ~9 %. This is essentially the algorithm provided with the HOBILABS HydroScat instruments. The algorithm recommended for use with the WETLABS ECO-VSF instrument uses the 3-angle scattering measurements to adjust (4.6) for variations in the shape of the phase functions, but the underlying premise and approach to estimating the backscattering coefficient are otherwise similar (Beardsley and Zaneveld 1969; Zaneveld and Twardowski, Pers. Comm.).

Boss and Pegau (2001) separated the VSF and backscattering coefficient as

$$\begin{aligned} \beta(\lambda, \Psi) &= \beta_w(\lambda, \Psi) + \beta_p(\lambda, \Psi) \text{ and} \\ b(\lambda) &= b_w(\lambda) + b_b(\lambda), \end{aligned} \quad (4.7)$$

where the subscripts “p” and “w” designate contributions due to particles and water, respectively. The scaling factor $\chi(\Psi^*)$ is correspondingly partitioned as

$$\chi(\Psi^*) = \chi_p(\Psi^*) \frac{\beta_p(\lambda, \Psi^*)}{\beta(\lambda, \Psi^*)} + \chi_w(\Psi^*) \frac{\beta_w(\lambda, \Psi^*)}{\beta(\lambda, \Psi^*)}. \quad (4.8)$$

Analyses similar to those of Oishi (1990) and Maffione and Dana (1997), but in this partitioned framework, led Boss and Pegau (2001) to conclude that $\chi(\Psi^*) = \chi_p(\Psi^*) = \chi_w(\Psi^*) \equiv 1.1$ only when $\Psi^* = 117^\circ \pm 3^\circ$, consistent with the results of Oishi (1990). For measurements at other scattering angles, they recommend modifying Equation (4.6) to correct for the water scattering contribution as

$$\hat{b}_b(\lambda) = 2\pi\chi_p(\Psi^*) [\beta(\lambda, \Psi^*) - \beta_w(\lambda, \Psi^*)] + b_{bw}(\lambda). \quad (4.9)$$

They provide equations for estimating $\beta_w(\lambda, \Psi)$ and $b_w(\lambda)$, based on the theoretical equations and experimental results of Morel (1974), and tabulate estimates of $\chi_p(\Psi^*)$ in the range $90^\circ \leq \Psi^* \leq 170^\circ$.

Measurements of backward scattering have also been made using benchtop laboratory instruments, and either discrete water samples, or water pumped in a “flow-through” mode. Tassan and Ferrari (1995), for example, used a dual-beam spectrophotometer, with an integrating sphere attachment, to measure total and backward scattering by mineral particles suspended in water. Balch *et al.* (1999) used a benchtop laser

device manufactured by Wyatt Technologies to measure $\bar{\beta}(\bar{\lambda}, \bar{\Psi}; c)$, in discrete and flow-through sampling modes, at several angles and two wavelengths. The coefficient $b_b(\lambda)$ was then estimated by fitting measurements at $\bar{\Psi} = 45^\circ, 90^\circ$ and 135° to the function recommended by Beardsley and Zaneveld (1969), and then integrating that function from 90° to 180° .

Calibration of the Wyatt Technologies volume scattering device uses a solid isotropic scattering standard provided by the manufacturer. The composition of the standard is a proprietary secret of Wyatt Technologies, and only the calibration coefficients are provided to the user. Because of the undisclosed properties of its calibration standard, the Wyatt Technologies device must be viewed as a “black box” that must be evaluated through independent comparisons with other known standards, before its use can be accepted as part of a general protocol.

4.7 CALIBRATION OF METEOROLOGICAL SENSORS

The uncertainties of several meteorological variables are significant components of uncertainty budgets associated with using *in situ* measurements to validate satellite ocean color measurements and algorithms. Uncertainty in barometric pressure can affect that of absorption terms in atmospheric correction algorithms. Uncertainty in surface wind velocity directly affects sun and sky glint reflection estimates used to correct water-leaving radiance determinations from satellites and *in situ* above-water radiometers. Anemometers, barometers, thermometers (air temperature), and hygrometers should be calibrated using methods and at intervals recommended by the World Meteorological Organization (WMO). Calibration services and certification are available through the vendors who supply meteorological instruments, and in the laboratories of some academic oceanographic and/or atmospheric institutions.

4.8 CTD CALIBRATION

The conductivity probe, temperature probe, and pressure transducer of the CTD should be recalibrated before and after each major cruise by a properly equipped physical oceanographic laboratory, including those maintained by many university oceanography departments and CTD manufacturers. In addition, the conductivity probe should be independently calibrated during the course of each cruise by obtaining salinity water samples simultaneous with CTD readings. These salinity samples are to be analyzed, either at sea or ashore, with a laboratory salinometer calibrated with International Association for the Physical Sciences of the Ocean (IAPSO) Standard Seawater.

4.9 PRESSURE TRANSDUCER CALIBRATIONS

It is important to frequently calibrate pressure transducers on oceanographic profiling instruments. For purposes of these protocols, the pressure in decibars is equivalent to depth in meters. Adjustments for the density of seawater are negligible in the present context. On the other hand, inaccurate calibration of the pressure sensor will lead to artifacts and increased uncertainty in, *e.g.*, the computation of the diffuse attenuation coefficients $K(z, \lambda)$. If an instrument's pressure transducer port is equipped with a threaded fitting, a hose filled with distilled water may be used to connect it to a hand-pump and NIST traceable dead weight tester (several models are commercially available). Another common arrangement is to immerse the instrument in a pressure chamber, which is connected in turn to the pump and pressure calibration device. In either case, water pressure is increased in steps to produce several readings spanning the operating range of the instrument under test, and a polynomial equation is fit to the data to relate transducer output to the pressures measured with the dead-weight tester. Detailed methods and a certificate of NIST traceable calibration should be obtained from the manufacturer of the pressure calibration device. Calibration services of this type are readily available, on a fee-for-service basis, at laboratories maintained by many oceanography departments and commercial vendors of oceanographic equipment.

If simultaneous deployment of the CTD with optical instruments having independent pressure transducers is practical, the two depths measured by the different instruments should be compared over the range of the cast. If depth measurements disagree significantly, these comparisons may be used to correct

whichever transducer is found to be in error through analysis of pre- and post-cruise pressure transducer calibrations.

REFERENCES

- Balch, W.M., D.T. Drapeau, T.L. Cucci, R.D. Vaillancourt, K.A. Kilpatrick and J.J. Fritz, 1999: Optical backscattering by calcifying algae separating the contribution by particulate inorganic and organic carbon fractions. *J. Geophys. Res.* **104**: 1541-1558.
- Balch, W.M., P.M. Holligan, S.G. Ackleson, and K.J. Voss, 1991: Biological and optical properties of mesoscale coccolithophore blooms in the Gulf of Maine. *Limnol. Oceanogr.*, **36**: 629-643.
- Beardsley, G.F. and J.R.V. Zaneveld, 1969: Theoretical dependence of the near-asymptotic apparent optical properties on the inherent optical properties of sea water. *J. Optical Soc. Amer.* **59**: 373-377.
- Biggar, S.F. 1998: Calibration of a visible and near-infrared portable transfer radiometer. *Metrologia*, **35**: 701-706.
- Boss, E. and W.S. Pegau, 2001: Relationship of light scattering at an angle in the backward direction to the backscattering coefficient. *Appl. Opt.*, **40**: 5503-5507.
- Fargion, G.S. and J.L. Mueller, 2000: *Ocean Optics Protocols for Satellite Ocean Color Sensor Validation, Revision 2*, NASA TM 2001-209955, NASA Goddard Space Flight Center, Greenbelt, Maryland, 184.
- Hooker, S.B. and J. Aiken, 1998: Calibration evaluation and radiometric testing of field radiometers with the SQM. *J. Atmos. Oceanic Tech.*, **15**: 995-1007.
- Johnson, B.C., S.S. Bruce, E.A. Early, J.M. Houston, T.R. O'Brian, A. Thompson, S.B. Hooker and J.L. Mueller, 1996: The Forth SeaWiFS Intercalibration Round-Robin Experiment (SIRREX-4), May 1995. *NASA Tech. Memo. 104566, Vol. 37*, S.B. Hooker, E.R. Firestone and J.G. Acker, Eds., NASA GSFC, Greenbelt, Maryland, 65 pp.
- Johnson, B.C., P-S. Shaw, S.B. Hooker and D. Lynch, 1998: Radiometric and engineering performance of the SeaWiFS Quality Monitor (SQM): a portable light source for field radiometers. *J. Atmos. Oceanic Tech.*, **15**: 1008-1022.
- Maffione, R.A. and D.R. Dana: Instruments and methods for measuring the backward-scattering coefficient of ocean waters. *Appl. Opt.* **36**: 6057-6067.
- Mobley, C.D., L.K. Sundman and E. Boss, 2001: Phase function effects on oceanic light fields. *Appl Opt.*, (In press).
- Mueller, J.L., 1995: Comparison of irradiance immersion coefficients for several marine environmental radiometers (MERs), In: Mueller, J.L. and others, Case Studies for SeaWiFS Calibration and Validation, Part 3. *NASA TM 104566, Vol. 27*: 3-15, Hooker, S.B., E.R. Firestone and J.G. Acker, Eds.
- Mueller, J.L., and R.W. Austin, 1995: Ocean Optics Protocols for SeaWiFS Validation, Revision 1. *NASA Tech. Memo. 104566, Vol. 25*, S.B. Hooker, E.R. Firestone and J.G. Acker, Eds., NASA GSFC, Greenbelt, Maryland, 67 pp.
- Mueller, J.L., B.C. Johnson, C.L. Cromer, S.B. Hooker, J.T. McLean and S.F. Biggar, 1996: The Third SeaWiFS Intercalibration Round-Robin Experiment (SIRREX-3), 19-30 September 1994. *NASA Tech. Memo. 104566, Vol. 34*, S.B. Hooker, E.R. Firestone and J.G. Acker, Eds., 78 pp.
- Morel, A., 1974: Optical properties of pure water and pure sea water. In: *Optical Aspects of Oceanography*, N.G. Jerlov and E.S. Nielson, Eds., pp1-23.
- Neckel, H., and D. Labs, 1984: The solar radiation between 3,300 and 12,500 Å. *Solar Phys.*, **90**: 205--258.
- Oishi, T., 1990: Significant relationship between the backward scattering of sea water and the scatterance at 1020. *Appl. Opt.* **29**:4658-4665.

- Petzold, T.J., 1972: Volume Scattering Functions for Selected Ocean Waters. *SIO Ref. No. 72--78*, Scripps Institution of Oceanography, La Jolla, California, 79 p.
- Pope, R.M. and E.S. Fry. 1997: Absorption spectrum (380-700 nm) of pure water. II. Integrating cavity measurements. *Appl. Opt.* **36**: 8710-8723.
- Riley, T. and S. Bailey, 1998: The Sixth SeaWiFS Intercalibration Round-Robin Experiment (SIRREX-6) August—December 1997. *NASA/TM-1998-206878*. NASA, Goddard Space Flight Center, Greenbelt, MD. 26pp.
- Schmid, B., P.R. Spyak, S.F. Biggar, C. Wehrli, J. Seider, T. Ingold, C. Matzler and N. Kampfer. 1998: Evaluation of the applicability of solar and lamp radiometric calibrations of a precision Sun photometer operating between 300 and 1025 nm. *Appl. Opt.* **37**: 3923-3941.
- Smart, J.H., 1992: Empirical relationships between optical properties in the ocean. In: *Ocean Optics XI, SPIE*, **1,750**, 276-298.
- Smith, R.C. and K.S. Baker. 1981: Optical properties of the clearest natural waters (200-800 nm). *Appl. Opt.* **20**:177-184.
- Sogandares, F.M. and E.S. Fry. 1997: Absorption spectrum (340-640 nm) of pure water. I. Photothermal measurements. *Appl. Opt.* **36**: 8699-8709.
- Tassan, S. and G.M. Ferrari, 1995: Proposal for the measurement of backward and total scattering by mineral particles suspended in water. *Appl. Opt.* **34**: 8345-8353.
- Thuillier, G., M. Herse, P.S. Simon, D. Labs, H. Mandel, D. Gillotay and T. Foujols. 1998: The visible solar spectral irradiance from 350 to 850 nm as measured by the SOLSPEC spectrometer during the Atlas I mission. *Solar Phys.* **177**: 41-61.
- Twardowski, M.S., J.M. Sullivan, P.L. Donaghay and J.R.V. Zaneveld. 1999: Microscale quantification of the absorption by dissolved and particulate material in coastal waters with an AC-9. *J. Atmos. Oceanic Tech.* **16**: 691-707.

Chapter 5

Instrument Performance Specifications

James L. Mueller and Roswell Austin

Center for Hydro-Optics and Remote Sensing, San Diego State University, California

5.1 INTRODUCTION

This report describes measurements of optical properties, and other variables, necessary for validating data obtained with satellite ocean color instruments, and for the development of in-water and atmospheric algorithms. The specifications herein are those required of instruments used on ships, or other platforms, to acquire that *in situ* data. In some cases, the specifications have been selected to allow use of instruments that are affordable and that either currently exist, or that can be developed without major improvements in today's state-of-the-art technology. In a few cases, new or improved instruments must be developed to realize the specified performance characteristics. The data uncertainty requirements for this program are more severe than those for a general ocean survey. Here, various investigators use a variety of instruments that are calibrated independently at a number of facilities, and contribute data to a common database used to validate SeaWiFS, and other satellite, ocean color measurements. The resulting radiometric and bio-optical database provides an essential means of detecting and quantifying on-orbit changes in the satellite instruments relative to their prelaunch calibrations and characterizations. This chapter specifies instrument characteristics and data uncertainties thought to be necessary, as well as sufficient, for this task. The validation analysis would be significantly degraded should calibration errors or differences of even a few percent, or wavelength errors or differences of a few nanometers, occur in (between) the instruments used to acquire the validation *in situ* bio-optical database.

5.2 IN-WATER RADIOMETERS

This section specifies radiometric characteristics for instruments that are used to measure $E_d(z, \lambda)$, $E_u(z, \lambda)$ and $L_u(z, \lambda)$. The specifications are applicable to filter radiometers and to spectroradiometers based on monochromators. Minimum performance characteristics are specified for spectral resolution, radiometric responsivity and resolution, signal-to-noise ratios (SNRs), radiometric saturation and minimum detectable values, angular response, temporal sampling resolution, linearity, and stability.

Spectral Characteristics

In-water radiometers shall be capable, as a minimum, of making measurements at the wavelengths shown in Table 5.1, which refers specifically to the SeaWiFS channels. The SeaWiFS channel wavelength combination is consistent with the recommended preferred ocean radiance channel combination (C3) recommended by the International Ocean Color Coordinating Group (IOCCG 1998), albeit with wider spectral bandwidths. For the SIMBIOS *in situ* validation database, the wavelength combinations in Table 5.1 must be expanded to provide radiance and irradiance measurements at the greater number of wavelengths represented by the full ensemble of ocean color sensors (Appendix A). For example, OCTS and POLDER each had a channel at 565 nm, rather than that at 555 nm on SeaWiFS. For purposes of these protocols, in-water radiometer channels at these additional wavelengths must match the satellite channel wavelengths and have full-width at half-maximum (FWHM) bandwidths within the same tolerances described below with reference to Table 5.1.

Table 5.1 presumes the use of properly blocked interference filters to provide the required spectral bandpass and out-of-band rejection (10^{-6} or better). Care must also be taken to avoid possible out-of-band leakage due to fluorescence by filter, or other optical component, materials. Filter radiometers should have channels with center wavelengths, as measured in the assembled instrument, matching those given in Table 5.1 to within 1 nm for 410 nm and 443 nm, and within 2 nm for all other spectral bands. Shifts of these magnitudes in center wavelengths will result in changes in measured radiometric values of approximately

1 % or less (R. Booth pers. comm.) and this specification should be met if possible. It is recognized, however, that enforcing a 1 nm hard-and-fast specification could be prohibitively expensive, and this tolerance should be regarded as a goal. With knowledge, to less than 0.2 nm, of the actual center wavelengths and complete spectral response functions, corrections probably can be made to infer effective radiometric quantities for the satellite instrument channels. Bandwidths must be 10 ± 2 nm FWHM. They are made narrower than, for example, the SeaWiFS channels to reduce the skewing of the parameters derived from underwater irradiance, or radiance, profiles in spectral regions where absorption by natural seawater exhibits rapid variation with wavelength.

Table 5.1: Recommended spectral bands for discrete-wavelength filter radiometers using 10nm FWHM bandwidths. In addition, out-of-band blocking in the tails of the instrument response functions should be 10^{-6} or better.

SeaWiFS Band	Wavelengths [nm]	E_d, E_u, L_u [nm]	E_s [nm]
1	402-422	412 ¹	412
2	433-453	443,435 ²	443
3	480-500	490	490
4	500-520	510	510
5	545-565	555	555
6	660-680	665,683	665
5	545-565	555	555
6	660-680	665,683	665 ³
7	745-785	⁴	780
8	845-885	⁴	875

1. A preferred option is to replace two separate 10nm FWHM bands centered at 406 and 416 nm with a single 412 nm channel. The two channels would allow more accurate modeling of L_{WN} (412), matching SeaWiFS characteristics.
2. An optional extra band is used to improve modeling of $L_{WN}(\lambda)$ radiances to match the SeaWiFS 443 nm channel.
3. E_s deck, only channel in this band is necessary.
4. Due to the specialized nature of infrared in-water measurements, specialized sensors will be needed.

To maintain the above tolerances, it is anticipated that filters will be ordered to a center wavelength λ_0 with a tolerance of ± 1 nm and a FWHM bandwidth of 8.5 ± 1 nm. When the filter is installed in a radiometer with a 10° (half-angle) FOV, however, the spectral bandpass will broaden by 2 nm to 3 nm, and the center wavelength will shift. Furthermore, as a filter ages in use, its transmission curve may undergo changes to further broaden the FWHM bandpass and shift the peak. The tolerances specified above include an allowance for some degradation before expensive filter and detector changes must be done. In a single instrument, all channels at a given nominal wavelength should match within 1 nm, if possible. It is desirable, therefore, to obtain all of the filters used by an investigator for measurements at any nominal wavelength (λ_n) from a single manufacturing lot when possible. If this is done, $E_s(\lambda_n)$, $E_d(\lambda_n)$, $E_u(\lambda_n)$, and $L_u(\lambda_n)$, and any atmospheric radiometric quantities measured with that investigator's systems, would all have a greater likelihood of being measured over the same range of wavelengths, for each nominal wavelength (λ_n). In any event, the actual spectral response function of each instrument channel must be measured and known with an uncertainty less than 0.2 nm.

High-resolution monochromator-based spectroradiometers, with adequate sensitivity and stray light rejection characteristics, are also suitable instruments and are recommended for many algorithm development studies. Suitable specifications for such instruments are given in Table 5.2. (These instruments must also meet the specifications summarized in Tables 5.1 and 5.3.)

It is extremely difficult, if not impossible, to optically reject stray light within a single-grating spectrometer at the level specified in Table 5.1. On the other hand, recent capabilities developed at the National Institute of Standards and Technology (NIST) may be used to characterize the spectral stray-light response distribution function of a spectrometer using a set of tunable lasers (Brown et al. 2000). Stray light correction algorithms based on NIST characterizations are being developed for application to the Marine Optical Buoy (MOBY) spectroradiometers (Chapter 11). This correction is expected to reduce stray light uncertainties well below the level specified in Table 5.2. The tunable laser based stray light characterization procedure is too expensive to apply to every radiometer used in this program, but its application is essential for key transfer radiometers. The radiometers in the MOBY facility, for example, are used to provide a common vicarious calibration reference for all satellite ocean color sensors embraced within the SIMBIOS program (Chapter 11), and the expense is well justified in this instance.

Table 5.2: Minimum specifications for the characteristics of high-resolution spectroradiometers.

<i>Optical Sensors</i>	
Spectral Range:	380 to 750 / 900 nm
Spectral Resolution:	5 nm (or less FWHM)
Wavelength Accuracy:	10 % FWHM of resolution (0.5 nm)
Wavelength Stability:	5 % FWHM of resolution (0.25 nm)
Signal-to-Noise Ratio:	1,000:1 (at minimum)
Stray Light Rejection:	10^{-6}
Radiometric Accuracy:	3 %
Radiometric Stability:	1 %
FOV Maximum:	10° (for radiance)
Temperature Stability:	Specified for 0–35°C
Linearity:	Correctable to 0.1 %
<i>Ancillary Sensors</i>	
Temperature:	0.2°C
Pressure:	0.1 % (full scale)
Horizontal Inclination:	1° over 40° range

Responsivity, SNR, and Resolution

The expected operating limits for radiometric responsivities, SNR, and digital resolution are specified in Table 5.3, the limits for which were derived as follows:

1. An E_d saturation value of $300 \mu\text{W cm}^{-2} \text{ nm}^{-1}$ is assumed at all wavelengths.
2. Implicit, but not stated, in Table 5.3 is that the minimum required $E_d(0)$ is $20 \mu\text{W cm}^{-2} \text{ nm}^{-1}$; it will not be appropriate to occupy validation stations when illumination is less than this minimum.
3. The minimum $E_d(0)$ implies a minimum detectable $E_d(z)$ value of $1 \mu\text{W cm}^{-2} \text{ nm}^{-1}$ at 3 optical depths (3/K).
4. Digital resolution must be less than or equal to 0.5 % of the reading to maintain a 100:1 SNR. To permit a 1 % uncertainty in absolute calibration, if that goal can be met in the calibration laboratory, the instrument must digitally resolve 0.1 % of the irradiance (radiance) produced by the laboratory standards used; typical irradiance (radiance) values for calibration using 1,000 W FEL standard lamps traceable to the National Institute of Standards and Technology (NIST), and required digital resolutions at these signal levels, are given in Table 5.3 as “Calibration Irradiance” and “Digital Resolution (cal.)”, respectively. A SNR of 100:1 requires a resolution in $E_d(z)$ at three optical depths to $0.005 \mu\text{W cm}^{-2} \text{ nm}^{-1}$ per count, i.e., 2.5 digit resolution. At the surface, $E_d(0)$ should be resolved to $0.05 \mu\text{W cm}^{-2} \text{ nm}^{-1}$ per count.

5. The Case-1 saturation values of $E_d(0)$ represent the *Instrument Specification Subgroup's* (Mueller and Austin 1992) estimate of maximum reflectances to be expected in ordinary Case-1 waters: 12.5 % at 410 nm, 7.5 % at 488 nm and 0.5 % at 670 nm. These saturation values will be too low for measurements in Case-2 waters, or coccolithophorid blooms. In these situations, a maximum expected reflectance of 40 % for $\lambda < 660$ nm and 20 % for $\lambda \geq 660$ nm is assumed. This implies that the expected maximum irradiance in $E_u(0)$ should be $80 \mu\text{W cm}^{-2} \text{ nm}^{-1}$ for $\lambda < 660$ nm and $40 \mu\text{W cm}^{-2} \text{ nm}^{-1}$ for $\lambda \geq 660$ nm.
6. The minimum required irradiances at three optical depths (as given in Table 5.3) assumes minimum reflectances of 1 % at 410 nm, 2 % at 488 nm, and 0.15 % at 670 nm.
7. The saturation and minimum radiances, and radiance responsivity resolutions, for $L_u(0)$ and $L_u(3/K_d)$ are calculated as $L_u/E_u = Q^{-1}$ times the corresponding specification for $E_u(0)$ or $E_u(z)$. In Mueller and Austin (1995) it was assumed that $Q = 5$, a constant at all wavelengths and depths. Morel and Gentili (1996) showed that Q actually varies between approximately 3.14 and 5 at 410 nm and 488 nm, and between approximately 3.14 and 5.7 at 670 nm (see Chapter 13). Saturation radiances, for the extreme minimum case of $Q = 3.14$ (very clear waters with the sun nearly overhead), are increased by a factor of 1.6 at all three wavelengths relative to Mueller and Austin (1995). Minimum radiances at 670 nm, for the extreme maximum case of $Q = 5.7$ (turbid waters and solar zenith angle $> 60^\circ$), are decreased by a factor of 0.75, and the implied digital resolution at 670 nm was changed accordingly. Minimum expected radiances and required digital resolution at 410 nm and 488 nm are unchanged.

The specifications in Table 5.3 are meant as guidance to interpret the following required performance requirements:

1. The instrument must maintain a 100:1 SNR at every operating range encountered, during field measurements.
2. The data for measurements obtained in the field must be recorded with a digital resolution less than or equal to 0.5 % of reading.
3. The dynamic range of the instrument's linear sensitivity must extend to include the signal levels encountered during laboratory calibrations, and the calibration signals must be recorded with a digital resolution of 0.1 % of reading to permit 1 % uncertainty in calibration.

In general, the above performance specifications do not pose exceptionally difficult engineering challenges, with the possible exception of the full dynamic range implied by Case-2 or coccolith saturation radiance $L_u(665)$ to minimum expected $L_u(665)$. In any event, this situation will require specially designed radiometers (see also “*Red and Near-Infrared Wavelengths*” below). It is not necessary that every radiometer used for satellite ocean color sensor validation operate over the full dynamic ranges given in Table 5.3. A radiometer is merely required to maintain the above performance specifications over the dynamic ranges of irradiance and radiance existing at locations and associated illumination conditions where it is used for validation or algorithm development.

Table 5.3: Required instrument and sensitivities for SeaWiFS validation and algorithm development as a function of radiometric measured variable and wavelength.

<i>Property</i>	<i>Variable</i>	410 nm	488 nm	665 nm	<i>Comment</i>
$E_d(z, \lambda)$,	$E_d(0)_{\max}$	300	300	300	Saturation Irradiance
Downwelled	$E_d \left(\frac{3}{K_d} \right)$	1	1	1	Minimum Expected Irradiance
Irradiance	$\frac{dE}{dN}$	5×10^{-3}	5×10^{-3}	5×10^{-3}	Digital Resolution (profiles)
	$\frac{dE}{dN}$	5×10^{-2}	5×10^{-2}	5×10^{-2}	Digital Resolution (surface unit)
$E_u(z, \lambda)$,	$E_u(0)_{\max}$	120	120	60	Saturation Irradiance (Case-2/coccoliths)
Upwelled		37	22	1.5	Saturation Irradiance (Case-1)
Irradiance	$E_u \left(\frac{3}{K_d} \right)$	1×10^{-2}	2×10^{-2}	1.5×10^{-3}	Minimum Expected Irradiance
	$\frac{dE}{dN}$	5×10^{-4}	5×10^{-4}	5×10^{-5}	Digital Resolution (surface unit)
	$\frac{dE}{dN}$	5×10^{-5}	5×10^{-5}	5×10^{-6}	Digital Resolution (profiles)
$L_u(z, \lambda)$,	$L_u(0)_{\max}$	38	38	13	Saturation Radiance (Case-2/coccoliths)
Upwelled		12.0	7.2	0.5	Saturation Radiance (Case-1)
Radiance	$L_u \left(\frac{3}{K_d} \right)$	2×10^{-3}	4×10^{-3}	2.25×10^{-4}	Minimum Expected Radiance
	$\frac{dL}{dN}$	5×10^{-4}	5×10^{-4}	5×10^{-5}	Digital Resolution (surface unit)
	$\frac{dL}{dN}$	5×10^{-5}	5×10^{-5}	1×10^{-6}	Digital Resolution (profiles)
E_{cal} , Source	E_{cal}	2	5	15	Calibration Irradiance
Irradiance	$\frac{dE}{dN}$	2×10^{-3}	5×10^{-3}	1×10^{-2}	Digital Resolution (E_d , E_s , E_u cal.)
L_{cal} , Source	L_{cal}	0.6	1.5	4.5	Calibration Radiance
Radiance	$\frac{dL}{dN}$	6×10^{-4}	1×10^{-3}	4×10^{-3}	Digital Resolution (L_u cal.)

Notes: 1. E_u and E_d are in units of $\mu\text{W cm}^{-2} \text{ nm}^{-1}$ and L_u is in units of $\mu\text{W cm}^{-2} \text{ nm}^{-1} \text{ sr}^{-1}$.
 2. Responsivity resolution in radiometric units per digital count at the minimum required signal level.
 3. Specified ranges should maintain a 100:1 SNR.

Linearity and Stability

Errors attributable to linearity or stability should be less than 0.5 % of the instrumental readings over the dynamic ranges specified in Table 5.3. This is a challenging goal, but one which must be met if the equally challenging goal of achieving 1 % uncertainty in absolute calibration is to be meaningful.

Sampling Resolution

Sampling frequency should be compatible with the profiling technique being used. For the preferred multispectral filter radiometers and spectroradiometric (dispersion) instruments using array sensors, the minimum sampling frequencies are determined by the profiling rate and the depth resolution required. In general, five or more samples per meter should be obtained at all wavelengths. All channels of $E_d(z, \lambda)$, $E_u(z, \lambda)$ and $L_u(z, \lambda)$ at all wavelengths should be sampled within 10^{-2} s at each given depth. Alternatively, grating spectrometers using detector arrays to sample all channels simultaneously may be integrated for longer periods to achieve necessary signal-to-noise ratios.

The time response of the instrument to a full-scale (saturation to dark) step change in irradiance should be less than one second to arrive at a value within 0.1 %, or one digitizing step, whichever is greater, of steady state. In addition, the electronic e -folding time constant of the instrument must be consistent with the rate at which the channels are sampled, *i.e.*, if data are to be acquired at 10 Hz, the e -folding time constant should be 0.2 s to avoid aliasing. Individual data scans may be averaged to improve signal-to-noise performance, provided adequate depth resolution is maintained.

Angular Response Characteristics

Irradiance: The response of a *cosine collector* to a collimated light source incident at an angle (θ) from the normal must be such that:

1. for $E_u(\lambda)$ measurements, the integrated response to a radiance distribution of the form $L(\lambda, \theta) \propto 1 + 4 \sin \theta$ should vary as $\cos \theta$, within 2 %; and
2. for E_d measurement, the response to a collimated source should vary as $\cos \theta$ within less than 2 % for angles $0 \leq \theta \leq 65^\circ$ and 10 % for angles $65^\circ \leq \theta < 90^\circ$.

Departures from $\cos \theta$ will translate directly to approximately equal errors in E_d in the case of direct sunlight.

Radiance: The in-water FOV for upwelled radiance bands should be approximately 10° (half-angle). The resulting solid angle FOV (approximately 0.1 sr) is large enough to provide reasonable levels of flux, using silicon detectors, yet small enough to resolve the slowly varying (with \bullet for $\bullet < 30^\circ$) field of upwelled radiance. Smaller FOV sensors are appropriate, of course, if all of the other performance specifications are satisfied.

Operating Depth

Instruments used for profiling in clear to moderately turbid Case-1 waters shall be capable of operating to depths of 200m. Depths should be measured with an uncertainty of 0.5 m and a repeatability of 0.2 m for radiometric profiles at visible wavelengths.

Instruments used for profiling in very turbid Case 1 and Case 2 waters require a much lower maximum pressure rating. On the other hand, in these waters it is necessary to resolve depth with an uncertainty < 5 cm, and with a differential uncertainty of approximately 2 cm.

Instrument Attitude

The orientations of the instrument with respect to the vertical shall be within $\pm 10^\circ$, and the attitude shall be measured with orthogonally oriented sensors from 0-30° with an uncertainty of $\pm 1^\circ$ in a static mode; it is not intended that this uncertainty be maintained while an instrument is subject to large accelerations induced by surface waves. These data shall be recorded with the radiometric data stream for use as a data quality flag.

Red and Near-Infrared Wavelengths

The fact that red and near-IR channels - e.g. SeaWiFS bands 6, 7, and 8 at wavelengths of 665 nm, 780 nm, and 865 nm, respectively - have such short attenuation lengths in water requires that special attention must be paid to these measurements. Problems due to instrument self-shading (Gordon and Ding 1992) and very rapid attenuation of $L_u(z, \lambda)$ must be considered at these wavelengths. Large diameter instruments, and radiometers mounted on large instrument packages, are not adaptable to these measurements.

Suggested procedures for making the measurements are to use either fiber optic probes carrying light back to a remote instrument, or very small single-wavelength discrete instruments. Each of these concepts is adaptable to deployment from a small floating platform. Care must be taken to avoid direct shading by the supporting platform, but at these wavelengths, the large attenuation coefficients of water makes shadowing by objects more than a few meters away irrelevant.

The minimum measurement scheme would be two discrete (10 nm FWHM) channels at 780 nm and 875 nm. Additional channels at 750 nm and 850 nm, or more elaborately, high-resolution spectroradiometry, would be useful in determining the spectral distribution of the upwelling light field in these bands.

These measurements should be performed as part of the standard validation data acquisition, because of their importance in the atmospheric correction algorithms. It is anticipated that in the majority of cases, and particularly in most Case-1 waters, these measurements will show negligible upwelling light. In Case-2 waters, cases of extremely high productivity, or in coccolithophorid blooms, reflectance at these wavelengths may be significant, and these measurements will become very important. When in-water measurements are performed at these wavelengths, the deck cell channels should be expanded to include bands at 750 and 875 nm (Table 5.1).

5.3 SURFACE IRRADIANCE

The spectral irradiance incident at the ocean surface shall be measured at wavelengths that correspond to the SeaWiFS spectral bands (Table 5.1), but with 10 nm FWHM bandwidth. A total radiation pyrometer may provide helpful ancillary information, but this is not a required instrument. Instruments mounted aboard ships must be positioned to view the sky with minimum obstruction or reflections from the ship's superstructure, antennas, etc. Particular care must be taken to prevent sun shadows from antennas falling on the irradiance-collecting surface. Gimbal mounting of the deck sensor may be helpful to keep the surface of the sensor horizontal. Improperly designed gimbal systems, however, can accentuate fluctuations caused by ship motion, and if there is obvious oscillation in the measured irradiance, the gimbal mechanism should be improved to eliminate the problem.

An intuitively attractive technique, which was suggested in previous versions of the optics protocols (Mueller and Austin 1992, 1995), would be to measure irradiance with a sensor floated a fraction of a meter below the sea surface, far enough away from the ship to avoid ship shadows. The flotation assembly would be designed to avoid shadowing the radiometric FOV and to damp wave-induced motions. This type of arrangement has an additional potential for supporting a small sensor to also measure upwelling radiance, $L_u(z, \lambda)$, just below the surface. Over the past several years, however, the ocean color community has gained experience with this approach, and has encountered consistent and significant difficulties due to wave-induced fluctuations in near-surface E_d . Zaneveld *et al.* (2001) compare theoretical characteristics of the effects of surface waves on near surface irradiance with examples of such measurements under low wind speed conditions. In the case of coherent surface waves, these effects become more pronounced and

do not average linearly over time (Zaneveld, personal communication). The in-water reference radiometer method is no longer recommended for determining either $E_d(0^-, \lambda)$ or $E_s(\lambda)$. An acceptable variant of the approach is to use a similar flotation assembly, tethered to allow the instrument to drift away from the ship, but with the irradiance collector raised 50 to 100 cm above the sea surface to measure $E_s(\lambda)$ in air.

Surface Radiometer Characteristics

The specified number of channels and spectral characteristics of deck cells are the same as those for subsurface irradiance measurements as shown in Table 5.1, augmented as necessary for validation of satellite sensors other than SeaWiFS (Appendix A). Saturation irradiances are the same as for $E_d(\lambda)$ (Table 5.3). The dynamic operating range for these sensors needs to only be 25 db, with a SNR of 100:1, but it must include the nominal calibration irradiance (Table 5.3). Linearity must be within $\pm 5\%$. Sampling frequency should match the frequency of the underwater radiometer, which should be 1 Hz or faster, and all wavelengths should be sampled within an interval less than or equal to 10^{-2} s. Cosine response characteristics should give relative responsivity to a collimated source (in air) which matches $\cos\theta$ within 2 % for $0 \leq \theta \leq 65^\circ$, and within 10 % for $65^\circ \leq \theta < 90^\circ$.

For some oceanographic process studies, it may be acceptable to use a radiometer measuring $E_s(\lambda)$ at only a single wavelength. If only a single channel deck radiometer is available, its spectral characteristic should closely match one of channels 2 through 5 (Table 5.1) with a 10 nm FWHM bandwidth. A broadband, or photosynthetically available radiation (PAR), radiometer should never be used for this purpose.

5.4 ABOVE-WATER RADIOMETRY

The performance characteristics to be specified for an above-water ocean color radiometer will vary, depending on how a particular instrument is to be employed in satellite ocean color sensor validation experiments. For radiometric comparisons with, *e.g.*, SeaWiFS and in-water measurements, the fundamental criterion to be met is that estimates of normalized spectral water-leaving radiance derived from shipboard or airborne measurements must have the same uncertainty specified for those derived from in-water measurements of $L_u(z, \lambda)$ (Table 5.3). A less accurate radiometer may be used to semi-quantitatively characterize spatial variability near ship stations.

In general, the spectral characteristics of above-water radiometers should match those specified for $L_u(\lambda)$ in Table 5.1. In some cases, however, it may be acceptable for a radiometer to match the SeaWiFS – or other sensor – specifications, which specify center wavelength within 2 nm and 20 nm FWHM bandwidth. Recalling the sensitivity of solar radiometry to the exact center wavelength and detailed spectral response function (Section 5.1), any use of airborne radiometers must quantitatively account for the different spectral responsivity functions between measurements of radiance by, *e.g.*, SeaWiFS, in-water radiometers, and above-water radiometers at each channel's nominal center wavelength.

A high-altitude imaging radiometer must have a radiometric uncertainty and SNR in all channels equal to those of the satellite ocean color instrument if its imagery is to be used for direct radiometric verification of the satellite sensor's radiometric performance. In some cases, the requisite SNR may be realized through pixel averaging to a 1 km spatial resolution commensurate with that of, *e.g.*, SeaWiFS. Direct radiometric comparisons between aircraft and SeaWiFS radiances, however, also require that the different atmospheric path effects be carefully modeled, and that the uncertainty in those modeled adjustments be independently estimated. This can be done most effectively when the aircraft measurements are combined with the full suite of shipboard in-water, atmospheric, and ancillary measurements (Chapter 3, Table 3.1). In this case, direct comparisons between aircraft and ship radiometry may require that both the SNR and the uncertainties realized in combined analyses of the two data sets will represent a smaller spatial resolution than the nominal 1 km instantaneous field-of-view (IFOV) for SeaWiFS and other satellite sensors. Finally, the viewing zenith and azimuth angles at the matched pixel must also be nearly the same for both sensors, if uncertainties associated with modeled corrections for the ocean's surface and internal bidirectional reflectance distribution function (BRDF) are to be minimized (Chapters 12 and 13).

Performance characteristic specifications are similar for ocean color radiometers used to measure water-leaving radiance from either the deck of a ship or an aircraft flown at low altitude, *i.e.*, 200m altitude or lower. Radiometric characteristics should match the criterion set forth for in-water $L_u(\lambda)$ radiometers in Section 5.1 and Tables 5-1 through 5-3. The instrument FOV should be between 5° and 10° (full angle), and all wavelengths must be coregistered within 10 % of the IFOV. All channels must be scanned simultaneously, or within less than 10^{-2} s (depending on the digitizing design), to avoid aliasing due to varying wave reflectance in shipboard measurements, and to avoid time-space aliasing in airborne measurements. This constraint precludes use of filter wheel radiometers and others which scan channels sequentially over a time interval greater than 10^{-2} s. Sampling over longer periods of time may be done by either electronic integration of all channels simultaneously, or by averaging multiple scans.

A radiometer's sensitivity to the polarization of aperture radiance is critical for ocean color remote sensing applications. Polarization sensitivity is likely to be present in any radiometer having mirrors, prisms or gratings in its optical path. To measure accurate water-leaving radiances using instruments of these types, it is necessary to depolarize aperture radiance using either fiber optics or a *pseudo-depolarizer*. Shipboard and airborne ocean color radiometers must have a polarization sensitivity of less than 2 % in all channels. The sole exception to this rule will occur in the case of instruments designed to actually measure the polarization components of aperture radiance, *e.g.* the polarization channels of the French Polarization and Directionality of the Earth's Reflectances (POLDER) instrument and of the hand-held SIMBAD radiometers.

Each application of a particular above-water radiometer system, if it is proposed for satellite ocean color sensor validation, must be evaluated on its own merits. The instrument's responsivity, uncertainty, stability, FOV, and spectral characteristics must be evaluated in the context of the models to be used to compare its radiance measurements to in-water, or *e.g.* SeaWiFS, radiance measurements. The suitability of spatial averaging to improve SNRs must be evaluated in terms of the spatial variability prevailing in the experiment site, particularly when in-water and aircraft radiances are to be directly compared. Finer resolution aircraft imagery, or low-altitude trackline data, will often be essential for determining the validity of attempts to directly compare in-water and, *e.g.*, SeaWiFS radiances measured at a particular site.

In summary, airborne and shipboard above-water radiometry can obviously contribute valuable data for validating the radiometric performance of satellite ocean color instruments and the algorithms employed with their data. There is, however, a wide possible range of radiometer characteristics that can be applied to this program, and detailed specification of required characteristics can only be done in the context of each particular experiment's design. Only the guiding principals and desired end-to-end performance are specified here.

5.5 INHERENT OPTICAL PROPERTY INSTRUMENTS

The primary Inherent Optical Properties (IOP) are:

1. the beam attenuation coefficient, $c(z, \lambda)$, in units of m^{-1} ;
2. the absorption coefficient, $a(z, \lambda)$, in units of m^{-1} ; and
3. the volume scattering function, $\beta(z, \lambda, \Psi)$, in units of $\text{m}^{-1} \text{sr}^{-1}$, describing the distribution of photons scattered from an incident (path) direction (θ_o, ϕ_o) through an angle Ψ .

These quantities are defined in greater detail in Chapter 2.

The integral of the volume scattering function over 4π sr is the total scattering coefficient, $b(z, \lambda)$, with units of m^{-1} . The integral of the volume scattering function over the back hemisphere is the backscattering coefficient, $b_b(z, \lambda)$, with units of m^{-1} .

It is possible to measure vertical profiles of $a(z, \lambda)$ and $c(z, \lambda)$ *in situ*. Instruments for making these measurements should, at a minimum, have the characteristics given in Table 5.4. In the case of beam attenuation coefficients, the requirements for uncertainty and precision correspond to changes in $c(\lambda)$

resulting from changes in concentration of approximately 5 and 2 $\mu\text{g L}^{-1}$ of suspended mass, respectively. Stability should be tested with instruments connected to the data acquisition system. Stability between successive calibrations should be better than 0.005 m^{-1} .

Dual path (reflective tube and open path) instruments for measuring $a(z, \lambda)$ and $c(z, \lambda)$ *in situ* are commercially available, meet the specifications of Table 5.4 for SeaWiFS wavelengths, and have found widespread use in the ocean optics and color communities. In some cases, two such instruments are mounted together, one having a 0.2 μm filter attached to the water inlet port. The filtered input instrument measures absorption and beam attenuation by dissolved substances, which allows the total absorption and attenuation measured by the unfiltered instrument to be partitioned into dissolved and particulate components. Hyperspectral resolution (<10 nm) instruments of this type are also commercially available, but the community has not yet established that the performance characteristics of these more sophisticated underwater spectrophotometers reliably meet the specifications of Table 5.4.

Table 5.4: Minimum instrument characteristics for measuring spectral absorption & attenuation coefficients.

Instrument Characteristics	
Spectral Resolution:	410, 443, 490, 510, 555 & 670 nm
Bandwidth:	10 nm
Uncertainty:	0.005 m^{-1}
Precision for $\lambda < 650$ nm:	0.002 m^{-1}
Precision for $\lambda \geq 650$ nm:	0.005 m^{-1}
Stability with Temperature:	0.005 m^{-1} over 0–25° C
Sampling Interval:	≥ 4 samples m^{-1}
Source Collimation Angle:	≤ 5 mrad
Detector Acceptance Angle:	≤ 20 mrad
Depth Capability:	200 m

The spectral total scattering coefficient cannot be measured directly. It can be obtained from $b(\lambda) = c(\lambda) - a(\lambda)$, with an uncertainty equal to the quadrature sum of the uncertainties in those measurements.

Using commercially available instruments, it is also possible to measure photons scattered at one or more fixed angles in the backward direction, and to estimate from this measurement $b_b(\lambda)$ *in situ*. The spectral backscattering coefficient, $b_b(\lambda)$ has the same requirements for spectral resolution, bandwidth, and linearity as $a(\lambda)$ and $c(\lambda)$ (Table 5.4). Since $b_b(\lambda)$ is not a transmission-like measurement, however, the uncertainty of its determination will be approximately 10 %.

The shape of the volume scattering function, $\beta(z, \lambda, \Psi)$, has until recently been determined *in situ* only crudely with devices like the ALPHA and Scattering Meter (ALSCAT) and the General Angle Scattering Meter (GASM), which were built more than two decades ago at the Visibility Laboratory of the Scripps Institution of Oceanography. These are single angle measurement devices, which must be scanned as a function of angle and wavelength. Because measuring scattering with these old instruments is a slow process, they do not lend themselves readily to incorporation into other instrument platforms. Recently developed new instruments, designed to measure the full scattering function with modernized optical and electronic components, show considerable promise (*e.g.* Mobley *et al.* 2001) and protocols defining more detailed specifications and procedures should evolve in the near future.

5.6 ATMOSPHERIC AEROSOLS

Sun photometers should be used to measure atmospheric aerosol optical thickness. These sun photometers should have specifications in agreement with (or exceeding) the World Meteorological Organization (WMO) sun photometer specifications (Frohlich 1979). Specifically, the instruments should have a 2° FOV, temperature stabilization, and a precision of ± 0.01 %. The specific wavelengths of channels should correspond to the recommended WMO wavelengths of 380 nm, 500 nm, 675 nm, 778 nm, and 862 nm. Additional wavelengths corresponding to the SeaWiFS (Table 5.1), or other satellite ocean color sensor (Appendix A), channel combinations may be desirable in some applications, but they are not required for the SIMBIOS validation database. More detailed specifications associated with specific photometers are given in Chapters 7 and 14.

5.7 SPECTRAL SKY RADIANCE

Measurements of spectral sky radiance distribution should be made using a photoelectric all-sky camera. Spectral characteristics of the sky radiance camera channels are those specified for $E_s(\lambda)$ (Table 5.1). Data should be in a format such that absolute radiance values can be obtained with an uncertainty of 5 % and sky irradiance can be determined from integrals of the data to within 10 %. If the dynamic range of the camera is insufficient to capture both the sun and sky distribution, neutral density filters (or some other method) should be used so that radiance from both the sun and sky can be measured.

Alternatively, sky radiance distributions are determined using radiometers that are mechanically scanned through the solar principal plane. More detailed specifications for these instruments are described in Chapters 7 and 14.

5.8 PHYTOPLANKTON PIGMENTS

HPLC equipment and associated standards must conform to protocols specified in Chapter 16. Bench fluorometers used to measure chlorophyll *a* concentration must conform to protocols specified in Chapter 17. *In situ* fluorometers should resolve chlorophyll *a* concentration to 0.001 mg m^{-3} , or better.

5.9 CTD PROFILES

A calibrated CTD system should be used to make profiles of Conductivity, Temperature and Depth to maximum depths between 200 m and 500 m. The instrument should meet the minimum specifications given in Table 5.5.

Table 5.5: The minimum instrument characteristics for the measurement of hydrographic profiles.

<i>Parameter</i>	<i>Range</i>	<i>Uncertainty</i>	<i>Resolution</i>
Pressure [dbars]	0–500	0.3 %	0.005 %
Temperature [°C]	–2– 35	0.015° C	0.001° C
Salinity [PSU]	1– 45	0.03 PSU	0.001 PSU

REFERENCES

- Brown, S.W., G.P. Eppeldauer and K.R. Lykke, 2000: NIST facility for spectral irradiance and radiance response calibrations with a uniform source. *Metrologia*, **37**: 579-589.
- Frohlich, C., 1979: WMO/PMOD Sun photometer: instructions for manufacture. *World Meteor. Org.*, Geneva, Switzerland, 3 pp., (plus tables and drawings).
- Gordon, H.R., and K. Ding, 1992: Self shading of in-water optical instruments. *Limnol. Oceanogr.*, **37**, 491--500.
- IOCCG 1998. Minimum Requirements for an Operational Ocean-Colour Sensor for the Open Ocean. *Reports of the International Ocean-Colour Coordinating Group, No. 1*, IOCCG, Dartmouth Canada, 46pp.
- Mobley, C.D., L.K. Sundman and E. Boss, 2001: Phase function effects on oceanic light fields. *Appl Opt.*, (In press).
- Morel, A. and B. Gentili, 1996. Diffuse reflectance of oceanic waters. III. Implication of bidirectionality for the remote-sensing problem.
- Mueller, J.L., and R.W. Austin, 1992: Ocean Optics Protocols for SeaWiFS Validation. *NASA Tech. Memo. 104566, Vol. 5*, S.B. Hooker and E.R. Firestone, Eds., NASA Goddard Space Flight Center, Greenbelt, Maryland, 43 pp.
- Mueller, J.L., and R.W. Austin, 1995: Ocean Optics Protocols for SeaWiFS Validation, Revision 1. *NASA Tech. Memo. 104566, Vol. 25*, S.B. Hooker and E.R. Firestone, Eds., NASA Goddard Space Flight Center, Greenbelt, Maryland, 66 pp.
- Zaneveld, J.R.V., E. Boss and A. Barnard, 2001. Influence of surface waves on measured and modeled irradiance profiles. *Appl. Opt.*, **40**(9): 1442-1449.

Chapter 6

Characterization of Oceanographic and Atmospheric Radiometers

James L. Mueller and Roswell Austin

Center for Hydro-Optics and Remote Sensing, San Diego State University, California

6.1 INTRODUCTION

Presented in this chapter are procedures for characterizing environmental radiometers, including special characteristics of underwater radiometers, to verify compliance with the specifications of Chapter 4. The characterization of any radiometer used to acquire field data for Sensor Intercomparison for Marine Biology and Interdisciplinary Oceanic Studies (SIMBIOS) validation and algorithm development purposes shall include the determination of those instrument characteristics that affect its calibration as used in the field environment. These characteristics include a sensor's:

1. spectral irradiance, or radiance, responsivity calibration, traceable to National Institute of Standards and Technology (NIST) standards;
2. spectral response functions (bandpass) of the various measurement channels;
3. spectral, out-of-band stray light sensitivity;
4. effects on responsivity caused by water immersion;
5. angular response sensitivities in the medium, i.e., air or water, in which it is to be used;
6. the temporal response of the system; and
7. the effects of temperature and pressure on the above characteristics.

The elements of radiometer characterization and calibration are outlined schematically in Figure 6.1. For any instrument to provide suitable data for SIMBIOS and Sea-viewing Wide Field-of-view Sensor (SeaWiFS) applications, the investigator must be certain that the instrument characterization has not changed beyond accepted limits and that the time history of the calibration is traceable. Certain attributes, such as a sensor's angular response characteristics, are sufficiently constant that they only need to be determined once, unless the instrument is modified. The exact nature of instrument modifications during maintenance will determine which characterization procedures must be repeated. When practical, on the other hand, radiometric calibrations and the assessment of system spectral characteristics of filter radiometers should be repeated before and after each major field deployment.

6.2 RADIOMETRIC RESPONSIVITY CALIBRATION

Determination of the absolute radiometric responses of the irradiance and radiance sensors requires the availability of a properly manned and equipped radiometric calibration facility. Such a facility must be equipped with suitable stable sources and radiometric scale transfer sensors, *e.g.*, lamp standards of spectral irradiance and NIST calibrated transfer radiometers, respectively. The sources and transfer sensors must have defined spectral radiometric characteristics that are traceable to NIST. The calibration facility must also have a variety of specialized radiometric and electronic equipment, including: reflectance plaques, spectral filters, integrating spheres, and highly regulated power supplies for the operation of the lamps. Precision electronic measurement capabilities are also required, both for setting and monitoring lamp current and voltage and for measuring the output of the radiometer.

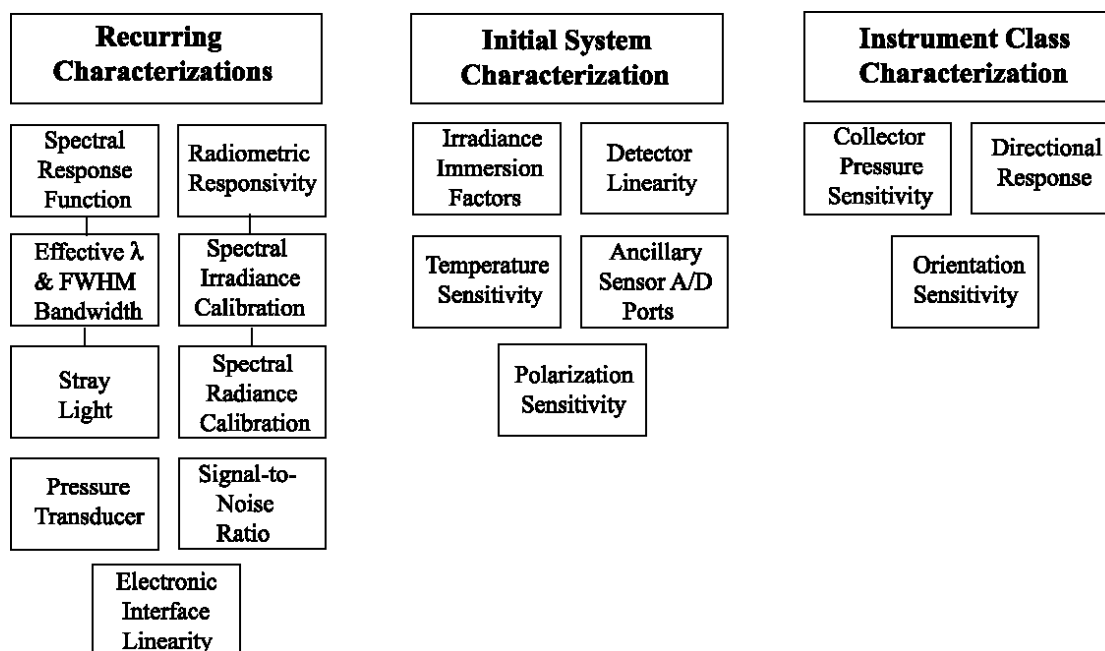


Figure 6.1: Elements of radiometer characterization and calibration.

It is not expected that every investigator will be able to independently perform radiometric calibrations. Instrument manufacturers and a few university laboratories are equipped and staffed to perform these calibrations for the ocean color research community. These facilities will perform frequent intercomparisons to assure the maintenance of the radiometric traceability to the NIST standard of spectral irradiance. The goal shall be to provide reproducible calibrations from 400 nm to 850 nm with 1 % uncertainty; the minimum requirement for radiometric data to be used in satellite ocean color sensor validation is for repeatable calibrations within less than 5 % (Chapter 1).

This section describes sources and methods by which the NIST scale of spectral irradiance is transferred to calibrate irradiance and radiance sensors. The principal working standards used for spectral irradiance responsivity calibrations are FEL-type lamps⁴ having assigned scales of spectral irradiance that have been transferred directly, or indirectly via secondary standards, from the scales of radiometric standards maintained by NIST. The spectral irradiance scales of the FEL lamps are in turn transferred to spectral radiance scales using plaques of known bidirectional reflectance, or integrating spheres, or both. The SeaWiFS Project Office initiated a series of SeaWiFS Intercalibration Round-Robin Experiments (SIRREXs) to assure internal consistency between the laboratories that calibrate radiometers for SeaWiFS validation (Mueller 1993 and Mueller *et al.* 1994). In SIRREX-3 (Mueller *et al.* 1996) and -4 (Johnson *et al.* 1996), it was demonstrated that with properly maintained FEL lamp secondary and working standards,

⁴ “FEL” is a commercial lamp-type designator. The 1000 W FEL-type lamps used for spectral irradiance calibration are modified by welding on a special base, which has much larger terminals than are provided with the stock commercial bulbs (Walker *et al.* 1987). Following this modification, the spectral irradiance output of each lamp is scanned with a high-resolution monochromator, to assure that its spectrum is smooth and free from unwanted emission lines. Finally, the candidate calibration source lamp is “seasoned” by initially burning it for approximately 40-hours, using a highly regulated current source; its spectral irradiance output and lamp terminal voltage are carefully monitored. Lamps that do not achieve stable performance during the seasoning process are discarded. Several commercial vendors offer both seasoned FEL-type lamps, and seasoned lamps with a certified scale of spectral irradiance transferred from another FEL-type secondary standard lamp acquired directly from NIST.

thorough training of laboratory personnel in calibration procedures, and careful attention to measurement setups, it was possible to maintain an uncertainty level of < 2 % for spectral irradiance and < 3 % for spectral radiance calibrations.

The variety of instruments available for validation measurements makes it imperative that some common calibration traceability exists. Recognizing that it would be impractical to characterize and calibrate all oceanographic and airborne radiometers at GSFC, several remote calibration facilities were identified (instrument manufacturers and a few laboratories at academic and government institutions), and working standards and protocols used at these facilities may be traced directly to the NIST scale (Johnson *et al.* 1996). This organizational structure is shown schematically in Figure 6.2. Methods of standards intercomparison may include use of NIST calibrated filter radiometers to track and document the operation of each facility (radiometer wavelengths for this intercomparison will be determined). Round-robin calibration comparisons of a reference set of field instruments were implemented to benchmark the internal consistency of calibrations performed at the various facilities involved with calibrations throughout the ocean color community; the first of these (SIRREX-6) determined that the level of relative uncertainty between these laboratories is approximately 2 % (Riley and Bailey, 1998).

In 2001, the SIMBIOS Project initiated a new series of SIMBIOS Radiometric Intercomparison (SIMRIC) round-robin comparisons of radiometric calibrations among the participating laboratories. Rather than comparing laboratory calibrations of radiance and irradiance sensors designed for field use, as in SIRREX-6, the SeaWiFS Transfer Radiometer SXR-II was used to compare the radiance scales of the calibration sources at the various laboratories (G. Meister, personal comm.). The SeaWiFS Transfer Radiometers, SXR and SXR-II, were built, and their calibrations are maintained directly, by NIST (Johnson *et al.* 1998). The SXR-II measures radiance in 6 wavelength-bands between 411 nm and 777 nm consistent with the SeaWiFS band (Table 5.1 of Chapter 5). Its angular Field of View (FOV) is approximately 2° Full-Width at Half-Maximum (FWHM) response. The SIMRIC-1 comparison procedure was to position the SXR-II to view the plaque, or sphere, radiance source(s) at each laboratory, and the instrument's calibrated response in each band was compared to the radiance scale at that wavelength interval as provided by the host laboratory; laboratory and SXR scales agreed within approximately 2 % for most wavelength bands (G. Meister, personal comm.).

Spectral Irradiance Calibrations

Radiometric calibrations of irradiance sensors will be performed after it has been ascertained that: the conformity of the sensor angular response to the required cosine function is satisfactory, the sensor linearity is satisfactory, and the spectral sensitivity, including out-of-band stray-light blocking, is known and satisfactory.

The options available for radiometric calibration standards are limited to standard sources or standard detectors. The FEL-type lamp standard of spectral irradiance is traditionally used for radiometric calibration, mainly because of its ease of use, compared to the spectral radiance lamp. FEL-type lamp standards of spectral irradiance are provided by NIST, and FEL-type lamp secondary standards, with NIST-traceable spectral irradiance scales, are available from various commercial standardizing laboratories and manufacturers. The uncertainty cited by NIST for these standards is, at best, 1 % in the visible and 2 % is a more realistic estimate of absolute uncertainty attainable using lamp standards alone. Over the calibration range from 250 nm to 2,500 nm, the uncertainty is approximately 6 % at the endpoints. NIST has published guidelines for the setup, alignment, and use of these standards (Walker *et al.* 1987). The vendors who manufacture and calibrate these lamps also issue guidelines for their use.

The irradiance calibration procedure (Walker *et al.*, 1987; Johnson, *et al.* 1996) may be summarized as follows:

- The irradiance sensor and a suitable lamp fixture for the FEL-type lamp standard are mounted on an optical bench. The lamp-sensor space shall be appropriately baffled and draped so that occulting the direct path between lamp and sensor will result in a response of less than 0.1 % of the response to the lamp flux.

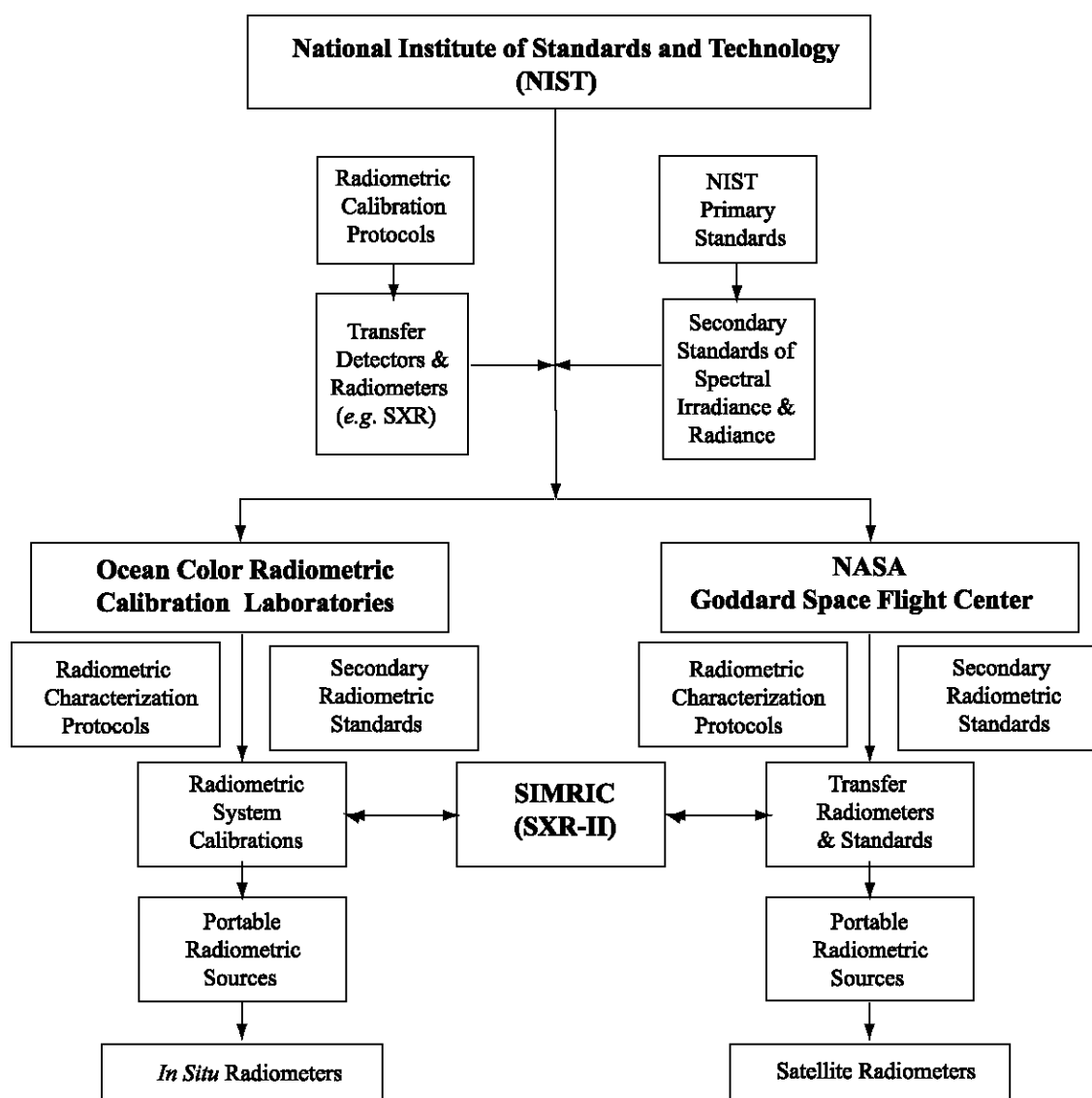


Figure 6.2: Organizational structure for radiometric instrument characterization and calibration within the SeaWiFS and SIMBIOS ocean color research community.

- An alignment reference target, having a window with cross hairs etched to mark the location of the lamp filament, is mounted in the lamp holder.
- An alignment LASER beam is directed normal to the target window; this alignment is achieved when the reflection from the window is directed back on the LASER aperture.
- The sensor is mounted on the optical bench with the irradiance collector centered on the alignment LASER beam, which marks the optical axis. The collector is aligned normal to the beam, using a mirror held flat against the collector to reflect the beam back through the lamp-target cross hairs to the LASER aperture.
- The FEL-type lamp spectral irradiance working standard is inserted into the lamp-holder, with its identification tag facing the sensor. The lamp terminals are connected to a current-regulated, direct current power supply, with careful attention to ensure proper polarity (as

marked on the lamp). The power supply is turned on and ramped-up to the proper current for the particular lamp (given with the lamp calibration certificate). A shunt and 4.5 digit voltmeter should be used to monitor lamp current to the nearest 0.001 A. Following a 15 min warm-up, irradiance calibration measurements may be taken. The voltage present across the lamp terminals should be measured at frequent intervals during a calibration run, and compared to the voltage measured when the lamp was calibrated. A significant change in the lamp's operating voltage (at the specified current) indicates that the irradiance output of the lamp has probably changed also, and that the lamp is no longer usable as a working standard of spectral irradiance.

- The distance r along the optical path between the collector surface and the lamp is measured to the front surface of the lamp's terminal post. The standard reference distance for all NIST traceable FEL-type lamp scales of spectral irradiance is $r = 50.0$ cm. When an irradiance sensor saturates when illuminated at a lamp distance of 50 cm, it will be necessary to reduce the irradiance level by increasing r , with the adjusted irradiance scale $E_r(\lambda)$ determined as

$$E_r(\lambda) = E_{50}(\lambda) \left[\frac{50}{r} \right]^2, \mu\text{W cm}^{-2}\text{nm}^{-1}, \quad (6.1)$$

where $E_r(\lambda)$ is the certified NIST-traceable scale of spectral irradiance at $r = 50.0$ cm.

- The irradiance sensors responses $V_r(\lambda)$ are recorded, usually as digital counts in modern practice, and the sensor's irradiance responsivity calibration factors (in air) are determined as

$$F_E(\lambda) = \frac{E_r(\lambda)}{V_r(\lambda)}, \mu\text{W cm}^{-2}\text{nm}^{-1} [\text{digital count}]^{-1}, \quad (6.2)$$

and applied to subsequent radiometric measurements as

$$E(\lambda) = F_E(\lambda) V(\lambda), \mu\text{W cm}^{-2}\text{nm}^{-1}. \quad (6.3)$$

Spectral Radiance Calibrations

Radiance calibration activities require a uniform, *i.e.* a Lambertian, source of known radiance that will fill the angular field of view of the radiance sensor. The two procedures that are most frequently used to calibrate ocean color radiance sensors are given below.

1. *Reflectance Plaque Radiance Calibrations:* An FEL-type lamp working standard of spectral irradiance is used, at a known distance r , to illuminate a plaque of near-Lambertian reflectance, with a known bidirectional reflectance distribution function (BRDF) $\rho(\lambda, \theta_o, \theta)$; the BRDF for plaques used in this procedure are most frequently calibrated for normal illumination, *i.e.* $\theta_o = 0$, and a viewing angle $\theta = 45^\circ$. For this geometry, the setup is identical to that described above for spectral irradiance calibration, with the reflectance plaque substituted for the irradiance collector. The procedure (see also Johnson et al. 1996) may be summarized as follows:

- The standard lamp is positioned on axis and normal to the center of the plaque at distance r . To assure uniform illumination across the surface of the plaque, r must typically be greater than 1.5 m, and for wide FOV instruments as large as 3 m.
- The radiance sensor is positioned to view the plaque at an angle $\theta = 45^\circ$, measured from the plaque normal (any other angle at which the diffuse reflectance of the plaque is known is acceptable also). It must be established that the plaque fills the sensor's FOV and that the presence of the sensor case has not perturbed the irradiance on the plaque.
- The radiance reflected by the plaque and viewed by the sensor in this geometry is determined as

$$L(\lambda) = \frac{1}{\pi} \rho(\lambda, 0^\circ, 45^\circ) E(\lambda), \quad (6.4)$$

where the spectral irradiance $E_r(\lambda)$ is calculated using Equation (6.1).

- The responses $V_r(\lambda)$ of the radiance sensor are recorded.
2. *Integrating Sphere Radiance Calibrations:* An alternative approach to calibrating multispectral radiance sensors is to view an integrating sphere that is uniformly illuminated by stable, appropriately baffled lamps, and that also has an exit port large enough to completely fill the sensor's FOV. The sphere and exit port must be large enough to place the radiance sensor far enough away to prevent significant secondary illumination of the sphere walls due to reflections off the sensor's entrance optics; if the sensor is too close, the reflected light will both increase and distort the uniformity of the radiance distribution within the sphere. The spectral radiance scale of an integrating sphere source may be transferred from the spectral irradiance scale of an FEL-type lamp standard, and then used to calibrate radiance sensors for field measurements, using the following procedure (Johnson *et al.* 1996):
- An irradiance scale transfer radiometer, configured with an integrating sphere having a circular entrance aperture of radius r_2 as its cosine collector, is calibrated using a FEL-type standard of spectral irradiance by the method outlined above under “*Spectral Irradiance Calibrations*”.
 - The irradiance scale transfer radiometer is positioned with the entrance aperture of its integrating sphere collector parallel to and centered coaxially at a distance d from the circular aperture, with radius r_1 , of the integrating sphere source.
 - The spectral irradiance $E(\lambda, d, r_1, r_2)$ of the integrating sphere source's exit port is measured using the irradiance scale transfer radiometer.
 - Assuming a uniform radiance distribution within the sphere's exit port, the spectral irradiance scale of the integrating sphere is calculated as (Johnson *et al.* 1995)

$$L(\lambda) = \frac{E(\lambda, d, r_1, r_2) [d^2 + r_1^2 + r_2^2]}{\pi r_1^2} [1 + \delta + \delta^2 + \dots], \quad (6.5)$$

where $\delta = r_1^2 r_2^2 (d^2 + r_1^2 + r_2^2)^{-2}$

- The radiance sensor to be calibrated is substituted for the transfer radiometer, and views the center of the source aperture. Its responses $V_r(\lambda)$ are recorded.

In either approach, the radiance responsivity calibration coefficients of the field radiometer are determined as

$$F_L(\lambda) = \frac{L(\lambda)}{V_r(\lambda)}, \mu\text{W cm}^{-2} \text{nm}^{-1} \text{sr}^{-1} [\text{digital count}]^{-1}, \quad (6.6)$$

and applied to derive radiance from field measurements $V(\lambda)$ as

$$L(\lambda) = F_L(\lambda) V(\lambda), \mu\text{W cm}^{-2} \text{nm}^{-1} \text{sr}^{-1}. \quad (6.7)$$

6.3 PORTABLE STANDARDS

The portable irradiance and radiance reference standard to be used to trace instrument stability during field deployments (Chapter 8) should be placed in position on the sensor immediately following the calibration to establish the instrument response to this reference unit. In the field, an instrument should be connected to the portable standard and its response recorded daily, keeping a record of instrument responsivity throughout an experiment. These comparison records provide an essential warning of problems, if they appear.

6.4 SPECTRAL BANDPASS CHARACTERIZATION

Oceanographic radiometers should be characterized to define the nominal wavelengths and bandwidths, defined as the full width of the passband as measured to the FWHM intensity points. The nominal, or center wavelength, will usually be defined as the wavelength halfway between wavelengths at which the normalized response is 0.5, and the channel is characterized by this wavelength and the FWHM bandwidth. The determination of the spectral response function, *i.e.* the passband, will be made for each channel with a scanning monochromatic source, with a bandwidth less than 0.2 nm; the source output must be normalized to a detector of known spectral sensitivity. The response function thus measured is then normalized to the maximum (peak).

Although the results of this characterization are usually represented by only the nominal wavelength and FWHM bandpass, the complete normalized response function should be recorded for use in detailed wavelength adjustments and comparisons with the SeaWiFS and other sensor channel response functions, which must be characterized before launch. It is further recommended that the internal instrument temperature be monitored during these tests, and that the test be repeated at two temperatures at least 15° C apart, *e.g.*, 10° and 25° C. If a significant shift, greater than 1.0 nm, with temperature of either the center wavelength or bandwidth is detected, then additional temperature calibration points are recommended. Dark offsets must be recorded during each test.

For spectral characterizations of irradiance diffusers, the entire surface of the diffuser should be illuminated by the monochromator's output. In the case of radiance detectors, a diffuser should be used to diffuse the monochromator slit image and uniformly fill the instrument's FOV.

The wavelength response of a monochromator-based radiometer is calibrated by scanning over line sources, with sharp peaks at well-known wavelengths. Suitable spectral calibration sources, such as, mercury, cadmium, and neon lamps, are provided by several vendors, together with tabulations of the wavelengths of the emission lines generated by each source.

The width of the slit function of a monochromator may be estimated by scanning over a laser line, *e.g.* helium-neon, at a very small wavelength interval. The instrument FOV must be filled during the test.

It is anticipated that the monochromator-based spectral characterization will not be able to adequately measure leakage of broadly distributed out-of-band radiation; therefore, blocking of blue light in channels longer than 540 nm must be routinely tested. Where continuous wave (CW) argon lasers are available, out-of-band response should be measured at 488 nm. One recommended test that can be performed during the absolute calibrations at $\lambda \leq 640$ nm is the sequenced measurement of three Schott BG-18 filters, each 1 mm thick, using a FEL-type light source. The procedure is to measure the channel signal using each filter separately, then in combination, and comparing the computed and measured transmissions. If a significantly higher combined transmission of the three filters, when they are used in combination, is measured relative to the calculated transmittance, then spectral leakage is present. At wavelengths greater than 640 nm, other filters that attenuate the wavelength of interest, with a transmission value of less than or equal to 0.1 and which pass shorter wavelength light with significantly greater transmission, should be substituted for the BG-18.

Consideration must also be given to unblocked fluorescence by the filters, or other optical elements, as a possible source of light leaks. Methods to test for fluorescence contamination specifically are not well established at this time.

While leakage of blue light into red channels is the most significant oceanographic optical problem, the leakage of red and IR light into blue channels can cause significant errors when the instrument is calibrated using a red-rich source. A convenient way to measure this leakage is to place a long wavelength-pass, sharp-cut, absorbing glass filter that does not exhibit fluorescence between a broadband (*e.g.*, incandescent) source and the sensor. A non-zero response indicates unwanted out-of-band red response and the need for improved red blocking.

Spectral Stray Light Characterization Using LASER-Illuminated Integrating Sphere Sources

Scientists at NIST have recently developed tunable, monochromatic sources that enable the characterization of a sensor's spectral responsivity, at the $<10^{-6}$ level, to illumination at wavelengths far outside its primary bandpass. This new NIST facility, named Spectral Irradiance and Radiance responsivity Calibrations with Uniform Sources (SIRCUS), is based on integrating sphere sources illuminated by LASERs; an ensemble of tunable and fixed frequency LASERs are utilized to cover the full spectral range of interest (Brown, Eppeldauer, and Lykke 2000). Very small exit apertures are used to provide sources of monochromatic irradiance, and large exit apertures are used as sources of monochromatic radiance, as appropriate to uniformly fill a particular sensor's entrance pupil. The source's absolute scale of spectral irradiance (radiance) at each monochromatic wavelength setting is transferred from the scale of a transfer radiometer calibrated, in turn, with a NIST primary standard. Thus, when the sensor under test views the source, its response is used to determine its absolute spectral irradiance (radiance) responsivity to the source wavelength at the sensor's nominal wavelength of interest. The absolute response function determination, using SIRCUS to provide monochromatic illumination scanned over the full spectral range of interest (*e.g.* 350 nm to 1000 nm) while the sensor's responses are recorded at all of its resolved wavelengths of interest, provides the information necessary for spectral stray light corrections with very low (albeit yet to be determined) uncertainty levels. Initial work to characterize the stray light responsivity functions of the spectrographs used to measure downwelled spectral irradiance and upwelled spectral radiance on the Marine Optical Buoy (MOBY), and more details about SIRCUS and its applications, are described in Chapter 11 and references cited therein.

6.5 IMMERSION FACTORS

Irradiance Sensor Immersion Factors

When a plastic, opal-glass, or Teflon diffuser is immersed in water, its light transmissivity is less than it was in air. Since an instrument's irradiance responsivity is calibrated in air, a correction for this change in collector transmissivity must be applied to obtain irradiance responsivity coefficients for underwater measurements.

The change in a collector's immersed transmissivity is the net effect of two separate processes: a change in the reflection of light at the upper surface of the collector, and internal scattering and reflections from the collector's lower surface. A small part of the light flux falling on the collector is reflected at the air-plastic, or water-plastic, interface, and the majority of the flux passes into the collector body. The relative size of this reflectance, called *Fresnel reflectance*, depends on the relative difference in refractive indices between the diffuser material and the surrounding medium.

The refractive index of the collector material is always larger than that of either water or air, and because the refractive index of water is larger than that of air, Fresnel reflectance is smaller at a diffuser-water interface than at a diffuser-air interface. Therefore, the initial transmission of light through the upper surface of an irradiance collector is larger in water than in air. The immersed upper surface is, on the other hand, also less effective at reflecting the upward flux of light backscattered within the diffuser body and light reflected at the lower diffuser-air interface in the instrument's interior, processes that are not affected by immersion. Therefore, a larger fraction of the internally scattered and upwardly reflected light passes back into the water column than would be lost into air. Because the increased upward loss of internally reflected flux exceeds the gain in downward flux through the diffuser-water interface, the net effect of these competing processes is a decrease in the collector's immersed transmissivity.

Experience has shown that the immersion factors for an irradiance collector must be experimentally characterized in the laboratory. Some manufacturers perform this characterization procedure only for a prototype of a particular collector design and material specification. They sometimes then provide only these nominal immersion factors for all production radiometers using that collector design. Mueller (1995) applied the characterization procedure described below to determine irradiance immersion factors for 11 radiometers having cosine collectors of the same design and material. The measurements were replicated 2 to 4 times for each radiometer, using independent setups on different days and varying the lamp-to-collector distance between replications, to determine that Type A uncertainty associated with the

experimental procedure is less than 1 %. On the other hand, root-mean-square differences between immersion factors in this group of irradiance sensors ranged from 3 % to 5 %, at different wavelengths, and differences between individual collectors were as large as 10 % at some wavelengths.

To measure this effect, a suggested and acceptable procedure (Petzold and Austin 1988) is as follows:

1. The instrument is placed in a tank of water with the irradiance collector level and facing upward.
2. A tungsten-halogen lamp with a small filament, powered by a stable power supply, is placed at a carefully measured distance above the surface of the irradiance collector. An initial reading is taken in air, before the water level in the tank is raised above the dry collector.
3. The water is raised initially to a carefully measured depth z above the collector surface and readings are recorded for all wavelengths.
4. The water level is then increased stepwise in, *e.g.*, 5 cm increments, and the instrument responses are measured and recorded for each depth z . A maximum water depth of 40 cm to 50 cm is normally adequate to obtain data covering a sufficient range of responses.
5. The water level is then lowered, and data recorded, over a similar series of incremental depths.
6. A final reading is taken with the water level below the collector, after drying the collector. It is recommended to then change and remeasure the lamp-to-collector distance d , and repeat the entire procedure to verify that a Type A experimental uncertainty less than 1 % has been achieved.

A minimum water depth of 5 cm is recommended to avoid artifacts due to multiple reflections between the collector and water surfaces. These reflections would otherwise artificially increase the transmitted flux, and therefore, decrease the apparent immersion effect. The magnitude of this artifact will increase with decreased depth z below some critical limit, which is the order of the diameter of the collector. With very small diameter collectors, it may be possible to acquire good immersion effect data at values of $z < 5$ cm, but the absence of this artifact should be demonstrated experimentally if this is done.

The amount of energy arriving at the collector varies with the water depth and is a function of several factors:

1. the attenuation at the air-water interface, which varies with wavelength;
2. the attenuation over the water pathlength, which is a function of depth and wavelength; and
3. the change in solid angle of the light leaving the source and arriving at the collector, caused by the light rays changing direction at the air-water interface, which varies with wavelength and water depth.

Using Fresnel reflectance equations, the transmittance through the surface is

$$T_s(\lambda) = \frac{4n_w(\lambda)}{[1 + n_w(\lambda)]^2}, \quad (6.8)$$

where $n_w(\lambda)$ is the index of refraction of the water at wavelength λ . The transmittance through the water path is given by

$$T_w(\lambda) = e^{-K(\lambda)z}, \quad (6.9)$$

where $K(\lambda)$ is the attenuation coefficient of the water and z is the path length in corresponding units.

The change with water depth z of the refracted solid angle subtended by the collector, as viewed from the lamp filament, is given by the factor

$$G(z, \lambda) = \left[1 - \frac{z}{d} \left(1 - \frac{1}{n_w(\lambda)} \right) \right]^{-2}, \quad (6.10)$$

where d is the distance of the lamp source from the collector surface.

The immersion correction factor $F_i(\lambda)$ for irradiance is then calculated for each depth z as

$$F_i(\lambda) = \frac{E_a(\lambda)}{E_w(\lambda, z)} T_s(\lambda) T_w(\lambda) G(z, \lambda), \quad (6.11)$$

where $E_a(\lambda)$ and $E_w(\lambda, z)$ are the irradiance in air and the irradiance underwater at depth z , respectively.

There are two unknowns in (6.8)-(6.11): the attenuation coefficient of the water $K(\lambda)$ and the immersion factor $F_i(\lambda)$. A minimum of three measurements must be made to solve for $F_i(\lambda)$ and $K(\lambda)$: one in air to get $E_a(\lambda)$, and two at different water depths for $E_w(\lambda, z)$. The recommended method is to take readings of $E_w(\lambda, z)$ at many water depths. If (6.9) is substituted into (6.11), and the result is log transformed and rearranged, each measurement $E_w(\lambda, z)$ and depth z may be expressed as

$$\ln \left[\frac{E_a(\lambda)}{E_w(\lambda, z)} T_s(\lambda) G(z, \lambda) \right] = \ln [F_i(\lambda)] + K(\lambda) z. \quad (6.12)$$

The unknown slope $K(\lambda)$, and intercept $\ln[F_i(\lambda)]$, are then determined by a linear least-squares regression analysis. The complete derivation of (6.8) – 6.11) is given in Petzold and Austin (1988).

Radiance Immersion Factors

The absolute calibration for the spectral radiance channels is found by viewing a surface of known radiance in air in the laboratory. When the instrument is submerged in water, a change in responsivity occurs and a correction must be applied. This change in responsivity is caused by the change in the indices of refraction of the different media in which the instrument is immersed--in this case air and water. Two optical changes occur, both of which are caused by the change in refractive index. The two effects to be corrected are:

1. the change in transmission through the interface between the air and the window during calibration, and the same effect through the water-window interface during data measurement, and
2. the change in the solid angle included in the underwater FOV relative to that in air.

Since $n_w(\lambda)$ is a function of wavelength, the correction factor $F_i(\lambda)$ is also a function of wavelength. If the refractive index of air is assumed to be 1.000 at all wavelengths, and if $n_g(\lambda)$ is the index of refraction for the (glass) window, the correction for the change in transmission through the window, $T_g(\lambda)$, is (Austin 1976)

$$T_g(\lambda) = \frac{[n_w(\lambda) + n_g(\lambda)]^2}{n_w(\lambda)[1 + n_g(\lambda)]^2}, \quad (6.13)$$

and the correction for the change in the FOV is

$$F_v(\lambda) = [n_w(\lambda)]^2. \quad (6.14)$$

The index of refraction of a PlexiglasTM window, $n_g(\lambda)$, may be computed, using an empirical fit to the Hartmann formula, as

$$n_g(\lambda) = 1.47384 + \frac{7.5}{\lambda - 174.71}, \quad (6.15)$$

where λ is the wavelength in nanometers (Austin 1976). The refractive indices of other window materials must be obtained from the manufacturer.

The index of refraction for seawater $n_w(\lambda)$ may be similarly computed, using an empirical fit of the data from Austin and Halikas (1976), as

$$n_w(\lambda) = 1.325147 + \frac{6.6096}{\lambda - 137.1924}. \quad (6.16)$$

Finally, the immersion factor $F_i(\lambda)$ for a radiance sensor is obtained as

$$F_i(\lambda) = T_g(\lambda) F_v(\lambda), \quad (6.17)$$

or by substitution from (6.13) and (6.14), in expanded form as

$$F_i(\lambda) = \frac{n_w(\lambda) [n_w(\lambda) + n_g(\lambda)]^2}{[1 + n_g(\lambda)]^2}. \quad (6.18)$$

6.5 RADIANCE FIELD-OF-VIEW

It is required that the radiance FOV of the instrument be known. The FOV should not normally enter into the absolute calibration, however, if the FOV is fully filled by a calibration source of uniform radiance.

In this test, the instrument is placed on a rotational stage with the entrance aperture of the radiometer over the rotation axis. A stable light source with a small filament is placed several meters in front of the instrument, which is then scanned from -30° to $+30^\circ$ in 2° increments. The uncertainty in angle positioning should be $\leq 0.1^\circ$. The on axis, *i.e.* 0° , mechanical alignment is made using the window surface as reference, by adjusting to get the reflection of the lamp filament to return on axis. The uncertainty in this alignment is approximately 0.1° . The in-air measurement angles θ_a are converted to

corresponding angles θ_w in seawater using the relation $\theta_w = \frac{\theta_a}{n_w(\lambda)}$, where $n_w(\lambda)$ is given by Equation (6.16).

6.6 COLLECTOR COSINE RESPONSE

The directional response of cosine collectors must be characterized. The directional response of the deck cell is determined in air, and those of the in-water instruments are measured immersed in water. Full spectral determinations are required. For instruments measuring upwelling irradiance $E_u(z, \lambda)$ it is recommended that the cosine response of each instrument be measured individually. For downwelling irradiance $E_d(z, \lambda)$ instruments, checking a production run may be satisfactory if the vendor's material and design are demonstrated to be uniform throughout the duration of the run. Given the variations observed in immersion factors of collectors of the same design and materials (Mueller 1995), however, this possibility should be accepted only with caution. Whenever possible, it is strongly recommended that the cosine response of irradiance collectors be characterized individually.

Absolute responsivity calibration of an irradiance meter is done in air, using light incident normal to the collector. To properly measure irradiance incident on the plane at all angles θ (relative to the normal), the instrument's response should follow a cosine function. In other words, for an instrument response $V(\lambda, 0)$ to a given collimated irradiance incident at $\theta = 0^\circ$, if the instrument is rotated to the angle θ away from the original normal axis, the response should be $V(\lambda, \theta) = V(\lambda, 0) \cos \theta$. If this criterion is met, then the on-axis calibration is sufficient and the device will correctly measure irradiance arriving at the plane of the collector, regardless of the directional distribution at which the light arrives.

The preferred in-water irradiance collector design has an improved cosine response over that of a simple flat plate diffuse collector (Boyd 1955 and Tyler and Smith 1979). This improvement is mostly for near-grazing angles (θ approaching 90° to the normal) and is particularly important when measurements of the upwelling underwater irradiance are made, *i.e.*, with the collector facing downward. In that case, most of the light is incident from the sides, *i.e.* in the region of these near-grazing angles.

Since $E_d(z, \lambda)$ and $E_u(z, \lambda)$ measurements are made underwater, the tests to determine the fidelity with which the instruments directional response follows the cosine function must be made with the instrument submerged. A description of the suitable experimental procedure follows (Petzold and Austin 1988).

The instrument is suspended in a tank of water while supported by a fixture designed to allow rotation about an axis through the surface and center of the collector. A tungsten-halogen lamp with a small filament is enclosed in a housing with a small exit aperture and placed approximately 1 m from a large window in the tank. The collector is placed approximately 25 cm behind this window. A circular baffle should be placed immediately in front of the window to reduce stray light. The water should be highly filtered to the extent that the effects of scattered light are indiscernible.

The equivalent air path lamp-to-collector distance should be approximately 1.25 m or greater. At this distance, the fall-off at the outer edge of a 6 cm diameter diffuse collector would be 0.9994, or -0.06 %, when the diffuser is at $\theta = 0^\circ$ with the normal. The net effect over the entire area of the diffuser would be 0.9997 or -0.03 %. When $\theta = 90^\circ$, with the diffuser edge-on to the lamp, the distance to the lamp varies for different points on the surface. The net error over the entire surface for this condition is 0.99997 or -0.003 %. All other angles fall between these limiting cases.

The $\theta = 0^\circ$ alignment should place the center of the collector on the axis of illumination, with the collector surface oriented normal to the axis. One method of effecting this alignment is to pass a laser (or autocollimator) beam through the location of the filament to the center of the collector. The collector is rotated until a mirror held flat against it reflects the laser (or autocollimator) beam back on itself. The rotational indexing scale should be zeroed in this position. With the alignment laser (or autocollimator) still in place, the collector should be slowly rotated to the $\theta = 90^\circ$; the beam should just graze the collector at $\theta = 90^\circ$ and remain in the center of the collector at the intermediate angles. The alignment and rotational apparatus should be adjusted until these angular alignment criteria are satisfied. Note that success in this alignment procedure also depends on orienting the illumination axis normal to the tank's window.

The instrument responses $V(\lambda, 0)$ are initially recorded for $\theta = 0^\circ$. The instrument alignment is rotated at 5° intervals to $\theta = 90^\circ$, and the instrument responses $V(\lambda, \theta)$ measured for each alignment angle. The $V(\lambda, 0)$ responses are recorded at the beginning, the middle, and the end of each run and examined as a measure of lamp and instrument stability over the time involved. If the angular indexing mechanism allows rotation in either direction, the procedure should then be repeated in the $-\theta$ direction to complete the characterization of directional response in one plane perpendicular to the collector surface. If the apparatus allows rotation in only one direction, then the instrument should be rotated about the optical axis (normal to the collector), and the procedure repeated to complete the plane. At least two sets of such runs should be made about different axes through the surface of the diffuser. The directional response of the instrument (for each azimuth scanned) is expressed as $\frac{V(\lambda, \theta)}{V(\lambda, 0)}$, which should ideally equal $\cos \theta$. The angular

distribution of relative error in a radiometer's cosine-response is, therefore, $\frac{V(\lambda, \theta)}{V(\lambda, 0) \cos \theta} - 1$.

Assuming the average response to the four measurements made at each θ_i (four separate azimuth angles about the normal to the collector) adequately represent the overall mean cosine response of the collector, then the error, ϵ in measuring irradiance for a uniform radiance distribution is approximately

$$\epsilon = \frac{\sum_{i=0}^N \bar{V}(\theta_i) \sin \theta_i \Delta \theta}{\sum_{i=0}^N \cos \theta_i \sin \theta_i \Delta \theta} - 1, \quad \theta_0 = 0, \quad \theta_N = \frac{\pi}{2} \quad \text{and} \quad \Delta \theta = \frac{\pi}{2N}, \quad (6.19)$$

using a simple trapezoidal quadrature. Similarly, for a radiance distribution of the form $1 + 4 \sin \theta$, to simulate upwelled irradiance, the approximate error is

$$\varepsilon = \frac{\sum_{i=0}^N \bar{V}(\theta_i)(1 + 4 \sin \theta_i) \sin \theta_i \Delta \theta}{\sum_{i=0}^N \cos \theta_i (1 + 4 \sin \theta_i) \sin \theta_i \Delta \theta} - 1, \quad \theta_0 = 0, \quad \theta_N = \frac{\pi}{2} \quad \text{and} \quad \Delta \theta = \frac{\pi}{2N}. \quad (6.20)$$

The asymmetry of the cosine response, δ is equivalent to an effective tilt of an ideal cosine collector with respect to the instrument's mechanical axis, which can be quantified as

$$\delta = \frac{\int_{\theta_i}^{\theta_2} \cos(\theta + \theta_i) \sin \theta d\theta}{\int_{\theta_i}^{\theta_2} \cos(\theta - \theta_i) \sin \theta d\theta}, \quad (6.21)$$

where θ_i is the tilt angle.

The measured asymmetry is computed as the ratio of sums of measurements at opposite azimuth angles $\phi(\theta \geq 0)$ and $-\pi(\theta < 0)$ in the same plane, that is,

$$\delta = \frac{\sum_{i=0}^N \bar{V}(\theta_i, 0) \sin \theta_i \Delta \theta}{\sum_{i=0}^N \bar{V}(\theta_i) \sin \theta_i \Delta \theta} - 1, \quad \theta_0 = 0, \quad \theta_N = \frac{\pi}{2} \quad \text{and} \quad \Delta \theta = \frac{\pi}{2N}. \quad (6.22)$$

Variations in asymmetry from channel to channel may be due to the placement of the individual detectors behind the diffuser. Any offset of the average asymmetry with the mechanical axis could be due to any one of a variety of causes:

- the alignment on the rotating test fixture not being correct,
- tilt of the diffuser,
- the detector array not being centered,
- nonuniformity of the reflectance of the internal surfaces of the instrument between the diffuser and the sensor array, or
- nonuniformity of the diffuser.

6.7 LINEARITY AND ELECTRONIC UNCERTAINTY

The linearity of the radiometric channels must be determined over their expected range of use. The above-surface (deck cell) and underwater irradiance sensors intended for the measurement of downwelling irradiance have full-scale (saturation) values that are not readily obtained with the usual incandescent blackbody sources, such as 1000 W, 3200 K tungsten-halogen projection lamps. The linearity at the high end of the calibrated range may be determined by using 900 W to 2,000 W high pressure xenon arc lamps, which provide a small, stable source of high intensity (approximately 6000 K) radiation. With such lamps, irradiance levels approximating full sunlight can be attained. Using such sources for the high-end of the sensor's response range, and the more easily managed tungsten-halogen lamps over the range below 20 % to 30 % of full scale, the linearity of the response characteristic of the radiometric channels can be assessed. The flux should be changed in 5 db (0.5 log), or less, steps using a proven and accepted procedure for controlling irradiance such as inverse square law, or calibrated apertures. These suggested procedures for testing linearity at the higher levels are not well established in practice, and research is needed to determine the precision that can be attained.

If departures from linearity are found, they must be incorporated into the calibration function for the instrument and be properly applied to the raw data to obtain calibrated irradiance and radiance data.

It is recommended that all instruments utilizing inputs from ancillary sensors, e.g., transmissometers, be characterized for the linearity and uncertainty of the voltage measurement covering the full output range of the ancillary sensor. For instruments with range dependent gain changing, either manual or automatic, the scale offset and linearity for each range should, at a minimum, be tested annually. Uncertainties exceeding 0.1 % of any reading within the normal working range must be investigated and corrected.

Other characteristics of electronic sensor systems may adversely affect measurement uncertainty. During the design and engineering prototype development of a radiometer, the design and implementation must be analyzed to characterize, and correct as needed, possible effects of hysteresis, overload, recovery times, cross talk between either optical transducers or electronic channels, and sensitivity to orientation in the Earth's magnetic field, which is particularly likely with photomultiplier tubes.

6.8 TEMPORAL RESPONSE

The temporal response of a spectrometer may be examined by introducing a step function of near full-scale flux to the system using an electrically operated shutter and measuring the system's transient response at 0.1 s, or shorter, intervals. The response should be stable within one digitizing step, or 0.1 %, whichever is greater, of the steady state value in one second or less.

6.9 TEMPERATURE CHARACTERIZATION

Two major types of temperature-induced variation may be seen in an optical radiometric instrument: 1) offset or *dark* changes, and 2) scale *responsivity* changes. Each underwater instrument must be individually characterized over the range of -2°C to 40°C . In the case of deck cells, the temperature range for testing should be extended to 10°C to 45°C . Sensors exhibiting temperature coefficients greater than 0.01 % per $^{\circ}\text{C}$ over this temperature range, should be fully characterized over their respective ranges to establish the means and precision with which post-acquisition processing can be used to correct for temperature dependency. Although knowledge of the zero, or dark current, drift is essential for working at the lowest radiances or irradiances, it should be emphasized that more significant near-surface errors may be induced by temperature variations in responsivity.

These possible responsivity changes must be individually determined across the spectrum. In the above discussion, the temperatures cited are *environmental* temperatures, but it should be emphasized that any correction must use the temperature of the affected element, which is normally in the interior of the instrument. This is best accomplished by routinely using temperature sensors placed at critical locations within the instrument. For highest precision, dynamic temperature testing involving temporal transients, as well as possible temperature gradients within an instrument, may be appropriate.

6.10 PRESSURE EFFECTS

Pressure can cause radiometric measurement errors by deforming irradiance collectors. Pressure coefficients associated with polytetrafluoroethylene (PTFE) based irradiance diffusers are known to exist, but they are not uniform and there may be hysteresis effects. It is recommended that each type of irradiance detector be examined for variations in responsivity with pressure. If a significant effect is observed, then pressure-dependent responsivity coefficients should be determined separately for each instrument and collector. The pressure characterization should also test for, and quantify, hysteresis and temporal transients in responsivity under a time varying pressure load. The characterization of pressure effects has not previously been common practice, and the requisite procedures are therefore poorly defined; new protocols must be developed.

6.11 PRESSURE TRANSDUCER CALIBRATION

The radiometer's pressure transducer, which is used to measure instrument depth during profiles, should be tested and calibrated before and after each major cruise (Chapter 4, Sect. 4.10).

6.12 POLARIZATION SENSITIVITY

Polarization sensitivity is more critical in above-water radiometry than underwater radiometry. If a radiometer measures polarization components of radiance, then its responsivity and rejection of cross-polarization radiance must be characterized for each component channel. For above-water scalar radiance instruments, as with the SeaWiFS and other ocean color radiometers, sensitivity to linear polarization must be less than 2 %, and the actual degree of polarization sensitivity must be characterized for each channel. A protocol for characterizing the polarization sensitivity of a radiometer is described in Chapter 7 (Sect. 7.3).

REFERENCES

- Austin, R.W. and G. Halikas, 1976: The index of refraction of seawater. *SIO Ref. 76-1*, Vis. Lab., Scripps Inst. of Oceanography, La Jolla, California, 64pp.
- Brown, S.W., G.P. Eppeldauer and K.R. Lykke, 2000: NIST facility for spectral irradiance and radiance response calibrations with a uniform source. *Metrologia*, **37**: 579-589.
- Johnson, B.C., S.S. Bruce, E.A. Early, J.M. Houston, T.R. O'Brian, A. Thompson, S.B. Hooker and J.L. Mueller, 1996: The Fourth SeaWiFS Intercalibration Round-Robin Experiment (SIRREX-4), May 1995. *NASA Tech. Memo. 104566, Vol. 37*, S.B. Hooker, E.R. Firestone and J.G. Acker, Eds., NASA GSFC, Greenbelt, Maryland, 65 pp.
- Johnson, B. C., J.B. Fowler, and C.L. Cromer, 1998: The SeaWiFS Transfer Radiometer (SXR). *NASA Tech. Memo. 1998-206892, Vol. 1*, S.B. Hooker and E.R. Firestone, Eds., NASA Goddard Space Flight Center, Greenbelt, Maryland, 58 pp.
- McLean, J.T., and B.W. Guenther, 1989: Radiance calibration of spherical integrators. Optical Radiation Measurements II, *SPIE*, **1,109**,114--121.
- Mueller, J.L., 1993: The First SeaWiFS Intercalibration Round-robin Experiment SIRREX-1, July 1992. *NASA Tech. Memo. 104566, Vol. 14*, S.B. Hooker and E.R. Firestone, Eds., NASA Goddard Space Flight Center, Greenbelt, Maryland, 60 pp.
- Mueller, J.L., 1995: Comparison of irradiance immersion coefficients for several marine environmental radiometers (MERs), In: Mueller, J.L. and others, Case Studies for SeaWiFS Calibration and Validation, Part 3. *NASA TM 104566, Vol. 27*: 3-15, Hooker, S.B., E.R. Firestone and J.G. Acker, Eds.
- Mueller, J.L., B.C. Johnson, C.L. Cromer, J.W. Cooper et al. 1994: The Second SeaWiFS Intercalibration Round-robin Experiment SIRREX-2, June 1993. *NASA Tech. Memo. 104566, Vol. 16*, S.B. Hooker and E.R. Firestone, Eds., NASA Goddard Space Flight Center, Greenbelt, Maryland, 121 pp.
- Mueller, J.L., and R.W. Austin, 1995: Ocean Optics Protocols for SeaWiFS Validation, Revision 1. *NASA Tech. Memo. 104566, Vol. 25*, S.B. Hooker and E.R. Firestone, Eds., NASA Goddard Space Flight Center, Greenbelt, Maryland, 66 pp.
- Mueller, J.L., B.C. Johnson, C.L. Cromer, S.B. Hooker, J.T. McLean and S.F. Biggar, 1996: The Third SeaWiFS Intercalibration Round-Robin Experiment (SIRREX-3), 19-30 September 1994. *NASA Tech. Memo. 104566, Vol. 34*, S.B. Hooker, E.R. Firestone and J.G. Acker, Eds., 78 pp.
- Petzold T.J. & R.W. Austin 1988: Characterization of MER-1032. *Tech.Memo.EV-001-88t*, Vis.Lab.,Scripps Institution of Oceanography, La Jolla, California,56 pp.
- Riley, T. and S. Bailey, 1998: The Sixth SeaWiFS Intercalibration Round-Robin Experiment (SIRREX-6) August—December 1997. *NASA/TM-1998-206878*. NASA, Goddard Space Flight Center, Greenbelt, MD. 26pp.

- Walker, J.H., R.D. Saunders, J.K. Jackson, and D.A. McSparron, 1987: Spectral Irradiance Calibrations. NBS Special Publication 250--20, U.S. Dept. of Commerce, National Bureau of Standards, Washington, DC, 37 pp. plus appendices.
- Walker, J.H., C.L. Cromer, and J.T. McLean, 1991: Technique for improving the calibration of large-area sphere sources. *Ocean Optics*, B.W. Guenther, Ed., SPIE, **1,493**, 224-230

Chapter 7

Calibration of Sun Photometers and Sky Radiance Sensors

Christophe Pietras¹, Mark Miller², Kirk D. Knobelspiesse³, Robert Frouin⁴, Brent Holben⁵ and Ken Voss⁶

¹*Science Applications International Corporation, Beltsville, Maryland*

²*Department of Applied Science, Brookhaven National Laboratory, Upton, New York*

³*Science Systems and Applications, Inc., Greenbelt, Maryland*

⁴*Scripps Institution of Oceanography, University of California, San Diego, California*

⁵*Biospheric Sciences Branch, NASA Goddard Space Flight Center, Greenbelt, Maryland*

⁶*Physics Department, University of Miami, Florida*

7.1 INTRODUCTION

Atmospheric sensors are designed to measure direct solar signals and sky radiances in order to retrieve the radiative properties of the atmosphere. There are two major types of instruments in use to perform these measurements: sun photometers and sky radiance scanning systems including fast rotating shadow-band radiometers.

Sun photometers capture photometric intensity of the direct solar beam. Their fields of view are small, typically between 1° and 3°, in order to minimize contamination of the transmitted solar signal by scattered skylight. Some photometers are manually aimed at the sun using sun-sighting optics, while other types of photometers are fixed in place and are equipped with automatic sun-tracking mechanisms.

MicroTops II (Morys *et al.* 1998; Porter *et al.* 1999) and SIMBAD (Deschamps *et al.* 2000; Fougnie *et al.* 1999a, 1999b) are two examples of hand-held sun photometers. The fields of view (FOV) of hand-held sun photometers are typically between 2° and 3°, which is generally larger than the FOVs of the automatic sun-tracking photometers (Table 7.1). The wider FOV allows the user to manually aim the instrument at the sun from the rolling deck of a ship. The even wider field of view of SIMBAD (Table 7.1) is intended to measure marine reflectance as well as the solar signal. An improved version, called SIMBADA, has been recently developed and is available since 2001. SIMBADA new features are an integrated GPS and 11 channels.

Examples of fixed, automated tracking sun photometers include the CIMEL (Holben *et al.*, 1998) and the PREDE (Nakajima *et al.*, 1996). The design of a particular sun tracking mechanism is dependent on whether it is to be used on a moving platform (e.g., PREDE POM-01 Mark II), or on a stable station (e.g., CIMEL, PREDE POM-01L). CIMEL and PREDE instruments perform both sun photometric and sky radiance measurements. In sky radiance mode, these instruments measure sky radiances within 3° of the sun in the aureole, and also scan the sky radiance distribution in the principal solar plane. The FOV of the CIMEL and PREDE instruments are less than 1.5° and the instruments are equipped with collimators for stray light rejection (O'Neill *et al.*, 1984; Holben *et al.* 1998; Nakajima *et al.* 1996).

Fast rotating shadow-band radiometers measure solar intensity values indirectly from diffuse and global upper hemispheric irradiance. They have a 2 π FOV and are equipped with a solar occulting apparatus. Finally, electronic camera systems equipped with “fisheye” lenses may be used to measure the full sky radiance distribution (Voss *et al.* 1989).

Sun photometers and sky radiometers commonly have several channels from 300 nm to 1020 nm and narrow bandwidths (approximately 10 nm). Their characteristics are summarized in Table 7.1. This chapter will describe calibration techniques, and uncertainties of the sun photometers and sky radiometers. Measurement and data analysis protocols and procedures are discussed in Chapter 14.

7.2 CALIBRATION TECHNIQUES FOR SUN PHOTOMETERS

To calibrate sun photometers, it is necessary to take into account degradation of detectors and interference filters. The absolute calibration using lamp standards is generally not recommended for the retrieval of aerosol optical thickness (AOT). However, in case of a strong loss of sensitivity over time, Schmid *et al.* (1998) advised combining lamp calibration with solar calibration and discussed the applicability and accuracy of the method. The following subsections will present techniques commonly used with sun photometers and their validities.

Langley – Bouguer Technique

The signal measured by a sun photometer, assuming that the instrument is aimed directly into the sun and its spectral channels are not affected by gaseous absorption, may be expressed as

$$V(\lambda) = V_o(\lambda) \left(\frac{d_o}{d} \right)^2 e^{-M(\theta_o) [\tau_R(\lambda) + \tau_{O_3}(\lambda) + \tau_a(\lambda)]}, \quad (7.1)$$

where $V_o(\lambda)$ is the signal representing the instrument response to solar flux at the top of the atmosphere

(TOA) as derived from the Langley-Bouguer calibration procedure, $\left(\frac{d_o}{d} \right)^2$ is the earth-sun distance

correction obtained according to Iqbal (1983), θ_o is the solar zenith angle, air mass $M(\theta_o)$ is a function of the solar zenith angle computed according to Kasten and Young (1989), $\tau_R(\lambda)$ is the Rayleigh optical thickness calculated according to Penndorf (1957), $\tau_{O_3}(\lambda)$ is the ozone optical thickness calculated from the ozone amount retrieved from a satellite ozone sensor, such as Total Ozone Mapping Spectrometer (TOMS), and $\tau_a(\lambda)$ is the aerosol optical thickness.

The purpose of the Langley-Bouguer technique is to obtain the unknown instrument response to the solar flux at the top of the atmosphere, $V_o(\lambda)$. This is achieved by plotting the logarithm of the signal $V(\lambda)$ against the air mass $M(\theta_o)$, and extrapolating the signal to $M = 0$. The slope of the logarithmic signal is the total optical depth (Rayleigh, ozone and aerosol). The protocol is detailed below:

1. As $M(\theta_o)$ varies from 1 to 6 over the course of the day, take five successive measurements each time the air mass changes by 0.25.
2. Measure the dark current frequently to avoid temperature effects.
3. Record the sky condition in case of clouds or thin cirrus occurrences (includes cloud coverage and cloud positions in the sky).
4. Stop when M reaches 7, or the sky condition changes.

The main constraint in the Langley-Bouguer technique is the stability of the atmospheric optical extinction. Hence, the uncertainty greatly depends on the geographical location of the calibration experiment. The calibration is generally performed in conditions where the stability of the atmosphere and a low aerosol contribution enable high accuracy of the method (Holben *et al.* 1998; Schmid *et al.* 1998). The site of Mauna Loa Observatory (MLO), Hawaii, is particularly well suited for calibrating optical instruments. The facilities and research activities at the observatory are reported on its web site <http://mloserv.mlo.hawaii.gov/>. The altitude of the Mauna Loa site (3397 m) reduces the uncertainties due to variability in aerosols and water vapor, both of which commonly affect measurements in the lower atmospheric layers.

Variations in the atmosphere dramatically affect $V_o(\lambda)$ retrievals. Several improvements to the Langley-Bouguer technique have been proposed, such as using a calibrated reference channel (Soufflet *et al.* 1992) and the circumsolar radiation (Tanaka *et al.* 1986). A review of different methods and their uncertainties are discussed in Forgan, 1994.

Uncertainty of the Langley – Bouguer Technique

The Langley-Bouguer technique has been commonly used, although it is not an absolute calibration method and has large uncertainties. Combining several Langley-Bouguer sessions in high altitude conditions minimizes the uncertainties. AERONET reference instruments are typically recalibrated at MLO every 2-3 months using the Langley-Bouguer technique. According to Holben *et al.* (1998), the uncertainties in TOA voltages are estimated to be as low as 0.2 % to 0.5 % for the MLO calibrated instruments. Therefore, the uncertainty in AOT due to the ambiguities in TOA voltages for the reference instruments is better than 0.002 to 0.005 in absolute values.

Figure 7.1 presents typical Langley-Bouguer plot for CIMEL #101 at MLO (circles) and at GSFC (squares). The total optical thickness at MLO is nearly half that of GSFC. The maximum difference in AOTs derived from GSFC and MLO sites is 0.05 for the air mass of 1. Therefore, MLO is an attractive calibration site for this technique.

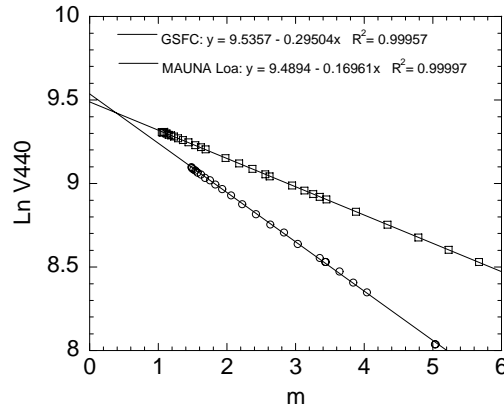


Figure 7.1: The Langley-Bouguer technique applied to CIMEL # 10 sun photometer measurements at 440nm. (o) - Mauna Loa Observatory, September 11, 1999, and () - GSFC, October 15, 1999.

In addition to the uncertainty in the retrieval of $V_o(\lambda)$, there are other sources of uncertainty in the Langley-Bouguer technique, including computations of the solar zenith angle, air mass, earth-sun distance and Rayleigh and ozone corrections:

1. **Solar zenith angle computation:** The solar position is retrieved using a simple algorithm based on codes from Michalsky (1988) and Spencer (1989), and *The Astronomical Almanac*. The uncertainty of the solar position calculated using this algorithm is 0.01° until the year 2050.
2. **Earth-sun distance correction:** The earth-sun distance correction $\left(\frac{d_o}{d}\right)^2$ is dependent on the ratio of the average to the actual earth-sun distance. It can be computed according to Iqbal (1983) as

$$\left(\frac{d_o}{d}\right)^2 = 1 + \left[0.034 \cos\left(\frac{2\pi J}{365}\right)\right], \quad (7.2)$$

where J is the sequential day of the year. This factor is sometimes computed using an alternative approximation due to Platriidge (1977). Differences between the two algorithms vary between 0 and 3%.

3. **Air mass computation.** The precise Langley-Bouguer technique requires taking into account the structure of atmospheric constituents that attenuate sunlight (Schotland *et al.* 1986; Forgan

1988). $M(\theta_o)$ can be computed according to Kasten (1966), or Kasten and Young (1989) [used here as Equation (14.3) in Chapter 14]. For solar zenith angles $\theta_o \leq 75^\circ$, the differences between these two formulations are lower than 0.1 %. For larger zenith angles, the air mass changes differently for different atmospheric attenuation components. This problem is avoided by limiting the range of θ_o in the Langley-Bouguer technique. Various authors use different computations of the air mass for determining attenuation by ozone. Holben *et al.* (1988) used the ozone air mass calculation proposed by Komhyr *et al.* (1989), while Schmid *et al.* (1998) used the formulation introduced by Stäehelin *et al.* (1995).

4. **Ozone and Rayleigh correction:** The ozone optical depth is determined from TOMS measurements of ozone amounts in Dobson units. Ozone absorption coefficients are derived from Nicolet *et al.* (1981). The Rayleigh optical depth is computed using values from Penndorf (1957), corrected for the site elevation, but Deschamps *et al.* (1983) use a different algorithm. Differences between the results are less than 2.5 % in the spectral range from 300 nm to 1020 nm. The principal uncertainty in the Rayleigh optical thickness is associated with variability in atmospheric pressure. Eck *et al.* (1989) computed the combined uncertainties associated with calibration, ozone optical thickness, and Rayleigh optical thickness. The total combined uncertainty in AOT was estimated to range between 0.010 to 0.021 for field instruments, and 0.002 to 0.009 for the reference instruments calibrated using the Langley-Bouguer technique.

Cross-Calibration Technique

The cross-calibration technique is a cost-effective and efficient method for calibrating sun photometers relative to instruments that have been calibrated using the demanding Langley-Bouguer method at ideal locations like MLO. The cross-calibration technique is based on simultaneous measurements taken from both calibrated and non-calibrated sun photometers. Observations with minimal time differences between measurements and an air mass less than 3 are required. TOA voltages are computed as

$$V_o(\lambda) = V_o^{\text{ref}}(\lambda) \frac{V(\lambda)}{V^{\text{ref}}(\lambda)}, \quad (7.3)$$

where $V_o^{\text{ref}}(\lambda)$ is the TOA signal of a reference CIMEL sun photometer calibrated at Mauna Loa by the Langley-Bouguer technique and $V(\lambda)$ and $V^{\text{ref}}(\lambda)$ are the signals measured by the non-calibrated and reference sun photometers, respectively, for channels at the same wavelength λ .

Some sun photometers have channels λ_i that are slightly different from the wavelengths of any of the channels of the reference sun photometer. In this situation, the channel of the reference sun photometer with the wavelength λ_j that is nearest to λ_i is used. To calculate TOA voltages as

$$V_o(\lambda_i) = V_o^{\text{ref}}(\lambda_j) \frac{V(\lambda_i)}{V^{\text{ref}}(\lambda_j)} e^{M(\theta_o) \{ [\tau_R(\lambda_i) - \tau_R(\lambda_j)] + [\tau_{O_3}(\lambda_i) - \tau_{O_3}(\lambda_j)] + \tau(1 \mu\text{m}) (\lambda_i^\alpha - \lambda_j^\alpha) \}}, \quad (7.4)$$

where the exponential term is the ratio of transmittances expressed as differences in Rayleigh, ozone and aerosol optical depths for wavelengths λ_i and λ_j , which in this instance are expressed in μm . The variables α and $\tau_a(1 \mu\text{m})$ are, respectively, the Angström coefficient and the aerosol optical thickness at $\lambda = 1 \mu\text{m}$, determined from the reference CIMEL measurements using the Angström law, is conveniently expressed in the form

$$\tau_a(\lambda) = \tau_a(1 \mu\text{m}) \lambda^{-\alpha}. \quad (7.5)$$

The reference sun photometer is one of a selected set of CIMEL sun photometers managed by the AERONET group and calibrated every three months, using the Langley-Bouguer technique at MLO. As shown in Table 7.2, most of the sun photometers have common channels with the CIMEL reference sun photometer, allowing for the application of the cross-calibration technique. The stability of the aerosol

extinction is not very critical with this method. However, standard deviations of TOA voltages over time still need to be determined. The protocol is summarized below:

1. Set the GMT time on both calibrated and non-calibrated sun photometers.
2. Initiate measurements as soon as the calibrated sun photometer starts working.
3. Take measurements concurrently with the calibrated sun photometer.
4. Take all the measurements between 10 a.m. and 3 p.m. local time to have suitable air mass.
5. Measure the dark current in order to avoid temperature effects.
6. Record the sky condition in case of clouds or thin cirrus occurrences (cloud coverage and cloud positions in the sky).
7. Stop when M reaches 3 or the sky condition changes.

Accuracy and Limitations of the Cross Calibration Technique

SIMBIOS sun photometers are routinely cross-calibrated at least every three months, or before each campaign. Calibrations are performed during days with clear and stable atmospheric conditions (AOT at 440 nm typically lower than 0.15). The uncertainties of the cross-calibration are composed of uncertainties in the calibrated reference sun photometer and the non-calibrated sun photometer. The calibration of the reference sun photometers is performed by the AERONET group. The calibration transfer from the MLO reference sun photometers to non-calibrated instruments at least doubles the $V_o(\lambda)$ uncertainty for instruments of the same design. According to Holben *et al.* (1998), the uncertainty in AOTs obtained for cross-calibrated CIMEL instruments are estimated to be 0.01 to 0.02. The uncertainties are higher when the cross-calibrated sun photometer is not of the same design as the reference sun photometer.

For cross-calibrated MicroTops, SIMBAD and PREDE the TOA voltages are determined with uncertainties lower than 1 % (i.e. 0.02 in terms of AOT). Figure 7.2 shows the time series of TOA voltages obtained at GSFC since 1998 (in 2001 for the PREDE). Channels 440 nm and 870 nm are presented. Four reference CIMELs were (S/N 94, 37, 27 and 101) calibrated at MLO were used. TOA voltages retrieved in all bands are reported in Table 7.2. The decay of calibration over time is generally less than 5% per year for SIMBAD and MicroTops. A cross calibration every 3 months allows accounting for the decay over time. However, a larger decay (10%/yr) is observed in some of the channels of MicroTops. The decay is significant and requires a change of the corresponding filter and eventually the photodiode of the instrument. The main source of error in retrieving AOT using sun photometry is the TOA voltages. Since Voltz (1959), several papers have discussed different methods to improve the solar calibration. Schmid *et al.* (1998) used lamp and solar calibrations in conjunction with each other. O'Neill *et al.* (1984) combined solar aureole and solar beam extinction. Soufflet *et al.* (1992) and Holben *et al.* (1998) used a well-calibrated sun photometer as a reference.

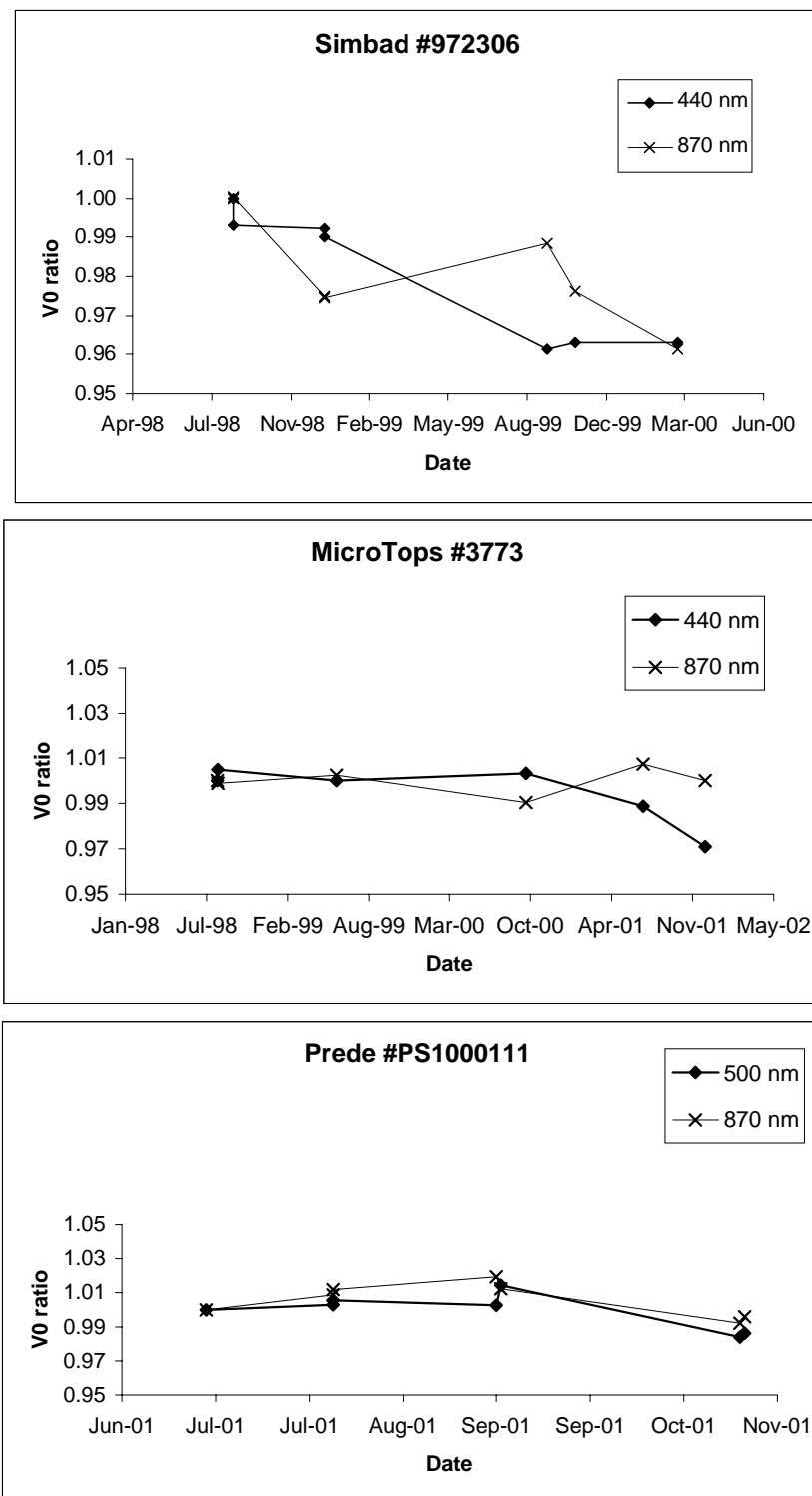


Figure 7.2: Time series of cross calibration since 1998 for SIMBAD and MicroTops, in 2001 for PREDE

The degradation of interference filters is the most important source of the long-term variability in the cross calibration. Although major improvements have been made on the filter design (e.g., ion-assisted deposition interference filters), degradation over time in filter spectral transmittances remains as the main factor limiting the performance of sun photometers. Degradation of filters necessitates frequent calibration

of sun photometers, and measurements of the filter transmission or the relative system response (Schmid *et al.*, 1998). The degradation of the filters mounted on the CIMEL sun photometers has been monitored since 1993. Degradation reported by Holben *et al.* (1998) was between 1 and 5% during the first 2 years of CIMEL operation by the AERONET Project.

7.3 CALIBRATION TECHNIQUES FOR SKY RADIOMETERS

Sky radiance scanning systems are automated instruments dedicated to measure sky radiances in the aureole and in the principle plane of the sun. Radiative properties of aerosols are retrieved using an inversion algorithm of the sky radiances (Dubovik *et al.* 2000; Nakajima *et al.* 1996) and of the polarized component of the sky radiances (Vermeulen *et al.* 2000). This section is dedicated to the description of calibration techniques for accurate retrievals of sky radiances.

Calibration of Unpolarized Sky Radiometers

Unpolarized radiometers, such as CIMEL and PREDE, are calibrated using an integrating sphere (Chapter 6, Sect. 6.2). The radiometer is aligned in front of the sphere (Figure 7.3, top) and 10 measurements are taken for each channel. Radiances of the integrating sphere are then integrated through the domains of each channel of the radiometer. As a result, ratios of raw radiometer voltages to the integrated sphere radiances are obtained. These ratios constitute radiometer calibration parameters C_i :

$$C_i = \frac{V_i}{\int L(\lambda) R_n^i(\lambda) d\lambda}, \quad (7.6)$$

where V_i is the voltages measured in the considered channel i , $R_n^i(\lambda)$ is the normalized spectral response function of the radiometer channel, and $L(\lambda)$ is the spectral radiance scale of the integrating sphere.

Uncertainty of the Calibration of Unpolarized Sky Radiometers

The accuracy of the radiometer calibration is dependent on the calibration of the integrating sphere, sphere's size, clarity of the calibration protocols and precision of the calibration process. A two-meter integrating sphere is available and managed by NASA GSFC Calibration Facility (<http://spectral.gsfc.nasa.gov/>). The uncertainty of the radiances provided by this integrating sphere is estimated to be less than 5%.

Calibration of Polarized Sky Radiometers

The technology to calibrate polarized sun photometers is now available to the SIMBIOS Project. The method was initially designed by the Laboratoire d'Optique Atmosphérique (LOA), Lille, France, for the calibration of POLDER sensor (POLarization and Directionality of the Earth's Reflectances), its airborne (Deuze *et al.* 1992) and space version (Bret-Dibat T. *et al.* 1995; Hagolle *et al.*, 1999).

The polarization box named "POLBOX" is a passive system including neither optical source nor electrical power supply. POLBOX transforms natural light to polarized light. The user's guide for the device (Balois 1999) is available at LOA and GSFC. A Lambertian source is necessary to provide the input light to the box, therefore, an integrating sphere is usually used. POLBOX is composed of two adjustable glass blades that have a high refractive index. The blades are placed in a black anodized aluminum alloy box. The box can turn around the optical axis. The degree of polarization and the direction of the linear polarization plane are tunable by the user by adjusting the position of the box and the blades. The alignment of the blades, relative to the optical axis, is performed by auto-collimation using a basic laser and a mirror. Alignment is required each time the blades are cleaned and replaced in the POLBOX. The required equipment consists of:

1. Polarization device POLBOX.
2. Calibrated light source (integrating sphere).

3. Lambertian light source (integrating sphere or lamp with scattering opaline diffuser).
4. Sun photometer.

The calibration process for polarized radiometers is composed of the following steps:

1. Perform the absolute calibration using the calibrated sphere (Figure 7.3, top) for all radiometer channels, including the polarized ones.
2. Place POLBOX between an integrating sphere and the sun photometer (Figure 7.3, bottom). The integrating sphere is highly recommended for the stability, but its calibration is not essential for determining the relative polarized responses of the instrument.
3. Perform one measurement for each tilt of both blades in POLBOX. A combined tilt is defined and measured by the rotating unit. The tilt of each blade is identical in absolute degrees but shifted in opposite directions.
4. The degree polarization of the light transmitted through the POLBOX to the sensor is given by:

$$P_c(\theta_i) = \frac{A(n)\cos^2(2\theta_i) + B(n)\cos(\theta_i) + C(n)}{D(n)\cos^2(2\theta_i) + E(n)\cos(\theta_i) + F(n)}, \quad (7.7)$$

where A , B , C , D , E , and F are functions of the refractive index n of the blades, and θ_i is the tilt angle of the blades (the same but opposite).

5. Plot the computed degree of polarization against the measured polarization and obtain the intercept of 0° polarization and the slope.

Due to the mechanical limitations of the POLBOX system the maximum degree of polarization that can be reached is 60 %. A 100 % polarization can be obtained using an analyzing polarizing sheet. If needed, the orientation of the polarization can also be determined using POLBOX. Indeed, the orientation of the polarized light is marked on the POLBOX device and a rotating system allows turning POLBOX around the optical axis in order to change the orientation.

The polarized version of CIMEL sun photometers has three polarized channels, each with identical spectral characteristics centered at 870 nm. The polarization axes of the three channels are positioned at intervals exactly 120° apart. The rotating filter wheel of the CIMEL photometer has 9 filter positions, including one opaque filter to measure the dark current. Polarizing covers attached to the filter wheel allow measurement of the three components of the polarized light.

The CIMEL calibration process measures non-polarized signals from the calibrated integrating sphere. The signals are noted V_s^0 , $V_s^{-60^\circ}$, and $V_s^{+60^\circ}$. The use of an unpolarized source implies that each polarized channel measures the same signal. A normalization of the measured signals is then required in order to define the coefficients K_1 and K_2 as

$$K_1 = \frac{V_s^0}{V_s^{-60^\circ}}, \text{ and } K_2 = \frac{V_s^0}{V_s^{+60^\circ}}. \quad (7.8)$$

Next, the sun photometer is placed in front of the POLBOX device and an integrating sphere is used as a light source (Figure 7.3, bottom). Polarized signals are measured in the three polarized channels and noted V_0 , V_{-60} , V_{+60} . The degree of polarization of the light is consequently derived as

$$P_m = \frac{2\sqrt{K_1^2 V_{-60}^2 + V_0^2 + K_2^2 V_{+60}^2 - K_1 V_{-60} V_0 - K_2 V_{+60} V_0 - K_1 K_2 V_{-60} V_{+60}}}{K_1 V_{-60} + V_0 + K_2 V_{+60}}. \quad (7.9)$$

The calibration is accomplished by plotting the computed degree of polarization against the measured polarization to obtain the 0° of polarization, P_0 , and the slope b . Figure 7.4 presents the calibration of the CIMEL #191 performed at GSFC in May 1999. The angle of the polarized light (Ψ) may also be retrieved as

$$\tan(2\Psi) = \frac{\sqrt{3}(V_{+60} - V_{-60})}{2V_0 - V_{+60} - V_{-60}}. \quad (7.10)$$

Uncertainty of the Calibration of Polarized Sky Radiometers The uncertainty of the calibration of polarized radiometers depends on the uniformity of the “Lambertian” light source, and on the optical characteristics of the polarization device, which must be kept in good condition. Dirty glass blades may introduce a polarization by the device itself. Greasy prints on blade surfaces need to be avoided when manipulating the device during cleaning and maintenance.

The degree of polarization obtained at the output of the device is 60% at maximum due to the mechanical design of POLBOX. 100% of degree of polarization can be obtained using polarizing sheets placed in front of the radiometer. However, it is highly recommended to use the same polarizing sheets as those mounted on the radiometer. Then, adjustment of the polarizing sheets to obtain the extinction of the signal can be performed accurately.

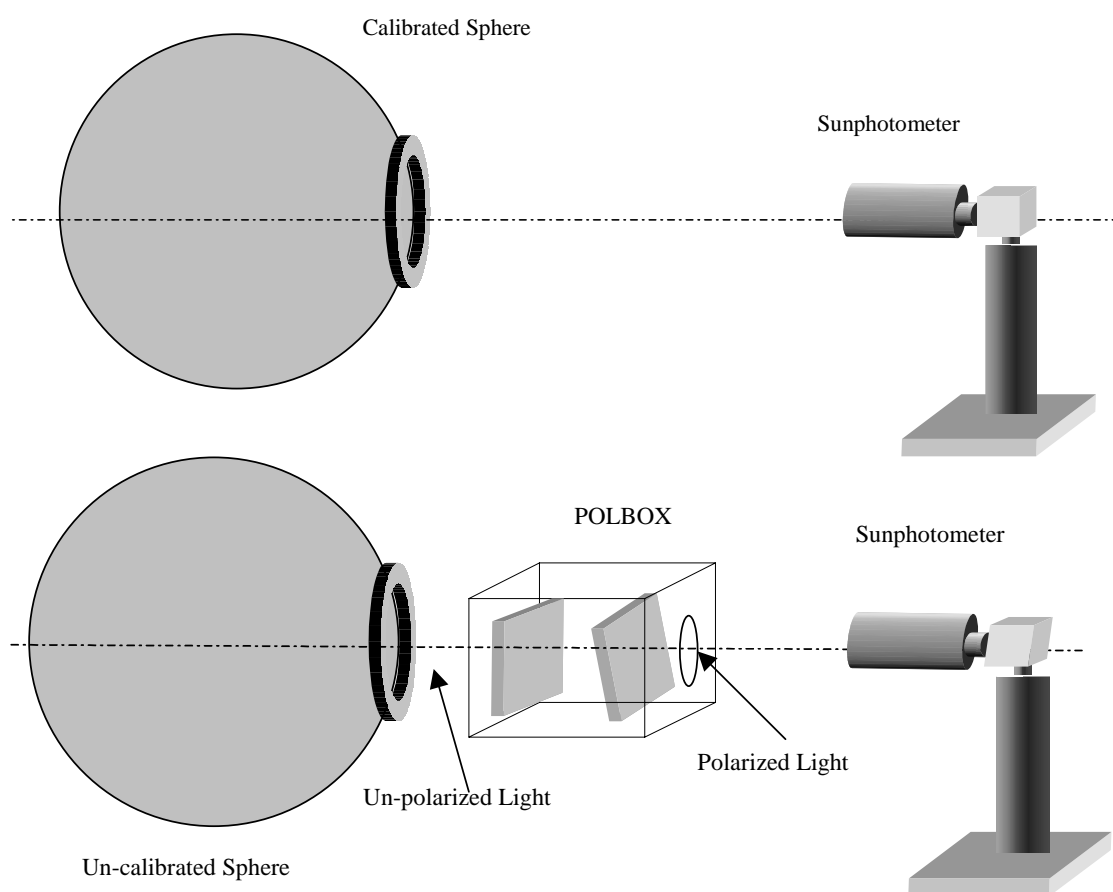


Figure 7.3: Absolute calibration of the CIMEL sun photometer (top); and calibration of the polarized channels of the CIMEL sun photometer (bottom).

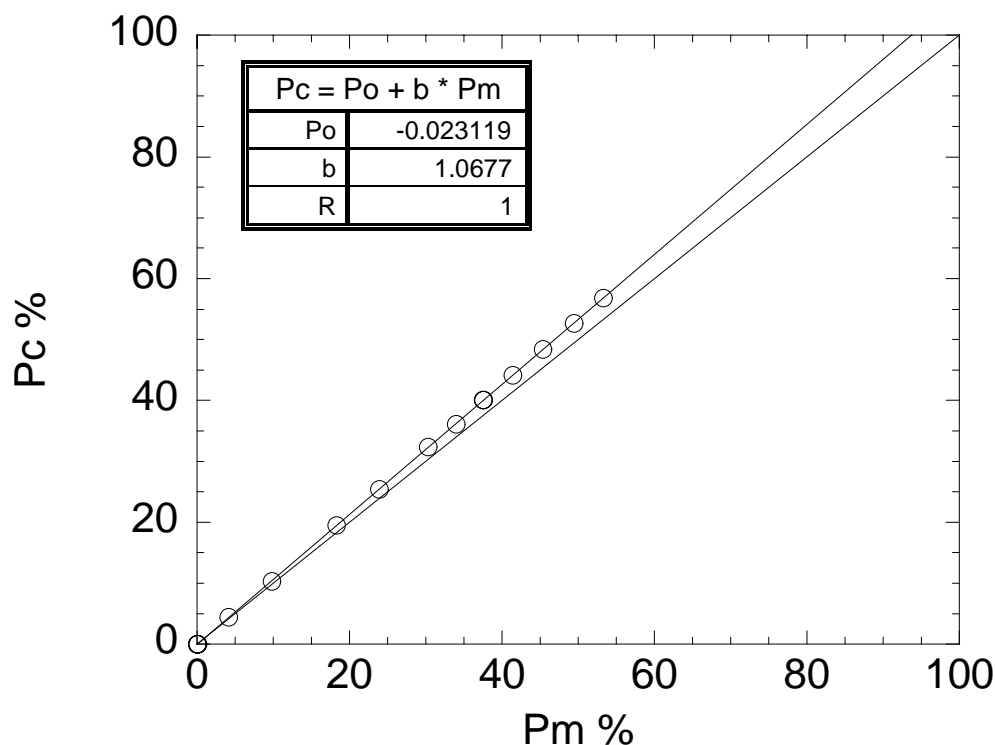


Figure 7.4: Degree of computed polarization versus measured polarization by the CIMEL #191 in May 1999 at GSFC Calibration Facilities.

Calibration and Characterization of Sky Radiance Distribution Cameras

Camera systems for sky radiance distribution measurements, and their uses, are described in Chapter 14 of these protocols. Absolute and spectral response calibrations should be performed on the radiance distribution camera before and after each cruise. A full characterization of the instrument should be performed initially, including camera lens roll-off characteristics for each camera (Voss and Zibordi 1989), in addition to the characterization protocols specified in Chapter 6. If attenuation devices are used to prevent solar saturation, these should be calibrated frequently to track drift. Linearity calibrations should also be performed with the same frequency as the absolute and spectral response calibrations. Procedures for characterizing this class of instruments are essentially the same as for other radiance detector systems (Chapter 6). Each individual detector element in the detector array is essentially regarded as an independent radiometer.

7.4 CALIBRATION OF SHADOW-BAND IRRADIANCE RADIOMETER

Calibration is the most essential element of the shadow-band radiation measurement program. A thorough and on-going calibration process is required before the fast rotating shadow-band radiometer (FRSR) can make accurate radiometric measurements at sea. To insure accurate measurements, there are two important elements for FRSR measurement protocol: calibration of the instrument circuitry, which includes temperature stabilization of the detector during measurements, and determination of the extra-terrestrial constants. The following two subsections discuss these elements and establish protocols.

Calibration of Instrument Circuitry and Temperature Stabilization of the Detector

Laboratory calibration is done in two parts: the optical detector and the electronics attached to the detector. The electronic gains are combined with the direct-normal detector irradiance gains coefficients to make a single calibration equation relating direct-normal irradiance to the electronic measurement in mV.

Initial values for the detector calibration, band-pass response, and zenith angle correction are supplied by the vendor. In addition, the instrument should be periodically recalibrated using the protocols of Chapter 6. Each of the narrow-band filters has a bandwidth of approximately 10 nm and the vendor calibration provides gains at 1 nm spacing. The zenith angle correction is measured on two planes, one on a south-to-north plane and one on a west-to-east plane. The zenith angle corrections are determined by holding the head in a tilting fixture under a collimated beam and tilting the head through 180° in one-degree steps from horizon to horizon in each plane (see also Chapter 6, Section 6.6)

The end-to-end electronic gains are calibrated using the data collection software and a precision reference voltage source in place of each radiometer channel. One-minute averages and standard deviations of voltages for each channel are logged for a full range of input voltages. Electronic calibrations are repeated at regular intervals and for a variety of ambient temperatures. Calibration of the electronics is performed before and after each deployment.

A silicon cell photodiode has a small leakage current which is called a “dark current”. After amplification in the electronics a “dark voltage” results, and if the dark voltage is not negligible, it must be measured and removed. In some instruments, such as the MICROTOPS II hand-held sun photometer, the operator covers the detector before taking a solar measurement. For an autonomous instrument an electronic design eliminates the dark voltage. For the FRSR, the largest deviation from a straight-line fit is less than 0.1 % of full scale and no “dark voltage” adjustment is required.

Calibration drift in the multi-frequency head has caused a great deal of concern in the sun photometer community. Calibration shift is detectable as a permanent change in the apparent extraterrestrial irradiance E_o as computed by the Langley-Bouguer technique. Calibration shift is erratic and quite variable; it can occur suddenly, over a few weeks, or can degrade slowly over months. The 610 nm and 660 nm channels are most prone to drift, though all narrow-band channels are suspect due to gain drift and shifting bandpass response functions. In earlier heads, the filter material, a stack of laminated films, apparently became delaminated as a result of temperature cycling and humidity. A different filter material became available after approximately December 1998 and many researchers are in the process of retrofitting their heads with the new material.

Determination of the Extra-terrestrial Constants

The Langley-Bouguer technique works whenever the skies are perfectly clear, no cirrus or other layers are present, and if the atmospheric optical depth τ is constant over the time duration of the observations. In practice, a Langley-Bouguer calibration can be produced from about one hour of clear sky in the early morning just after sunrise, or late evening just before sunset when $2 < M(\theta_o) < 6$ (i.e. $60^\circ < \theta_o < 80^\circ$). All measurements of E_N , the normal-beam solar irradiance (see section 14.4), are plotted on a log-linear plot and a best estimate straight line is fitted to the data. For sites other than ideal calibration locations, such as the MLO described below, a median-fitting algorithm provides the best objective fit to the data. Over the

ocean, there are almost always clouds on the horizon. In the tropics these are usually high cumulus clouds or cirrus. As a result, Langley-Bouguer measurements from ships are rare gems that must be collected whenever they occur.

As a protocol, E_o 's used in final data products should be computed using the Langley-Bouguer technique at Mauna Loa. The Langley-Bouguer technique should also be used at sea as often as possible as a quality assurance tool, because it provides an excellent means of detecting calibration changes. The top-of-the-atmosphere irradiance, $F_o(\lambda)$, depends on the sun-earth separation, but its mean value, should not change significantly over time. The absolute calibration of the instrument can be compared to the mean reference solar irradiance at the top of the atmosphere, $\bar{F}_o(\lambda)$ (Neckel and Labs, 1984) by integrating the reference solar spectrum over the bandpass of each channel to obtain

$$\bar{F}_o = \frac{\int_0^\infty R_n(\lambda) \bar{F}_o(\lambda) d\lambda}{\int_0^\infty R_n(\lambda) d\lambda}, \quad (7.11)$$

where R_n is the normalized spectral response function of the channel under consideration. For a well-calibrated absolute instrument, $E_o \cong \bar{F}_o$. However, as long as the calibration constant, E_o , is constant, as determined from multiple applications of the Langley-Bouguer technique, accurate AOT estimates are possible. While many investigators use raw voltages to calibrate their instruments, the extra step of computing E_o is important, since it defines the radiative impact of the aerosol at the surface.

Uncertainty of the Calibration of Shadow-Band Irradiance Radiometers

The filter material in shadow-band radiometers is sensitive to temperature. If the head temperature varies from 20 °C to 30 °C, the 500 nm filter will drift by less than 1 nm (Mark Beaubean, Yankee Environmental Systems, personal communication, 1999). Keeping the temperature of the optical detector relatively stable over the range of conditions encountered on a ship can be a challenge. The internal heater in the optical detector is occasionally insufficient for the observed conditions. Providing adequate insulation is the best deterrent, although this issue remains problematic in some conditions and is the subject of current engineering efforts.

The calibration of the shadow-band radiometer is realized using the Langley-Bouguer technique. The technique is subject to the same accuracy constraints and limitations as the Langley-Bouguer calibrated sun photometers described earlier in the chapter.

REFERENCES

- Balois J.Y., 1998: Polarizing box POLBOX User's Guide, *Tech. Report*, Laboratoire d'Optique Atmosphérique, Lille, France, 12pp.
- Bret-Dibat T., Y. Andre' and J.M. Laherrere, 1995: Pre-flight calibration of the POLDER instrument, in *SPIE Proc. Infrared spaceborne remote sensing III*, **2553**, 218-231.
- Deschamps P. Y., B. Fougnie, R. Frouin, P. Lecomte and C. Verwaerde, 2000: SIMBAD: an advanced field radiometer to measure aerosol optical thickness and marine reflectance, *Applied Optics* (submitted).
- Deschamps P. Y., M. Herman M. and D. Tanre, 1983: Model calculation of the reflected solar radiation by the atmosphere and the earth between 0.35 and 4 μm ., *ESA Report*, **4393/80/F/DD**, 156pp.
- Deuze J.L., F.M. Breon, P.Y. Deschamps, P. Goloub and M. Herman, 1992: Polarization measurements with the airborne version of the POLDER instrument, in *SPIE Proc. Polarization and Remote Sensing*, **1747**, 178-187.

- Dubovik O., and M.D. King, 2000: A flexible inversion algorithm for retrieval of aerosol optical properties from Sun and sky radiance measurements, *J. Geophys. Res.* (submitted).
- Eck, T.F, B.N. Holben, J.S. Reid, O. Dubovik, A. Smirnov, N.T. O'Neill, I. Slutsker and S. Kinne, 1999: The wavelength dependence of the optical depth of biomass burning urban and desert dust aerosols, *J. Geophys. Res.*, **104**, 31, 333-31,350.
- Forgan B. W., 1988: Bias in a solar constant determination by the Langley method due to Structured atmospheric aerosol: comment, *App. Opt.*, **27**, **12**, 2546-2548.
- Forgan B. W., 1994: General method for calibrating Sun photometers, *App. Opt.*, **33**, **21**, 4841-4850.
- Fougnie B., R. Frouin, P. Lecompte and P.Y. Deschamps, 1999a: Reduction of skylight reflection effects in the above-water measurements of diffuse marine reflectance, *Appl. Opt.*, **38**, **18**, 3,844-3,856.
- Fougnie B., P.Y. Deschamps, R. Frouin, 1999b: Vicarious Calibration of the POLDER ocean color spectral bands using in situ measurements, *IEEE Trans. Geosc. & Remote Sensing*, ADEOS special issue, **37**, **3**, 1,567-1,574.
- Goloub P., J.L. Deuze, M. Herman and Y. Fouquart, 1994: Analysis of the POLDER polarization measurements performed over cloud covers, *IEEE Trans Geosc. & Remote Sensing.*, **32**, **1**, 78-88.
- Hagolle O., P. Goloub, P.Y. Deschamps, H. Cosnefroy, X. Briottet, T. Bailleul, J.M. Nicolas, F. Parol, B. Lafrance and M. Herman, 1999: Results of POLDER in-flight calibration, *IEEE Trans. Geosc. & Remote Sensing*, **37**, **3**, 1550-1566.
- Holben B.N., T.F. Eck, I. Slutsker, D. Tanre, J.P. Buis, A. Setzer, E. Vermote, J.A. Reagan, Y.L. Kaufman, T. Nakajima, F. Lavenue, I. Jankowiak, A. Smirnov, 1998: A federated instrument network and data archive for aerosol characterization, *Remote Sens. Environ.*, **66**, 1-16.
- Iqbal M., 1983: An introduction to Solar Radiation, Academic, San Diego, CA, 390pp.
- Kasten F. and A.T. Young, 1989: Revised optical air mass tables and approximation formula, *Appl. Opt.*, **28**, **22**, 4735-4738.
- Kasten F., 1965: A new table and approximation formula for relative optical airmass, *Arch. Meteorol. Geophys. Bioklimatol. Ser.*, **B14**, 206-223.
- Komhyr W. D., R.D. Grass, and R.K. Leonard, 1989: Dobson Spectrophotometer 83: a standard for total ozone measurements, 1962-1987, *J. Geophys. Res.*, **94**, 9847-9861.
- Morys, M., F.M. Mims, S.E. Anderson, 1998: Design calibration and performance of MICROTOS II hand-held ozonemeter, <http://www.solar.com/ftp/papers/mtops.pdf>, 12pp.
- Nakajima T., G. Tonna, R. Rao, P. Boi, Y.L. Kaufman, B. Holben, 1996: Use of Sky brightness measurements from ground for remote sensing of particulate polydispersions, *Appl. Opt.*, **35**, **15**, 2672-2686.
- Neckel, H. and D. Labs, 1984: The solar radiation between 3,300 and 12,500 AA. *Solar Phys.*, **90**, 205-258.
- Nicolet M., 1981: The solar spectral irradiance and its action in the atmospheric photodissociation processes, *Planet. Space Sci.*, **29**, 951-974.
- O'Neill N.T., and J.R. Miller, 1984: Combined solar aureole and solar beam extinction measurement, 1: Calibration considerations, *Appl. Opt.*, **23**, 3691-3696.
- Penndorf R., 1957: Tables of the refractive index for standard air and the Rayleigh scattering coefficient for the spectral region between 0.2 and 20.0 microns and their application to atmospheric optics, *J. Opt. Soc. Am.*, **47**, 176-182.
- Porter, J.N., M. Miller, C.Pietras, C. Motell, 1999: Ship Based Sun Photometer Measurements Using Microtops Sunphotometers, *J. Atmos. Ocean. Technol.* (submitted), 21pp.
- Schmid B. and C. Wehrly, 1995: Comparison of Sun photometer calibration by Langley technique and standard lamp, *Appl. Opt.*, **34**, 4500-4512.

- Schmid B., P.R. Spyak, S.F. Biggar, C. Wehrli, J. Sekler, T. Ingold, C. Mätzler, and N. Kämpf, 1998: Evaluation of the applicability of solar and lamp radiometric calibrations of a precision Sun photometer operating between 300 and 1025 nm, *App. Opt.*, **37**, **18**, 3923-3941.
- Schotland R. M. and T.K. Lea, 1986: Bias in a solar Constant Determination by the Langley Method due to Structured Atmospheric Aerosol, *App. Opt.*, **25**, 2486-2491.
- Soufflet V., C. Devaux, D. Tanre, 1992: A modified Langley Plot method for measuring the spectral aerosol optical thickness and its daily variations, *Appl. Opt.*, **31**, 2154-2162.
- Stahelin J., H. Schill, B. Högger, P. Viatte, G. Levrat, and A. Gamma, 1995: Total ozone observation by Sun photometry at Arosa, Switzerland, *Opt Eng.*, **34**, 1977-1986.
- Tanaka M., T. Nakajima, M. Shiobara, 1986: Calibration of a sunphotometer by simultaneous measurements of direct-solar and circumsolar radiations, *App.Opt.*, **25**, **7**, 1170-1176.
- Vermeulen A., C. Devaux., and M. Herman, 2000: Retrieval of the scattering and microphysical properties of aerosols from ground-based optical measurements including polarization, *Appl.Opt.* (submitted).
- Volz F., 1959: Photometer mit selen-photoelement zur spectralen messung der sonnenstrahlung und zur bestimmung der wellenlangenabhängigkeit der dunsttrübung, *Arch. Meteor. Geophys. Bioklimatol. Ser.*, **B10**, 100-131.
- Voss, K.J., and G. Zibordi, 1989: Radiometric and geometric calibration of a spectral electro-optic ``fisheye" camera radiance distribution system. *J. Atmos. Ocean. Technol.*, **6**, 652-662.

Table 7.1: Characteristics of sun photometers.					
Channels (nm)	MicroTops	SIMBAD	SIMBADA	CIMEL	PREDE
315					✓
340				✓	
350			✓		
380			✓	✓	
400					✓
410			✓		
440	✓	✓	✓	✓	
490		✓	✓		
500	✓			✓	✓
510			✓		
560		✓	✓		
620			✓		
675	✓	✓	✓	✓	✓
750			✓		
870	✓	✓	✓	✓	✓
940	✓			✓	✓
1020				✓	✓
FOV	2.5°	3°	3°	1.2°	1.5°

Table 7.2: Top-of-atmosphere (TOA) voltages since 1998 for three sun photometers cross-calibrated with respect to reference CIMELs.

MicroTops 03773	Cimel#	440 nm	500 nm	675 nm	870 nm	
8/21/1998	37	1244	988	1218	824	
6/9/1999	101	1238	987	1198	827	
9/20/2000	37	1242	984	1194	817	
7/6/2001	101	1224	980	1202	831	
12/6/2001	101	1202	984	1208	825	
SIMBAD 932706		440 nm	490 nm	560 nm	675 nm	870nm
8/21/1998	37	388591	479121	406870	421086	304820
12/14/1998	94	388269	473101	394874	410455	311944
9/23/1999	94	376205	464224	391526	416182	300000
10/28/1999	101	376820	462637	387034	410887	302475
3/6/2000	37	382815	465574	382168	408538	301005
Land Prede PS1000111		440 nm	500 nm	675 nm	870 nm	1020 nm
7/6/2001	101	1.480E-04	2.866E-04	3.643E-04	2.743E-04	1.530E-04
8/2/2001	101	1.446E-04	2.874E-04	3.668E-04	2.767E-04	1.530E-04
9/6/2001	94	1.451E-04	2.873E-04	3.646E-04	2.796E-04	1.552E-04
9/7/2001	94	1.460E-04	2.907E-04	3.635E-04	2.777E-04	1.542E-04
10/28/2001	94	1.817E-04	2.820E-04	3.557E-04	2.721E-04	1.533E-04

Chapter 8

Stability Monitoring of Field Radiometers Using Portable Sources

Stanford B. Hooker

NASA Goddard Space Flight Center, Greenbelt, Maryland

8.1 INTRODUCTION

Mueller and Austin (1995) included a discussion on tracking instrument performance in between calibration activities with stable lamp sources in rugged, fixed geometric configurations. The recommended specifications of the device included the stability of the lamp output and the repeatability of measurement must be sufficient to detect 2 % variations in an instrument's performance. In terms of the protocols for using the source, it was recommended that an instrument should be connected to the portable standard and its response recorded daily, keeping a record of instrument responsivity throughout an experiment. Furthermore, these sources would provide an essential warning of problems if they appear.

One of the more important requirements in the use of the portable source was it must be available when the complete radiometric calibrations are performed, so a baseline may be established and maintained for each sensor channel, but recognizing that the source cannot be a substitute for complete calibrations. The temporal record they provide will, however, be invaluable in cases where the pre-and post-cruise calibrations disagree or if the instrument is disturbed, e.g., opened between calibrations, subjected to harsh treatment during deployment or transport, or if the data quality are otherwise suspect. These portable standards are an important part of the recommended instrument package.

8.2 The SQM

Although Mueller and Austin (1995) specified the need for, and described some of the requirements of, a portable source, no such device was then commercially available. In response to the need for a portable source, NASA and NIST developed the SQM. The engineering design and characteristics of the SQM are described by Johnson et al. (1998), so only a brief description is given here. A separate rack of electronic equipment, composed principally of two computer controlled power supplies and a multiplexed, digital voltmeter (DVM), are an essential part of producing the stable light field. All of the external components are controlled by a computer program over a general purpose interface bus (GPIB).

The SQM has two sets of halogen lamps with eight lamps in each set; both lamp sets are arranged symmetrically on a ring and operate in series, so if one lamp fails, the entire set goes off. The lamps in one set are rated for 1.05 A (4.2 V) and are operated at 0.95 A, and the lamps in the other set are rated for 3.45 A (5.0 V) and are operated at 3.1 A; the lamp sets are hereafter referred to as the 1 A and 3 A lamps, respectively. The lamps are operated at approximately 95 % of their full amperage rating to maximize the lifetime of the lamps.

A low, medium, and high intensity flux level is provided when the 1 A, 3 A, and both lamp sets are used, respectively. Each lamp set was aged for approximately 50 hours before deploying the SQM to the field. The interior light chamber has bead-blasted aluminum walls, so the diffuse component of the reflectance is significant. The lamps illuminate a circular plastic diffuser protected by safety glass and sealed from the environment by o-rings. The diffuser is resilient to ultraviolet yellowing, but can age nonetheless. The exit aperture is 20 cm in diameter and has a spatial uniformity of 98 % or more over the interior 15 cm circle. The SQM does not have, nor does it require, an absolute calibration, but it has design objectives of better than 2 % stability during field deployments.

A faceplate or *shadow collar* provides a mounting assembly, so the device under test (DUT), usually a radiance or irradiance sensor, can be positioned in the shadow collar. The DUT has a D-shaped collar fitted to it at a set distance, 3.81 cm (1.5 inch), from the front of the DUT. This distance was chosen based on the most restrictive clearance requirement of the radiometers used in the different deployment rigs. The D-shaped collar ensures the DUT can be mounted to the SQM at a reproducible location and orientation

with respect to the exit aperture each time the DUT is used. The former minimizes uncertainties (principally with irradiance sensors) due to distance differences between measurement sessions, while the latter minimizes uncertainties (principally with radiance sensors) due to inhomogeneities in the exit aperture light field. In either case, the D-shaped collar keeps these sources of uncertainties below the 1 % level. A schematic of the original SQM is given in Fig.8.1. The SQM faceplate can be changed to accept a variety of instruments from different manufacturers. Radiometers above a certain size, approximately 15 cm, would be difficult to accommodate, but the entire mounting assembly can be changed to allow for reasonable viewing by seemingly difficult to handle radiometers. To date, three radiometer designs have been used with the SQM, and there were no problems in producing the needed faceplates, D-shaped collars, or support hardware to accommodate these units.

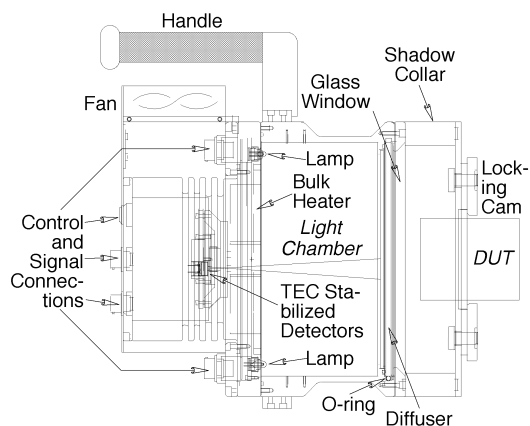


Figure 8.1: A schematic of the SQM showing a DUT kinematically mounted to the shadow collar.

The SQM light field can change because of a variety of effects; for example, the presence of the DUT, the aging of the lamps, a deterioration in the plastic diffuser, a change in the transmittance of the glass cover, a drift in the control electronics, a repositioning of a mechanical alignment, etc. To account for these changes, three photodiodes, whose temperatures are kept constant with a precision thermoelectric cooler (± 0.01 K), measure the exit aperture light level: the first has a responsivity in the blue part of the spectrum, the second in the red part of the spectrum, and the third has a broadband or *white* response. All three internal monitors view the center portion of the exit aperture. A fan cools the back of the SQM to prevent a build up in temperature beyond that which the thermoelectric cooler can accommodate. The SQM has an internal heater to help maintain temperature stability in colder climates and to shorten the time needed for warming up the SQM.

Another SQM quality control procedure is provided by three special DUTs called *fiducials*: a white one, a black one, and a black one with a glass face (the glass is the same as that used with the field radiometers). A fiducial has the same size and shape of a radiometer, but is non operational. The reflective surface of a fiducial is carefully maintained, both during its use and when it is not being used. Consequently, the reflective surface degrades very slowly, so over the time period of a field expedition, it remains basically constant. A field radiometer, by comparison, has a reflective surface that is changing episodically from the wear and tear of daily use. This change in reflectivity alters the loading of the radiometer on the SQM and is a source of variance for the monitors inside the SQM that are viewing the exit aperture, or the radiometer itself when it is viewing the exit aperture. The time series of a fiducial, as measured by the internal monitors, gives an independent measure of the temporal stability of the light field.

The SQM has been used to track changes in instruments between calibrations and on multiple cruises lasting approximately 5--6 weeks each (Hooker and Maritorena 2000). Although there was some controversy at the design stage about operating the lamps below their rated current (approximately 95 % of rating), there has been no observable degradation in the performance of the lamps as a result of this--indeed, they have survived long shipment routes (US to UK to Falkland Islands and back) on repeated occasions, as well as, the high vibration environment of a ship. The SQM is clearly a robust instrument well suited to the task of calibration monitoring in the field at the 1 % level (Hooker and Aiken 1998). There are two commercialized versions of the SQM: the OCS-5002 built by Yankee Environmental

Systems (YES), Inc. (Turners Falls, Massachusetts), and the SQM-II built by Satlantic, Inc. (Halifax, Canada). Although both companies based their designs on the SQM, the OCS-5002 is most like the original.

8.3 OCS-5002

The OCS-5002 is composed of the lamp housing, with shadow collar and kinematic mounting system, plus a power supply, both of which are operated and monitored via a serial port interface to a computer. All system operations, including powering on and off the lamps, controlling the cooling fan and preheater, as well as monitoring system performance during warm up and operation are controlled by the external software. The power supply and control system were specially designed to enhance performance and are enclosed in a waterproof enclosure. A picture of the lamp housing with shadow collar attached is shown in Fig. 8.2.

An internal thermally stabilized current regulation circuit ensures precise current regulation to the two independent lamp sets (with low- and high-power lamps). The lamps in the original design were potted into aluminum mounts that held the bulbs in their correct orientations. The mounts were soldered to a circular circuit board and were difficult to replace. In the OCS-5002, porcelain sockets are used for each lamp, which are held in place with epoxy in aluminum mounting rings. This design allows for rapid individual bulb replacement.

Shunt temperatures as well as the lamp housing temperatures are monitored during operation. A two-channel filter-detector and a third unfiltered detector are positioned within the lamp housing to permit direct optical monitoring of the lamp rings and the integrating cavity itself. These three detectors are thermally stabilized via a thermoelectrically cooled housing to approximately 35°C, and their outputs are continuously monitored during system operation.



Figure 8.2: A picture of the OCS-5002 without a DUT mounted to the shadow collar

8.4 SQM-II

The main difference between the SQM-II (Fig. 8.3) and the original unit is the high degree of integration in the former. The entire system consists of two components, a deck box that provides DC power to the SQM-II, and the SQM-II itself (McLean et al. 1998). The latter contains the lamp rings (which use the same lamps as the original SQM), heating and cooling subsystems, control circuitry, the system computer, plus display and data storage. The SQM-II system is designed to be self contained and does not require a computer to operate. Only two cables are required to complete system assembly (an AC power cord for the deck box and a DC power cord to link the deck box to the SQM-II). Although this integration reduces system complexity, it comes with increased vulnerability: a failure in any one of the subsystems can render the entire system inoperable with no opportunity for simply swapping in a new (external) subassembly, like a power supply or DVM. As was done with the original SQM, Satlantic recommends running the SQM-II on an uninterruptible power supply (UPS).

User input to start and monitor the system is via a simple 4-button keypad and a 4 x 20 fluorescent display at the rear of the device. Commands can be entered using the menus on the display or remotely from a computer. A computer can also be connected to the system to log data during a measurement session, or the data can be stored internally in a flash card and downloaded later.

The differences between the two SQM units are not restricted to their control architecture. The SQM-II has many improvements that use of the original unit has shown to be desirable under different circumstances:

1. The bulbs are mounted at the front, facing away from the exit aperture, which increases the average path length of the light emitted by each bulb, and it makes it easier to service the lamps (individually and as a subassembly);
2. The light chamber is lined with Spectralon, so the emitted flux is higher, and the aperture uniformity is greater; and
3. At 490 nm, the SQM-II is about seven times more intense than the SQM (the apparent blackbody temperature of the SQM-II is 3,100 K, whereas, the SQM is about 2,400 K).

Although the greater flux of the SQM-II is a desirable attribute for the blue part of the spectrum, the high output in the red saturates many in-water field radiometers. This was subsequently corrected by adding a blue filter to the exit aperture.

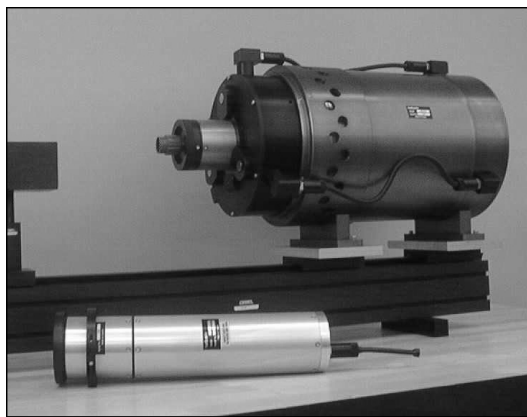


Figure 8.3: A picture of the SQM-II with a DUT mounted to the shadow collar.

8.5 METHODOLOGY

To check the stability of radiometers in the field, and to monitor the performance of the SQM, a calibration evaluation and radiometric testing (CERT) session and a data acquisition sequence (DAS) needs to be defined. In its simplest form, a CERT session is a sequence of DAS events, which are executed following a prescribed methodology. Each DAS represents enough data to statistically establish the

characteristics of the instrument involved within a reasonable amount of time. In most cases, 3 minutes is sufficient. A typical sequence of procedures for each CERT session is as follows:

1. The electronics equipment (the lamp power supplies and the digital multimeter, the SQM fan and internal heater power supplies, the lamp timers, etc.) is turned on 1-2 hours before the CERT session begins. The total numbers of hours on each lamp set are tracked by recording the starting and ending number of hours on each lamp set.
2. The SQM is preheated using the internal electrical heater for 30--60 minutes, depending on the environmental conditions at the time. This is done to achieve a time efficient thermal equilibrium of the instrument from the power dissipation of the lamps.
3. If the mixture of radiometers used in the CERT sessions change over time, at least one radiometer (preferably two of different types, i.e., radiance and irradiance) should be recurrently used in all sessions. The first data collected during the CERT session should be the dark voltages for this radiometer (usually achieved by putting an opaque cap on the radiometer) and the SQM internal dark voltages (usually acquired by blocking the SQM exit aperture with a fiducial).
4. Once the SQM is powered up at the selected lamp level, it should be allowed to warm up for at least 1 hour (and frequently for as long as 2 hours in highly variable environments). The warm-up period can be considered completed when the internal SQM monitor data are constant to within 0.1 %. The radiometric stability usually coincides with a thermal equilibrium as denoted by the internal thermistors.
5. Upon the completion of the warm-up period, the individual radiometers are tested sequentially. First, the previous DUT is removed and replaced with a fiducial. Second, dark voltages for the radiometer to be tested and SQM monitor data for glass fiducial are simultaneously collected. Third, the fiducial is removed from the SQM and replaced with the radiometer. Finally, data from the SQM and the radiometer are recorded. Each time a DUT is mounted to the SQM, the lamp voltages and internal temperatures of the SQM are recorded.
6. If multiple flux levels are to be measured, and the current lamp set is not to be used, it is powered down. The needed lamp set is powered on and allowed to warm up for 1-2 hours. The individual radiometers are tested sequentially with fiducial measurements taken during dark voltage measurements (step 5).
7. Before the SQM is finally shut down, any remaining fiducials are measured. These measurements, plus the fiducial data acquired in between the radiometer dark and light (SQM) measurements, are the primary sources for tracking the stability of the SQM flux. After the lamps are powered down, the ending number of hours on each lamp set is recorded.

It is important to note the warm-up process only involves the SQM and it is done only once before the individual DUTs are measured; the DUTs are not warmed up *per se*, although, they are usually kept in the same room as the SQM, so they are at room temperature.

The point for radiometric stability of the internal SQM monitors (0.1 %) is usually achieved within 30-90 minutes of powering up the lamps, depending on the amount of preheating. In general, the warm-up period is extended another 30 minutes past this point to ensure that stability can be maintained. The radiometric stability of the SQM immediately after powering on the lamps (*i.e.*, within 1 minute) is usually less than 0.2 % with preheating, and as much as 2 % without preheating depending on the environmental conditions. If a radiometer is subjected to some kind of trauma and needs to be checked as quickly as possible for an impending deployment, it is usually possible to check it to within reasonable limits using a rapid start of the SQM, particularly if the SQM is kept in the preheated mode.

If CERT sessions are conducted outside, the SQM should be shaded from direct sunlight and ambient wind conditions to prevent rapid changes in heating and cooling. A major source of noise in the stability of the lamps is vibration, particularly if the SQM is used at sea. Vibration damping is recommended under such conditions and 0.5 in. high density felt has been demonstrated to be a good damping material.

8.6 DATA ANALYSIS

The approach for presenting the data analysis procedures is assumed to involve more than one radiometer, since most deployment systems involve a solar reference and one or more above- or in-water instruments. In the most general terms, the quantity of interest is a voltage or digital count level associated with a radiometer (or DUT), $V^C(\lambda_i, t_i)$, where V is the voltage of the radiometer under illumination at the time of the measurement, C is the instrument code of the DUT, λ_i is an individual wavelength or channel of the instrument, and t_j is a particular time for the data record. The instrument code is just a simple mnemonic for keeping track of which DUT was measured when. A suitable coding scheme is to assign a letter for a particular type of radiometer (e.g., R for radiance, I for irradiance, etc.) and then to add on the serial number).

An SQM has two lamp sets, so multiple flux levels are possible. Under most circumstances the lamp sets are different, so three basic voltage levels for the SQM monitors and for the radiometers while they are mounted to the SQM are possible: L, M, and H, which correspond to low, medium, and high lamp levels, respectively. (In situations where the two lamp sets are identical, it is customary to denote the two levels as L and M.) In addition, dark voltages are measured for the radiometers (D^C) and the SQM internal monitors (D_S). For the latter, the S code denotes the internal monitor channel (B for blue, R for red, and W for white or broadband.) Note the SQM-II has a single internal monitor in the blue part of the spectrum. All of the data for a particular CERT session are acquired at a single lamp level.

The process of determining a parameter for monitoring the radiometric stability of a radiometer during a field deployment begins by first defining the average signal level acquired with the radiometer during a DAS:

$$\bar{V}^C(\lambda_i, \bar{t}_k) = \frac{1}{n} \sum_{j=1}^n V^C(\lambda_i, t_j), \quad (8.1)$$

where $\bar{V}^C(\lambda_i, \bar{t}_k)$ denotes a time average of the total number of samples, n , collected during a DAS, and \bar{t}_k is the average time over DAS time period k . Following (8.1), the average dark voltage for a DAS is defined as

$$\bar{D}^C(\lambda_i, \bar{t}_k) = \frac{1}{n} \sum_{j=1}^n D^C(\lambda_i, t_j). \quad (8.2)$$

In (8.2), the temporal assignment for the average dark voltage is associated with the average signal level even though the dark values are taken a few minutes before the signal data (this is a simplification in the process that is purely cosmetic).

The average internal monitor signal level acquired during a DAS while the DUT was mounted to the SQM is

$$\bar{V}_S(\bar{t}_k) = \frac{1}{n} \sum_{j=1}^n V_S(t_j), \quad (8.3)$$

where, again, S is used to denote the internal SQM monitor used for normalization: B, R, or W. The average dark voltage for an internal monitor is defined as

$$\bar{D}_S(\bar{t}_k) = \frac{1}{n} \sum_{j=1}^n D_S(t_j), \quad (8.4)$$

The internal monitor dark data is collected before the lamps are warmed up, so the temporal information is not important and has been omitted.

While the dark readings for a radiometer were being collected, a fiducial was placed inside the SQM and the signals from the internal SQM monitors were recorded. The voltages from the monitors are denoted by X_S^C where X can be either L, M, or H depending on the selected SQM lamp level, C is the instrument code for the DUT in the SQM, and S indicates the internal monitor under consideration: B for the blue monitor, R for the red monitor, and W for the broad-band or white monitor.

Changes in a radiometric signal can arise from changes in the light source, the digitization electronics, or the detector electronics. Tracking the performance of a radiometer over extended time periods must take into account these three influences on the signal. The basic parameter for tracking the radiometers is constructed by taking the average voltage from the radiometer when it was mounted to the SQM, subtracting the average dark voltage, and then normalizing the difference by one of the average internal SQM monitor voltages yields

$$\tilde{V}_s^c(\lambda_i, \bar{t}_k) = \frac{\bar{V}_s^c(\lambda_i, \bar{t}_k) - \bar{D}_s^c(\lambda_i, \bar{t}_k)}{\bar{V}_s^c(\bar{t}_k) - \bar{D}_s^c}, \quad (8.5)$$

where \tilde{V}_s^c denotes a normalized result for a DAS. Within the uncertainties of the measurements, $\tilde{V}_s^c(\lambda_i)$ should be a constant from one CERT session to the next, since an increase (decrease) in SQM intensity should coincide with an increase (decrease) in the radiometer signal.

If N is the total number of CERT sessions at a particular lamp level, the average normalized signal for a particular radiometer at that lamp level is given by

$$\hat{V}_s^c(\bar{t}_k) = \frac{1}{N} \sum_{j=1}^N \tilde{V}_s^c(\lambda_i, t_j), \quad (8.6)$$

where $\hat{V}_s^c(\bar{t}_k)$ denotes the average of the normalized signals.

The temporal performance of a radiometer is determined by calculating the percent deviation of the radiometer (during a particular DAS time, t_k) from the average of all of the normalized signals (8.4) as

$$\tilde{\tilde{V}}_s^c(\lambda_i, \bar{t}_k) = 100 \left[\frac{\tilde{V}_s^c(\lambda_i, \bar{t}_k)}{\hat{V}_s^c(\lambda_k)} - 1 \right], \quad (8.7)$$

where $\tilde{\tilde{V}}_s^c$ denotes the percent deviation of the normalized signals with respect to the average for a particular lamp level, the average being determined from the time series of data collected during a field deployment. Thus, $\tilde{\tilde{M}}_w^{R21}(421)$ is the percent deviation of the radiances for the 412 nm channel of radiometer OCR-200 serial number 21 (instrument code R21) at the medium lamp level normalized with the white SQM internal monitor.

The time series of corresponding fiducial measurements are formed in a similar fashion. The only data available for a fiducial is the internal SQM monitor data, so the equivalent of (8.5) for a fiducial is simply the average signal level for the monitor minus the average dark level, *i.e.*

$$\tilde{V}_s^c(\lambda_i) = \bar{V}_s^c(\bar{t}_k) - \bar{D}_s^c, \quad (8.8)$$

where C is the DUT code for a glass, black, or white fiducial (usually G, B, and W, respectively, although when many fiducials are available, the serial numbers of the fiducials are included in the coding scheme). The average signal over all CERT sessions is calculated using (8.6) and the individual percent deviations using (8.7).

The time series of fiducial measurements within a CERT gives the performance of the SQM during the CERT, and the time series of all fiducial measurements across the CERT sessions gives the long-term performance of the SQM. Because one fiducial is being used repeatedly, and two others are being used only once per CERT session, the ability to discern short- and long-term changes in the SQM is available, with the longer-term changes being measured by more than one fiducial.

8.7 FUTURE APPLICATIONS

Figure 8.4 presents a summary of SQM performance during three at-sea deployments. The data is from Atlantic Meridional Transect (AMT) cruises (Aiken et al. 2000) AMT-5 through AMT-7 plus laboratory experiments, and covers a time period of approximately 460 days. It shows the internal blue monitor signal as measured with the glass fiducial as a function of time, but presented as the percent difference with respect to the mean value for the entire time period (*i.e.*, across all CERT sessions). A confirmation of the signal is given by the R035 radiometer for the 443 nm channel (which is very similar to

the blue internal monitor for the SQM), and it very nearly mirrors the internal monitor signal. The two detectors yield similar decay rates of approximately 0.007 % per day, or approximately 0.25 % for a 35 day cruise. This is an underestimate, however, because the degradation is due mostly to lamp usage, and this is obviously most significant during use, and not during shipping and storage. This is best seen by perusing the data from individual cruises, and comparing them to results of laboratory work done following AMT-7.

The stability and behavior of the SQM during AMT-5 was very similar to its performance on AMT-3 when it was first commissioned for field use (Hooker and Aiken 1998): the data indicate a stepwise change in the SQM flux level halfway through the cruise.

All three detectors show the change, and if the three detector signals are averaged together, the emitted flux of the SQM decreased by approximately 0.87 %. The change in flux was due to a partial short in one of the bulbs, which resulted in a 1.2 % decrease in the operating voltage of the lamp. The stability of the SQM during the periods before and after the change in light output, as estimated by one standard deviation (1σ) in the average of the three internal monitor signals, was to within 0.60 % and 0.53 %, respectively.

During AMT-6, the 1σ values of the red, blue, and white detectors while measuring the glass fiducial were 0.36 %, 0.46 %, and 0.39 %, respectively. The performance of the SQM during AMT-6 was the best out of all the cruises; no lamp anomalies were experienced and the standard deviation in the emitted flux was the lowest ever recorded in the field. The AMT-7 data show a stepwise change halfway through the cruise, as was seen during AMT-3 and AMT-5. Although the stability for the entire cruise was very good, to within ± 0.43 % as measured by the blue detector, the stability improves to ± 0.38 % and ± 0.28 % if the cruise is split into a first and second half, respectively.

Lamp performance after AMT-7 in the laboratory was very similar to that seen during AMT-6: the changes are all within 1 %. The long- and short-term stability of the SQM raises the possibility that this device can be used for absolute calibrations in the laboratory and in the field. Although a definitive analysis of using the SQM in this fashion has not been completed, one of the objectives of SIRREX-7 was to evaluate several SQMs for this purpose (Hooker *et al.* 2000). The preliminary results indicate this may be possible, but a well-prescribed protocol is contingent upon completion of the SIRREX-7 data analysis and on acceptance through a rigorous independent review.

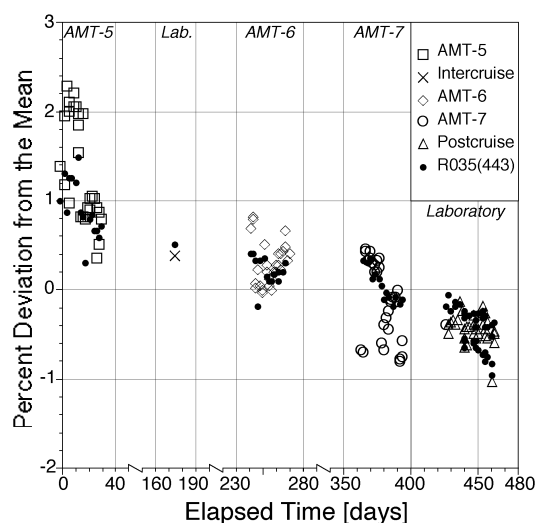


Figure 8.4: The long-term stability of the original SQM as measured, using its internal blue monitor and one radiometer (R035) at 433 nm, on a series of AMT cruises and laboratory exercises.

REFERENCES

- Aiken, J., D.G. Cummings, S.W. Gibb, N.W. Rees, R. Woodd-Walker, E.M.S. Woodward, J. Woolfenden, S.B. Hooker, J-F. Berthon, C.D. Dempsey, D.J. Suggett, P. Wood, C. Donlon, N. González-Benítez, I. Huskin, M. Quevedo, R. Barciela-Fernandez, C.de Vargas, and C. McKee, 1999: AMT-5 Cruise Report. *NASA Tech. Memo. 1998--206892, Vol. 2*, S.B. Hooker and E.R. Firestone, Eds., NASA Goddard Space Flight Center, Greenbelt, Maryland, 113 pp.
- Aiken, J., N. Rees, S. Hooker, P. Holligan, A. Bale, D. Robins, G. Moore, R. Harris, and D. Pilgrim, 2000: The Atlantic Meridional Transect; overview and synthesis of data. *Prog. Oceanogr.*, (in press).
- Hooker, S.B., and J. Aiken, 1998: Calibration evaluation and radiometric Testing of field radiometers with the SeaWiFS Quality Monitor (SQM). *J. Atmos. Oceanic Tech.*, **15**, 995-1,007.
- Hooker, S.B. and S. Maritorena, 2000: An evaluation of oceanographic radiometers and deployment methodologies. *J Atmos. Oceanic Technol.*, 17,811-830.
- Hooker, S.B., S. McLean, J. Sherman, M. Small, G. Zibordi, and J. Brown, 2000: The seventh SeaWiFS Intercalibration Round-Robin Experiment (SIRREX-7), March 1999. *NASA Tech. Memo. 2000--206892, Vol. 13*, S.B. Hooker and E.R. Firestone, Eds., NASA Goddard Space Flight Center, (in prep.)
- Johnson, B.C., P-S. Shaw, S.B. Hooker, and D. Lynch, 1998: Radiometric and engineering performance of the SeaWiFS Quality Monitor (SQM): A portable light source for field radiometers. *J. Atmos. Oceanic Tech.*, **15**, 1,008-1,022.
- McLean, S., S. Feener, J. Scrutton, M. Small, S. Hooker, and M. Lewis, 1998: SQM-II: A commercial portable light source for field radiometer quality assurance. *Proc. SPIE Ocean Optics XIV*, (in press).
- Mueller, J.L. and R. W. Austin, 1995: Ocean Optics Protocols for SeaWiFS Validation, Rev 1. *NASA Tech. Memo. 1995--104566, Vol. 25*, S.B. Hooker, E.R. Firestone and J.G. Aker, Eds., NASA Goddard Space Flight Center, Greenbelt, Maryland, 67 pp.

Chapter 9

Overview of Measurement and Data Analysis Protocols

James L. Mueller

Center for Hydro-Optics and Remote Sensing, San Diego State University, California

9.1 INTRODUCTION

Variables to be measured at each validation station are summarized in Table 3.1 (Chapter 3). This present chapter covers, in varying detail, the methods of measurement and data analysis associated with each of the variables listed in Table 3.1. The level of detail presented for each topic area falls into one of three categories:

1. Complete protocol descriptions that are not covered elsewhere in individual chapters;
2. Brief abstracts of protocols covered in other chapters of this document; and
3. Abstracted reviews of validation measurement and analysis methods for which comprehensive, up-to-date protocol descriptions are not yet available to be included in this document.

Clearly, the Category 3 topics are prime candidates for workshops, and supporting research, to develop protocols for future revisions to the Ocean Optics Protocols. The following outline is presented as a guide to the contents of this chapter. “Category 1” entries (material covered only here) are highlighted in bold text, “Category 2” entries (material covered in other chapters) are listed in normal text, and “Category 3” entries (material covered only here, but inadequately) are underlined.

9.2 VALIDATION SAMPLING STRATEGIES

Initialization and Validation

Case-1 Water: Sampling Strategies

Case 2 Waters: Sampling Strategies

9.3 RADIOMETRIC MEASUREMENTS AND ANALYSIS PROTOCOLS

In-Water Radiometric Profiles (Chapter 10) MOBY, A Radiometric Buoy for Performance Monitoring and Vicarious Calibration of Satellite Ocean Color Sensors: Measurement and Data Analysis Protocols (Chapter 11).

Above-Water Remote-Sensing Reflectance (Chapter 12)

Normalized Water-Leaving Radiance and Remote-Sensing Reflectance: Bidirectional Reflectance and Other Factors (Chapter 13)

Sun and Sky Radiance Measurements (Chapter 14)

9.4 INHERENT OPTICAL PROPERTY MEASUREMENTS AND ANALYSIS PROTOCOLS

In situ Reflective-Tube Absorption and Beam Attenuation Meters

Absorption Using Gershun’s Equation

Absorption Spectrophotometry of Filtered Particles and Dissolved Materials (Chapter 15)

Comparative Analyses of Absorption Coefficients

Single-Wavelength Transmissometers

Volume Scattering Function and Backscattering Meters

Laboratory Measurements of Scattering in Water Samples

9.5 BIOGEOCHEMICAL AND BIO-OPTICAL PROTOCOLS

High Performance Liquid Chromatography (HPLC) Measurements and Analysis (Chapter 16)

Fluorometric Measurement of Chlorophyll a Concentration (Chapter 17)

Phycocerythrin and other Phycobiliproteins

Suspended Particulate Matter

Particle Size Distributions

9.6 ANCILLARY MEASUREMENTS AND METADATA

Logbooks

Wind Speed and Direction

Barometric Pressure

Cloud Conditions

Wave Height

Secchi Depth

Conductivity, Temperature and Depth (CTD) Profiles

Metadata

9.7 RADIOMETRIC AND BIO-OPTICAL MEASUREMENTS FROM MOORED AND DRIFTING BUOYS.

9.8 AIRBORNE MEASUREMENTS

9.2 VALIDATION SAMPLING STRATEGIES

The following discussion of bio-optical sampling protocols is organized into three subtopics: sampling for the initial and ongoing validation of a satellite radiometric system's performance, algorithm development and validation in Case-1 waters, and algorithm development and validation in Case-2 waters. The distinction between the first subtopic and the second two is clear-cut, but what precisely is meant by *Case-1* and *Case-2* water masses?

In its literature and reports, the ocean color research community has formally adopted definitions originally due to Morel and Prieur (1977), who stated:

“Case-1 is that of a concentration of phytoplankton [which is] high compared to that of other particles. The pigments (chlorophyll, [and] carotenoids) play a major role in actual absorption. In contrast, the inorganic particles are dominant in Case-2, and pigment absorption is of comparatively minor importance. In both cases, [the] dissolved yellow substance is present in variable amounts and also contributes to total absorption.”

In practice, however, only those water masses where the CZCS-type blue-green ratio algorithms for phytoplankton pigment concentration (chlorophyll *a* plus pheopigment *a*) work reasonably well have been treated as *Case-1*. All other water masses have often been loosely lumped into the *Case-2* definition, albeit with considerable confusion over how to categorize coccolithophorid blooms, and waters in which strong concentrations of Gelbstoff vary independently from pigment concentration. By a strict interpretation of the original definition, both of these latter cases would be classified as Case-1.

In the present discussion of sampling protocols, Case-1 will be considered to refer to what might be called *ordinary open ocean Case-1* waters, wherein scattering and absorption are dominated by phytoplankton, pigments, and Gelbstoff concentrations, and where *global* blue-green color ratio algorithms for chlorophyll *a* concentration and *K*(490) work well. Most areas in the deep ocean belong to this case. Water masses that do not satisfy these criteria will be grouped under the heading Case-2. Within Case-2, by this definition, water masses with a wide diversity of bio-optical characteristics will be found. Prominent subcategories include:

1. Coccolithophorid blooms, wherein the detached coccoliths dominate light scattering and remote sensing reflectance independently from pigment concentration;
2. Coastal areas, wherein DOM of terrestrial origin contributes a strong absorption component which does not co-vary with pigment concentration;
3. Phytoplankton blooms with unusual accessory pigment concentrations, *e.g.*, *red tides*, which require the use of special regional or local ocean color algorithms; and
4. Classical extreme Morel and Prieur (1977) Case-2 waters where optical properties are dominated by inorganic particles, with many possible variations in chemical and geometric characteristics.

It is important to recognize that some aspects of the water mass distinctions given above are dependent on the spectral regions in which measurements are to be made. Strong absorption at UV, red, and near-IR wavelengths requires the use of radiometric techniques similar to those required for Case-2 waters.

In addition to determining the bio-optical category and characteristics of a particular water mass, the validation sampling strategy must be concerned with spatial and temporal variability. Spatial and temporal variability in bio-optical properties will profoundly affect the validity of comparisons between satellite and in-water optical measurements. A single SeaWiFS instantaneous FOV measurement, for example, will integrate $L_w(\lambda)$ over approximately a square kilometer, or a larger area at viewing angles away from nadir.

Furthermore, the location uncertainty for a single pixel may be several kilometers, except in near-shore areas where image navigation can be improved by using land-navigated anchor points.

Bio-optical profiles measured at a single station are representative of a spatial scale that is only a small fraction of a kilometer. Data from a grid of several station locations may be required to estimate the spatial averages of optical properties represented by a satellite pixel, or a block of pixels. Because the ship measurements over the grid are not instantaneous, temporal variability in bio-optical properties can add additional uncertainty to the comparisons. Aircraft radiometric observations can, conceptually, be used both to locate comparison sites away from areas of strong spatial variability and to document changes in the pattern of spatial variability over the period required for a ship to occupy all stations in a comparison grid.

Vertical stratification of water temperature, salinity, and density often affect the vertical structure of variability in bio-optical properties. This variability, in turn, affects the remote sensing reflectance. Vertical stratification of the water column becomes especially important in many Case-2 waters, where the top attenuation depth may be as shallow as 1 m to 2 m and the entire euphotic zone may be confined to less than 10 m depth. It is important, therefore, to minimize ship-induced disruption of vertical stratification in the water column. Whenever possible, the ship should be maneuvered as little as possible with its propellers and bow thruster, and the practice of backing down hard to stop quickly when on station should be strongly discouraged. If wind and sea conditions permit, the preferred method of approaching a station is to take enough speed off the ship to coast to a stop over approximately the last 0.5 Km of approach to the station. The approach should be planned to allow the ship to be turned, preferably using only the rudder, to place the sun abaft the beam, or off the stern, depending on where the radiometers will be deployed. It must be realized, however, that depending on wind and sea conditions, and a particular ship's hull and superstructure configuration, it may not be possible to maintain an acceptable orientation, with respect to the sun, while the ship is adrift. In these situations, some use of the engines to maintain an acceptable ship's heading may be unavoidable.

The chief scientist should also consult with the ship's captain and chief engineer to avoid, or at least minimize, overboard discharges while the ship is on station. Material from a ship's bilge or sewage treatment system can significantly change near-surface chemical and optical properties if discharged near the immediate site of a bio-optical profile, or water sample.

In some coastal areas, where a relatively transparent water mass overlies a highly reflective bottom, $L_w(\lambda)$ includes light reflected from the sea floor. These cases require special treatment of bottom reflectance effects, whether the local water mass regime is Case-1, Case-2, or a combination of both. Methods of measurement, experiment design, and sampling strategies to study bottom reflectance effects are beyond the scope of this revision to the ocean optics protocols. There is a significant current research effort focused in this area (Carder *et al.* 1993, Hamilton *et al.* 1993, and Lee *et al.* 1998, 1999), and new protocols in this topic area may be included in a future revision of this document.

The bottom reflection of areas with a water depth exceeding 30 m normally does not contribute to the water leaving radiance, $L_w(\lambda)$. Areas with a depth shallower than 30 m are flagged in the SeaWiFS level two data product. Pixels covering very turbid waters may, however, even be usable even in shallower areas. As a general rule, the water depth should be deeper than 2.5 attenuation lengths, $1/K(490)$, at all ocean color algorithm development and validation stations. The prime exception to this rule is in developing local ocean color algorithms where bottom reflectance contributions must be taken into account (Lee *et al.* 1998, 1999).

Initialization and Validation

Data intended for direct comparisons between *exact normalized water-leaving radiances* (Chapter 13) $L_{wN}^{ex}(\lambda)$ determined from *in situ* measurements and from satellite data should usually be acquired in areas where bio-optical variability is known to be very small. This will ordinarily dictate that such data be acquired from optically clear and persistently oligotrophic Case-1 water masses. Potentially suitable sites include the northeastern Pacific central gyre off Baja, California (to the southwest), and the central Sargasso Sea. When planning validation cruise locations and timing, seasonal and regional cloud cover statistics should also be considered in order to maximize the likelihood of simultaneous satellite and shipboard observations. A Moored Optical BuoY (MOBY) is maintained and operated in a semi-

oligotrophic site in the Northeast Pacific, near Hawaii, to provide continuous time-series radiometric comparisons with SeaWiFS, MODIS and other satellite $L_{WN}^{ex}(\lambda)$ estimates (Chapter 11; Clark *et al.* 1997).

A series of radiometric comparison stations should be made over a wide range of latitude in both the Northern and Southern Hemispheres, to look for evidence of cyclic thermal sensitivity affecting a satellite ocean color sensor. The spacecraft and instrument will be heated by sunlight throughout the descending (daylight) data acquisition segment of each orbit and will be cooled by thermal radiation while in the Earth's shadow throughout the remainder of the orbit. This cycling is likely to induce transient thermal gradients in the instrument, as well as a time varying cycle in the temperatures of its detectors and other components; these thermal variations could affect the spectral bandpass or responsivity of one or more of its channels. Unfortunately, a set of stations covering the full range of latitudes cannot all be sited in regions where mesoscale variability in ocean optical properties can be neglected.

As when acquiring data for developing and validating Case-1 bio-optical algorithms (see below), a significant effort must be exerted to quantify spatial variability in normalized water-leaving radiance. When possible, airborne radiometer data, in combination with careful characterization of atmospheric aerosol and cloud conditions, should be employed to augment shipboard radiometry at the stations selected for this aspect of the validation. If aircraft support is not available, semi-synoptic shipboard transects covering a $20 \times 20 \text{ Km}^2$ grid should be used to characterize spatial bio-optical variability near a sampling station (Clark *et al.* 1997).

The minimum set of variables to be measured for “match-up” validation analyses are those identified as “Required” in Table 3.1. Measurements used to calculate normalized water-leaving radiance for direct comparison to satellite sensor radiances must be made under cloud-free conditions and within five minutes of the satellite overpass.

Case-1 Water: Sampling Strategies

In open-ocean oligotrophic water, it is usually practical to assume that a station is in a Case-1 water mass, although some caution must be taken to detect coccolithophorid blooms and suspended coccoliths. In more turbid coastal transition regimes, however, the classification of the local water mass as Case-1 or Case-2 may be less obvious. In this environment, moreover, Case-1 and Case-2 water masses may both be present in the domain sampled by a ship. One example of this situation would be Case-1 water within an eddy-like intrusion from offshore into coastal areas normally occupied by Case-2 water masses. Another would be Case-2 waters in a major river plume intruding into an ambient Case-1 water mass regime. In general, a water mass may be categorized as Case-1 if:

1. Gelbstoff [Colored Dissolved Organic Matter (CDOM)] absorption at 380 nm, $a_g(380)$, is less than 0.1 m^{-1} ;
2. Total Suspended Particulate Matter (TSM) concentration is less than 0.5 mg L^{-1} (dry weight);
3. measured $L_{WN}(\lambda)$ values, used in the ocean color Case-1 algorithm, predict measured fluorometric chlorophyll *a* concentration within 35 %; and
4. measured $L_{WN}(\lambda)$, used in the ocean color algorithm, predicts measured remote sensing $K(490)$ within 20 %.

The determination of criterion 2 above (Doerffer pers. comm.) will ordinarily require retrospective analysis. On the other hand, *in situ* $a_g(z, 380)$ profiles (*e.g.* using an AC9 – see below), radiometric profiles, and fluorometric pigment samples can ordinarily be analyzed on board to allow determination of criteria 1, 3 and 4 shortly after the samples are acquired.

Ocean color Case-1 algorithm development and validation requires measurements from Case-1 water masses spanning a wide range of optical properties and phytoplankton pigment concentrations. In optically transparent low-chlorophyll oligotrophic water masses, spatial variability is usually small and a station location and sampling strategy like that discussed above under *Initialization and Validation* is appropriate.

In high-chlorophyll mesotrophic Case-1 water masses with increased turbidity, mesoscale and smaller scale variability is often significant. In very productive Case-1 water masses, station placement and many

other aspects of sampling schemes are similar to those discussed below under *Case-2 Waters: Sampling Strategy*. At algorithm development stations, where measurements need neither be coincident with, nor matched to, satellite observations, it will be necessary to characterize spatial and temporal variability only over the relatively short scales distinguishing the separate in-water radiometric, optical, and pigment measurements. Airborne ocean color, or LIDAR, characterizations of spatial variability in the vicinity of these stations will not usually be essential, although such additional information may be very helpful.

At stations where data are acquired for algorithm validation, and where a match to concurrent satellite ocean color measurements is required, it will be necessary to determine the patterns of spatial variability over a domain extending approximately $20 \times 20 \text{ Km}^2$ centered at the station, and to place the ship in a $2 \times 2 \text{ Km}^2$ domain over which $K(490)$ and chlorophyll concentrations vary less than 35 % about the mean. Within a few hours before and after a satellite overpass, in-water measurements should be made at several random locations to characterize variability within the $2 \times 2 \text{ Km}^2$ validation comparison site. In some cases, it may be possible to determine spatial variability adequately from ship station data and alongtrack measurements alone. One approach is to measure the alongtrack profile of *in situ* chlorophyll *a* fluorescence at a depth of approximately 3 m, calibrated by filtered samples to determine chlorophyll *a* concentration at 15 min intervals (Section 9.5 and Chapter 17). The model of Gordon *et al.* (1988) may then be used to estimate $L_{WN}(\lambda)$ from the alongtrack chlorophyll profile (Clark *et al.* 1997). In regions of strong mesoscale variability, concurrent aircraft ocean color, or LIDAR, measurements are also valuable as a guide for selecting the ship's location, and as a basis for spatially extrapolating the in-water measurements to match the much coarser resolution of the satellite ocean color measurements.

Case 2 Waters: Sampling Strategies

Although coastal and continental shelf areas comprise only 10 % of the total ocean area, they provide roughly half of the oceanic new production and most of the sequesterable DOC (Walsh *et al.* 1981). These areas are typically higher in phytoplankton pigment concentration, and may include colored terrigenous constituents such as CDOM and suspended sediments. In these *Case-2* waters, the global color ratio algorithms break down because two or more substances with different optical properties are present which do not co-vary with chlorophyll *a* concentration. These might be waters with exceptional plankton blooms (such as red tides), areas discolored by dust transported by the wind from deserts into the sea, or coastal areas influenced by river discharge of mineral and organic suspended materials, and Colored Dissolved Organic Materials (CDOM, *i.e.* *gelbstoffe*) such as humic acids.

It is not always easy to decide to which case a water mass belongs. As a starting point, the water belongs to *Case-2* if any of the four *Case-1* criteria set forth above, are not satisfied. For *Case-2* waters defined by any one of these criteria, it remains a further problem to determine the specific bio-optical characteristics that distinguish it from *Case-1*. *Case-2* sampling must usually include both the "Required" and "Highly Desired" variables, as identified in Table 3.1, plus TSM. For example, it may be necessary to determine complete pigment composition and other optically important characteristics of exceptional phytoplankton blooms for such planktonic groups as *Coccolithophorids*, *Trichodesmium*, diatoms, cyanobacteria, or dinoflagellates.

To achieve valid comparisons between the ship and satellite data, sharp horizontal gradients and sub-pixel patchiness must be avoided, and accurate image navigation requires land anchor points near the study site. Suitable landmarks are usually available in near-shore coastal waters. The other conditions are difficult to meet in *Case-2* water masses, where mesoscale and sub-mesoscale variability is typically very strong. Sub-pixel variations of no more than $\pm 35 \%$ of the mean pixel chlorophyll will be tolerated, but variability must be measured and taken into account statistically in the analysis (see below).

From the above generalities, it is clear that significant problems are encountered in near-shore coastal waters characterized by small-scale patchiness and dynamic variability due to tidal currents. A particular problem occurs in the shallow areas that are influenced by strong tidal currents - areas that are normally well mixed during part of the tidal cycle. In the slack water tidal phase, however, a vertical gradient of the suspended matter concentration may form, which may cause problems in relating water-leaving radiance to the concentration of suspended matter. During calm periods with strong insolation, even water that is normally well mixed can become stratified. In these cases, the formation of very dense phytoplankton

blooms, such as red tides, can be observed. Such blooms will occur in coastal seas when nutrient concentrations are elevated by the influx of river water. In these circumstances, it is especially critical to avoid disturbing the vertical stratification of the water column with the ship's propellers.

One approach to sampling in this environment has been suggested by R. Doerffer (pers. comm.). In order to get a good statistical base, water samples are first taken in a random order within the area under research. The concentrations derived from the satellite image data are then compared with the ground truth data by statistical parameters, such as the mean, median, standard deviation, and the shapes of histograms (frequency distribution). For this type of statistical comparison, only sections of satellite images that match the area covered by the ship should be analyzed. Water samples and satellite data should also be temporally concurrent within the same tidal phase to avoid biases due to temporal variability. In these regimes, analyses to validate algorithms cannot be based on satellite ocean color data directly, but must instead be based on water-leaving radiance spectra measured *in situ* (Chapter 10) or from above the water surface (Chapter 12). This approach has the advantage that water samples and radiance spectra are taken nearly simultaneously.

Using either flow-through pumping systems, or systems towed outside the ship's wake, fluorometry can be used to assess chlorophyll patchiness if frequent, *i.e.* every 10 min to 15 min, chlorophyll fluorescence-yield calibration measurements are performed. Towed absorption, scattering, reflectance, and beam transmission meters can also be used to characterize spatial variability. Within a few hours of the overpass, the ship should occupy several stations at random locations within a $2 \times 2 \text{ Km}^2$ area central to the area selected for comparison with satellite data. Sampling stations placed across a tidal front during a satellite overpass may help to identify two different water masses, even when the front has moved. Comparisons between *in situ* and satellite data in patchy coastal areas may be enhanced by using horizontal radiance profiles measured from an aircraft flying at low altitude (Section 9.9). Subsets of such airborne profiles allow direct comparisons with shipboard data. A corresponding profile may then be extracted from the satellite image data for a direct comparison to the aircraft trackline profiles. In Case-2 situations, such direct radiometric comparisons are valuable for validating and tuning local algorithms, but are not appropriate for satellite ocean color sensor system validation *per se*.

To validate ocean color atmospheric corrections, water-leaving radiances measured *in situ* from the ship should be compared with those derived from the satellite data. Sample matching problems aside, Case-2 waters are often characterized by strongly varying patchiness in optical properties, pigment concentrations, and remote sensing reflectance at spatial scales smaller than a single pixel resolution of any of the current generation of ocean color sensors. Because of the nonlinear relationship between absorption by pigments, through $b_b(\lambda)/a(\lambda)$, and *exact normalized remote-sensing reflectance* $L_{\text{WN}}^{\text{ex}}(\lambda)/\bar{F}_o(\lambda)$ (Chapters 2, 12 and 13), the pigment concentration derived from spatially averaged satellite radiance data will systematically underestimate the true spatial average concentration by as much as a factor of 2 when sub-pixel variability is significant. It is, therefore, essential to describe sub-pixel scale variability in Case-2 waters both statistically and in terms of organized structure. Such a description may be accomplished through rapid sampling at closely spaced ship stations in combination with airborne ocean color or LIDAR measurements -- for this purpose, trackline data from low altitudes and high-resolution imagery from high altitudes are both acceptable (Section 9.9).

Absorption coefficients are large enough in all Case-2 waters to require instrument self-shading corrections to $L_u(0^-, \lambda)$, even though the correction model (Gordon and Ding 1992) has been experimentally verified only for the case where $a(\lambda)r$ is less than 0.1 (Section 10.4). In extreme Case-2 waters, large values of spectral absorption may confine the first optical attenuation depth to the top 1 m to 2 m, where it is difficult to measure remote sensing reflectance *in situ*. Such short absorption scale lengths lead to instrument self-shading effects in $L_u(0^-, \lambda)$ that are correctable within ~5 % only for instruments with diameters no larger than approximately 1 cm (Gordon and Ding 1992). Radiometers with such a small shadow cross section are conceptually feasible, and a few prototype instruments exist which may be suitable, but they are not commercially available, and self-shading sensitivities have not yet been experimentally verified for these extreme conditions. In these extreme cases, direct *in situ* measurements of $a(\lambda)$, $c(\lambda)$ and $b_b(\lambda)$ (Sections 4.6 and 9.4), together with $L_{\text{WN}}(\lambda)$, or $R_{\text{RS}}(\lambda)$, determined from above-water radiometric measurements (Chapter 12), may provide the only practical means of developing and

validating semi-analytic Case-2 algorithms. This topic remains an important area for near-term research and development.

9.3 RADIOMETRIC MEASUREMENTS & ANALYSIS PROTOCOLS

In-Water Radiometric Profiles (Chapter 10)

Methods for measuring radiometric profiles of spectral upwelled radiance $L_u(z, \lambda)$, downward irradiance $E_d(z, \lambda)$, upward irradiance $E_u(z, \lambda)$ and surface incident irradiance $E_S[t(z), \lambda]$ (above-water) are presented in Chapter 10. The notation $t(z)$ indicates that $E_S[t(z), \lambda]$ is measured simultaneously with the underwater measurements at depth z . The content of this chapter is largely derived from Mueller and Austin (1995), but the presentation was reorganized in Revision 2 of the protocols to treat the topic in a more unified way (Fargion and Mueller 2000, where it appeared as Chapter 9). The measurement methods protocols address ship shadow avoidance, depth resolution in profiles, acquisition of instrument dark readings, and instrument attitude alignment. The protocols identify ancillary measurement and metadata to be acquired and recorded in a log during each radiometric profile measurement. Data analysis recommendations include methods for determining of the respective diffuse attenuation coefficients $K_L(z, \lambda)$, $K_d(z, \lambda)$ and $K_u(z, \lambda)$ profiles, extrapolating $L_u(z, \lambda)$ to the surface to determine $L_u(0^-, \lambda)$ and its transmission through the interface to estimate water-leaving radiance $L_w(\lambda)$ and remote sensing reflectance $R_{RS}(\lambda)$. The omission of directional notation in these quantities (*cf.* below) indicates they are oriented normal to the sea surface, *e.g.* $L_w(\lambda)$ is emitted from the surface in the zenith direction $\theta = 0$. The analysis protocols also address application of instrument calibration factors, dark corrections and depth offsets, as well as a recommended method for instrument self-shading corrections of $L_u(0^-, \lambda)$. The effects that finite bandwidths and Raman scattering have on the radiometric quantities are briefly reviewed, but the present version of the protocols does not include a recommended method for corrections related to either phenomenon. Methods for including Raman scattering corrections in the computation of exact water-leaving radiance $L_{wN}^{ex}(\lambda)$ from $L_w(\lambda)$ are described in Chapter 13.

MOBY, A Radiometric Buoy for Performance Monitoring and Vicarious Calibration of Satellite Ocean Color Sensors: Measurement and Data Analysis Protocols. (Chapter 11)

The Moored Optical Buoy (MOBY) is a unique ocean color observatory that provides the primary *in situ* radiometric measurements for vicarious calibration of satellite ocean color sensors. MOBY and its radiometric and optical sensors are maintained and operated at a location just west of the island of Lanai, Hawaii. The mooring site meets the criteria for validation and initialization measurements, as described in Section 9.2 above. The radiometers and other sensors on MOBY meet, or exceed, the specifications of Chapter 5, and the methods used for instrument characterization and calibration, measurements and data analysis are consistent with the protocols given elsewhere throughout this document. However, the central role of the MOBY observatory in vicarious calibration of satellite ocean color sensors demands, and justifies, extraordinary efforts to assure the highest possible compliance with the protocols in every area. As background for investigators using the MOBY time-series of $L_{wN}^{ex}(\lambda)$ for vicarious calibration of satellite ocean color sensors, the MOBY system design, instrument characteristics, and protocols used by the MOBY Operations Team for sensor characterization and calibration, quality assurance, measurements, and data analysis are documented in Chapter 11.

Above-Water Remote-Sensing Reflectance (Chapter 12)

Proposed protocols are reviewed in Chapter 12 for deriving water-leaving radiance $L_w(\lambda, \theta, \phi \in \Omega_{FOV}; \theta_o)$ and remote-sensing reflectance $R_{RS}(\lambda, \theta, \phi \in \Omega_{FOV}; \theta_o)$ from above-water measurements of radiance emitted from the sea surface and sky at zenith and azimuth angles (θ, ϕ) and $(\theta_{sky}, \phi_{sky})$, respectively, with the sun at zenith angle θ_o . In the convention adopted for these protocols, azimuth angles ϕ are measured relative to the sun's azimuth. The explicit directional notation used in this

context arises, because of the directional nature of skylight reflection (Chapter 12) and the bidirectional nature of ocean's remote sensing reflectance (Chapter 13). Both $L_w(\lambda, \theta, \phi \in \Omega_{FOV}; \theta_o)$ and $R_{RS}(\lambda, \theta, \phi \in \Omega_{FOV}; \theta_o)$ are AOP, which for any combination of IOP in a water mass, are dependent on the incident radiance distribution at the sea surface. For clear sky conditions, variations in surface radiance distribution are governed primarily by variations in solar zenith angle θ_o and aerosol types and amounts. For a given radiance distribution, the radiance measurements are sensitive to the observation angles (θ, ϕ) relative to the sun's principal plane and the unit vector normal to the sea surface, and to a lesser extent, to the magnitude of the radiometer's solid angle field of view Ω_{FOV} sr.

Chapter 12 is organized around 3 alternative proposed $R_{RS}(\lambda, \theta, \phi \in \Omega_{FOV}; \theta_o)$ measurement concepts:

1. Calibrated radiance and irradiance measurements;
2. Uncalibrated radiance and reflectance plaque measurements; and
3. Calibrated polarized surface radiance measurements with modeled irradiance and sky radiance.

The discussion of provisional protocols for measurement and analysis methods distinguish between special considerations applicable to methods 1, 2 and 3. Required ancillary measurements include sun photometer measurements of aerosol optical depth, wind speed and direction, and cloud conditions – variables of special significance for removing reflected sky radiance from the measured surface radiance. The sky radiance reflectance of the sea surface, its sensitivity to (θ, ϕ) and θ_o , and proposed methods for estimating it under clear and cloudy sky conditions, are reviewed in Section 12.4.

This chapter has not changed significantly from Revision 2 to these protocols (Fargion and Mueller 2000), where it appeared as Chapter 10. The Mueller and Austin (1995) provisional protocols for above-water radiometric measurements are seriously flawed and should not be used under any circumstances.

Currently, there is no firm basis for recommending any of the three proposed measurement concepts, and the protocols remain provisional in many respects. For any of the three methods, recommended viewing angles are $(\theta, \phi) = (40^\circ, 135^\circ)$. Specific recommendations are also made regarding preferred methods for estimating skylight reflectance under clear and overcast sky conditions; corrections for skylight reflectance under partially cloudy skies are problematic.

The specific recommendations for viewing angles and skylight correction methods are not unanimously endorsed by the co-authors of Chapter 12. Z.P. Lee (personal comm.), for example, takes strong exception to the superiority of the $\theta = 40^\circ$ viewing angle, especially at wind speeds $> 5 \text{ m s}^{-1}$ using a radiometer with a 20° FOV (full-angle). In this context, he points out correctly, that the angular and wind-speed dependencies of the reflectance of the sea surface are both much stronger in the range $30^\circ \leq \theta \leq 40^\circ$ than they are in the range $20^\circ \leq \theta \leq 30^\circ$. The angular and wind speed W dependencies of surface reflectance $\rho(\theta, \theta', W)$ closely resemble the inverse of the function $\Re(\theta', \theta, W)$ (Chapter 13, Figure 13.4), as these attributes of that function are dominated by the factor $[1 - \rho(\theta', \theta, W)]$ and $\rho(\theta, \theta', W) = \rho(\theta', \theta, W)$. It is apparent that viewing angle and wind-speed related uncertainties of both skylight reflection from, and upward radiance transmission through, the interface are much larger at the larger viewing angles. As a partial exception to this criticism, a 20° FOV is probably too large for either pointing angle, but the point is otherwise well taken.

There are other comments and criticisms in this vein, both from co-authors of Chapter 12 and others in the community, that should be addressed to update and revise the protocols for above-water radiometric measurements and analyses in the next revision to this protocol document.

Normalized Water-Leaving Radiance and Remote-Sensing Reflectance: Bidirectional Reflectance and Other Factors (Chapter 13)

The water-leaving radiances and remote-sensing reflectances defined in Chapters 9 and 10 are apparent optical properties which vary as functions of the solar zenith angle θ_o , the radiance viewing azimuth and zenith angles (θ, ϕ) , the earth-sun distance d on a particular day of the year, the transmission of the sun through the earth's atmosphere, and the ocean's Bidirectional Reflectance Distribution Function (BRDF) (Morel and Gentili 1990, 1993, 1996; Morel *et al.* 1995). The ocean's BRDF is a function of the sea state and seawater IOP: $a(\lambda)$, $b(\lambda)$, $b_b(\lambda)$ and scattering phase function $\beta(\lambda, \Psi)/b(\lambda)$. Chapter 13 reviews the physical process at the interface and in water that act, in concert with the vector radiance field transmitted across the interface, to create the ocean BRDF. These process lead, in turn to the bidirectional properties of water-leaving radiance $L_w(\lambda, \theta, \phi)$, normalized water-leaving radiance $L_{wn}(\lambda)$ (Gordon and Clark 1981), and remote-sensing reflectance $R_{rs}(\lambda, \theta, \phi; \theta_o)$ (Chapter 12). A general method is presented, by which radiative transfer solutions for particular boundary conditions (the downward radiance field above the surface and the wind speed dependent surface reflectance) and IOP profiles, may be used to transform $L_{wn}(\lambda)$ to exact normalized water-leaving radiance $L_{wn}^{ex}(\lambda)$, which no longer has bidirectional properties. For vertically homogeneous Case-1 waters with $Chl \leq 3 \text{ mg m}^{-3}$, Chapter 13 also presents and describes in detail the characteristics of a simplified, approximate solution for transforming $L_{wn}(\lambda)$ to $L_{wn}^{ex}(\lambda)$; the IOP are parameterized as functions of Chl , and lookup tables are available on-line over the Internet (Morel and Maritorena 2001).

Sun and Sky Radiance Measurements (Chapter 14)

Protocols for atmospheric radiometric measurements were addressed only superficially in Mueller and Austin (1995). A new chapter on this subject first appeared as Chapter 11 in Revision 2 to these protocols (Fargion and Mueller 2000), and is included in the present publication, with only modest editorial revisions, as Chapter 14. Chapter 14 provides detailed protocols for two types of radiometric measurements essential to verify atmospheric correction algorithms and to calibrate vicariously satellite ocean color sensors. The first type is a photometric measurement of the direct solar beam to determine the optical thickness of the atmosphere. The intensity of the solar beam can be measured directly, or obtained indirectly from shadow-band radiometer measurements of diffuse global upper hemispheric irradiance. The second type is a measurement of the solar aureole and sky radiance distribution using a radiance distribution camera, or a scanning radiometer viewing in and perpendicular to the solar principal plane. From the two types of measurements, the optical properties and concentration of aerosols can be derived.

Chapter 14 presents measurement protocols for radiometers commonly used to measure direct atmospheric transmittance and sky radiance, namely standard sun photometers, fast-rotating shadow-band radiometers, automating sky scanning systems, and CCD cameras. Discussed are methods and procedures to analyze and maintain quality control over the data, as well as proper measurement strategies for evaluating atmospheric correction algorithms and satellite-derived ocean color products.

9.4 INHERENT OPTICAL PROPERTY MEASUREMENTS AND ANALYSIS PROTOCOLS

The present version of the protocols does not include a comprehensive, up-to-date set of protocols for measuring inherent optical properties (IOP). Refer to Chapter 2 the brief discussion in Section 4.6 for more background on this topic. It is planned to remedy this situation and add IOP protocol chapters to a future revision of Ocean Optics Protocols, but for the present IOP protocols are presented here only as brief abstracts of the current state-of-the-art. The main exception to this situation is that detailed protocols for spectrophotometric measurements of absorption by particles on filters, and by CDOM in filtrate, are presented in Chapter 15.

In Situ Reflective-Tube Absorption and Beam Attenuation Meters

For the development of bio-optical algorithms describing the inherent and apparent optical properties of the water, and for algorithms estimating primary productivity, more stringent requirements are recommended for transmissometer calibration and characteristics. Spectral measurements of beam transmittance should be made with absolute uncertainties of 0.1 % transmittance per meter, or 0.001 m^{-1} beam attenuation coefficient $c(\lambda)$. It is always best to determine optical properties *in situ*, if possible. Sampling variability, changes of light intensities, filtration procedures, and sample degradation over time all affect the particulate matter and distort its true optical properties as they existed in the ocean, and as they determine the remote sensing reflectance viewed by a satellite ocean color sensor.

The reflecting tube method has been used to measure spectral absorption in the laboratory for many decades (James and Birge 1938). In recent years, this method has been adapted for use in the ocean (Zaneveld *et al.* 1992). Suitable instruments are now commercially available and are coming into general use within the oceanographic community. Detailed protocols for using these instruments are not included in this revision of the Ocean Optics Protocols. This is also the situation regarding their calibration (Section 4.6). As with calibrations, protocols for using the instruments and analyzing the measurements are provided by the instrument manufacturer. The best known example of this type of instrument is, perhaps the AC9 manufactured by WETLABS Inc.; protocols and methods for using this instrument and analyzing its measurements are available at (www.wetlabs.com). As with the AC9 calibration protocols (Section 4.6), extensions to the manufacturer's measurement and analysis protocols are described by Twardowski *et al.* (1999) and on the web site maintained by the Oregon State University Optical Oceanography Group at (<http://photon.oce.orst.edu>) (S. Pegau, Pers. Comm.). Perhaps the most critical of the protocols and protocol extensions is the absolute necessity of calibrating the instrument daily with optically pure water if high quality measurements are to be made at sea (Twardowski *et al.* 1999; Pegau, Pers. Comm.).

The reflecting tube does not perfectly gather all scattered light and transmit it to the detector, and as a result, there is a scattering error on the order of 13 % of the scattering coefficient. This error can be largely corrected if the beam attenuation coefficient is measured simultaneously. In that case, the scattering coefficient is obtained as $b(\lambda) = c(\lambda) - a(\lambda)$. By assuming that the measured absorption is due to water and scattering error at a wavelength in the infrared, and by subsequent correction at other wavelengths using a provisional $b(\lambda)$, it is possible to correct the spectral absorption to within a few percent of the scattering coefficient. Only in waters with very high scattering and very low absorption would this error pose a serious absorption uncertainty (Zaneveld *et al.* 1994).

Corrections for ambient temperature and salinity (Pegau and Zaneveld 1993; Pegau *et al.* 1995) require that a CTD profile (Section 9.6) be acquired in conjunction with a profile made using an AC9 or similar instrument. It is strongly recommended that a CTD and the absorption and attenuation meter be attached together on the same profiling package. This ambient temperature correction is in addition to the correction for the instrument's internal temperature, as determined by the manufacturer's calibration (Section 4.6).

If the intake port of an AC9, or similar *in situ* reflecting tube meter, is fitted with a large area 0.2 m^2 filter, the spectral absorption of the dissolved component can be measured (Twardowski *et al.* 1999). A pair of reflecting tube absorption meters can be used thus to determine the separate constituents of absorption due to particulate and dissolved substances - a distinction of fundamental importance in relating absorption to remote sensing reflectance. More traditionally, the filtration and spectrophotometry

techniques developed over the last decade also lend themselves well to this task. Using the methods described in Chapter 12, the spectral absorption coefficient is partitioned into components associated with *gelbstoff*, pigments, and non-pigmented particles (the latter sometimes referred to misleadingly as *detritus*).

Absorption Using Gershun's Equation

In situ spectral absorption coefficient profiles can also be measured with spectral radiometers conforming to the performance specifications listed in Chapter 5, if the radiometric package is extended to measure $E_d(z, \lambda)$ and $E_u(z, \lambda)$, as well as scalar irradiances $\overset{\circ}{E}_d(z, \lambda)$ and $\overset{\circ}{E}_u(z, \lambda)$. This combination may be approached either using hemispherical collectors to measure upwelling and downwelling hemispherical irradiances (Hojerslev 1975), or by using cosine collectors on one radiometer in tandem with spherical collectors on another radiometer. Given these irradiance components, spectral absorption is then computed using Gershun's equation (Gershun 1939) as

$$a(z, \lambda) = \vec{K}(z, \lambda) \frac{\vec{E}(z, \lambda)}{\overset{\circ}{E}(z, \lambda)}, \quad (9.10)$$

where $\vec{E}(z, \lambda) = E_d(z, \lambda) - E_u(z, \lambda)$ is vector irradiance, $\vec{K}(z, \lambda)$ is the vertical attenuation coefficient for vector irradiance, and scalar irradiance $\overset{\circ}{E}(z, \lambda) = \overset{\circ}{E}_d(z, \lambda) + \overset{\circ}{E}_u(z, \lambda)$ (see also Chapter 2).

Comparisons between absorption profiles measured using Gershun's equation with $\vec{E}(z, \lambda)$ and $\overset{\circ}{E}(z, \lambda)$ (scalar irradiance) data, and absorption profiles measured with a reflecting tube instrument, agreed within 8% (Pegau *et al.* 1994). This level of agreement is well within the calibration uncertainties of the particular prototype instruments used for that experiment, which were approximately 10% uncertainties in both the scalar irradiance radiometer and in the reflecting tube instrument. Less than 5% uncertainties in absorption are expected in future experiments, assuming the data are properly averaged to remove near-surface irradiance fluctuations caused by surface waves (Zaneveld *et al.* 2001). In very clear oligotrophic water, moreover, uncertainty in water absorption values may make it impossible to realize this level of relative agreement.

Radiometers equipped with hemispherical irradiance collectors, a prerequisite to application of this method, have only recently become commercially available (HOBILABS Inc; www.hobilabs.com). To date, there is insufficient community experience, in the form of published results based on measurements with this instrument, to include more detailed protocols and uncertainty estimates for this approach. Expanded protocols for Gershun measurements of absorption may appear in a future revision to this document.

Absorption Spectrophotometry of Filtered Particles and Dissolved Materials (Chapter 15)

Protocols in Chapter 15, by Mitchell *et al.*, describe methods for filtering seawater to capture suspended particles on GF/F filters, and for measuring the absorption spectra of the particle-laden filters with a laboratory spectrophotometer. Methods are also described for extracting phytoplankton pigments from the filters, and measuring the residual spectrum of particulate materials other than phytoplankton. Finally, laboratory methods are also described for measuring the absorption spectrum of CDOM in filtered seawater samples. The material in this chapter derives from the results of recent experimental intercomparison workshops in which the authors participated, as well as from the published literature.

Comparative Analyses of Absorption Coefficients

Data from a reflective tube absorption and beam attenuation meter may be analyzed to obtain vertical profiles of $a(z, \lambda)$, $a_g(z, \lambda)$, and $c(z, \lambda)$, and by difference $b(z, \lambda) = c(z, \lambda) - a(z, \lambda)$ and $a_p(z, \lambda) = a(z, \lambda) - a_g(z, \lambda)$. Optical density spectra for filtrate and filtered water samples (Chapter 15) may be analyzed to obtain independent measures of $a_g(z, \lambda)$, $a_p(z, \lambda)$, and $a_d(z, \lambda)$, and by difference $a_\phi(z, \lambda) = a_p(z, \lambda) - a_d(z, \lambda)$.

Methods for merging and comparing the two independent types of absorption measurements, and for interpreting the results in terms of remote sensing reflectance, are the subject of currently active research by several investigators. Future revisions this document may be expected to contain extensive modifications and extensions of these protocols.

Single-Wavelength Transmissometers

Single wavelength transmissometers based on Light Emitting Diode (LED) sources have been in widespread use for more than 20 years. The initial LED transmissometers all measured beam transmission in the red, at wavelengths near 660 nm. Based on recent improvements in LED technology, transmissometers of this type are now also available at blue and green wavelengths. The discussion in Section 4.6 related to the calibration of this type of transmissometer is also relevant to the present subsection.

The windows on the beam transmissometer must be cleaned with lens cleaner, or a mild detergent solution, and a soft cloth, or tissue, rinsed with distilled water, then rinsed with isopropyl alcohol and wiped dry. An approximate *air calibration* reading should be made before every cast to verify that the windows are clean. A transmissometer *dark voltage* should also be measured at this time. These on-deck air calibrations should be logged and compared to the more careful air calibrations done under dry laboratory conditions before and after each cruise (Section 4.6). If pre- and post-cruise air calibrations are significantly different, the time history should indicate whether the change occurred suddenly (*e.g.* a scratch in the window), or as a drift over time.

Raw beam transmissometer voltage profiles, $\tilde{V}(z)$, are first corrected for any range-dependent bias of the A/D data acquisition system [Equation (4.1)]. The corrected voltages, $\hat{V}(z)$, are then further adjusted for instrument drift (occurring subsequent to the factory calibration) with the equation

$$V(z) = \left[\hat{V}(z) - V_{\text{dark}} \right] \frac{V'_{\text{air}}}{V_{\text{air}}}, \quad (9.11)$$

where V_{dark} is the instrument's current dark response with the light path blocked, and V'_{air} and V_{air} are, respectively, the current air calibration voltage (Section 4.6) and the air calibration voltage recorded when the instrument was calibrated at the factory. $V(z)$ is then converted to transmittance, $T_r(z, \lambda)$ over the transmissometer's path length, r [m^{-1}], following the manufacturer's instructions for the particular instrument. The beam attenuation coefficient $c(z, \lambda)$ is then computed as

$$c(z, \lambda) = -\frac{1}{r} \ln \left[T_r(z, \lambda) \right], \text{ m}^{-1}. \quad (9.12)$$

The apparent values of $c(z, \lambda)$ should be further corrected, again following the manufacturer's instructions, for the finite acceptance angle of the instrument's receiver; this is usually a small, but significant, correction. Finally, the beam attenuation coefficient due to particles is computed as

$$c_p(z, \lambda) = c(z, \lambda) - c_w(\lambda), \quad (9.13)$$

where $c_w(\lambda)$ is the beam attenuation coefficient, *i.e.*, $c_w(\lambda) = a_w(\lambda) + b_w(\lambda)$ for pure water. The recommended values of $a_w(\lambda)$ are Pope and Fry (1997), and of $b_w(\lambda)$ are Morel (1974) over the spectral range of interest here (Section 4.6 and Chapter 2).

Scattering Coefficient Determinations

Given measurements of absorption and beam attenuation coefficients, corrected as outlined above, the volume scattering coefficient may computed simply as

$$b(z, \lambda) = c(z, \lambda) - a(z, \lambda), \text{ m}^{-1}. \quad (9.14)$$

Volume Scattering Function and Backscattering Meters

The relationships between the volume scattering function $\beta(\lambda, \Psi)$, the integral moment measurements $\bar{\beta}(\bar{\lambda}, \bar{\Psi}; c)$ made by scattering sensors, and the backscattering coefficient $b_b(\lambda)$ are explained in Chapter 2 and Section 4.6. That information will not be repeated here. Maffione and Dana (1996) describe the methods for estimating $b_b(\lambda)$ from scattering measurements at a single angle in the backward direction, *e.g.* using a HOBILABS HydroScat instrument and following protocols provided by the manufacturer (www.hobilabs.com). WETLABS provides protocols for estimating $b_b(\lambda)$ from scattering measurements at 3 angles using their ECO-VSF instrument (www.wetlabs.com). Boss and Pegau (2001) modified these algorithms by partitioning $\beta(\lambda, \Psi)$ into components associated with particles and pure water to obtain more accurate estimates of $b_b(\lambda)$, especially in clear, oligotrophic waters (see the discussion in Section 4.6).

Stramska *et al.* (2000) combined measured IOP and AOP in a radiative transfer model, and calculated backscattering coefficients agreeing with measurements using a HydroScat sensor within reasonable uncertainty. As emphasized in Section 4.6, while discussing the methods for calibrating scattering sensors, additional research and evaluation are needed to address several key questions before the community will converge on a consensus supporting detailed protocols for backscattering measurements.

Laboratory Measurements of Scattering in Water Samples

Tassan and Ferrari (1995) proposed a method for measuring backscattering and total scattering using a standard dual-beam spectrophotometer and integrating sphere. Balch *et al.* (1999) describe methods for estimating backscattering coefficients using a commercial benchtop laser device. A comprehensive review and development of protocols for methods of this type are deferred to a later revision to this document.

9.5 BIOGEOCHEMICAL AND BIO-OPTICAL PROTOCOLS

High Performance Liquid Chromatography (HPLC) Measurements and Analysis (Chapter 16)

Mueller and Austin (1995) simply adopted the JGOFS HPLC protocols for measuring phytoplankton pigment concentrations by reference (UNESCO 1994), and supplemented them with some brief instructions on sampling and sample handling procedures. Although this approach embraced protocol documentation describing a complete methodology, and represented a community consensus, the lack of a comprehensive end-to-end protocol statement has proved to be a source of confusion and debate within the ocean color community. Furthermore, the JGOFS protocols (UNESCO 1994) specified that pigment concentrations should be reported in units of pigment mass per mass of seawater (ng Kg^{-1}), rather than in units of pigment mass per volume of seawater (either $\mu\text{g L}^{-1}$, or mg m^{-3}). The use of volumetric concentrations is critical because radiative transfer in the ocean, and absorption by pigments, are volumetric processes. One could use the mass concentration values preferred by JGOFS, but it would be essential to supplement them with densities computed from CTD data, and make the conversion to volumetric concentrations. Therefore, a complete set of protocols for HPLC measurement of phytoplankton pigment concentrations was added as Chapter 13 of Revision 2.0 to the Ocean Optics Protocols (Fargion and Mueller 2000), and an updated version of that chapter appears in the present document as Chapter 16. Chapter 16 provides complete protocols for obtaining water samples, filtering them, freezing the filtered samples in liquid nitrogen, sample handling and storage, extraction, HPLC calibrations and measurements, data analysis and quality control.

*Fluorometric Measurement of Chlorophyll *a* Concentration (Chapter 17)*

For reasons similar to those described above for HPLC pigment measurements, it was decided that the protocols for fluorometric measurement of chlorophyll *a* and phaeopigments were too briefly abstracted in Mueller and Austin (1995). Therefore, new detailed protocols for this measurement were added as Chapter 14 to Revision 2 (Fargion and Mueller 2000), and an updated version of those protocols appears in the

present document as Chapter 17. Chapter 17 provides complete protocols for obtaining water samples, filtering them, freezing the filtered samples in liquid nitrogen, sample handling and storage, extraction, fluorometer calibrations and measurements, data analysis and quality control.

In addition, Chapter 17 discusses geographic and temporal variability in the relationship between fluorometric chlorophyll concentrations and combined concentrations of total chlorophyll pigments determined by the HPLC methods (Chapter 16). It is both easier and less expensive to measure chlorophyll *a* and pheopigment concentrations using the fluorometric method, which has the added advantage of allowing shipboard analyses at sea during lengthy cruises. When these data are used for remote sensing algorithm development or validation, however, regional and temporal (*i.e.* cruise-to-cruise) dispersions and/or biases may be introduced unless the fluorometric data are first statistically adjusted (on a local basis) to agree with HPLC determinations of the concentration of total chlorophylls. A cost-effective strategy is to acquire, on each cruise, a majority of filtered pigment samples for fluorometric chlorophyll *a* and pheopigment analysis, supplemented by a smaller number of replicate samples for HPLC pigment analysis. The HPLC replicates should provide a representative distribution over geographic location, depth and time during a cruise, and will be used to determine a local regression relationship between the two measurements. This approach is now required for pigment data submitted for SeaBASS archival and SIMBIOS validation analysis.

Finally, Chapter 17 includes protocols for measuring and analyzing profiles of *in situ* fluorescence by chlorophyll *a*, $F(z)$ (Table 3.1). Together with $c(z,660)$ profiles (Section 9.4), the structure of $F(z)$ provides valuable guidance for selecting depths of water samples, analyses of structure in $K(z,\lambda)$ derived from radiometric profiles, and various aspects of quality control analysis. It is often useful to also digitally record one-minute averages of $F(z, lat, lon)$ in water pumped from a near-surface depth ($z \sim 3$ m) to measure horizontal variability while underway steaming between stations, especially in water masses where mesoscale and sub-mesoscale variability is strong (Section 9.2). If supplemented by frequent fluorometric chlorophyll *a* samples filtered from the flow-through system, the alongtrack profile of $F(z, lat, lon)$ can be “calibrated” in units of chlorophyll *a* concentration (mg m^{-3}).

Phycoerythrin and other Phycobiliproteins

$R_{RS}(\lambda)$ may be enhanced by fluorescence by phycoerythrin (PE) in a band near 565 nm (*e.g.* Hoge *et al.* 1998; Wood *et al.* 1999). The detection from aircraft of laser-induced phycoerythrin fluorescence is already well established (Hoge *et al.* 1998). It is more difficult to detect and quantify solar induced phycoerythrin fluorescence, but some work has been done in that area as well (Morel *et al.* 1993; Morel 1997; Hoge *et al.* 1999; Subramaniam *et al.* 1999).

Various phycoerythrins differ from one another in chromophore composition. All phycoerythrins contain phycoerythrobilin chromophores [PEB; maximum $a(\lambda)$ near $\lambda \sim 550$ nm]; many others also contain phycourobilin chromophores [PUB; maximum $a(\lambda)$ near $\lambda \sim 500$ nm], which extends the range of wavelengths absorbed by the pigment molecule into the blue regions of the spectrum. The ratio of PUB:PEB chromophores in the PE pigments synthesized by different *Synechococcus* strains greatly affects the absorption spectrum of the whole cells (Wood *et al.* 1985). Clearly, the dependence of $a(\lambda)$ on the PUB:PEB ratio of phycoerythrin will affect also $R_{RS}(\lambda)$ in water masses dominated by cyanobacteria. The PUB:PEB ratio for the PE in a given water mass may be characterized using scanning fluorescence spectroscopy (Wood *et al.*, 1999; Wyman, 1992).

The measurement of phycoerythrin is not yet as routine, nor as accurate, as the measurements of chlorophylls and carotenoids. The techniques introduced by Stewart and Farmer (1984) work well for measuring biliproteins in freshwater and estuarine species, but are less successful for natural populations of marine species. Wyman (1992) reported a linear relationship between the *in vivo* fluorescence emission intensity of PE measured in the presence of glycerol and the PE content of *Synechococcus* strain WH7803. Scanning spectral fluorescence measurements have been used to estimate PE concentration of extracted bulk samples (Vernet *et al.*, 1990). Nevertheless, there are few direct measurements of separated PE proteins from natural samples. High Performance Capillary Electrophoresis (HPCE) is a powerful analytical tool currently used in clinical, biochemical, pharmaceutical, forensic, and environmental research. In HPCE, high voltages (typically 10-30 KV) are used to separate molecules rapidly in narrow-

bore (25-100 μm), fused-silica capillaries based on differences in the charge-to-mass ratio of the analytes. HPCE is an automated analytical separation system with reduced analysis times and on-line quantification of compounds, ideally suited to the separation and quantification of water-soluble proteins (like phycobilins) from seawater. HPCE methods for separation analyses of phycoerythrin from cyanobacterial cultures and natural samples are currently under development and may be included in a future revision to the ocean optics protocols (C. Kinkade, Pers. Comm.).

Suspended Particulate Matter

All total suspended particulate material (TSM) dry weight (mg L^{-1}) will be determined gravimetrically as outlined in Strickland and Parsons (1972)⁵. In general, samples are filtered through preweighed 0.4 μm polycarbonate filters. The filters are washed with three 2.5 - 5.0 mL aliquots of DIW and immediately dried, either in an oven at 75°C, or in a dessicator. The filters are then reweighed in a laboratory, back on shore, using an electrobalance with at least seven digits of precision.

Particle Size Distributions

Particle size distributions can potentially provide important information about the shape of the volume scattering function, which strongly influences the bidirectional aspects of remote-sensing reflectance (Chapter 13 and, *e.g.*, Morel and Gentili 1996). Particle size distributions have been measured for many years using Coulter Counters and related to IOP, including $c(\lambda)$ (*e.g.* Kitchen *et al.* 1982). More recently, several investigators have used the Spectrix Particle Size Analyzer to measure particle size distributions. Again, specific manufacturers and equipment items are mentioned here as examples only and no recommendations are to be implied. Protocols for measurements and analyses of particle size distributions (*e.g.*, Chapter 11) are not included in this version of the ocean optics protocols, but should be written and added to a future revision.

9.6 ANCILLARY MEASUREMENTS AND METADATA

The “Required” and “Highly Desired” ancillary measurements and metadata are listed in Table 3.1. Ancillary observations are often of key importance in flagging and interpreting apparently aberrant data. In addition, some of ancillary measurements are essential for corrections to optical measurements, for example the Temperature and Salinity dependence of spectral absorption by pure water must be used in the processing and analysis of AC9 data (Pegau and Zaneveld 1993; Pegau *et al.* 1997). Metadata peculiar to a particular type of measurement, such as instrument calibration information, serial numbers, etc., are specified in the protocols for making those measurements. The present section identifies recommended methods for acquiring and recording the information and data of more general applicability.

Logbooks

The person, or group, making a particular set of measurements normally maintains a separate logbook to record complete metadata unique to a particular instrument, including names of measurement and dark reference data files. It is the chief scientist’s responsibility to also maintain a master logbook in which essential metadata (event, time, location) and general environmental conditions are recorded to link all measurements and samples acquired at each station. At the end of each cruise, the chief scientist should also obtain a photocopy of the ship’s bridge log from the vessel’s master.

Wind Speed and Direction

If possible, anemometer measurements of wind speed and direction should be recorded continuously throughout each station, and underway between stations if alongtrack data are recorded. As a precaution, the wind speed and direction should be read and recorded manually in the master and individual instrument

⁵ In previous versions of the Ocean Optics Protocols (Mueller and Austin 1992, 1995; Fargion and Mueller 2000), it was incorrectly stated that suitable protocols were part of the JGOFS core measurements protocols (UNESCO 1994). The JGOFS protocols do not include TSM measurements of the type specified here.

log entries for each measurement made during a station. If the only available anemometer is not digitally recorded, these manual log entries will obviously be the only record available.

Barometric Pressure

Surface barometric pressure should be read from both the ship's barometer, and from any barometer that is part of an automatically recorded meteorological system, and recorded in the chief scientist's master logbook. This information should be manually logged at the beginning, end, and hourly during sampling at each station. If possible, it is also desirable to digitally record barometric pressure, along with wind speed and direction, throughout each station and while steaming between stations, if other alongtrack meteorological data are recorded.

Cloud Conditions

The percent of the sky covered by clouds should be logged at the time of each measurement event. Identification of cloud types, including such comments as "thin cirrus", is "Highly Desired", but not "Required" (Table 3.1). It is also very useful, for broken and partial overcast conditions, to comment on the relationship between locations of clouds and the zenith and azimuth angles of the sun and satellite, and whether the sun is occluded. For validation cruises, predictions of approximate satellite and solar zenith and azimuth angles for given locations and days are available on request from the SIMBIOS Project Office.

All-sky photographs, using a digital camera equipped with a fisheye lens are useful documentation of sky conditions. Digital photographs of segments of the sky, using a camera with a smaller field-of-view lens, are also useful if annotated with zenith and azimuth pointing angles.

Wave Height

The overall wave height, peak to trough in m, estimated visually by a trained and experienced observer is adequate for purposes of these protocols. As is explained in any introductory textbook on general oceanography, this type of height estimate closely corresponds to *Significant Wave Height*, defined as the average of the highest one-third waves in a 20 min record of measured wave amplitudes. More sophisticated measurements of ocean surface wave characteristics are beyond the scope of these protocols. Where the protocols for a particular measurement require it, *e.g.* above-water remote-sensing reflectance protocols (Chapter 12) or computation of $L_{\text{WN}}^{\text{ex}}(\lambda)$, the wave slope spectrum is calculated from wind speed. Estimates of the percent of the surface covered by whitecaps are also useful as comments, but this may usually be adequately estimated from wind speed as well. Digital photographs of the sea surface conditions are useful documentation of sea state and whitecap conditions at the time of radiometric measurements.

Secchi Depth

A *Secchi Disk* is a white circular disk, approximately 25 cm in diameter, attached to a line marked with a stripe at 25 cm intervals and a broader stripe (or double stripe) at each full meter. A lead weight (~5 Kg) is attached to the bottom of the rig to maintain the disk in a horizontal orientation as it is lowered and raised through the water. The disk should be lowered through the ship's shadow on the side away from the sun to reduce surface glint. The observer pays out the line, lowering the disk until it just disappears from his view and then raises it until just the depth where it again becomes discernable. The depth indicated by the line markings at the water surface when the disk disappears from the observer's view is recorded as Secchi depth in m.

At depths shallower than Secchi depth, the high reflectance of the white disk (~90 %) produces a target with strong visual contrast to the lower reflectance (~2 %) of the ambient water column. As the disk is lowered deeper in the water, irradiance illuminating the disk is reduced and the light reflected from it is also attenuated during its transmittance to the sea surface. Therefore, the apparent contrast between the target and surrounding water is reduced with increasing depth, until at Secchi depth, the contrast disappears between the target and water column. The reader interested in a more quantitative analysis and interpretation of Secchi depth should begin with the treatment by Preisendorfer (1986).

Secchi depth should be taken at least once at each station and recorded in the chief scientist's master log, and in the separate logbooks maintained for radiometric, IOP and CTD-Rosette profiles. It is the author's experience that in optically deep water masses, Secchi depths, in m, display a strong linear correlation with $K(490)^{-1}$, also in m. $K(490)$ is the diffuse attenuation coefficient $K_d(z, 490)$ averaged over the top diffuse attenuation length, and its inverse corresponds to the depth at which measured $E_d(z, 490)$ is 37 % of $E_d(0, 490)$. A useful quality control procedure is to plot Secchi depth against $K(490)$ for every station on a cruise. Departures from a strong linear trend between these variables are indicative of either suspect data, or of anomalous conditions. For instance, if bottom reflectance is significant at a station, then the Secchi depth from that station will be significantly less than that predicted by its deep water correlation with $K(490)^{-1}$. This occurs because the ambient background brightness is enhanced by light reflected by the bottom, and the disk's contrast disappears at a shallower depth that would have occurred in deeper water with the same $K(490)$.

Conductivity, Temperature and Depth (CTD) Profiles

Although Temperature $T(z)$ and Salinity $S(z)$ profiles measured with a CTD are listed as only "Highly Desired" in Table 3.1, these measurements are essential for corrections to *in situ* absorption measurements (see above). Moreover, the availability of a combined CTD and Rosette-sampling system strongly affects the quality of discrete water samples acquired to measure phytoplankton pigment concentrations, which are important "Required" measurements. This is particularly true if the CTD+Rosette system is also equipped with a single-wavelength beam transmissometer to measure, *e.g.*, $c(z, 660)$ (Section 9.4), and a fluorometer to measure *in situ* chlorophyll *a* fluorescence intensity $F(z)$ (Section 9.5). The recommended sampling protocol is to measure, and display in real time on a computer monitor during the downcast, profiles of $T(z)$, $S(z)$, the sea water density anomaly $\sigma_t(z)$, $c(z, 660)$, and $F(z)$. The profile of $\sigma_t(z)$ provides the best indicator of the depth of the mixed layer and strength of the underlying pycnocline. Structure in the $T(z)$ and $S(z)$ profiles may be used to indicate the presence of interleaving water masses with possibly different bio-optical origins and characteristics. The $F(z)$ profiles will identify depths of subsurface maxima and strong gradient features in the chlorophyll profile. The $c_p(z, 660) = c(z, 660) - c_w(z, 660)$ profile will reveal depths of gradients, maxima, and minima in the concentration of suspended particulates. This graphical information can be used to quickly select appropriate depths at which water samples will best represent the bio-optical structure of the water column. Finally, during the upcast, the CTD+Rosette package is stopped at each selected depth, a selected bottle is closed, and its identification number and digitally displayed depth from the CTD unit are recorded in the water sample log.

The combined CTD, transmissometer and fluorescence profiles should be measured in conjunction with, preferably immediately before and after, the irradiance and radiance profile measurements. This is feasible, because more than one cast is typically required to obtain enough water samples for all measurements on each station. The $c_p(z, 660)$ and $F(z)$ profiles are very useful as guides for, and constraints on, the determinations of attenuation coefficients $K(z, \lambda)$ from the radiometric profiles (Chapter 10). These data are also useful information for analyses to develop and validate pigment and primary productivity algorithms. Vertical profiles of CTD should be measured to at least the depth of the deepest bio-optical profile. If the station schedule will permit it, sections of CTD casts extending to 500 m, or deeper, will be useful for computing relative quasi-geostrophic currents and shear that may affect the advection and mixing of bio-optical properties during a cruise.

If possible, a few deep (1,500 m depth or greater) CTD and bottle sample profiles should be made during each cruise to obtain data for calibrating the CTD's conductivity probe. During these *CTD calibration casts*, water samples should be taken at depths where the vertical gradient of salinity is very small. This practice will minimize errors in the conductivity calibration resulting from the spatial separation of the water bottle and CTD profile. The bottled salinity samples may be stored for post-cruise analyses ashore at a laboratory equipped with an accurate salinometer and IAPSO Standard Seawater, if suitable equipment and standard water are not available aboard the ship (Section 4.9).

Each CTD profile should be prefiltered to remove any depth reversal segments resulting from violent ship or hydrowire motions. This will remove many instances of salinity spiking, an artifact which occurs when water temperature changes at a faster rate than the conductivity probe can follow. The CTD data

should then be processed to profiles of potential temperature ($^{\circ}\text{C}$), salinity (Practical Salinity Units [PSU] based on the Practical Salinity Scale of 1978, PSS78), and density (kg m^{-3}) using the algorithms that have been endorsed by the United Nations Educational, Scientific, and Cultural Organization (UNESCO)/SCOR/International Council of Exploration of the Seas (ICES)/IAPSO Joint Panel on Oceanographic Tables and Standards, and also by SCOR Working Group 51 (Fofonoff and Millard 1983).

At this stage, each set of CTD profiles should be carefully examined to detect any significant static instability artifacts resulting from salinity spiking. After any such major artifacts are removed by editing, the data should be further smoothed by averaging temperature and conductivity data into 2 m depth bins, and the final profiles of salinity, density, and other derived parameters should be recomputed using the smoothed CTD profile.

For any hydrographic station, descriptive hydrographic analyses should include T - S profile characterizations of water masses. Features in the density profile that appear to be related to physical mixing and stability should be compared with features in the corresponding bio-optical profiles. CTD profiles from horizontal transects (*i.e.*, two-dimensional grids) should be used in the computation of two-dimensional sections, or three-dimensional gridded arrays, for such variables as geostrophic currents, temperature, salinity, and the density anomaly σ_t . These analysis products, together with corresponding two- or three-dimensional representations of bio-optical variability, can be used to estimate the relative importance of advection and isopycnal mixing in redistributing or modifying upper ocean optical properties during a cruise.

Metadata

For each water sample and measured variable (of all categories) listed in Table 3.1, it is critical to record the date, time (UTC), and geographic position (latitude and longitude in decimal degrees to the nearest 0.001°) of its acquisition or measurement. Position and time metadata should be obtained using a Global Positioning System receiver, if possible.

Depths of measurements made with profiling instruments are usually recorded electronically in the profile data records and files. If measurements are made at depths determined by means other than a pressure transducer integrated with the data acquisition system, then the source of that information must be logged (*e.g.* reference to another file containing time synchronized depth records from an independent instrument on the same package). In the case of a visually read depth scale (*e.g.* line markings, or a rigid scale attached above an instrument), as is sometimes done to obtain depths with uncertainty < 1 cm in very turbid Case-2 waters under calm conditions, each individual depth must be identified with the measurement and entered in a logbook.

The depth from which each water sample is acquired must be recorded in a log, together with all other information required for each measurement to be made from that sample, including pigments (Chapters 16 and 17) and spectrophotometric absorption measurements (Chapter 15). This depth is ordinarily read from the CTD system attached to a rosette sampler. If a CTD, or other instrument equipped with a pressure transducer, and rosette sampler are not used (*e.g.* as with bottles hung directly on the hydro-wire), then the method used to determine bottle depth on closing must be fully described, together with an estimate of the uncertainty in each depth, in comments accompanying the data.

Wire angles should be logged at different depths during each instrument and bottle sampling cast. These entries are critically important for radiometric casts, and for bottle casts when a CTD+Rosette system is not used.

The depth of the water column should be read from the vessel's fathometer and recorded in the log. If the water depth exceeds the range of the fathometer, the recorded depth should be taken from a navigation chart. The distance off the ship of a profiling radiometer, and its direction, and that of the sun, relative to the ship's heading provides an important indication of the likelihood that ship shadow effects may be present in the data. Similarly, the ship's heading relative to the sun may help identify possible shading (or reflection) artifacts in $E_S(\lambda)$ if the shipboard reference radiometer cannot be mounted higher than all masts, antennas, and superstructure elements. It is usually adequate to simply enter a sketch in the log showing the sun and package positions relative to the ship. Of course if the ship's compass heading (in degrees –

Magnetic or True) are recorded, the solar azimuth and zenith may be easily computed from the time and position metadata.

9.7 RADIOMETRIC AND OPTICAL MEASUREMENTS FROM MOORED AND DRIFTING BUOYS

Radiometric and bio-optical measurements from buoys are becoming increasingly common within the ocean color and bio-optical research community. The Moored Optical Buoy (MOBY), a sophisticated radiometric array sited in the lee of Lanai, Hawaii, has proved a key source of water-leaving radiance data for radiometric validation and vicarious calibration of OCTS, SeaWiFS and MODIS ocean color systems (Chapter 11; Clark *et al.* 1997; Fargion *et al.* 1999). The protocols used to acquire time series data at the highly specialized MOBY observatory, as a primary reference for vicarious calibration of satellite ocean color sensors, are documented here in Chapter 11. Other examples of long-term moored arrays incorporating commercially available radiometers of the same type used for underwater profiles (Chapters 5, 6 and 10) include the bio-optical sensors on the Tropical Atmosphere Ocean mooring array (Chavez *et al.* 1998), the Bermuda Test-bed Mooring (Dickey 1995) and a mooring in Bedford Basin (Cullen *et al.* 1997). Examples of radiometers mounted on drifting buoys, and applications to ocean color science, are described in Abbott *et al.* (1995) and Cullen *et al.* (1997).

The applications of moored radiometric arrays within a satellite ocean color validation sampling strategy are briefly described in Section 9.3. There is a powerful potential for combining satellite ocean color imagery with data from moored and drifting radiometers and bio-optical sensors for cost-effective long term monitoring of the ocean. A prime example of this potential was the description of the biological and chemical response of the Equatorial Pacific Ocean to the 1997-98 El Nino observed by combining time series of SeaWiFS and AVHRR imagery with bio-optical and chemical data from the TAO array (Chavez *et al.* 1999). Cullen *et al.* (1997) and Schofield *et al.* (1999) discuss the combined roles of optical buoys and satellite ocean color image data in proposed systems for monitoring harmful algal blooms. Although the present scope of the Ocean Optics Protocols does not embrace a monitoring sampling strategy, it may be appropriate and beneficial to do so in a future revision.

It is planned to add a new chapter to future revision of these protocols that will further address the specialized aspects of radiometric, IOP and fluorometric measurements from buoys. These special considerations include the need to extrapolate radiometric measurements made at fixed near-surface depths to the surface, and bio-fouling of windows and other optical surfaces during extended, unattended deployments. In the present version of the protocols (Revision 3), some of these topics are covered in Chapter 11, as they apply to the MOBY radiometric observatory. The new chapter will address more general applications and methods associated with long-term deployments of moored and drifting bio-optical buoys that cannot be tended to as frequently and closely as is MOBY.

9.9 AIRBORNE MEASUREMENTS

Many references are made in the protocols, for example in Section 9.2, to potential applications of airborne measurements in validation of satellite ocean color systems and data products. Unfortunately, protocols comparable to those in Chapters 5, 6 and 10 – 12, describing accepted instruments and methods for *in situ* ocean radiometry, have not yet been distilled and articulated for airborne remote sensing. An effort will be made to enlist the input of such protocols from key members of the aircraft ocean remote sensing community as an addition to a future protocol revision. For the present, some of the discussion of this topic in Mueller and Austin (1995) is abstracted below.

Airborne measurements of fluorescence by chlorophyll, CDOM, and phycoerythrin, both by LASER and solar excitation, are useful to evaluate spatial and temporal variability near ship and mooring stations and to provide independent assessments of bio-optical algorithms (*e.g.* Hoge *et al.* 1998, 1999).

Airborne ocean color data may also be used to determine spatial variability in ocean optical properties during shipboard algorithm development and validation experiments. Ocean color may be measured from aircraft using either imaging radiometers (usually flown at high altitude), or single FOV spectral radiometers (usually flown at low altitude to measure profiles of ocean color beneath an aircraft's

trackline). Aircraft measurements observe the horizontal variability in ocean color radiance spectra on spatial scales that are much smaller than individual pixels in satellite ocean color images; therefore, these data are more comparable to shipboard measurements. At a qualitative level, this information can indicate how well shipboard radiometric and bio-optical measurements can be compared to satellite ocean color data at typically 1 Km pixel resolution. In this context, airborne ocean color measurements will be especially valuable in productive Case-1 and Case-2 waters, where variability in ocean optical properties can be large over mesoscale and smaller distances. Synoptic maps of ocean color distributions can be advantageously utilized to guide sampling by ships. They can also be used to place in-water data from an individual station in context with respect to nearby variability, and thus provide a basis for spatial interpolation and averaging when comparing in-water bio-optical measurements with, *e.g.*, SeaWiFS image data. This application can be accomplished using aircraft radiometers meeting somewhat less stringent performance specifications than is demanded for direct validation comparison between satellite and aircraft radiance measurements.

For more quantitative work, an airborne radiometer's characteristics must be comparable to radiometric specifications of Chapter 5. Moreover, accurate corrections must be applied for atmospheric and surface reflection (sun and sky glitter) effects. Methods for atmospheric correction and estimation of normalized water-leaving radiances from high altitude airborne ocean color imagery are nearly identical to, and as challenging as, those methods which must be applied to satellite ocean color sensor data itself (Carder *et al.* 1993 and Hamilton *et al.* 1993). These problems and their solutions lie beyond the scope of the ocean optical protocols *per se*, at least in this revision.

REFERENCES

- Abbott, M.R., K.H. Brink, C.R. Booth, D. Blasco, M.S. Swenson, C.O. Davis and L.A. Codispoti, 1995: Scales of variability of bio-optical properties as observed from near-surface drifters. *J. Geophys. Res.*, **100**:13333-13344.
- Austin, R.W., 1974: The remote sensing of spectral radiance from below the ocean surface. In: *Optical Aspects of Oceanography*, N.G. Jerlov and E.S. Nielson, Eds., pp 317-344..
- Balch, W.M., D.T. Drapeau, T.L. Cucci, R.D. Vaillancourt, K.A. Kilpatrick and J.J. Fritz, 1999: Optical backscattering by calcifying algae – separating the contribution by particulate inorganic and organic carbon fractions. *J. Geophys. Res.* **104**: 1541-1558.
- Beardsley, G.F. and J.R.V. Zaneveld, 1969: Theoretical dependence of the near-asymptotic apparent optical properties on the inherent optical properties of sea water. *J. Optical Soc. Amer.* **59**: 373-377.
- Boss, E. and W.S. Pegau, 2001: Relationship of light scattering at an angle in the backward direction to the backscattering coefficient. *Appl. Opt.*, **40**: 5503-5507.
- Carder, K.L., P. Reinersman, R. Chen, F. Muller-Karger, and C.O. Davis, 1993: AVIRIS calibration and application in coastal oceanic environments. *Remote Sens. Environ.*, **44**: 205--216.
- Chavez, F.P., P.G. Strutton, G.E. Friederich, R.A. Feeley, G.C. Feldman, D.G. Foley and M.J. McPhaden, 1999: Biological and chemical response of the Equatorial Pacific Ocean to the 1997-98 El Nino. *Science* **286**:2126-2131.
- Chavez, F.P., P.G. Strutton and M.J. McPhaden, 1998. Biological-physical coupling in the central Pacific during the onset of the 1997-1998 El Nino, *Geophys. Res. Lett.* **25**: 3543.
- Clark, D.K., H.R. Gordon, K.J. Voss, Y. Ge, W. Broenkow, and C.C. Trees, 1997: Validation of atmospheric correction over oceans. *J. Geophys. Res.*, **102**: 17,209-17217.
- Cullen, J.J., A.M. Ciotti, R.F. Davis and M.R. Lewis, 1997: Optical detection and assessment of algal blooms. *Limnol. Oceanogr.*, **42**(5, Part 2): 1223-1239.
- Dickey, T. 1995: Bermuda testbed mooring program. *Bull. Amer. Meteor. Soc.* **76**: 584.
- Fargion G.S., C.R. McClain, H. Fukushima, J.M. Nicolas and R.A. Barnes, 1999: Ocean color instrument intercomparisons and cross-calibrations by the SIMBIOS Project. *SPIE Vol.* **3870**,397-403.

- Fofonoff, N.P., and R.C. Millard, Jr., 1983: Algorithms for computation of fundamental properties of seawater. *UNESCO Tech. Papers in Marine Science*, **44**, UNESCO, 53 pp.
- Gershun, A., 1939: The light field. *J. Math. Phys.* **18**: 51-151.
- Gordon, H.R., and D.K. Clark, 1981: Clear water radiances for atmospheric correction of Coastal Zone Color Scanner imagery. *Appl. Opt.*, **20**: 4,175--4,180.
- Gordon, H.R., and K. Ding, 1992: Self shading of in-water optical instruments. *Limnol. Oceanogr.*, **37**: 491-500.
- Gordon, H.R., O.B. Brown, R.H. Evans, J.W. Brown, R.C. Smith, K.S. Baker, and D.K. Clark, 1988: A semi-analytic radiance model of ocean color. *J. Geophys. Res.* **93**(D9): 10,909-10,924.
- Gordon, H.R., O.B. Brown and M.M. Jacobs, 1975: Computed relationships between the inherent and apparent optical properties of a flat homogeneous ocean. *Appl. Opt.* **14**(2): 417-427.
- Hamilton, M.K., C.O. Davis, W.J. Rhea, S.H. Pilorz, and K.L. Carder, 1993: Estimating chlorophyll content and bathymetry of Lake Tahoe using AVIRIS data. *Remote Sens. Environ.*, **44**: 217--230.
- Hoge, F.E., C.W. Wright, T.M. Kana, R.N. Swift and J.K. Yungel. 1998: Spatial variability of oceanic phycoerythrin spectral types derived from airborne laser-induced fluorescence emissions. *Appl. Opt.*, **37**(21): 4744-4749.
- Hoge, F. E., C. W. Wright, P. E. Lyon, R. N. Swift, and J. Yungel. 1999: Satellite retrieval of the absorption coefficient of phytoplankton phycoerythrin pigment: Theory and feasibility status. MODIS ATBD document 27.
- Hojerslev, N.K., 1975: A spectral light absorption meter for measurements in the sea. *Limnol. Oceanogr.*, **20**: 1024-1034.
- James, H.R., and E.A. Birge, 1938: A laboratory study of the absorption of light by lake waters. *Trans. Wis. Acad. Sci.*, **31**: 1--154.
- Kitchen, J.C., J.R.V. Zaneveld and H. Pak, 1982: Effect of particle size distribution and chlorophyll content on beam attenuation spectra. *Applied Optics*. **21**: 3913-3918.
- Lee, Z.P., K.L. Carder, C.D. Mobley, R.G. Steward and J.S. Patch, 1998: Hyperspectral remote sensing for shallow waters: 1. A semianalytical model. *Appl. Opt.*, **37**(27): 6329-6338.
- Lee, Z.P., K.L. Carder, C.D. Mobley, R.G. Steward and J.S. Patch, 1999: Hyperspectral remote sensing for shallow waters: 2. Deriving bottom depths and water properties by optimization. *Appl. Opt.*, **38**(18): 3831-3843.
- Maffione, R.A. and D.R. Dana, 1996: Instruments and methods for measuring the backward-scattering coefficient of ocean waters. *Appl. Opt.* **36**: 6057-6067.
- Morel, A., 1974: Optical properties of pure water and pure sea water. In: *Optical Aspects of Oceanography*, N.G. Jerlov and E.S. Nielson, Eds., pp1-23.
- Morel, A. 1997: Consequences of a Synechococcus bloom upon the optical properties of oceanic (case 1) waters. *Limnol. Oceanogr.*, **42**: 1746-1754.
- Morel, A., Y.H. Ahn, F. Partensky, D. Vaultot, and H. Claustre. 1993: *Prochlorococcus* and *Synechococcus*: A comparative study of their optical properties in relation to their size and pigmentation. *J. Mar. Res.*, **51**: 617-647.
- Morel, A. and B. Gentili, 1991: Diffuse reflectance of oceanic waters: its dependence on sun angle as influenced by the molecular scattering contribution. *Applied Optics*. **30**(30): 4427-4438.
- Morel, A. and B. Gentili, 1993: Diffuse reflectance of oceanic waters. II. Bidirectional aspects. *Appl. Opt.* **32**(33): 6864-6879
- Morel, A. and B. Gentili, 1996: Diffuse reflectance of oceanic waters. III. Implication of bidirectionality for the remote-sensing problem. *Appl. Opt.*, **35**(24): 4850-4862.

- Morel, A., and L. Prieur, 1977: Analysis of variations in ocean color. *Limnol. Oceanogr.*, **22**: 709--722.
- Morel, A., K.J. Voss, and B. Gentili, 1995: Bidirectional reflectance of oceanic waters: a comparison of modeled and measured upward radiance fields. *J. Geophys. Res.* **100**: 13,143-13,151.
- Mueller, J.L., and R.W. Austin, 1995: Ocean Optics Protocols for SeaWiFS Validation, Revision 1. *NASA Tech. Memo. 104566*, Vol. **25**, S.B. Hooker, E.R. Firestone and J.G. Acker, Eds., NASA Goddard Space Flight Center, Greenbelt, Maryland, 67 pp.
- Neckel, H., and D. Labs, 1984: The solar radiation between 3,300 and 12,500 Å. *Solar Phys.*, **90**: 205--258.
- Pegau, W.S. and J.R.V. Zaneveld, 1993: Temperature dependent absorption of water in the red and near infrared portions of the spectrum. *Limnol. Oceanogr.*, **38**(1): 188-192.
- Pegau, W.S., J.S. Cleveland, W. Doss, C.D. Kennedy, R.A. Maffione, J.L. Mueller, R. Stone, C.C. Trees, A.D. Weidemann, W.H. Wells, and J.R.V. Zaneveld, 1995: A comparison of methods for the measurement of the absorption coefficient in natural waters. *J. Geophys. Res.*, **100**(C7): 13,201-13,220.
- Pegau, W.S., D. Gray and J.R.V. Zaneveld, 1997: Absorption and attenuation of visible and near-infrared light in water: dependence on temperature and salinity. *Appl. Opt.*, **36**(24): 6035-6046.
- Pope, R.M. and E.S. Fry. 1997: Absorption spectrum (380-700 nm) of pure water. II. Integrating cavity measurements. *Appl. Opt.* **36**: 8710-8723.
- Preisendorfer, R. W., 1986: Secchi disk, science: Visual optics of natural waters. *Limnol. Oceanogr.*, **31**(5): 909-926.
- Stewart, D.E. and F.H. Farmer. 1984: Extraction, identification, and quantification of phycobiliprotein pigments from phototrophic plankton. *Limnol. Oceanogr.*, **29**: 392-397.
- Schofield, O., J. Grzymski, W.P. Bissett, G.J. Kirkpatrick, D.F. Millie, M. Moline and C.S. Roesler, 1999: Optical monitoring and forecasting systems for harmful algal blooms: Possibility or pipe dream?, *J. Phycol.* **35**: 1477-1496.
- Stramska, M., D. Stramski, B.G. Mitchell and C.D. Mobley. 2000: Estimation of the absorption and backscattering coefficients from in-water radiometric measurements. *Limnol. Oceanogr.*, **45**: 628-641.
- Strickland, J.D.H., and T.R. Parsons, 1972: *A Practical Handbook of Sea Water Analysis*, Fisheries Research Board of Canada, 310 pp.
- Subramaniam, A., E. J. Carpenter, and P. G. Falkowski, 1999: Bio-optical properties of the marine diazotrophic cyanobacteria *Trichodesmium* spp. II. A reflectance model for remote sensing. *Limnol. Oceanogr.*, **44**: 618-627.
- Tassan, S. and G.M. Ferrari, 1995: Proposal for the measurement of backward and total scattering by mineral particles suspended in water. *Appl. Opt.* **34**: 8345-8353.
- Twardowski, M.S., J.M. Sullivan, P.L. Donaghay and J.R.V. Zaneveld. 1999: Microscale quantification of the absorption by dissolved and particulate material in coastal waters with an ac-9. *J. Atmos. Oceanic Tech.* **16**: 691-707.
- UNESCO, 1994: Protocols for the Joint Global Ocean Flux Study (JGOFS) Core Measurements, Manuals and Guides **29**: 170pp
- Vernet, M., B.G. Mitchell, and O. Holm-Hansen. 1990: Adaptation of *Synechococcus in situ* determined by variability in intracellular phycoerythrin-543 at a coastal station off the Southern California coast, USA. *Mar. Ecol. Prog. Ser.*, **63**: 9-16.
- Walsh, J.J., G.T. Rowe, R.L. Iverson, and C.P. McRoy, 1981: Biological export of shelf carbon is a sink of the global CO₂ cycle. *Nature*, **291**: 196--201.

- Wood, A.M., P.K. Horan, K. Muirhead, D. Phinney, C.M. Yentsch, and J.M. Waterbury, 1985: Discrimination between types of pigments in marine *Synechococcus* by scanning spectroscopy, epifluorescence microscopy, and flow cytometry. *Limnology and Oceanography*, **30**: 1303-1315.
- Wood, A.M., M. Lipsen and P. Coble, 1999: Fluorescence based characterization of phycoerythrin-containing cyanobacterial communities in the Arabian Sea during the Northeast and early Southwest Monsoon (1994-1995). *Deep-Sea Res. II*, **46**: 1769-1790.
- Wyman, M. 1992: An in vivo method for the estimation of phycoerythrin concentrations in marine cyanobacteria (*Synechococcus* spp.). *Limnol. Oceanogr.*, **37**: 1300-1306.
- Zaneveld, J.R.V., E. Boss, and A. Barnard, 2001: Influence of surface waves on measured and modeled irradiance profiles. *Appl. Opt.*, **40**: 1442-1449.
- Zaneveld, J.R.V., J.C. Kitchen, A. Bricaud, and C. Moore, 1992: Analysis of *in situ* spectral absorption meter data. *Ocean Optics XI*, G.D. Gilbert, Ed., SPIE, 1750, 187--200.
- Zaneveld, J.R.V., J.C. Kitchen, and C. Moore, 1994: The scattering error correction of reflecting-tube absorption meters. *Ocean Optics XII, Proc. SPIE*, **2258**: 44-55.

Chapter 10

In-Water Radiometric Profile Measurements and Data Analysis Protocols.

James L. Mueller

Center for Hydro-Optics and Remote Sensing, San Diego State University, California

10.1 INTRODUCTION

Determinations of in-water spectral downwelling irradiance $E_d(z, \lambda)$, upwelling irradiance $E_u(z, \lambda)$ and upwelling irradiance $L_u(z, \lambda)$, both near the surface and as vertical profiles, are required for calibration and validation of the water-leaving radiance as retrieved from the SeaWiFS and other satellite ocean color sensors. Near-surface measurements should profile through at least the top three optical depths to reliably extrapolate to $z = 0$; it is essential to obtain a profile through at least the top optical depth. To better characterize the water column for remote sensing applications, *e.g.*, primary productivity estimation, deeper vertical profiles should be made to 200 m, or seven diffuse attenuation depths whenever possible. Sea bed reflection influences on $L_u(z, \lambda)$ and $E_u(z, \lambda)$ should be avoided for satellite ocean color sensor validation and algorithm development by collecting data only from water deeper than six diffuse attenuation depths for $E_d(490)$; remote sensing applications for optically shallow situations where bottom reflectance is present are not within the scope of these protocols.

At the present state of the art, the most reliable *in situ* method of determining water-leaving radiance $L_w(\lambda)$ is to extrapolate an in-water profile measurement of $L_u(z, \lambda)$ to the sea surface to estimate $L_u(0^-, \lambda)$. Then, $L_w(\lambda) = t L_u(0^-, \lambda) n^{-2}$, where t is the upward Fresnel transmittance of the air-sea interface (~ 0.975) and n is the refractive index of seawater. It is also necessary to measure incident spectral irradiance $E_s(\lambda)$ above the sea surface to determine remote sensing reflectance $R_{RS}(\lambda) = L_w(\lambda) / E_s(\lambda)$. Recent intercomparisons have demonstrated the uncertainty in $L_w(\lambda)$ and $R_{RS}(\lambda)$ determined by this approach to be $< 5\%$ under varied cloud and sea state conditions and for Case 1 waters, at least in the sense of internal consistency of the measurements (Hooker and Maritorena 2000). To date, the best demonstrated uncertainties are $> 10\%$ in $R_{RS}(\lambda)$ determined from above-water measurements of water and sky radiances and $E_s(\lambda)$ (see Chapter 11), due primarily to difficulty in accurately removing the contribution of skylight reflected from a wave-roughened sea surface (*e.g.* Toole *et al.* 2000).

10.2 MEASUREMENT METHODS

There are three primary sources of uncertainty in the determination of $E_d(z, \lambda)$, $E_u(z, \lambda)$, and $L_u(z, \lambda)$ and their respective attenuation coefficients $K_d(z, \lambda)$, $K_u(z, \lambda)$, and $K_L(z, \lambda)$: the perturbation of the in-water radiant energy field by the ship (Gordon 1985, Smith and Baker 1986, Voss *et al.* 1986, and Helliwell *et al.* 1990), shading of the measured water volume by the $E_u(z, \lambda)$, or $L_u(z, \lambda)$, sensor itself (Gordon and Ding 1992), and atmospherically induced variability in radiant energy incident on the sea surface during in-water measurements (Smith and Baker 1984). The influence of ship shadow on the vertical profiles of $E_d(z, \lambda)$, $E_u(z, \lambda)$, and $L_u(z, \lambda)$ is dependent upon the following variables: solar zenith angle, the spectral attenuation properties of the water column, cloud cover, ship size (length, beam, draft, and freeboard) and color, and the geometry of instrument deployment. Self-shading is dependent on

solar zenith angle, the fractional contributions of direct sunlight and diffuse skylight to total incident irradiance, and the diameter of the instrument relative to the absorption scale length $a(\lambda)^{-1}$ of the water in which the measurement is made. Atmospheric variability is primarily dependent upon sun elevation and variations in cloud cover. The near surface in-water data also show variability caused by wave focusing, which can be minimized at a fixed depth by averaging over several wave periods, but which can pose severe problems in vertical profiles during which the instrument descends at speeds of 0.5—1 m s⁻¹ (Zaneveld *et al.* 2001). Raman scattering and fluorescence result in second-order errors near 490 nm (CDOM fluorescence), and at longer wavelengths, contributions from phycoerythrin and fluorescence and water Raman scattering are significant. Based on recent experimental measurements of the Raman scattering cross section and its wavelength dependence (Bartlett *et al.* 1998, and references cited therein), Gordon (1999) recently determined that Raman contributions to remote sensing reflectance are 50 % to 100 % larger than had been previously estimated and is significant at all wavelengths of interest to ocean color remote sensing.

Ship Shadow Avoidance

The complete avoidance of ship shadow, or reflectance, perturbations is a mandatory requirement for all radiometric measurements to be incorporated into the SIMBIOS validation and algorithm database. The influence of ship shadow is best characterized in terms of attenuation length $1/K_d(\lambda)$ (Gordon 1985). Because $L_w(\lambda)$ is required with an uncertainty of 5 % or better, the protocol requires that vertical profiles be measured outside the effects of ship perturbation to the radiant energy field. To accomplish this, the instrument must be deployed from the stern, with the sun's relative bearing aft of the beam. Yet a better approach is to deploy a free falling, profiling radiometer well away from the ship on an umbilical tether.

Estimates of the minimum distance away from the ship, under conditions of clear sunny skies, are given below. The distances are expressed in attenuation lengths to minimize error. For $E_d(z, \lambda)$ measurements, the general equation for distance away, ξ in meters, is given as

$$\xi = \frac{\sin(48.4^\circ)}{K_d(\lambda)}. \quad (10.1)$$

The distance from the ship is required to be $3/K_u(\lambda)$ m for $E_u(z, \lambda)$ and $1.5/K_L(\lambda)$ m for $L_u(z, \lambda)$ measurements. These distances should be increased if the instrument is deployed off the beam of a large vessel. A variety of methods have been used to deploy optical instruments beyond the influence of the ship. During CZCS algorithm development, floating plastic frames were equipped with small winches and instruments to obtain near surface optical profiles at some distance away from the ship. An umbilical cable provided power and data transfer. These platforms, while being somewhat difficult to deploy, worked well at avoiding ship shadow. Alternatively, extended booms can be used to deploy the instrument away from the ship and have the advantages of allowing relatively rapid deployment and simultaneous rosette bottle sampling. As a point of caution, however, very long booms may accentuate unwanted vertical motions due to ship pitch and roll.

Waters *et al.* (1990) used an optical free-fall instrument (OFFI) that allows optical data to be obtained outside the influence of ship perturbation. In addition, the OFFI approach allows optical data to be obtained independently from violent ship motion, which may be transmitted to the instrument via the hydrowire, especially on a long boom. Over the past few years, OFFI-like radiometer systems have become commercially available from several manufacturers and have found widespread use in the ocean color community. In comparisons between several deployment configurations (Hooker and Maritorena 2000), free-fall radiometer systems, in combination with shipboard surface irradiance sensors, yielded water-leaving radiances with the lowest uncertainties. Yet another method for the deployment of optical sensors is via an ROV. Some groups, *e.g.*, Smith (pers. comm.), have deployed a spectrometer on an ROV and obtained data completely free of ship influences.

The above criteria for ship shadow avoidance are admittedly very conservative. Unfortunately, the above cited models and observations provide only approximate guidance on minimum distances at which ship reflectance and shadow effects become insignificant under all circumstances. Therefore, the

SIMBIOS ocean optics protocols embrace relatively extreme distance criteria, recognizing that in many specific combinations of lighting conditions, ships and optical properties, ship shadow, and reflection effects may become unimportant much closer to the ship. The essential requirement is that each investigator establishes that any measurements of $E_d(z, \lambda)$, $E_u(z, \lambda)$, and $L_u(z, \lambda)$ submitted for SIMBIOS validation and algorithm development are free from ship-induced errors. The simplest way to do this is to adhere to the above distance criterion, which is not difficult when using either a tethered free-fall system or instruments mounted on an ROV. In other cases, it is incumbent on the investigator to otherwise demonstrate the absence of ship effects, *e.g.*, through analysis of a series of profiles at increasing distance.

Depth Resolution in Profiles

The instrument sampling rate and the speed at which the instrument is lowered or raised through the water column should yield at least two, and preferably six to eight, samples per meter.

Instrument Dark Readings

The dark current of optical sensors is frequently temperature dependent. As a consequence, accurate radiometric measurements require that careful attention be given to dark current variability. It is recommended that each optical measurement be accompanied by a measurement of the instrument dark current. When there is a large temperature difference between the instrument on the deck and the water temperature, the instrument should be allowed to equilibrate with ambient water temperature at the beginning of each cast.

Deep casts, *e.g.*, 500 m, may permit the determination of the dark current in each optical channel at the bottom of each cast. Many instruments are not designed to be lowered safely to 500 m, however, and this approach is usually not feasible. Furthermore, there is some intrinsic uncertainty over possible contamination by bioluminescence when dark readings are obtained in this way. If the instrument is equipped with a shutter, dark currents can be measured at any depth in the cast. If the dark current is not determined during the cast, it should be determined as soon as possible after the instrument is returned to the deck.

Temperature effects on sensor responsivity can be significant and should not be ignored. Therefore, sensors should be equipped with thermistors on detector mounting surfaces to monitor temperatures for data correction. Otherwise, deck storage should be under thermally protected conditions prior to deployment and on-deck determination of dark voltages.

Surface Incident Irradiance

Atmospheric variability, especially under cloud cover, leads directly to variability of the in-water light field and must be corrected to obtain accurate estimations of optical properties from irradiance or radiance profiles. First order corrections for this variability can be made using above water (on deck) measurements of downwelling spectral irradiance, $E_s(\lambda) = E_d(0^+, \lambda)$. Smith and Baker (1984) and Baker and Smith (1990) theoretically computed the irradiance just below the air-water interface, $E_d(0^-, \lambda)$, from deck measurements to correct in-water profile data.

The deck sensor must be properly gimballed to avoid large errors in $E_s(\lambda)$ due to ship motion in a seaway. Improper gimbaling can actually accentuate sensor motion under some circumstances, however, and this aspect of a shipboard radiometer system must be engineered with some care.

In early versions of the ocean optics protocols (Mueller and Austin 1992, 1995), it was suggested that an improved, more direct determination of $E_d(0^-, \lambda)$ might be obtained by deploying a floating instrument to obtain continuous downwelling irradiance data just below the air-water interface (Waters *et al.* 1990). Over the past several years, instruments implementing this concept have become commercially available and the ocean color community has used them extensively. Unfortunately, experience has demonstrated that downwelling irradiance fluctuations associated with focusing and defocusing of sunlight by surface

waves renders such measurements far noisier than measurements of $E_s(\lambda)$ made above the sea surface. A variant on this approach, wherein the sensor is floated away from the ship but is elevated a meter or so above the water surface, has proved to be a viable alternative, especially in circumstances when it is impossible to install and/or gimbal a deck cell properly.

Instrument Attitude

An instrument's attitude with respect to the vertical is a critical factor in measurements of $E_d(z, \lambda)$ and $E_u(z, \lambda)$, and is only slightly less critical for $L_u(z, \lambda)$. Roll and pitch sensors must, therefore, be installed in the underwater radiometers used for acquiring SIMBIOS validation data. The data from these attitude sensors are to be recorded concurrently with the data from the radiometric channels and are to be used as a data quality indicator. It is not deemed necessary to determine or control attitude determination errors resulting from surface wave-induced accelerations at very shallow depths.

10.3 ANCILLARY MEASUREMENTS AND LOGS

The following ancillary data and information must be recorded in header files and/or logs for each radiometric profile cast:

1. date and time (UTC) of the station and cast;
2. geographic location (latitude and longitude in decimal degrees to the nearest 0.001);
3. the distance between the profiling sensor and the ship, and its direction relative to the ship's heading;
4. the direction of the sun relative to the ship's heading;
5. Secchi depth;
6. cloud cover and sky conditions;
7. wind speed and direction;
8. barometric pressure;
9. dark (zero-offset) data file, to be recorded at the time of the cast and the dark filename logged with the profile entry;
10. times, locations and file identification of associated CTD, in situ fluorescence, and inherent optical property profiles, if any;
11. depths and times of associated water samples, if any;
12. names of files with data from comparisons with a portable irradiance and radiance reference standard made in the field and used to track the instrument's stability during a deployment (Chapter 7);
13. instrument identification;
14. calibration date and file identification (constant throughout a cruise, usually); and
15. depth offsets (to nearest cm) between the pressure transducer and all sensor probes, including $L_u(z, \lambda)$ window, $E_d(z, \lambda)$ and $E_u(z, \lambda)$ collectors, and all ancillary probes on a package.

10.4 DATA ANALYSIS METHODS

This section provides descriptions and discussion of the methods and procedures required to process profile measurements of $E_d(z, \lambda)$, $E_u(z, \lambda)$, and $L_u(z, \lambda)$ from raw counts to radiometric units and attenuation coefficient profiles $K_d(z, \lambda)$, $K_u(z, \lambda)$, and $K_L(z, \lambda)$, and for extrapolating the data to the

sea surface to determine $E_d(z, \lambda)$, $E_u(0^-, \lambda)$, and $L_u(z, \lambda)$. Water-leaving radiance is then determined as

$$L_w(\lambda) = \frac{1-\rho}{n^2} L_u(0^-, \lambda), \quad (10.2)$$

where $\rho \cong 0.025$ is the Fresnel reflectance of the air sea interface and $n \cong 1.34$ is the refractive index of seawater. The term $\frac{1-\rho}{n^2} \cong 0.543$ is the upward radiance transmittance of the sea surface for normal incidence from below, and is not sensitive to wind speed (Austin 1974; see also Chapter 13).

Remote sensing reflectance is then calculated as

$$R_{RS}(\lambda) = \frac{L_w(\lambda)}{E_s(\lambda)}, \quad (10.3)$$

where $E_s(\lambda)$ is downwelling incident irradiance measured above the sea surface, and is equivalent to $E_d(0^+, \lambda)$. It is not recommended to estimate $E_d(0^+, \lambda)$ from in-water determinations of $E_d(0^-, \lambda)$, because wave-focusing effects yield uncertainties approaching 10 % under even ideal circumstances (Siegel *et al.* 1995; Zaneveld *et al.* 2001). The lack of directional notation in (10.2) and (10.3) signifies that the quantities represent nadir viewing values of $L_w(\lambda)$ and $R_{RS}(\lambda)$. Directional (off-nadir at a given azimuth angle from the sun) above-water measurements of surface radiance and remote-sensing reflectance are discussed in Chapters 12 and 13.

Normalized water-leaving radiance, as defined by Gordon and Clark (1981) may be calculated from $L_w(\lambda)$ and $E_s(\lambda)$ as

$$L_{WN}(\lambda) = \frac{L_w(\lambda)}{E_s(\lambda)} \bar{F}_o(\lambda), \quad (10.4)$$

where $\bar{F}_o(\lambda)$ is the mean solar flux immediately above the earth's atmosphere (Neckel and Labs 1984).

The intended effect of (10.4) is to scale each measured $L_w(\lambda)$ to a value consistent with surface illumination by the sun at zenith with no atmosphere, and at the mean earth-sun distance (see also the discussion in Chapter 13). If $E_s(\lambda)$ measurements of acceptable uncertainty are not available, the ratio

$\frac{\bar{F}_o(\lambda)}{E_s(\lambda)}$ may be calculated as in Chapters 11 and 13. The Gordon and Clark (1981) normalization

embodied in (10.4) takes account only of the *intensity* of surface illumination, and neglects the dependence of $L_u(0^-, \lambda)$ on solar zenith angle θ_o and the bidirectional nature of the ocean's reflectance (Morel and Gentili 1996; Chapter 13 and other references cited therein). A further transformation to remove the bidirectional effect and determine a quantity called **exact normalized water-leaving radiance**, $L_{WN}^{ex}(\lambda)$, is necessary to compare $L_{WN}(\lambda)$ based on nadir-viewing field measurements with each other (for differing θ_o and inherent optical properties), or with $L_{WN}(\lambda)$ derived from radiances measured above water from a satellite, aircraft, or ship (Chapter 13).

Dark Corrections

The instrument's dark responses in each channel, which should be recorded either during or immediately after each profile, must be subtracted from the raw data prior to further processing.

Instrument Calibration Analysis

Instrument data from pre- and post-deployment calibrations should be compared with: (1) each other; (2) the long-term history of an instrument's calibrations; and (3) the record of comparisons with a portable field irradiance and radiance standard, to be made frequently during a cruise (Chapter 8).

Based on this analysis of the instrument's history, a calibration file will be generated and applied to transform the dark-corrected data from raw counts to radiance and irradiance units. This analysis, and the rationale for adopting a particular set of calibration coefficients, both for responsivity and wavelength, should be fully described in the documentation accompanying the data set, preferably in an ASCII file to be retained on line with each data set.

Depth Offset Adjustments

The distance of each irradiance collector and radiance window above, or below, the instrument's pressure transducer port must be subtracted, or added, to the nominal recorded depth so that $E_d(z, \lambda)$, $E_u(z, \lambda)$, and $L_u(z, \lambda)$ are associated with the depths where they were actually measured. These depth adjustments may be applied either before, or during, attenuation profile analysis, but in either case must be applied before extrapolating values to the sea surface.

Profile Normalization by Surface Irradiance

The dominant uncertainties in measured $K(z, \lambda)$ profiles result from changes in cloud cover during a cast. Cloud cover variability causes strong variations in incident surface irradiance, $E_s[t(z), \lambda]$ measured at time $t(z)$, over the duration of a radiometric cast. In present usage, $E_s[t(z), \lambda]$ refers to incident spectral irradiance measured with a deck cell aboard a ship. It is strongly recommended that all incident irradiance measurements be made above the sea surface. Smith and Baker (1984 and 1986) discuss a method for propagating $E_s(\lambda)$ through the sea surface to estimate $E_d(0^-, \lambda)$, and they also present a model for adjusting $E_d(0^-, \lambda)$ to compensate for solar zenith angle (see also Chapter 13, Sections 13.1 and 13.2). An alternative scheme for estimating $E_d(0^-, \lambda)$ by measuring $E_d(z, \lambda)$ with a radiometer floated away from the ship and held at a shallow depth z_r during a cast (Waters *et al.* 1990) was also recommended in Mueller and Austin (1995). However, community experience has since demonstrated in-water estimates of $E_d(0^-, \lambda)$ to be far noisier than those based on measurements of $E_s[t(z), \lambda]$ made above the sea surface (Siegel *et al.* 1995; Hooker and Maritorena 2000; Zaneveld *et al.* 2001).

The record of $E_s[t(z), \lambda]$ is recorded simultaneously and together with profiles of $E_d(z, \lambda)$, $E_u(z, \lambda)$, and $L_u(z, \lambda)$. Assuming that transmission of $E_s[t(z), \lambda]$ through the surface does not vary with time, then a simple and effective normalization of the profiles is obtained as

$$\hat{E}_d(z, \lambda) = \frac{E_d(z, \lambda) E_s(t(0^-), \lambda)}{E_s(t(z), \lambda)}, \quad (10.4)$$

where $E_s[t(z), \lambda]$ is the deck cell irradiance measured at the time $t(z)$ when the radiometer was at depth z and $E_s[t(0^-), \lambda]$ is the measurement at time $t(0^-)$ when the radiometer was at the surface.

Some investigators have used $E_s[t(z), \lambda]$ at a single reference wavelength, *e.g.*, 550 nm, to normalize profiles, and have thus ignored the usually small spectral variations in incident irradiance. For SIMBIOS validation and algorithm development, however, the recommended protocol is to use multispectral $E_s[t(z), \lambda]$ measurements. Under no circumstances should a PAR, or other broad-band (*e.g.* photopic response), sensor ever be used for this purpose.

Because of spatial separation between the surface and underwater radiometers, cloud shadow variations are neither measured identically, nor in phase, by the two instruments. The $E_s[t(z), \lambda]$ profiles should, therefore, be smoothed to remove high frequency fluctuations while retaining variations with periods of 15 seconds or greater. The smoothed $E_s[t(0^-), \lambda] / E_s[t(z), \lambda]$ profiles should then be applied as a normalizing function to adjust the measured irradiance and radiance profiles to correct for variations in incident irradiance during a cast.

Some investigators (*e.g.* Sorensen *et al.* 1995), who are faced with the need to process hundreds of radiometric profiles, have implemented automated, semi-autonomous processing and analysis systems which do not include a profile normalization like that embodied in (10.5). In this approach, radiometric profiles are simply rejected and not analyzed if overall variability in $E_s[t(z), \lambda]$ exceeds a minimum

acceptance threshold. For all accepted profiles, it is implicitly assumed that $\frac{E_s[t(0^-), \lambda]}{E_s[t(z), \lambda]} \equiv 1.0$ and is constant throughout the measurement. The only drawback to this approach is that many otherwise usable profiles are not analyzed.

K-Analysis

Normalized profiles of $E_d(z, \lambda)$, $E_u(z, \lambda)$, and $L_u(z, \lambda)$ (with z corrected for pressure transducer depth offset relative to each sensor) should be fit to the equations

$$E_d(z, \lambda) = E_d(0^-, \lambda) e^{-\int_0^z K_d(z', \lambda) dz'}, \quad (10.6)$$

$$E_u(z, \lambda) = E_u(0^-, \lambda) e^{-\int_0^z K_u(z', \lambda) dz'}, \quad (10.7)$$

and

$$L_u(z, \lambda) = L_u(0^-, \lambda) e^{-\int_0^z K_L(z', \lambda) dz'}, \quad (10.8)$$

respectively. The vertical profiles of attenuation coefficients $K_d(z, \lambda)$, $K_u(z, \lambda)$, and $K_L(z, \lambda)$, together with the respective values of $E_d(0^-, \lambda)$, $E_u(0^-, \lambda)$, and $L_u(z, \lambda)$ at the surface, provide the needed specifications for the smoothed irradiance and radiance profiles.

If the natural logarithm of (10.6), (10.7), or (10.8) is taken, an equation of the following form is obtained:

$$-\int_0^z K(z') dz' = \ln[E(z)] - \ln[E(0^-)], \quad (10.9)$$

so that

$$K(z) = - \left. \frac{d \ln[E(z)]}{dz} \right|_z. \quad (10.10)$$

The traditional method of K-analysis, *e.g.*, Smith and Baker (1984 and 1986), is to estimate $K(z)$ as the local slope of $\ln[\hat{E}(z)]$ measured within a depth interval spanning a few meters, and centered at depth z_m . It is assumed that $K(z)$ is constant over the depth interval centered at z_m , so that

$$\ln[E(z)] \cong \ln[\hat{E}(z_m)] - (z - z_m) K(z_m). \quad (10.11)$$

The unknowns $\ln[\tilde{E}(z_m)]$ and $K(z_m)$ are determined as the intercept and (negative) slope of a least-squares regression fit to measured $\ln[\hat{E}(z_m)]$ data within the depth interval $(z_m - \Delta z) \leq z < (z_m + \Delta z)$. The half-interval Δz is somewhat arbitrary. Smith and Baker (1984 and 1986) suggest a Δz of approximately 4 m, but for noisy profiles, a Δz as large as 10 m may be needed to smooth over incident irradiance fluctuations left as residuals by the deck cell normalization.

When this method is used, the shallowest possible values in the smoothed $\ln[\tilde{E}(z_m)]$ and $K(z_m)$ profiles are at depth Δz m and the deepest values are Δz m above the deepest measurements in the profile. If obvious ship shadow effects are present in the data, the shallowest valid smoothed data point will be at depth $(z_s + \Delta z)$ where z_s is the depth to which the data are regarded as contaminated and are excluded from the analysis. It is often convenient, although not necessary, to pre-average radiometric data into, *e.g.*, 1 m, bins prior to performing the least-squares analysis. If this is done, the data should be pre-filtered to remove any noise spikes and then averaged before it is log-transformed.

Each step in the analysis yields increasingly refined information, which requires various amounts of intervention from the analyst. After appropriate editing to remove artifacts, such as the effects of ship shadow, vertical profiles of $K(z, \lambda)$ are computed from the logarithmic decrement with depth of the radiometric profiles. Direct derivative method calculations of $K(z, \lambda)$ profiles using computer techniques (see above) may require the use of a depth interval as large as 20 m, with the result that information about the slope, and hence, about $K(z, \lambda)$ near the top and bottom of the profile, is lost. Averaging over such a large interval also causes the slopes in sharply defined layers, *e.g.*, regions of high gradients, to be poorly represented. Attempts to reduce these effects by using a significantly smaller depth interval often results in unacceptably noisy $K(z, \lambda)$ profiles.

An alternative method of determining K-profiles (Mueller 1995) is to keep (10.9) in integral form, expressed in terms of diffuse attenuation depth (optical depth) $\tau(z, \lambda)$ as

$$\tau(z, \lambda) = -\int_0^z K(z', \lambda) dz' = \ln \left[\frac{E(0^-)}{E(z)} \right]. \quad (10.12)$$

The K-profile is represented analytically by Hermitian cubic polynomials with unknown coefficients, consisting of $K(z_n)$ and its derivative $dK(z_n)/dz$, at each of several discrete depths dividing the profile into finite depth elements. [Hermitian cubic polynomials are defined in any text on finite element modeling, *e.g.*, Pinder and Gray (1977).] The measured set of equations (10.12), corresponding to each measured value $E(z)$ in the profile and depth z in the profile, are assembled into matrix form and the unknown set of coefficients $K(z_n)$ and $dK(z_n)/dz$ are determined using classical least-squares minimization. $E(0^-)$ must be specified externally, and in the current implementation is estimated from the profile itself and adjusted iteratively to yield a minimum least-squares solution to the overall profile. The complete formulation of the method is given in Mueller (1995). Compared to results of the derivative solution, the integral method yields significantly more detailed representation of very sharp layers in bio-optical profiles (when compared to concurrent beam attenuation and chlorophyll fluorescence profiles). The integral solution is more robust in handling data gaps, *e.g.* due to extreme cloud shadows which are not corrected by deck-cell normalization. The integral solution automatically extrapolates the profile to $E(0^-)$ based on a best fit to the entire profile, and not simply to the noisy near-surface layer. On the other hand, the integral method of solution is considerably more difficult to implement than the derivative approach. Moreover, the approach requires an interactive analysis of each profile, and is more time consuming than an automated analysis using the derivative method. For these reasons, the integral solution is not widely used within the ocean color community.

Extrapolation to the Sea Surface

Because of surface waves, it is rarely possible to measure $E_d(z, \lambda)$, $E_u(z, \lambda)$, and $L_u(z, \lambda)$ at depths that closely approximate $z \cong 0^-$. The shallowest reliable readings typically occur at depths ranging from 0.5—2 m. The data from this zone usually exhibit strong fluctuations associated with surface waves, and

thus require some form of smoothing or averaging. It is almost always necessary to apply some means of extrapolating the data upward to the sea surface. Whatever method is used should reconcile extrapolated $E_d(0^-, \lambda)$ with deck measurements of $E_s(\lambda)$.

If $K(z)$ profiles are determined using the derivative method, the shallowest smoothed estimates will occur at depth $z_o = \Delta z$, if there are no ship shadow effects. The usual procedure is to extrapolate values to $z = 0^-$ as

$$E_d(0^-, \lambda) = E_d(z_o, \lambda) e^{K_d(z_o, \lambda) z_o}, \quad (10.13)$$

$$E_u(0^-, \lambda) = E_u(z_o, \lambda) e^{K_u(z_o, \lambda) z_o}, \quad (10.14)$$

and

$$L_u(0^-, \lambda) = L_u(z_o, \lambda) e^{K_L(z_o, \lambda) z_o}. \quad (10.15)$$

If ship shadow is present, z_o may be 20 m or more, and the extrapolation becomes somewhat tenuous.

If $K(z)$ profiles are determined by means of the integral method, then $E_d(0^-, \lambda)$, $E_u(0^-, \lambda)$, and $L_u(0^-, \lambda)$ are automatically determined as part of the fitting procedure. The surface values thus obtained are not necessarily superior to those obtained by extrapolating the derivative method solutions, but they do have the advantage of representing an internally consistent least-squares fit to the entire profile beneath the surface boundary layer.

By either method, extrapolating measured $E_d(z, \lambda)$, $E_u(z, \lambda)$, and $L_u(z, \lambda)$ to $z = 0^-$ becomes very difficult at $\lambda \geq 650$ nm. At these wavelengths, the rapid decrease in daylight over an extremely shallow first attenuation length may compete with an increase in flux with depth due to inelastic scattering. Indeed, it is not unusual to find negative values of $K_d(z, \lambda)$ and $K_L(z, \lambda)$ in strong chlorophyll maxima. Additional research is needed to address measurement and estimation of $E_d(0^-, \lambda)$, $E_u(0^-, \lambda)$, and $L_u(0^-, \lambda)$ at these wavelengths, especially in chlorophyll-rich case 2 waters.

Instrument Self-Shading

Gordon and Ding (1992) modeled the errors introduced by an instrument's own shadow in direct measurements used to determine $E_u(0^-, \lambda)$ and $L_u(0^-, \lambda)$. For this source of error to be less than 5 %, without modeled corrections, the instrument radius r must satisfy $r \leq [40a(\lambda)]^{-1}$ for $E_u(0^-, \lambda)$ and $r \leq [100a(\lambda)]^{-1}$ for $L_u(0^-, \lambda)$. They calculate for $\lambda = 865$ nm in pure water, as an example, that the instrument radius must be approximately 0.3 cm to measure $E_u(0^-, \lambda)$ with a maximum of 5 % error; the instrument radius must be significantly smaller for direct measurement error in $L_u(0^-, \lambda)$ to be 5 % or less.

Gordon and Ding (1992) also propose a simple model for correcting $E_u(0^-, \lambda)$ and $L_u(0^-, \lambda)$ for the self-shadowing effect. They write

$$\tilde{L}_u(0^-, \lambda) = \frac{\hat{L}_u(0^-, \lambda)}{1 - \varepsilon(\lambda)}, \quad (10.16)$$

and

$$\varepsilon(\lambda) = 1 - e^{-\kappa' a(\lambda) r}, \quad (10.17)$$

where $\tilde{L}_u(0^-, \lambda)$ is the true value, $\hat{L}_u(0^-, \lambda)$ is the measured value, $\kappa' = \frac{y}{\tan \theta'_o}$ (θ'_o is the refracted solar zenith angle) and y is an empirical factor for which they give values determined by fitting their model results ($y \approx 2$). A similar correction, with a different table of values for y applies to $E_u(0^-, \lambda)$.

When the above geometric corrections are applied, Gordon and Ding (1992) estimate that errors less than or equal to 5 % in $L_u(0^-, \lambda)$ could be determined from measurements with instruments having maximum diameters of 24 cm for $\lambda \leq 650$ nm, and with instruments of maximum diameter 10 cm for $650 \text{ nm} < \lambda \leq 700$ nm at solar zenith angles $\theta_o \geq 20^\circ$, and maximum chlorophyll a concentrations of 10 mg m^{-3} . To measure $L_u(0^-, \lambda)$ correctable to less than 5 % error at $\theta_o = 10^\circ$ (with chlorophyll a concentrations $\leq 10 \text{ mg m}^{-3}$), maximum instrument diameters are 12 cm for $\lambda \leq 650$ nm and 5 cm for $650 \text{ nm} < \lambda \leq 700$ nm. Even with these corrections, however, instrument diameters of 1 cm or less must be used to assure self-shading $L_u(0^-, \lambda)$ errors are 5 % or less at 780 nm and 875 nm.

The Gordon and Ding (1992) model predictions were compared to experimental measurements of $L_u(0^-, \lambda)$ just beneath the sea surface, using a fiber-optic radiometric probe (Zibordi and Ferrari 1995). The experiment was performed in a lake, with solar zenith angles $25^\circ \leq \theta_o \leq 55^\circ$, on several days with cloud-free skies. Spectrophotometric methods (similar to those in Chapter 15) were used to measure absorption by particles and Gelbstoff. At wavelengths of 500 nm, 600 nm, and 640 nm, a series of discs was employed to vary instrument self-shading geometry in several steps over the range $0.001 < a(\lambda)r \leq 0.1$. The Gordon and Ding (1992) model predicted self-shading radiance and irradiance effects that may be applied as corrections, and which agreed with measured values within 5 % and 3 %, respectively. The model corrections were all biased high relative to the measured values. Zibordi and Ferrari (1995) chose to compare their measurements to the Gordon and Ding (1992) *point-sensor* model, and use of their *finite-sensor* model results may have further improved the comparisons.

This initial confirmation of the Gordon and Ding (1992) instrument self-shading model is confined to clear-sky conditions, solar zenith angles greater than 25° , near-surface $L_u(0^-, \lambda)$ and $E_u(0^-, \lambda)$, and $a(\lambda)r \leq 0.1$. Additional theoretical and experimental research will be necessary to generalize this correction for cloudy sky conditions and for variations with depth in $L_u(z, \lambda)$ and $E_u(z, \lambda)$ profiles. The above restrictions notwithstanding, the excellent agreement shown so far covers a very important range of conditions for SeaWiFS and SIMBIOS algorithm development and validation.

A provisional protocol is given here for radiometer self-shading corrections to $L_u(0^-, \lambda)$ and $E_u(0^-, \lambda)$ derived from in-water radiometric measurements. The protocol is based on the model of Gordon and Ding (1992) and the limited experimental confirmation by Zibordi and Ferrari (1995). Although additional research is necessary to extend and verify these correction algorithms, the results published to date show clearly that even a provisional correction will significantly improve $L_u(0^-, \lambda)$ and $E_u(0^-, \lambda)$ estimated from underwater measurements.

It is first necessary to measure or estimate the spectral absorption coefficient $a(\lambda)$, preferably using *in situ* instruments (Chapters 4 and 9), or if necessary, using the laboratory methods of Chapter 15. It is also possible to estimate $a(\lambda)$ using other approximations suggested by Gordon and Ding (1992), based either on measurements of phytoplankton pigment concentrations, or of irradiance attenuation coefficients.

It will also be necessary to measure, or estimate, the direct solar, $E_{\text{sun}}(\lambda)$ and skylight, $E_{\text{sky}}(\lambda)$ components of incident spectral irradiance, $E_s(\lambda)$, where $E_s(\lambda) = E_{\text{sun}}(\lambda) + E_{\text{sky}}(\lambda)$. The preferred method is to measure these components following the protocols of Chapter 14. Zibordi and Ferrari (1995)

also describe a method of estimating the ratio $\frac{E_{\text{sky}}(\lambda)}{E_{\text{sun}}(\lambda)}$, and Gordon and Ding (1992) suggest yet other alternatives.

Following Zibordi and Ferrari (1995), the coefficients, κ' , given in Table 2 of Gordon and Ding (1992), are fit to linear regression models as functions of the solar zenith angle θ_o in the range $30^\circ \leq \theta_o \leq 70^\circ$. The results given for $L_u(0^-, \lambda)$, with sun only, for a point sensor may be computed as

$$\kappa'_{\text{sun},o} \tan \theta'_o = 2.07 + 5.6 \times 10^{-3} \theta_o, \quad (10.18)$$

and for a finite sensor occupying the full diameter of the instrument,

$$\kappa'_{\text{sun},l} \tan \theta'_o = 1.59 + 6.3 \times 10^{-3} \theta_o, \quad (10.19)$$

where θ_o and θ'_o are the solar zenith angles [in degrees] in air and water, respectively. In practice, the diameter of the radiance sensor aperture is usually a small fraction of the instrument diameter. In the results reported by Zibordi and Ferrari (1995), the point sensor model always overestimated ϵ , and use of the finite sensor model (10.19) will always yield a lower estimate of ϵ . Pending new insights from future theoretical and experimental work, it is suggested to estimate

$$\kappa'_{\text{sun}} \tan \theta'_o = (1-f) \kappa'_{\text{sun},o} \tan \theta_o + f \kappa'_{\text{sun},l} \tan \theta_o, \quad (10.20)$$

where f is the ratio of sensor-to-instrument diameters. The coefficient, κ'_{sky} for the self-shading effect on $L_u(0^-, \lambda)$ caused by incident diffuse skylight is similarly estimated as

$$\kappa'_{\text{sky}} = 4.61 - 0.87 f, \quad (10.21)$$

where the coefficients are derived from values given in Table 3 of Gordon and Ding (1992). Self-shading errors $\epsilon_{\text{sun}}(\lambda)$ and $\epsilon_{\text{sky}}(\lambda)$ for $E_{\text{sun}}(\lambda)$ and $E_{\text{sky}}(\lambda)$ components, respectively, are then computed as

$$\epsilon_{\text{sun}}(\lambda) = 1 - e^{-\kappa'_{\text{sun}} a(\lambda) r}, \quad (10.22)$$

and

$$\epsilon_{\text{sky}}(\lambda) = 1 - e^{-\kappa'_{\text{sky}} a(\lambda) r}, \quad (10.23)$$

where r is the instrument radius in m, and the absorption coefficient $a(\lambda)$ is in units of m^{-1} .

The self-shading error in $L_u(0^-, \lambda)$ is then calculated as

$$\epsilon(\lambda) = \frac{\epsilon_{\text{sun}}(\lambda) + \epsilon_{\text{sky}}(\lambda)}{1+h}, \quad (10.24)$$

where

$$h = \frac{E_{\text{sky}}(\lambda)}{E_{\text{sun}}(\lambda)}. \quad (10.25)$$

Finally, the corrected radiance $\tilde{L}_u(0^-, \lambda)$ is estimated with Equation (10.16).

Similarly, for $E_u(0^-, \lambda)$, the values given in Tables 2 and 3 of Gordon and Ding (1992) determine that for a point irradiance sensor,

$$\kappa'_{\text{sun},o} = 3.41 - 1.55 \times 10^{-2} \theta_o. \quad (10.26)$$

For an irradiance collector with a diameter equal to that of the instrument,

$$\kappa'_{\text{sun},l} = 2.76 - 1.21 \times 10^{-2} \theta_o, \quad (10.27)$$

so that

$$\kappa'_{\text{sun}} = (1-f)\kappa'_{\text{sun},0} + f\kappa'_{\text{sun},1}, \quad (10.28)$$

where f is the ratio of the diameter of the irradiance collector to that of the instrument. For the sky component, κ'_{sky} is defined as

$$\kappa'_{\text{sky}} = 2.70 - 0.48f. \quad (10.29)$$

Values of κ'_{sun} and κ'_{sky} from (10.28) and (10.29) are then substituted in equations (10.21) and (10.22) to obtain $\varepsilon_{\text{sun}}(\lambda)$ and $\varepsilon_{\text{sky}}(\lambda)$ that are then used in (10.23) to solve for $\varepsilon(\lambda)$. Finally, corrected upwelled spectral irradiance $\tilde{E}_u(0^-, \lambda)$ is estimated as

$$\tilde{E}_u(0^-, \lambda) = \frac{\hat{E}_u(0^-, \lambda)}{1 - \varepsilon(\lambda)}, \quad (10.30)$$

where $\hat{E}_u(0^-, \lambda)$ is determined from the upwelled spectral irradiance profile. It is recommended that this correction algorithm be applied to all $L_u(0^-, \lambda)$ and $E_u(0^-, \lambda)$ measurements used for SeaWiFS and SIMBIOS validation and algorithm development. Recognizing the provisional nature of the correction, however, the uncorrected measured values must also be reported. Moreover, the method and data used to estimate $a(\lambda)$, $E_{\text{sun}}(\lambda)$ and $E_{\text{sky}}(\lambda)$ must be documented and reported with all data sets corrected using this protocol.

Finite Bandwidth Correction

In wavelength regions where the absorption coefficient of water varies rapidly (*e.g.* near 565 nm), sensors having Full-Width at Half-Maximum (FWHM) bandwidths exceeding 5 nm interact with water attenuation spectrum to shift the effective wavelength of attenuation coefficients computed from the data. A protocol is not currently provided for correcting this effect.

Siegel *et al.* (1986) and Marshall and Smith (1990) discuss the effects of finite spectral FWHM bandwidth, and the normalized spectral response function, on determination of the attenuation coefficient, $K(\lambda)$, for a vertically homogeneous water column. Given a channel's nominal wavelength, $\bar{\lambda}$ and normalized spectral response function, $R_n(\lambda)$, the apparent attenuation coefficient measured in a homogeneous water column is approximately

$$\hat{K}(z, \bar{\lambda}) = \frac{\int_0^\infty K(\lambda) R_n(\lambda) e^{-K(\lambda)z} d\lambda}{\int_0^\infty R_n(\lambda) e^{-K(\lambda)z} d\lambda}. \quad (10.31)$$

Marshall and Smith (1990) applied a correction for this effect to clear-water profiles of $E_d(z, \lambda)$ at $\lambda=589$ nm. In general, correction of $\hat{K}(z, \bar{\lambda})$ for finite bandwidth effects associated with K for pure water is straightforward. Additional research will be needed to model, from the spectral irradiance data itself, additional bandwidth effects associated with attenuation by phytoplankton and other particles, and to correct $\hat{K}(z, \bar{\lambda})$ accordingly.

Raman Corrections

Marshall and Smith (1990), and the references cited therein, show transpectral Raman scattering contributes significantly to measured irradiance between 500 nm and 700 nm. At a particular wavelength,

the Raman contribution is excited by ambient irradiance at a wavenumber shift of 3,400 cm⁻¹. For example, Raman scattering at a wavelength of 500 nm (20,000 cm⁻¹) is excited by light at wavelength 427 nm (23,400 cm⁻¹), and at 700 nm (14,286 cm⁻¹) by light at 565 nm (17,686 cm⁻¹). Marshall and Smith (1990) give a transverse Raman scattering cross section (at 90°) of 8.2×10⁻³⁰ cm²molecule⁻¹sr⁻¹, a value within the range of other published observations. By integration, they derive a total Raman scattering coefficient of:

$$b_r(488) = 2.6 \times 10^{-4} \text{ m}^{-1}, \quad (10.32)$$

a result recently confirmed by Bartlett *et al.* (1998), as well as by the in situ measurements of Hu and Voss (1997a, 1997b).

The wavelength dependence of the Raman scattering cross section is theoretically about the same as that for Rayleigh scattering

$$b_r(\lambda) \sim b_r(488) \left(\frac{\lambda}{488} \right)^{-4}. \quad (10.33)$$

Bartlett *et al.* (1998) recently measured the wavelength dependence of Raman scattering, however, and found that for excitation wavelengths

$$b_r(\lambda) = b_r(488) \left(\frac{\lambda}{488} \right)^{-5.5 \pm 0.4}, \quad (10.34)$$

for radiance expressed in energy units [μW cm⁻²nm⁻¹sr⁻¹].

A method for applying Raman corrections to measured profiles of irradiance and radiance is suggested and applied to homogeneous clear-water profiles by Marshall and Smith (1990). Additional work is needed to develop a robust Raman scattering correction model for general application in more turbid and vertically stratified water masses. The relative magnitude, and thus importance, of the Raman signal at each wavelength in the upper three attenuation lengths should also be investigated more thoroughly than has been done to date. Gordon (1999) applied the recent results of Bartlett *et al.* (1998), i.e the confirmation of (10.32) and wavelength dependence of (10.34), together with recently improved absorption coefficients for pure water (Sogandares and Fry 1997; Pope and Fry 1997), to model the relative contributions of Raman scattering to water-leaving radiance at wavelengths of interest for ocean color remote sensing. He found that Raman contributions ranged between 20 % and 30 % in clear, oligotrophic waters, and was ~8 % near chlorophyll concentrations of 1 mg m⁻³. Protocols given in Chapter 13 for determining exact normalized water-leaving radiance, $L_{\text{WN}}^{\text{ex}}(\lambda)$, include the effects of Raman scattering.

REFERENCES

- Austin, R.W., 1974. The remote sensing of spectral radiance from below the ocean surface. In: *Optical Aspects of Oceanography*, N.G. Jerlov and E.S. Nielson, Eds., pp 317-344.
- Baker, K.S., and R.C. Smith, 1990: Irradiance transmittance through the air/water interface. *Ocean Optics X*, R.W. Spinrad, Ed., *SPIE*, **1**,302, 556-565.
- Bartlett, J.S., K.J. Voss, S. Sathyendranath, and A. Vodacek, 1998: Raman scattering by pure water and seawater. *Appl. Opt.*, **37**: 3324-3332.
- Gordon, H.R., 1985: Ship perturbations of irradiance measurements at sea, 1: Monte Carlo simulations. *Appl. Opt.*, **24**: 4,172--4,182.
- Gordon, H.R., 1999: Contribution of Raman Scattering to water-leaving radiance: a reexamination. *Appl. Opt.*, **38**: 3166-3174.
- Gordon, H.R., and K. Ding, 1992: Self shading of in-water optical instruments. *Limnol. Oceanogr.*, **37**: 491-500.
- Helliwell, W.S., G.N. Sullivan, B. Macdonald, and K.J. Voss, 1990: Ship shadowing: model and data comparison. *Ocean Optics X*, R.W. Spinrad, Ed., *SPIE*, **1302**: 55-71.

- Hooker, S.B. and S. Maritorena, 2000: An evaluation of oceanographic radiometers and deployment methodologies. *J. Atmos. Oceanic Technol.*, (in press).
- Hu, C. and K.J. Voss, 1997a: Solar stimulated inelastic light scattering in clear sea water, In: Ackleson , S.G. and R. Frouin, Eds: *Ocean Optics XIII*. Proc. *SPIE*, **2963**, 266-271.
- Hu, C. and K.J. Voss, 1997b: In situ measurements of Raman scattering in clear ocean water, *Appl. Opt.* **36**,2686-2688.
- Marshall, B.R., and R.C. Smith, 1990: Raman scattering and in-water optical properties, *Appl. Opt.*, **29**: 71-84.
- Morel, A., and B. Gentili, 1996: Diffuse reflectance of oceanic waters. III. Implication of bidirectionality for the remote-sensing problem. *Applied Optics*, **35**: 4850-4862.
- Mueller, J.L., 1995: Integral method for analyzing irradiance and radiance attenuation profiles. Ch. 3 In: Siegel, D.A., *et al.* 1995: Results of the SeaWiFS Data Analysis Round Robin, July 1994 (DARR-94). *NASA Tech. Memo. 104566*, Vol. **26**, S.B. Hooker and E.R. Firestone, Eds., NASA Goddard Space Flight Center, Greenbelt, Maryland, pp 44-48.
- Mueller, J.L., and R.W. Austin, 1992: Ocean Optics Protocols for SeaWiFS Validation. *NASA Tech. Memo. 104566*, Vol. **5**, S.B. Hooker and E.R. Firestone, Eds., NASA Goddard Space Flight Center, Greenbelt, Maryland, 43 pp.
- Mueller, J.L., and R.W. Austin, 1995: Ocean Optics Protocols for SeaWiFS Validation, Revision 1. *NASA Tech. Memo. 104566*, Vol. **25**, S.B. Hooker, E.R. Firestone and J.G. Acker, Eds., NASA Goddard Space Flight Center, Greenbelt, Maryland, 67 pp.
- Neckel, H., and D. Labs, 1984: The solar radiation between 3,300 and 12,500 Å. *Solar Phys.*, **90**: 205--258.
- Pinder, G.F., and W.G. Gray, 1977: *Finite Element Simulation in Surface and Subsurface Hydrology*, Academic Press, 29 pp.
- Siegel, D.A., C.R. Booth, and T.D. Dickey, 1986: Effects of sensor characteristics on the inferred vertical structure of the diffuse attenuation coefficient spectrum. *Ocean Optics VIII*, M.A. Blizard, Ed., *SPIE*, **637**: 115--124.
- Siegel, D.A., M.C. O'Brien, J.C. Sorenson, D.A. Konnoff, E.A. Brody, J.L. Mueller, C.O. Davis, W.J. Rhea, and S.B. Hooker, 1995: Results of the SeaWiFS Data Analysis Round Robin, July 1994 (DARR-94). *NASA Tech. Memo. 104566*, Vol. **26**, S.B. Hooker and E.R. Firestone, Eds., NASA Goddard Space Flight Center, Greenbelt, Maryland, pp 44-48.
- Smith, R.C., and K.S. Baker, 1984: Analysis of ocean optical data, *Ocean Optics VII*, M. Blizard, Ed., *SPIE*, **478**: 119--126.
- Smith, R.C., and K.S. Baker, 1986: Analysis of ocean optical data. *Ocean Optics VIII*, P.N. Slater, Ed., *SPIE*, **637**: 95--107.
- Sorensen, J.C., M.C. O'Brien, D.A. Konnoff, and D.A. Siegel, 1995: The BBOP data processing system. Ch. 2 In: Siegel, D.A., *et al.* 1995: Results of the SeaWiFS Data Analysis Round Robin, July 1994 (DARR-94). *NASA Tech. Memo. 104566*, Vol. **26**, S.B. Hooker and E.R. Firestone, Eds., NASA Goddard Space Flight Center, Greenbelt, Maryland, pp 37-43.
- Toole, D.A., D.A. Siegel, D.W. Menzies, M.J. Neumann and R.C. Smith, 2000: Remote-sensing reflectance determinations in the coastal ocean environment: impact of instrumental characteristics and environmental variability. *Appl. Opt.*, **39**: 456-469.
- Voss, K.J., J.W. Noltén, and G.D. Edwards, 1986: Ship shadow effects on apparent optical properties. *Ocean Optics VIII*, M. Blizard, Ed., *SPIE*, **637**: 186--190.
- Waters, K.J., R.C. Smith, and M.R. Lewis, 1990: Avoiding ship induced light field perturbation in the determination of oceanic optical properties. *Oceanogr.*, **3**: 18--21.

- Zaneveld, J.R.V., E. Boss, and A. Barnard, 2001: Influence of surface waves on measured and modeled irradiance profiles. *Appl. Opt.*, **40**: 1442-1449.
- Zibordi, G., and G.M. Ferrari, 1995: Instrument self-shading in underwater optical measurements: experimental data. *Appl. Opt.* **34**: 2750--2754.

